Hierarchical Structure of Transition Metal-based Semiconductors for Energy related Applications

Thesis submitted for the degree of

Doctor of Philosophy (Science)

Of

Jadavpur University

By

KAUSIK CHANDA

Index No. : 38/17/Phys./25

THIN FILM & NANOSCIENCE LABORATORY

DEPARTMENT OF PHYSICS

JADAVPUR UNIVERSITY

KOLKATA - 700032

INDIA

2024

JADAVPUR UNIVERSITY

KOLKATA-700 032, INDIA

FACULTY OF SCIENCE

DEPARTMENT OF PHYSICS

Ref. No.

Dated:

CERTIFICATE FROM THE SUPERVISOR

This is to certify that the thesis entitled **"Hierarchical structure of transition metal-based semiconductors for energy related applications"** submitted by **Shri Kausik Chanda**, who got his name registered on 15.05.2017 [**Index No.: 38/17/Phys./25**] for the award of **Ph.D.** (Science) degree of Jadavpur University, is absolutely based upon his own work under the supervision of **Prof. Kalyan Kumar Chattopadhyay** and that neither this thesis nor any part of it has been submitted for either any degree/diploma or any other academic award anywhere before and all the resources have been used in this thesis is properly acknowledged with proper references.

4.03.2024

Prof. Kalyan Kumar Chattopadhyay

(Signature of the Supervisor, Date with Official Seal)

Dr. K. K. Chattopadhyay
Professor
Department of Physics
Jadavpur University
Kolkata-700 032

Dedicated to…

Baba-Ma

"Knowledge can only be got in one way, the way of experience; there is no other way to know."

— Swami Vivekananda

Acknowledgements

The final outcome of this thesis entitled ***"Hierarchical Structure of Transition Metal-based Semiconductors for Energy related Applications"*** *received a lot of guidance and assistance from many people and I am extremely fortunate to have got these people all along the completion of my Ph.D. study. There is too little room to accommodate all of you on this piece of paper, but be sure that there is always room in my heart and in my memory to cherish all those gold strings of bright moments that will be connecting us forever. First and foremost, I would like to express my great admiration and gratitude to my supervisor, Prof. Kalyan Kumar Chattopadhyay, for his precious teachings, guidance, and many interesting discussions, which have been of great help to me and also for his strong support in every moment of my research activity in these years. From that very beginning, he provided me with unflinching encouragement and support in various ways. Working in his laboratory was a pleasant experience, and I will forever cherish the valuable time I have spent with him. Prof. Chattopadhyay taught me that every mistake is a learning opportunity, and I am grateful to him for his patience and encouragement. I have learned enormous things from my supervisor. I hope that this is only the starting point of my future career. Thank you, Sir, for giving me the privilege to work in your research lab.*

Dr. Partha Bairi is the one person who has inspired me to pursue this career and has always understood all of my issues from both a scientific and personal standpoint. He is the only person with whom I can argue on personal and as well as on scientific issues. Without his mental support, this work would not have been completed.

I would like to express my deepest gratitude to my senior, Dr. Soumen Maiti, for the kind support that he provided during the course of this research work. I would especially want to thank Dr. Nirmalya Sankar Das for designing the Table of Contents of my research article. I convey my sincere gratitude to Dr. Samat Sarkar as well.

I would like to acknowledge my M.Sc. project supervisor, Prof. Anjan Barman for his inspirations that guided me to choose basic scientific research as my career. I am also grateful to all my respected teachers involved throughout my academic career for their proper guidance and influential teaching which helped me to achieve my goals. Especially, I should mention my favourite Physics teacher, Arun Kumar Mukherjee who developed my interest in physics.

Special thanks go to my great lab colleagues, who helped me to continue my research in a friendly atmosphere. I relished the time spent with my lab mates Subhasish, Nripen,

Anjan, Kausik, Dipayan, Ratna, Dipanwita, Suvankar, Karamjyoti, Saikat, Tufan, Shrabani, Madhupriya, Bikram, Souvik, Dimitra, Arnab and Anibrata who helped me to tackle all the difficulties, stood beside me and gave all kinds of support. I am sure there are some I may have missed, but they are no less appreciated.

I would like to acknowledge all the office, administration, and research cell staff of Jadavpur University for their kind help.

Last but not least, I thank my parents for the great gift of life in this beautiful world full of so nice things and challenging tasks. I will forever remain indebted to their unconditional love, encouragement and support to pursue my interests. My mother is like a big banyan tree where I can take shelter at every moment of my life. Thanks to my elder sister acting as a teacher, friend, and guide since my childhood. I would like to thank the junior most member of our family, my nephew Ankit for his love and blind support. I convey my gratitude to my Jamai Babu, all other relatives, and my late grandmother for their belief in me, endless encouragement, and well wishes. I gratefully acknowledge my parents for their encouragement, support, and sacrifice in making my research possible.

I gratefully acknowledge the Council of Scientific and Industrial Research for giving financial assistance, as well as the Thin Film & Nanoscience Lab, Jadavpur University, for providing me with this platform to accomplish my work.

Lastly, I would want to sincerely thank all of my well-wishers and friends whose memories and influence will always be a part of my life.

March 2024

Department of Physics,

Jadavpur University,

Kolkata 700032, India

Kausik Chanda

Contents

Abstract

Nanoscience and nanotechnology have emerged as the most promising field of research for the development of our society. Nanotechnology has become an extensively researched topic in various scientific domains, including physics, chemistry, biology, and engineering. The rapid pace of technological progress has inspired people to innovate and create technical solutions that are not only environmentally friendly but also cost-effective to fulfill their daily requirements. Nanomaterials have emerged as a solution to meet these demands due to their small size and improved physical properties as a result of their reduced dimensions. The physical properties of nanomaterials have been found to be significantly different and exciting from their bulk counterparts, primarily owing to the effect of quantum confinement. The electronic energy levels in nanomaterials are not continuous like they are in bulk materials. Instead, they are finite and discrete due to the electronic wave function being confined to the physical dimensions of the particles. Hence, the application potential of nanoscience and nanotechnology has significantly impacted optoelectronic devices, energy harvesting and storage devices, energy conversion devices, and more. Further, nanotechnology offers several advantages due to its ability to customize material structures at extremely small scales to meet specific requirements. This significantly expands the toolkit of materials science by enabling the creation of stronger, lighter, and more durable materials with improved reactivity, sieve-like properties, and better electrical conductivity, among other features.

The synthesis protocol of nanomaterials is the key aspect for extracting the highest performance from the pristine materials. Until now, many synthesis processes have been employed to modulate the size and morphology. Much effort has been put worldwide to innovate and improve the synthesis techniques, but still, the pristine materials suffer from

shortcomings like poor electrical conductivity, agglomeration, etc. Here comes into play the hybrid or hierarchical nanostructures whose realization can mitigate all the individual shortcomings of the constituents and result in novel interface phenomena.

In the recent developments of nanoscience and nanotechnology, hierarchical nanostructure, an integrated architecture with a higher assembly-level of constituents using low dimensional nano-building blocks (viz. nanoparticles, nanorods, nanowires, nanotubes and nanosheets, etc.), has drawn a lot of interest. The organized hierarchy of nanostructures may provide several advantages like increased active sites, synergistic effects due to the variety in their building blocks and geometric complexity, and multifunctional features. Hierarchical nanostructures possess remarkable characteristics that enable the development of advanced catalysts, highly responsive sensors, and exceptional adsorption materials, which can be utilized in various technological applications.

Humankind is now facing serious energy and environmental difficulties due to the depletion of fossil fuel reserves and the conspicuous environmental degradation they cause. Hence, clean, sustainable energy generation, storage, and its use have become a significant issue for the twenty-first century, and both academic and industrial domains are paying more and more attention to this subject. This issue further promises a spectacular opportunity to achieve the idea of rebuilding energy-supplying systems that can work indefinitely and without causing pollution. The realization of cutting-edge functional materials is essential for the production, storage, and consumption of energy. The field of energy has completely changed as a result of the development of nanotechnology and the fabrication of nanodevices. Hierarchical nanostructures are regarded as exceptional candidates as they can exhibit superior qualities to ordinary nanomaterials. Multicomponent hierarchical nanostructures are ideal for energy applications in fuel cells, supercapacitors (SCs), solar

cells, and other devices due to their improved electrocatalytic performance, high energy density, high flexibility, quick charge-discharge capability, specific capacitance, and prolonged cycle life, etc. These exceptional features can further be enhanced by modulating the smart design and structure.

For the past few decades, various transition metal-based semiconductors, such as RuO_2, MnO_2, Co_3O_4, NiO, and CuO, etc., have been extensively investigated as electrode materials for SCs and electrochemical water splitting as discussed in the introduction section. Transition metal-based materials can demonstrate superior electrochemical activity compared to carbonaceous (carbon-based) materials and conducting polymers. In order to enhance the electrochemical performance of the electrode materials further, the energy research community is currently focusing on hierarchically nanostructured transition metal-based compounds. Such materials have gained popularity due to their ability to offer numerous electroactive sites that can be accessed for redox reactions. Additionally, the hierarchical nanostructure helps to shorten the ion diffusion pathway.

The primary objective of this thesis is to concentrate on the engineering of hierarchical nanostructures of transition metal-based compounds that aim to provide a range of sustainable energy and device applications. Besides chemical synthesis and integration techniques, the potential use of hierarchical nanostructures in energy generation and storage devices has been studied. In this regard, flake-like nanostructures of $CuCo_2O_4$ were synthesized on flexible carbon fabric through a hydrothermal approach. The secondary growth of MnO_2 surrounding $CuCo_2O_4$ nanoflakes was realized further to get $CuCo_2O_4$@MnO_2 hierarchy on carbon fabric. A well-optimized $CuCo_2O_4$@MnO_2 hierarchy was used as electrode materials for SC. The electrode demonstrated a high specific capacitance of 1458 F g^{-1} at a current density of 0.5 A g^{-1} in 1 M KOH electrolyte, along with excellent cyclic stability. This result is almost two-fold higher than that offered

by the pristine $CuCo_2O_4$ electrode. The $CuCo_2O_4$@MnO_2 electrode was further devised to realize a flexible solid-state symmetric supercapacitor device, which offered a specific capacitance of 181.3 F g^{-1} at 2.8 A g^{-1} and a high energy density of 64.1 Wh kg^{-1} at a power density of 1.5 kW kg^{-1}. Besides, this symmetric supercapacitor device sustained a wide potential window of 1.6 V. The Symmetric supercapacitor device successfully managed to drive a number of electronic gadgets like different colored LEDs, a motor fan, a digital clock, etc.

Further, a hierarchy of nitrogen-doped carbon hollow spheres and MoS_2 (NC@MoS_2) was realized, and electrocatalytic hydrogen evolution activity (HER) was investigated. The optimized NC@$MoS_2$1100 electrode showed excellent HER activity with a low onset overpotential of 9 mV and an overpotential of 145 mV at a current density of −10 mA cm^{-2}. It also demonstrated a low Tafel slope of 39 mV dec^{-1} and excellent chronoamperometric stability.

A TiO_2@MoS_2 core@shell hierarchy was also realized and used as an electrode material for SC. This TiO_2@MoS_2 hybrid showed a specific capacitance of 152.2 F g^{-1} at 0.1 A g^{-1}, which was found to be 30-fold higher than pristine TiO_2 spheres.

Thus, this thesis highlights the importance of morphology engineering in hierarchical nanostructures of transition metal-based semiconductors to enhance electrochemical performance. The insights gained from this research may inspire future researchers to develop innovative ideas for the evolution of sustainable energy technology.

List Of Publications

1. Hierarchical Assembly of MnO_2 Nanosheet on $CuCo_2O_4$ Nanoflake over Fabric scaffold for Symmetric Supercapacitor, Kausik Chanda, Soumen Maiti, Samrat Sarkar, Partha Bairi, Subhasish Thakur, Kausik Sardar, Nripen Besra, Nirmalya Sankar Das and Kalyan Kumar Chattopadhyay, ACS Appl. Nano Mater. 2021, 4, 2, 1420–1433.

2. Crystallinity and Interfacial Mo-N-C Bond Engineered MoS_2 Embedded Graphitic Nitrogen Doped Carbon Hollow Sphere for Enhanced HER Activity, Kausik Chanda, Partha Bairi, Soumen Maiti, Anjana Tripathi, Ranjit Thapa, Shrabani Ghosh, Karamjyoti Panigrahi, Dipayan Roy, Ratna Sarkar and Kalyan Kumar Chattopadhyay, Int. J. Hydrog. Energy 2024, 56, 570–581.

3. Hierarchical Heterostructure of MoS_2 Flake Anchored on TiO_2 Sphere for Supercapacitor Application, Kausik Chanda, Subhasish Thakur, Soumen Maiti, Anubhab Acharya, Tufan Paul, Nripen Besra, Saikat Sarkar, Anjan Das, Kausik Sardar and Kalyan Kumar Chattopadhyay, AIP Conf. Proc. 1953, 030138 (2018).

4. Enhanced Interfacial Evaporation and Desalination by Solar Heat Localisation using Nitrogenated Graphitic Carbon and Co_3O_4 Nanorods, Dipanwita Mitra, Kausik Chanda, Souvik Bhattacharjee, Partha Bairi, Kalyan Kumar Chattopadhyay and Paramita Chattopadhyay, Sol. Energy Mater Sol. Cells 2023, 257, 112361.

5. Shape-Shifting via Salt Crystallization: Conversion of Nanostructured Polymer into Site-Selective Nitrogen-Doped Carbon Sheet with Enhanced Supercapacitive Performance, Partha Bairi, Kausik Sardar, Kausik Chanda, Madhupriya Samanta, Subhasish Thakur, Karamjyoti Panigrahi, Saikat Sarkar, Tufan Paul and Kalyan Kumar Chattopadhyay, ACS Appl. Energy Mater. 2020, 3, 6, 5984−5992.

6. Nanoporous Nitrogen-Doped Graphitic Carbon Hollow Spheres with Enhanced Electrochemical Properties, Partha Bairi, Kausik Sardar, Madhupriya Samanta,

Kausik Chanda and Kalyan Kumar Chattopadhyay, Mater. Chem. Front. 2021, 5, 7645-7653.

7. Hydrothermal Synthesis of GO Wrapped BiOCl Nanosheet and its Application in Visible Light Assited Catalytic Degradation of Rhodamine B dye, Ratna Sarkar, Dimitra Das, Kausik Chanda, Brahami Das, Subrata Sarkar and Kalyan Kumar Chattopadhyay, Mater. Chem. Phys. 2022, 279, 125796.

8. New Class of Trimetallic Oxide Hierarchical Mesoporous Array on Woven Fabric: Electrode for high-Performance and Stable battery type Ultracapacitor, Subhasish Thakur, Soumen Maiti, Kausik Sardar, Nripen Besra, Partha Bairi, Karamjyoti Panigrahi, Kausik Chanda, Tufan Paul and Kalyan Kumar Chattopadhyay, J. of Energy Storage 2021, 35, 102249.

9. Amalgamation of $MnWO_4$ Nanorods with Amorphous Carbon Nanotubes for Highly Stabilized Energy Efficient Supercapacitor Electrodes, Kausik Sardar, Subhasish Thakur, Soumen Maiti, Nripen Besra, Partha Bairi, Kausik Chanda, Gautam Majumdar and Kalyan Kumar Chattopadhyay, Dalton Trans. 2021, 50, 5327-5341.

10. Negative Capacitance Switching in Size-Modulated Fe_3O_4 Nanoparticles with Spontaneous non-Stoichiometry: Confronting its Generalized Origin in non-Ferroelectric Materials, Souvik Bhattacharjee, Anibrata Banerjee, Nilesh Mazumder, Kausik Chanda, Saikat Sarkar and Kalyan Kumar Chattopadhyay, Nanoscale 2020,12, 1528-1540.

11. Room Temperature Solution Processed Low Dimensional $CH_3NH_3PbI_3$ NIR Detector, Nripen Besra, Tufan Paul, Pranab Kumar Sarkar, Subhasish Thakur, Saikat Sarkar, Anajn Das, Kausik Chanda, Kausik Sardar and Kalyan Kumar Chattopadhyay, AIP Conf. Proc. 1953, 030210 (2018).

12. Low dimensional $CH_3NH_3PbBr_3$ Cubes for Persistent Luminescence: Energy Variation of Electron Excitation, Nripen Besra, Tufan Paul, Subhasish Thakur,

Saikat Sarkar, Kausik Sardar, Kausik Chanda, Anjan Das and Kalyan Kumar Chattopadhyay, AIP Conf. Proc. 1942, 120027 (2018).

13. Efficient Blue Emission from Ambient Processed all-Inorganic $CsPbBr_2Cl$ Perovskite Cubes, Tufan Paul, Biplab Kumar Chatterjee, Soumen Maiti, Nripen Besra, Subhasish Thakur, Saikat Sarkar, Kausik Chanda, Anjan Das, Kausik Sardar and Kalyan Kumar Chattopadhyay, AIP Conf. Proc. 1942, 120026 (2018).

14. Luminescence Behaviour of Room Temperature Chemical Processed All Inorganic $CsPbCl_3$ Perovskite Cubes, Tufan Paul, Biplab Kumar Chatterjee, Soumen Maiti, Nripen Besra, Subhasish Thakur, Saikat Sarkar, Kausik Chanda, Anjan Das, Pranab Kumar Sarkar, Kausik Sardar and Kalyan Kumar Chattopadhyay, AIP Conf. Proc. 1953, 030085 (2018).

Paper Presented in National/International Conferences

1. Hierarchical Heterostructure of MoS_2 Flake Anchored on TiO_2 Sphere for Supercapacitor Application, K. Chanda, S. Thakur, S. Maiti, A. Acharya, T. Paul, N. Besra, S. Sarkar, A. Das, K. Sardar and K. K. Chattopadhyay, 2nd International Conference on Condensed Matter and Applied Physics ***ICC-2017***, Bikaner, 24-25th November, 2017.

2. Facile Preparation of $CuCo_2O_4$@MnO_2 at Low Temperature: Efficient Visible-light Photocatalyst, K. Chanda, R. Sarkar, S. Maiti, and K. K. Chattopadhyay, 6th International Conference on Nanoscience and Nanotechnology ***ICONN-2021***, SRM IST, India, February 1-3, 2021.

3. Hierarchical Assembly of MnO_2 Nanosheet on $CuCo_2O_4$ Nanoflake over Fabric scaffold for Symmetric Supercapacitor, K. Chanda, S. Maiti, S. Sarkar, P. Bairi, S. Thakur, K. Sardar, N. Besra, N. S. Das and K. K. Chattopadhyay, 7th International Conference on Nanoscience and Nanotechnology ***ICONN-2023***, SRM IST, India March 27-29, 2023.

National/International Conferences/ Workshops Attended

1. 4th International Symposium on Semiconductor Materials and Devices ***ISSMD-4***, organized by School of Materials Science and Nanotechnology, Jadavpur University, 8-10th March, 2017.

2. Recent Advances in Materials Science ***RAMS-2017***, organized by Dept. of Industrial Chemistry & Applied Chemistry, Ramakrishna Mission Vidyamandira, 12th April, 2017.

3. 2nd International Conference on Condensed Matter and Applied Physics ***ICC-2017***, organized by Department of Physics, Engineering College, Bikaner, 24-25th November, 2017.

4. National Conference on Recent Developments in Nanoscience & Nanotechnology ***NCRDNN-2019***, organized by School of Materials Science and Nanotechnology, Jadavpur University, 29-31st January, 2019.

5. Recent Success and Challenges in Nanoscience and Nanotechnology (Experiment and Theory) ***RSCNN-2020***, Organized by School of Applied Sciences and Humanities, Haldia Institute of Technology, 25th-27th September, 2020.

6. Recent Trends in Condensed Matter Physics & Applications – ***RTCMPA-2020***, organized by Department of Physics in collaboration with IQAC, Kulti College, 22nd August 2020.

7. 6th International Conference on Nanoscience and Nanotechnology ***ICONN-2021***, organized by Department of Physics and Nanotechnology, SRM IST, India, February 1-3, 2021.

8. 7th International Conference on Nanoscience and Nanotechnology ***ICONN-2023***, organized by Department of Physics and Nanotechnology, SRM IST, India March 27-29, 2023.

Chapter 1:
Introduction & Objectives

1.1 Background

The world population is growing rapidly, and so is the demand for energy sources. Distinct countries around the world have different energy requirements. Compared to developing countries, energy requirement is higher in developed countries. As renewable energy sources are earth abundant, pollution-free, easily accessible, and less expensive, they are the sources of utmost concern for modern society. Hence, there is an urgent need for clean, efficient, and sustainable energy sources, as well as new technologies related to energy conversion and storage, given the rapid growth of the global economy and world population, the depletion of fossil fuels, and the rising environmental degradation [1–6]. Batteries, fuel cells, and supercapacitors (SCs), also coined as electrochemical capacitors or ultracapacitors, are some of the most efficient and practical technologies for electrochemical energy conversion and storage in numerous application areas [7–11].

Energy has taken centre stage in the attention of the global powers and scientific community in reaction to the shifting global landscape. The development and refinement of more effective energy storage devices have attracted much attention. The supercapacitor is one such device that has developed dramatically over the past 10 years and has the potential to enable considerable advancements in energy storage. Moreover, storage devices with greater capacity to store energy is the need of the hour as energy storage devices are critically needed in many applications, such as electric hybrid cars, standby power systems, and telecommunication equipment (mobile phones, remote communication, walkie-talkies, etc.)

SCs have garnered a lot of attention recently due to their high-power density, long lifespan, cyclic stability, outstanding reversibility and its capability to bridge the power-energy gap between conventional batteries/fuel cells, having high energy density and

regular dielectric capacitors, having high power density. SCs exploit high surface area electrode materials to generate capacitances that are several orders of magnitude higher than those of dielectric capacitors [12–14]. By doing this, SCs are able to achieve higher energy densities without sacrificing the high-power density of traditional dielectric capacitors. Dielectric capacitors have a lower specific energy density. However, the electrical energy they do store can be quickly released to provide a large amount of power, meaning that their power density is typically high. The same fundamental ideas that apply to supercapacitors. The SCs, however, use electrodes with significantly larger surface areas and thinner dielectrics, which reduce the distance between the electrodes. Figure 1.1 illustrates the SCs' performance plotted a graph coined as "Ragone plot". This kind of graph demonstrates the energy densities of different energy storage systems along the horizontal axis and their power densities along the vertical axis. SCs are observed in Figure 1.1 to be situated in between batteries and traditional capacitors [14]. Supercapacitors have higher capacitances than regular capacitors, but they still can't match the energy density of mid- to high-end batteries and fuel cells.

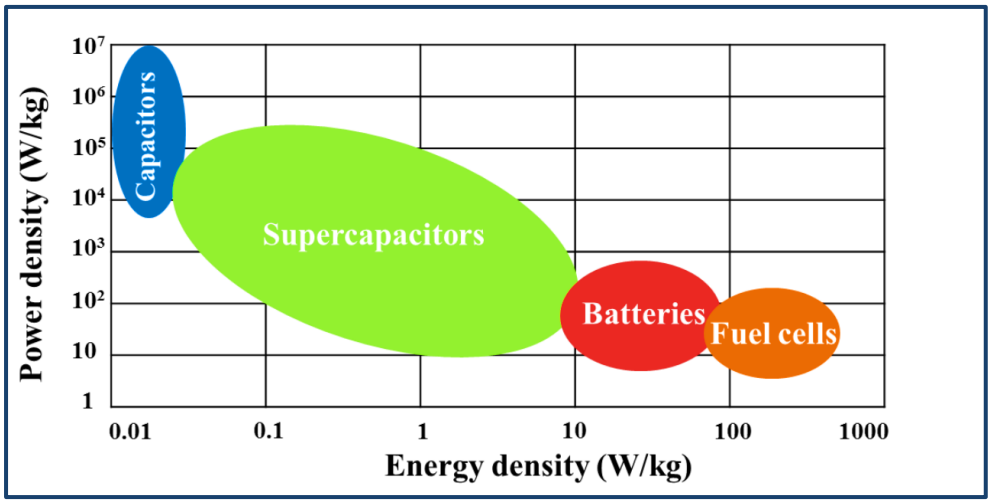

Figure 1.1: A Ragone plot depicting the relation of energy densities and power densities for different energy storage devices (*Wikimedia Commons*).

1.2 Supercapacitors: A Brief Outline

Supercapacitors (SCs) are electrochemical energy storage devices that have shown great promise and have garnered a lot of attention from academia and industry in recent decades owing to their fast charge-discharge rates, long cycle life, good power density, and superior energy density when compared to conventional capacitors [15–19]. Nowadays, supercapacitors are widely utilized to protect, improve, and/or replace batteries in a variety of applications, including consumer electronics, transportation, aerospace and the military, grid balancing, and power backup [20–26]. In-depth discussions on SCs' origins and history have been found in the literature [21–25]. In a nutshell, H. I. Becker from General Electric Company created a high surface-area carbon-coated metallic current collector in H_2SO_4 solution, which resulted in the first SC patent being granted in 1957. The first company to commercialize SCs was the Standard Oil Company of Ohio (SOHIO) in 1969 [21–24]. Nippon Electric Company (NEC) received the capacitor license from SOHIO in 1971. Later, NEC developed and launched the first commercially double-layer capacitor with success [27]. When SCs started to be used in conjunction with rechargeable batteries to supply extra power to electric and hybrid electric vehicles (HEVs) in the 1990s, it became noticeable. These SCs provided vehicle acceleration power by storing and capturing regenerative braking energy. Over the past few decades, SCs' applications have expanded significantly. These encompasses enhancing the manufacturing process, further development in electrolyte and electrode materials. In 1978, Panasonic created a unique type of supercapacitor coined as a "Gold capacitor" which was utilized for memory backup applications. Panasonic began producing button-cell capacitors in the middle of the 1980s in a variety of sizes, viz., 1/2, 1/3 farad (F). In the 1990s, Panasonic began producing more larger SCs, such as the 470F, 2.3V, 1500F, 2.3V. By utilizing metal oxide in the electrode, the Pinnacle Research Institute (PRI) developed the first high power double-layer

capacitors in 1982, which they called "PRI Ultracapacitors". B. E. Conway [24,28] introduced a novel idea for energy storage in supercapacitors between 1975 and 1981 by employing a RuO_2 layer in an aqueous H_2SO_4 electrolyte. The charge storage technique was denoted as a "pseudocapacitor", operated on a Faradaic principle that was obtained from surface redox processes. As part of research on hybrid electric cars, the US Department of Energy had Maxwell Laboratories establishing the Ultracapacitor Development Program in 1992. Nowadays, a multitude of organizations are producing supercapacitors due to the increase in global demand for alternative energy sources. Companies like Panasonic, ELNA, NEC, Epcos, AVX have produced a variety of electric double-layer capacitors (EDLCs). Additionally, integrated modules containing voltage balancing circuitry are developed by firms like Evans and Maxwell. Several EDLC module types are available in Russia from ESMA for use in electric car and power quality development applications. Nowadays, commercial supercapacitors are widely used as energy harvesters to collect and store solar energy collected from solar cells, uninterruptible power supplies for computers and standby power for random access memory devices [29,30]. Besides, solid state drives (SSD), cellphones, electric hybrid vehicles, electric tools and communication devices are all heavily dependent on commercial supercapacitors.

1.2.1 Conventional Dielectric Capacitor

Two conducting electrodes separated by an insulating dielectric material make up a conventional capacitor. On the surfaces of each electrode of a capacitor, opposing charges build up when a voltage is applied across the conducting electrodes. Charges are maintained apart by the dielectric, creating an electric field that enables energy storage in the capacitor. Figure 1.2 provides a schematic illustration of this.

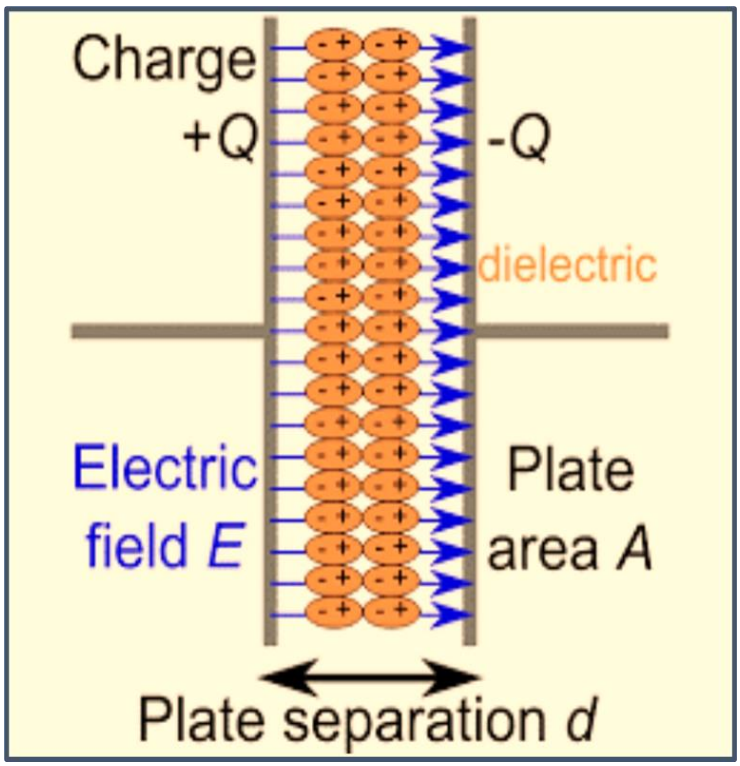

Figure 1.2: Schematic representation of a Conventional Dielectric Capacitor (*Wikimedia Commons*).

The ratio of the stored charge Q (in Coulombs) in the electrodes to the applied voltage V (in Volts) across the conducting electrodes is elucidated as the capacitance C (in Farads). Thus,

$$C = \frac{Q}{V} \tag{1}$$

In the case of a traditional capacitor, C is inversely proportional to the distance D between the electrodes and directly proportional to the surface area A of each electrode:

$$C = \frac{\varepsilon_0 \varepsilon_r A}{D} \tag{2}$$

The first two elements on the right side of the equation (2) are two constants namely dielectric constant/permittivity of free space (ε_0) and relative permittivity/dielectric constant (ε_r) of the medium between the electrodes.

The energy density and power density of a capacitor are its two main characteristics. The density can be computed as a quantity per unit mass or volume. The energy E stored by a capacitor is given by,

$$E = \frac{1}{2} CV^2 \tag{3}$$

Generally, the energy dissipated per unit of time is defined as the power P. As Figure 1.3 illustrates, capacitors are typically represented as a circuit in series with an external load resistance R. This makes it necessary to calculate Power P for a capacitor.

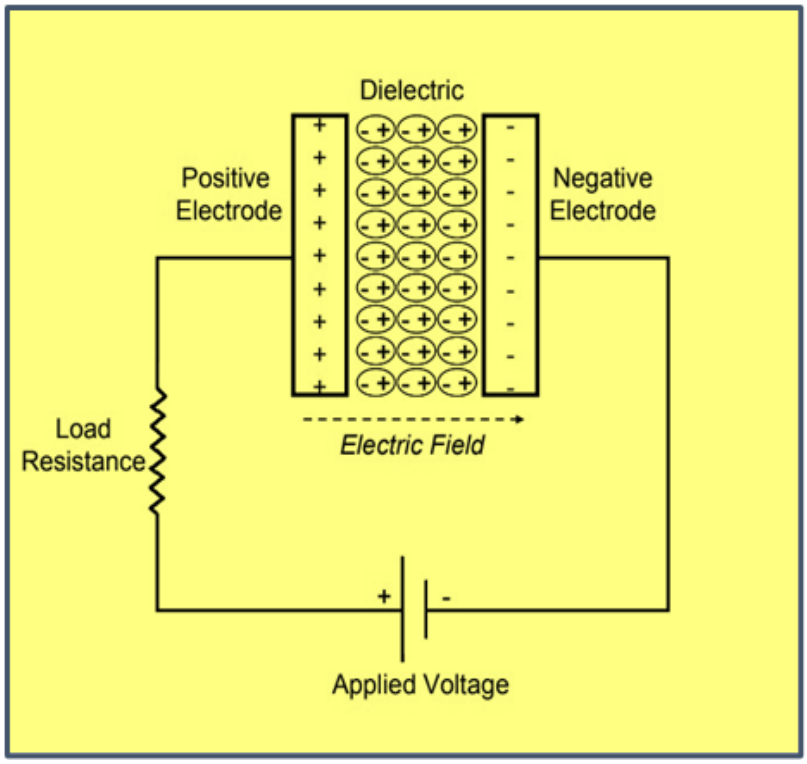

Figure 1.3: Circuit of a Conventional Capacitor in series with external Load Resistance and an Applied Potential [31].

The resistance is also influenced by the internal parts of the capacitor, such as the electrodes, dielectric material, and current collectors. These all resistances are added and expressed as an equivalent series resistance (ESR). These resistances govern the voltage

during capacitor discharge. According to Maximum Power Transfer Theorem, the maximum power P_{max} delivered by the capacitor [24,32,33] is determined when external load resistance R matches with ESR (*i.e.*, R = ESR) and is given by

$$P_{max} = \frac{V^2}{4 \times ESR} \tag{4}$$

This above equation (4) demonstrates how an ESR can affect a capacitor's maximum power. When compared to fuel cells and electrochemical batteries, conventional capacitors have relatively low energy densities but high-power densities. In other words, although a battery has a lower power density than a capacitor, it can store more energy overall and cannot release it as quickly. Comparatively, capacitors store less electrical energy per unit mass or volume; yet, because the electrical energy they do store may be swiftly released to produce a large amount of power, their power density is typically high.

1.2.2 Advantage of Supercapacitors over Dielectric Capacitors

The same fundamental ideas that apply to conventional capacitors also apply to SCs. Supercapacitors however, include electrodes with substantially larger surface areas (A) and significantly thinner dielectrics, which reduce the distance (D) between the electrodes. Moreover, comparable power densities can be attained in SCs while preserving the low ESR feature of conventional capacitors. In addition, supercapacitors are superior than fuel cells and electrochemical batteries in a number of ways, such as longer cycle and shelf lives, quicker charging times, and better power densities [15,24]. A large portion of the research conveyed o SCs in the past few decades has concentrated on manufacturing superior classes of SCs such that their energy densities can match to those of batteries. The

categorization of supercapacitors, unfolding in the following section includes all those aspects into account.

1.2.3 Construction of Supercapacitors

As depicted in Figure 1.4, the fundamental components of a supercapacitor are the two electrodes, the separator, and the electrolyte. The electrodes have a wide surface area and are very conductive. The use of active materials like carbon and metallic current conductors makes this possible. The separator between the two electrodes is a membrane which ions can cross but electrons cannot. Thus, the membrane restrains electronic conductance. Finally, the electrode-separator-electrode system is folded or rolled into a rectangular or cylindrical shape, piled in a container, and soaked in electrolyte. Depending on power demand, organic or aqueous or solid-state electrolytes are used. The voltage at which the electrolyte decomposes determines the operating voltage of the supercapacitor This break-down voltage is influenced by a number of factors such as surrounding environments, current intensity etc.

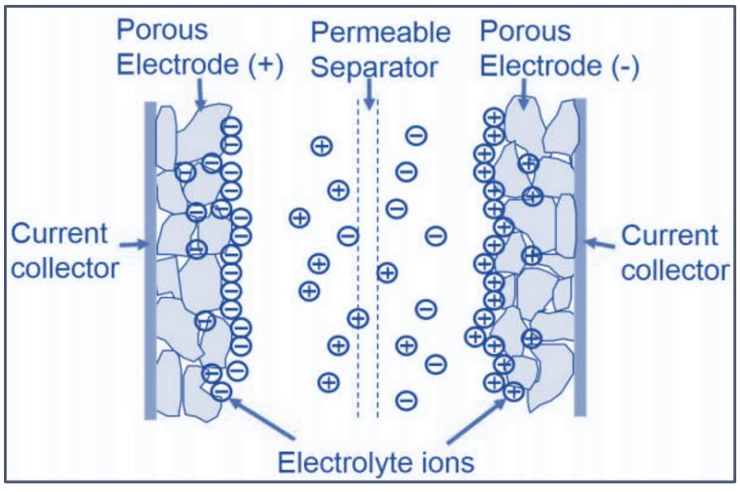

Figure 1.4: A schematic diagram of a supercapacitor [34].

The awkward bulk forms of traditional SCs *i.e.*, a separator sandwiched between two electrodes enclosed in a liquid electrolyte, hinder their deployment in wearable technology.

For instance, in order to stop the toxic liquid electrolyte from leaking, high-standard safety encapsulating materials and technology are needed. Moreover, integrating SC components with other functional systems on the electrical motherboard is challenging since they can only be assembled in a limited number of sizes and shapes, such as button and spiral wound cylinders. In order to get around these restrictions, a new class of energy storage devices known as flexible solid-state SCs (FSSCs) has arisen and garnered a lot of interest recently [35–41]. The components of FSSC devices include flexible electrodes, a separator, a solid-state gel electrolyte, and flexible packaging material resembling that of conventional SCs. The primary benefit of FSSCs over traditional SCs is its use of flexible electrodes and a solid-state gel electrolyte, which allow for the assembly of thin, light, and smart design in any size or form, increasing their potential application in flexible and wearable electronics.

1.2.4 Supercapacitor & its Charge Storage Mechanism

Supercapacitors can be categorized into three main groups as mentioned in earlier chapter, which are EDLC, pseudocapacitor and hybrid capacitor respectively. Charge storage mechanisms in SCs are discussed below.

1.2.4.1 Charge Storage Mechanism in EDLC

An electrolyte, a separator, and two carbon-based electrodes are the main components of an EDLC. Any boundary between two distinct materials or phases forms an interface. At the interface between the electrode and electrolyte, electrical charge is stored in EDLCs. It is believed that there are directed dipoles and a variety of charged particles at every interface. This array is referred to as an electrical double layer (EDLC), and a representative EDLC's schematic diagram is shown in Figure 1.5. On the electrode surface, there are no Faradaic reactions during the physical process of charge separation. EDLCs function similarly to conventional capacitors as there is no charge transfer between the

electrode and electrolyte. Therefore, the electrode's surface characteristics, such as the distribution of pore sizes and specific surface area (SSA) have a significant influence on double layer capacitance [42–48]. EDLCs store energy by use of an electrochemical double layer of charge. Due to enormous interfacial area and atomic-scale charge separation distances, SCs based on the EDLC mechanism have a substantially higher energy storage capacity than conventional dielectric capacitors. On the electrodes, charge builds up when a voltage is applied. Ions from the electrolyte solution recombine because they do not go backward after diffusing past the separator and into the pores of the electrode with the opposite charge. A double layer of charge forms at each electrode as a result of the accumulation of charged ions on the surfaces of the oppositely charged electrodes, which increases the energy density. Thus, greater surface area for the double layers further facilitates higher energy densities.

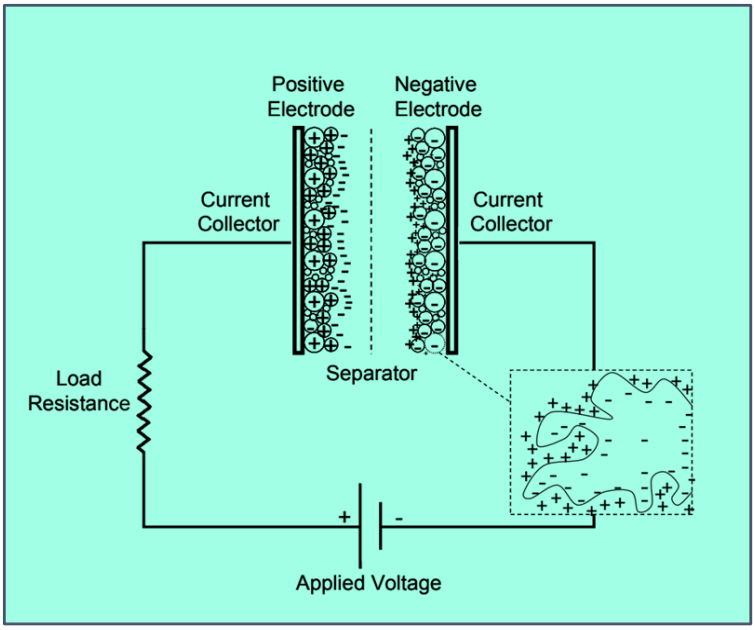

Figure 1.5: Schematic of an Electrochemical Double-Layer Capacitor [31].

Initially it was assumed that the pore size in porous EDLCs should be around double the size of the electrolyte ions to enable complete access into the pore walls. But some

investigations have discarded this assumption as they have produced record-breaking specific capacitance values by reducing the pore size smaller than twice the size of the bare ions [49–54]. In the end, it appears that there is no discernible relationship between the SSA and specific capacitance, suggesting that increasing the SSA and average pore size will not raise the capacitance [55]. Further, it was recently found that raising the specific capacitance is largely dependent on the carbon nanostructure and pore size rather than the SSA [56,57]. The physical mechanics and genesis of the charge storage mechanisms in carbon-based materials may be closely examined thanks to recent advancements in a variety of sophisticated in situ spectroscopic and modelling techniques.

As it was previously mentioned that there is no charge transfer between the electrode and electrolyte, non-Faradaic reactions do not result in any changes to chemical composition. The system has very high cycle stabilities and is reversible in the absence of any chemical change. The EDLCs can function with steady performance characteristics for a large number of charge-discharge cycles up to 10^6 cycles at times. However, the typical cycle life of electrochemical batteries is only roughly 10^3 cycles. EDLCs are employed in deep-sea or mountainous locations that are unsuitable for manual handling due to their high cycling stability.

1.2.4.2 Charging Discharging Function of an EDLC

The current flows as a result of the double layer's creation and removal, which makes the process extremely reversible and allows for millions of charge discharge cycles. The reversible adsorption/desorption of ions at the electrode/electrolyte interface causes the accumulation of charge in the EDLC. The electric double-layer capacitance develops at the electrode/electrolyte contact. The electric charges align themselves to preserve electroneutrality by causing the electrolyte ions with opposing charges to collect on the

electrolyte solution and the excess electric charges to build up on the electrode surface. When an external load is applied to charge the system, an electron moves from the negative to the positive electrode via the external load, creating a double layer at the interfaces as cations and anions migrate to the cathode and anode from the electrolyte solution (Figure 1.6). The opposite processes occur during discharge when the external load is eliminated. Because there is no ion exchange or charge transfer at interfaces during the charging and discharging process (a non-Faradaic process), the electrolyte concentration stays constant.

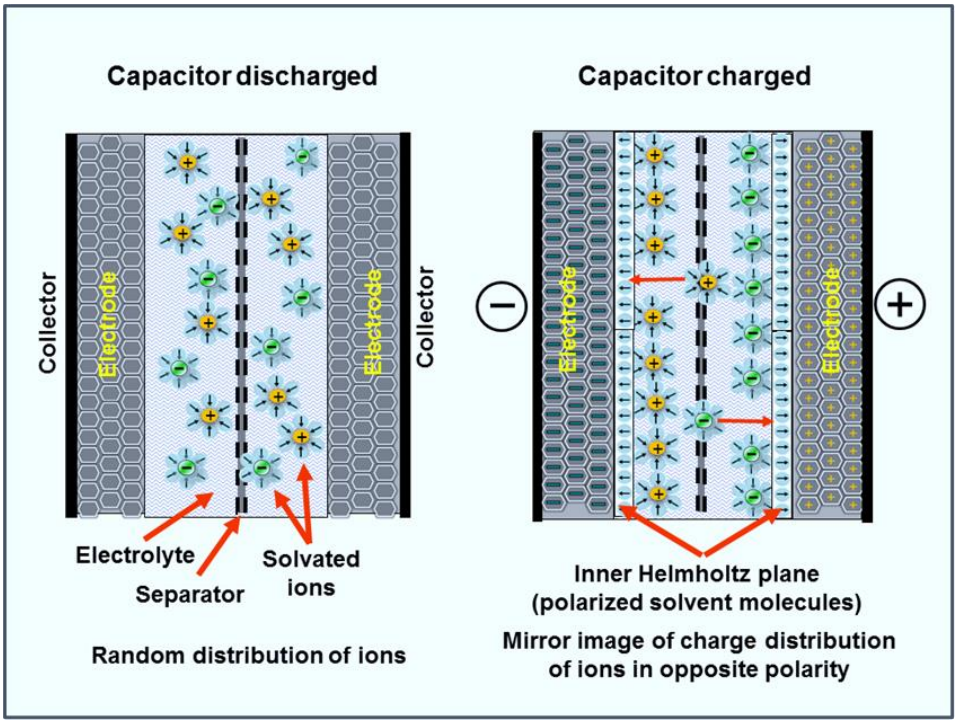

Figure 1.6: Structure and Charging Discharging function of an EDLC (*Wikimedia Commons*).

1.2.4.3 Models to Explain the Charge Storage in an EDLC

The charge storage mechanism in EDLCs is mostly explained by three basic concepts. These three models are the Helmholtz, Gouy–Chapman, and Stern model.

1.2.4.3.1 Helmholtz Model

As demonstrated by Helmholtz model, positive and negative charges accumulated at the interfaces may be thought of as corresponding to a basic parallel plate capacitor. (Figure 1.7a depicts the working principle of a double-layer capacitor based on the Helmholtz model. The following equation represents the relationship between the double layer potential v and the charge per unit area q :

$$q = \frac{\varepsilon_0 \varepsilon_r}{d} \times v \tag{5}$$

Where, ε_r is the dielectric constant of the medium,

ε_0 is the permittivity of the free space and

d is the interlayer spacing.

The above equation (5) yields the differential capacitance C_H per unit area as :

$$C_H = \frac{\partial q}{\partial v} = \frac{\varepsilon_0 \varepsilon_r}{d} \tag{6}$$

The prediction of constant differential capacitance at the interface by this model made it deem unsuccessful. As in real systems, differential capacitance keeps changing depending on double layer potential v . Therefore, it is incorrect to take constant interlayer spacing into account.

1.2.4.3.2 Gouy-Chapman Theory

According to this model, the concentration of electrolyte and the applied potential across the electrode determine the capacitance in the double layer. This model states that the polarity of the electrolyte ions as well as the thermal motion of the ions determine the electric forces. As a result, the electrolytic side of the interface forms the diffuse layer of

charges, and the average ion separation in the diffuse layer should be used in place of the constant diffuse layer separation in the Helmholtz model. As the diffuse layer gets more compact with the increase in applied potential Gouy and Chapman came to the conclusion that the capacitance is dependent on the applied potential on the electrode. Thus, significant advancements were made by Gouy and Chapman when they presented this diffuse model of the electrical double layer (Figure 1.7b) [58–60]. In this model:

(i) The disordering effect of thermal motion has been taken into consideration.

(ii) One layer is fixed on the electrode, whereas the oppositely charged layer is diffused or mobile on the electrolyte.

(iii) The solution side of the double layer extends somewhat distance into the liquid phase rather than being close to a single molecule in thickness.

(iv) Adsorbed counter-ions from the solution cause an exponential drop in potential at the surface.

(v) The ions disperse throughout the mixture. Due to thermal agitation and the free mobility of ions in the solution, the distribution of +ve and -ve charges is not uniform.

(vi) While thermal agitation strives to create disorderliness, the electrostatic attraction between opposite charges at the interface tries to bring orderliness.

(vii) The diffuse double layer theory is almost identical to the Debye-Huckel theory of the ionic environment surrounding a specific ion.

(viii) There is exponential potential shift from one layer to the next instead of a linear one.

The Poisson's equation and the Boltzmann distribution were used in the mathematical formulation of differential capacitance using this approach [58]. The

differential capacitance at the interface is determined by the following equation based on the Gouy-Chapman model:

$$C_{GC} = \frac{\partial q_m}{\partial \psi_0} = \left\{\frac{2Z^2 e^2 \varepsilon_0 \varepsilon_r n}{k_B T}\right\}^{1/2} \text{Cosh}\left(\frac{Ze\psi_0}{2k_B T}\right) = \kappa \varepsilon_0 \varepsilon_r \left(\frac{Ze\psi_0}{2k_B T}\right) = \frac{\varepsilon_0 \varepsilon_r}{\lambda_D}\left(\frac{Ze\psi_0}{2k_B T}\right) \quad (7)$$

Where, ψ_0 is the potential drop across the diffuse layer,

q_m is the solution phase charge density,

Z is the magnitude of charge on the ion,

e is the electronic charge,

n is the concentration of each ion in the solution,

ε_r is the dielectric constant of the medium,

ε_0 is the permittivity of the free space,

λ_D is the thickness of the diffusion layer,

k_B is the Boltzmann constant and

T is the absolute temperature.

For dilute aqueous solutions at 25°C, above equation can be written as,

$$C_{GC} = 228Z(C^*)^{1/2} Cosh(19.5Z\varphi_0) \quad (8)$$

where, C_{GC} is in mF/cm^2 and the bulk electrolyte concentration C* is in mol/L.

As because the ions in this model were treated as point charges, they might approach the electrode surface arbitrarily, which would cause the capacitance to grow infinitely with an increase in voltage. This is not the case in real systems.

1.2.4.3.3 Stern Model & its Modification

The Gouy-Chapman model's infinite increase in differential capacitance with $\bar{\varphi}_0$ can be attributed to the ion's unrestricted movement inside the solution phase. They are regarded as point charges that are capable of arbitrary close approaches to the surface. The effective separation distance between the metallic and solution-phase charge zones thus continually approaches zero at high polarization. Although compared to the Helmholtz model, a superior approximation was used by Gouy and Chapman to develop the theory, the approximation was predicated on the ideas that point charges like ions have no physical bounds on their approach to the surface.

This is not a realistic viewpoint. Hence, Stern suggested that because of the finite sizes ions can only approach the electrode surface in proximity to their ionic radius rather than indefinitely approaching it. Additionally, the strategy would be dependent on the ion's solvation in the solvent, which raises the ionic radius. The distance of closest approach by the ion is labelled as the outer Helmholtz plane (OHP) whereas the inner Helmholtz plane (IHP) is the plane created by the locus of the centers of the specifically adsorbed ions. Stern further divided the ions at the electrode-electrolyte interface into two regions namely, the compact/Stern layer and the diffuse layer by combining both the Helmholtz and Gouy-Chapman models (Figure 1.7c) [61]. It reveals that the solvated ions are virorously absorbed on the electrode surface in the compact layer whereas ions are consistently dispersed throughout the electrolyte in the diffuse layer. Moreover, Stern layer comprises both the specifically and non-specifically adsorbed counter-ions. The inner Helmholtz plane (IHP) and outer Helmholtz plane (OHP) separate the two types of ions. Total capacitance C_{DL} can be written as:

$$\frac{1}{C_{DL}} = \frac{1}{C_H} + \frac{1}{C_{GC}} \tag{9}$$

where C_{GC} and C_H stand for the diffuse layer's capacitance and the compact layer's capacitance, respectively. These are the conventional EDLC hypotheses, assuming that the electrolyte is a diluted solution. But these ideas don't hold good for ionic liquids or high concentration electrolytes because of the significant short-range Coulomb correlations.

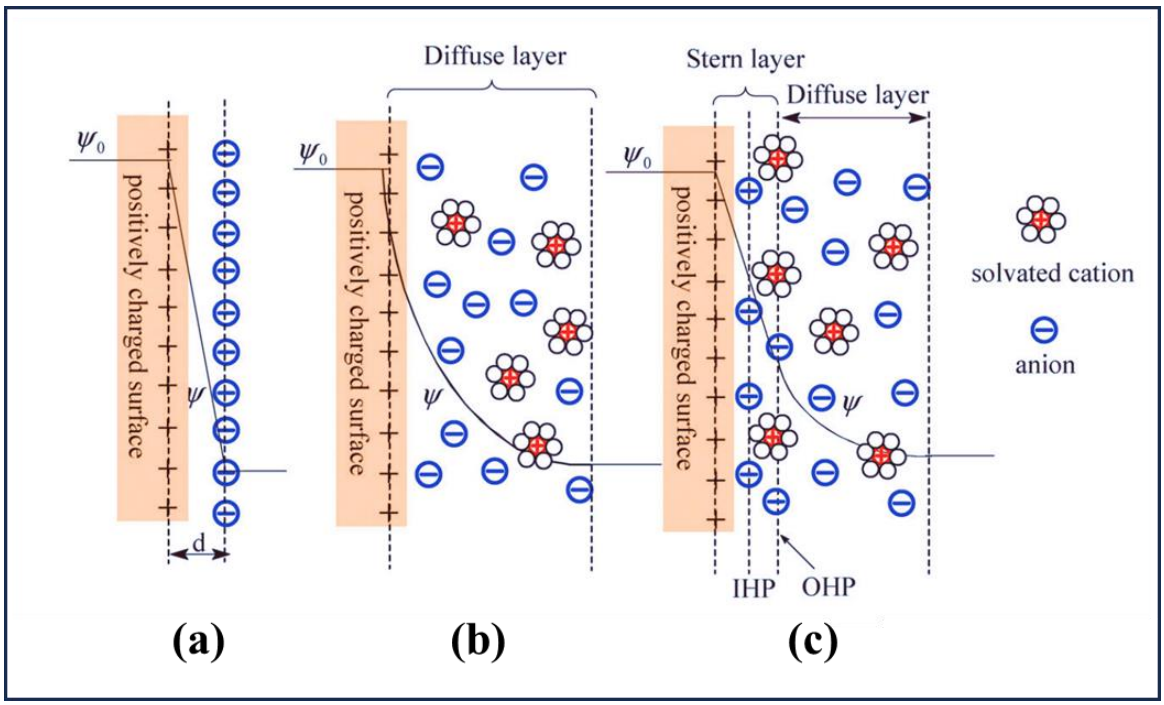

Figure 1.7: (a) Helmholtz model, (b) Gouy-Chapman model, and (c) Stern model of the EDL at a positively charged electrode. d is the electric double-layer distance in Helmholtz model, ψ_0 and ψ are the electrical potentials at the electrode surface and electrode/electrolyte interface, respectively [62].

According to studies [63,64], the overscreen effect is more pronounced for ionic liquids at low potential. This is because the first layer has more counter-ions than are needed to neutralize the electrode surface, and the next layer overscreens again because it shows a smaller net charge of the opposite ign. This process continues until electro-neutrality is reached (Figure 1.8a). The condensed layer created by counter-ions gradually replaces the overscreening structure as the voltage increases (Figure 1.8b), reaching complete lattice

saturation at a huge potential in the process. These ions are hard to accumulate, though, due to the repulsive forces that exist between ions that have the same charge. The superionic state was proposed by Kondrat et al. [65,66], where the repulsive forces between ions in

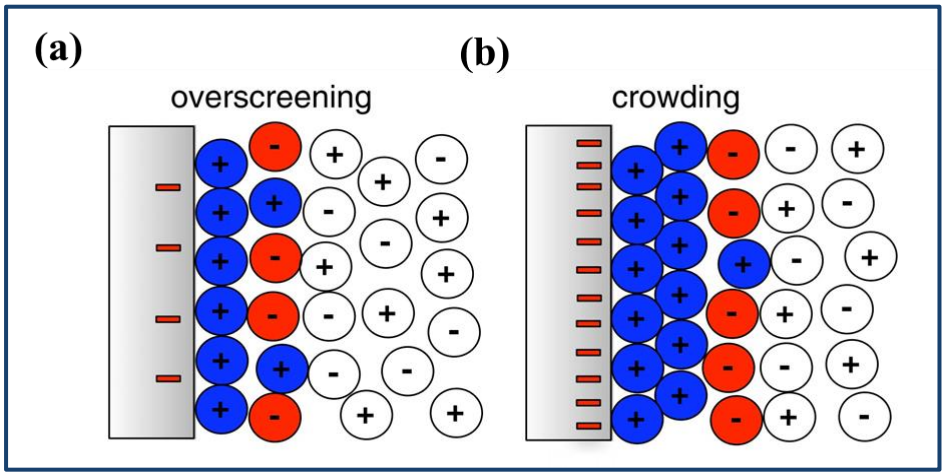

Figure 1.8: Structure of ionic liquid layer (a) at a moderate voltage of $V = 10k_BT/e$, and (b) at a high voltage of $V = 100k_BT/e$ [67].

the pores are exponentially screened out by the image forces. Recently, Simon et al. confirmed that the super-ion state exists in the pores that can only hold a single layer of ions using the hybrid reverse Monte Carlo (HRMC) simulation-aided X-ray scattering technique [68].

1.2.4.4 Charge Storage Mechanism in Pseudocapacitor

At some kinds of electrodes, the Faradaic charge transfer that occurs between the electrode and the electrolyte is what allows a second kind of capacitance known as pseudocapacitance to evolve and store electric energy. This type of capacitance is caused by charge acceptance (∇q) and a shift in potential (∇V) and and arises for thermodynamic reasons [69]. Hence, the derivative

$$C = \frac{d(\nabla q)}{d(\nabla V)} \tag{10}$$

is equivalent to a capacitance, described as a pseudocapacitance. The primary distinction between pseudocapacitance and EDL capacitance is that the former is a result of a diffusion induced redox reaction involving the electrolyte and electroactive species on the electrode surface, a process known as Faradaic process (the transfer of electrons across the electrode–electrolyte interface). The most well-known active substances exhibiting pseudocapacitance are surface functional groups that contain oxygen or nitrogen, electrically conducting polymers like polyaniline, ruthenium oxide, manganese oxide, vanadium nitride etc.

Pseudocapacitor has the disadvantage of having a low power density owing to its poor electrical conductivity and inferior cycling stability, even though its capacitance value can be larger than EDL capacitance. Although there are many examples of pseudocapacitance, the capacitance function is typically not constant and actually depends somewhat on the potential or state of charge. For RuO_2 electrode, a wide range of meaningful capacitance values result from a surface-limited process that proceeds in several one-electron steps. In these cases, the pseudocapacitance is nearly constant throughout the whole operational voltage range. Only at narrower working potential ranges, certain other metal oxides exhibit comparable behavior. With a cycle life of more than several hundred thousand cycles, the RuO_2 pseudocapacitance offers high reversibility, making it one of the best examples of electrochemical (pseudo) capacitance. Its capacitance is essentially constant throughout a large voltage range. Additionally, an electrochemical capacitor's capacitance can be increased by up to an order of magnitude using pseudocapacitance over that of the double-layer capacitance.

The charge storage mechanism in pseudocapacitive materials can be distinguished by evaluating the double-layer and diffusion-controlled charge contributions of the overall charge accumulated by the electrode utilizing cyclic voltammetric data taken at multiple

scan rate. In general, the current (i) depends on the scan rate (n) according to the relation:[70]

$$i = av^b \tag{11}$$

where a and b are variable parameters. Further, b can be evaluated from the slope of the log(i) vs. log(n) plot. For the diffusion-controlled faradaic intercalation process b = 0.5 which further suggests typical battery behavior where the current is proportional to the square root of the scan rate ($v^{1/2}$), as shown by the following equation:

$$i = nFAC^*D^{1/2}v^{1/2}\,(\alpha nF/RT)^{1/2}\pi^{1/2}\chi(bt) \tag{12}$$

where, $\chi(bt)$ is the normalised current,

C^* is the surface concentration at the electrode,

n is the number of electrons involved in the redox reaction,

A is the electrode material's surface area,

α is the transfer coefficient,

D is the chemical diffusion coefficient,

F is the Faraday constant,

R is the molar gas constant, and

T is the absolute temperature.

In contrast, the current response for the capacitive process is precisely proportional to the scan rate and in this case b = 1. The total charge stored in the electrode is typically equal to the sum of the currents coming from double-layer capacitance (k_1v) diffusion-controlled ($k_2v^{1/2}$) faradaic processes. Equation (11) can therefore be changed as follows:

$$i = k_1 v + k_2 v^{1/2} \quad (13)$$

Thus, the total of the diffusion-controlled faradaic contribution and double-layer capacitance contribution determines the current at a given potential [71]. Constants k_1 and k_2 can be evaluated from the slope and intercept of $i/v^{1/2}$ vs. $v^{1/2}$ plot.

1.2.5 Electrode Materials for Energy Storage

The overall performance of SCs relies on the choice of materials for the electrodes, electrolyte and separator because of their effect on the electrochemical performance of the SCs. The following elements need to be taken into account when selecting a material for a SC electrode:

- Pore size distribution,
- SSA of the electrodes,
- Electrical conductivity,
- The redox resistance,
- Wettability of electrolyte on the electrode,
- Electrochemical stability of the electrolyte.

When choosing and preparing an electrode for a SC, it's also crucial to take into account the size, geometry, and choice of fillers in the polymeric composite. Carbonaceous/carbon-based fillers are particularly popular because of their remarkable qualities, which include high conductivity, high surface area, exceptional chemical endurance, and mechanical durability. Energy in supercapacitors (SCs) is directly influenced by the electrode's capacitance, which can be increased by creating extremely porous carbon or adding

pseudocapacitive materials to the carbon network, also known as hybrid capacitor (HC). [72]. Chart 1.1 presents a graphical taxonomy of the various SC types and subclasses.

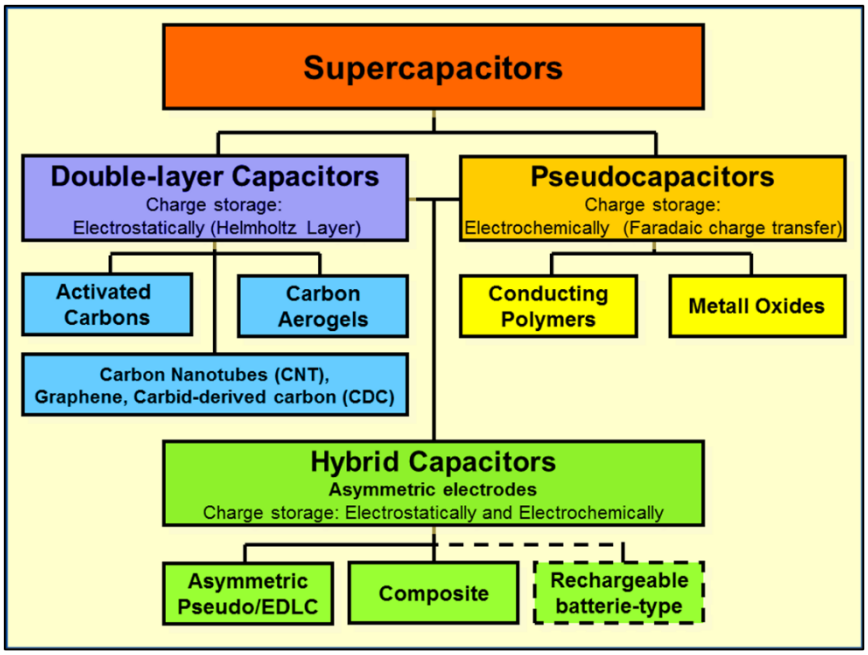

Chart 1.1: Taxonomy of the Supercapacitors.

1.2.6 Hybrid Capacitor

A viable substitute for traditional SCs is a hybrid system. In an effort to achieve improved Supercapacitive performances, HCs try to take advantage of the benefits and minimize the drawbacks of EDLCs and pseudocapacitors incorporating both Faradaic and non-Faradaic processes. HCs have attained energy density and power densities higher than EDLCs without sacrificing the cycling stability and affordability that have hindered the adoption of pseudocapacitors,. Three distinct forms of hybrid capacitors namely composite, asymmetric, and battery-type capacitors have been the subject of research. These types of capacitors are identified by their electrode design. The need for more powerful batteries and greater energy SCs is reflected in these unique arrangements.

1.2.6.1 Composite Electrode

Composite electrodes combine physical (non-Faradaic) and chemical (Faradaic) charge storage processes into a single electrode by combining carbon-based materials with conducting polymer or transition metal-based semiconductors. Besides, facilitating a capacitive double-layer of charge, the carbon-based materials offer a high-surface-area backbone that improves the interaction between the electrolyte and the deposited pseudocapacitive materials. The capacitance of composite electrode can be further enhanced by the pseudocapacitive materials via redox induced Faradaic reactions [73–76].

1.2.6.2 Asymmetric Hybrid

Asymmetric hybrids bridge an EDLC electrode to a pseudocapacitor electrode, integrating both Faradaic and non-Faradaic processes. A lot of attention has been paid to the couple activated carbon (as negative electrode) with transition metal-based semiconductors (as positive electrode) [77–80].

1.2.6.3 Battery-type Hybrid

Battery-type hybrids also couple two distinct electrodes just like an asymmetric hybrid. Pairing of a supercapacitor electrode with a battery electrode makes battery-type hybrids. This unique arrangement incorporates the energy properties of batteries with the power, cycle life, and recharge durations of supercapacitors to meet the demand for higher energy supercapacitors and higher power batteries. The main focus of research has been on two electrodes: activated carbon and nickel hydroxide, lead dioxide, and LTO ($Li_4Ti_5O_{12}$) [81–85]. Experimental data indicates that battery-type hybrids could be able to fill the gap between batteries and supercapacitors. Even with the encouraging outcomes, most experts

agree that further study will be required to fully understand the possibilities of battery-type hybrids.

1.2.7 Transition Metal-based Semiconductors as Supercapacitor

As discussed previously, depending on the charge storage mechanisms SCs can be classified into two main categories which are electrochemical double-layer capacitors (EDLCs) and pseudocapacitors. Each class has its unique way of storing charges: non-Faradaic (Figure 1.9a) and Faradaic reaction (Figure 1.9b). Faradaic reaction necessitates

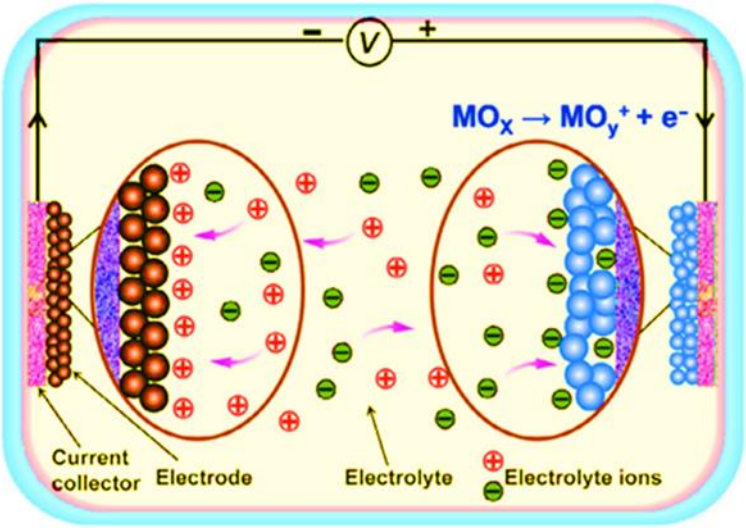

Figure 1.9: Schematic of the two mechanisms of SCs: (a) non-Faradaic in EDLCs and (b) Faradaic in pseudocapacitors [86].

the transfer of charge from electrode to electrolyte and vice versa, *i.e.*, oxidation-reduction (redox) reactions. In contrast, in EDLCs, non-Faradaic mechanism doesn't rely on the chemical one. Instead, physical ion adsorption process occurs rather than the creation or disruption of chemical bonds. Carbon-based materials [87,88] are typically utilized to realize EDLCs. Conversely, transition-metal-based oxides (TMOs), sulfides, halides, etc.

are typically used as the active electrode material in the fabrication of pseudocapacitors [89,90].

Transition metal oxides (TMOs) offer superior electrochemical stability over polymer materials and a greater energy density for Supercapacitor electrodes than traditional carbon materials. In addition to storing energy electrostatically or non-faradaically like carbon materials TMOs further manifest electrochemically reversible redox reaction, also known as faradaic interactions, between electrode materials and electrolytic ions within a suitable potential window. For TMOs to be used in Supercapacitor applications, they must meet some general requirements which are as follows:

(i) TMOs must be electronically conducting in nature.

(ii) Metals in TMOs can exist in two or more oxidation states that coexist over a continuous range without requiring phase changes that irreversibly modify the three-dimensional structure.

(iii) Protons must be free to intercalate into the oxide lattice during reduction and out of the lattice during oxidation, facilitating easy interconversion of $O^{2-} \leftrightarrow OH^{-}$. The oxides of ruthenium, manganese, cobalt, nickel, copper and vanadium have all been studied.

Before S. Trasatti and G. Buzzanca identified RuO_2's pseudo-capacitive nature and its theoretical specific capacitance value of 1400–2000 $Fg^{-1,}$ the charge storage mechanism of TMOs was uncharted. [91,92] One of TMOs' unique feature is their ability to transition between different oxidation states during electrochemical redox processes, extending the discharge period and resulting in better energy densities [93,94]. The scalable use of TMOs as supercapacitor electrodes is, however, hindered by their low electronic conductivity, slow diffusion rate, patchy potential window [95,96].In order to subjugate these obstacles,

Mixed Transition Metal Oxides (MTMOs) $A_xB_{3-x}O_4$; A, B=Co, Cu, Ni, Zn, Mn, Fe etc. have been employed as supercapacitor electrode materials, guaranteeing that the synergistic effect will be pronounced due to the incorporation of multiple metal ions. This, in succession, results in improved electronic conductivity, which opens the door to superior energy storage capacity [97,98].

The research focus in the field of supercapacitors has recently shifted towards hierarchically nanostructured TMO materials due to their unique structures [99–103]. These structures provide a large specific surface area, abundant electroactive sites, and a short ion diffusion pathway during the charge-discharge process [99–103]. Compared to common TMOs, hierarchically nanostructured TMOs exhibit higher power properties, larger specific capacitances, and more impressive cycle stabilities. In this thesis, we will mainly focus on the electrode materials for supercapacitors that are hierarchically nanostructured TMOs.

1.3 Background of Fuel Cell

Along with Supercapacitor and batteries, hydrogen has drawn a lot of attention as a potential zero-emission technology. Developing technologies for the conversion and storage of renewable energy is one realistic approach to reduce our dependency on fossil fuels like coal and gasoline as well as the emissions of waste gases like carbon dioxide, sulfur dioxide, and nitrogen oxides. Most people agree that hydrogen is a clean energy source with a high energy density and a potential replacement for fossil fuel-based economy [104–107]. Hydrogen has the capacity to transfer or store enormous amounts of energy. It is an energy transporter rather than an energy source. Fuel cells can produce power and heat or electricity by using hydrogen. Nowadays, the two industries that use hydrogen most frequently are fertilizer production and petroleum refining; utilities and transportation are

newer applications. When clean fuel hydrogen is used in a fuel cell, it simply creates heat, electricity, and water. With potential uses in almost every area, including transportation, business, industry etc. hydrogen and fuel cells can be valuable components of our country's energy strategy. Energy from hydrogen and fuel cells can be used for a variety of purposes, such as distributed or combined heat and power, backup power, renewable energy storing and enabling systems, portable power, auxiliary power for trucks, airplanes, trains, and ships. In many applications, hydrogen and fuel cells offer the potential to minimize greenhouse gas emissions owing to their high efficiency and zero-or almost zero-emissions operation.

Hence, development of scalable, fossil-free, sustainable pathway for producing high-quality hydrogen is a dire necessity. With the use of renewable energy, H_2 may be manufactured from earth abundant water. Solar-powered H_2 production methods including photocatalytic and photoelectrochemical water splitting have drawn a lot of attention in recent decades [108,109]. However, because of the low radiation power density of sunlight, these technologies are limited in their ability to convert solar energy into hydrogen fuel. Further, when driven by electricity from flexible renewable energy sources, electrochemical water splitting is more combative for large-scale H_2 generation [110]. Although water electrolysis is being studied over the past two centuries, still only 4% of entire H_2 production comes from it [111] because of its limited applications. Refinement in cost-effectiveness and improved energy efficiency are two essential components for the broad use of water electrolysis technologies.

The electrocatalytic hydrogen evolution reaction (HER), which produces high-purity H_2 under ambient atmosphere during water electrolysis, has garnered a lot of interest. The Volmer–Tafel and Volmer–Heyrovsky pathways are the two main pathways involved in HER [112]. The choice of catalysts has a major impact on the HER efficiency as in different

types of water electrolyzers, the electrocatalysts play a key role in stimulating the pace of electrode reaction and minimizing the energy loss. The cost, catalytic activity, and stability of an electrocatalyst are frequently linked to its application potential. HER can be carried out in alkaline, neutral, or acidic environments. Nowadays, the preferred catalysts for HER are materials based on platinum (Pt), ruthenium (Ru) and iridium (Ir) owing to their exceptional catalytic activity and durability under a range of pH environments. However, their prevalent applications have been hindered by their high price, limited supply, and inherent scarcity [113,114]. Therefore, investigating plentiful and affordable alternatives to lower the cost of water electrolysis systems is crucial and hence design of high-efficiency HER catalysts based on affordable, earthly materials has attracted a lot of attention. According to research, transition metal sulfides, phosphides, oxides, carbides, and nitrides have the superior catalytic activity towards HER [115–120].

1.4 Hydrogen : A Clean Fuel

To address environmental and energy concerns, it is essential to develop efficient energy storage and conversion technologies in addition to sustainable and renewable energy sources. Hydrogen is thought to be the best clean energy source because it has the highest mass-energy density of any fuel. One appealing method of producing clean hydrogen is electrochemical water splitting, which has the benefit of producing a high-purity H_2 with zero carbon emissions [121,122]. Water electrolyzers typically run at a substantially higher voltage of 1.8–2.0 V compared to the theoretical limit of 1.23 V. Incorporation of a cost-effective electrocatalyst in hydrogen/oxygen evolution reaction (HER/OER) can boost their slow kinetics and further reduce the overpotential [123]. Nowadays, the most groundbreaking HER and OER electrocatalysts available are Pt-based materials and Ru or Ir oxides as discusses in previous chapter. But these materials are very expensive and are

hardly earth abundant which obstruct their commercialisation [124,125]. Thus, manufacturing highly active earth-abundant catalysts ranks among the top goals for creating cost-effective and efficient water electrolysis systems. A lot of research has been pursued in developing nonprecious electrocatalysts, such as transition metal-based complexes [126,127] like dichalcogenides (TMDs) [128–133], carbides [134–136], nitrides (TMNs) [137,138], phosphides (TMPs) [139–142] etc. A range of heterostructured catalysts based on transition metal have been reported by demonstrating exceptional catalytic performance toward electrochemical water splitting [143–147]. For instance, by depositing MoS_2 on the surface of $CoSe_2$, Gao et al. developed a $MoS_2/CoSe_2$ heterostructure which demonstrated outstanding HER performance in 0.5 m H_2SO_4, along with a Tafel slope of 36 mV dec^{-1} and an overpotential of 68 mV at 10 mA cm^{-2} current density, supported by excellent durability [148]. Chen et al. reported a 3D core@shell heterostructure catalyst $Co@Co_3O_4$ consisting of metallic Co cores and amorphous Co_3O_4 shells which showed a low overpotential of only 90 mV in 1 M KOH at a current density of 10 mA cm^{-2} [149].

The idea of heterostructure first emerged from Semiconductor physics. As per the definition, heterostructures are semiconductor structures in which the chemical composition varies with position, and they comprise a large number of heterojunctions, which are the interfaces between distinct components [150]. Since knowledge networks are crossing and integrating, the idea of heterostructure has expanded beyond semiconductor physics. In a broader sense, heterostructures are composite structures made up of interfaces produced by several solid-state materials, such as semiconductors, insulators, and conductors. As a result, a heterostructured catalyst is made up of two or more different material types that are often joined by chemical or physical bonds. From the point of view of HER catalysis, the constituent parts of a heterostructure may be active or inert. However,

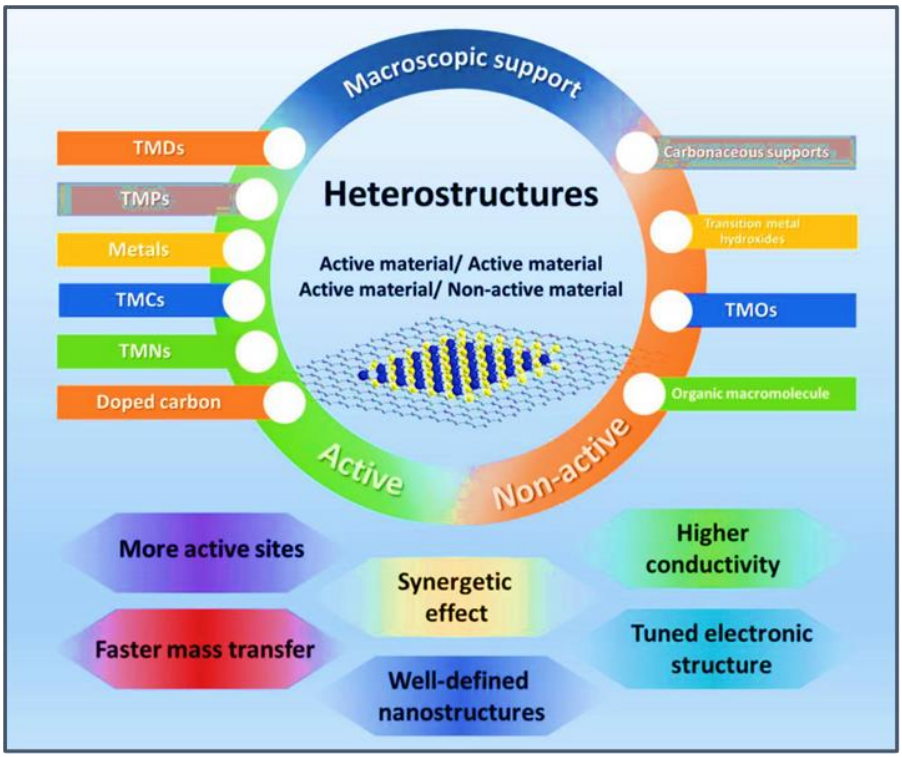

Figure 1.10: Heterostructured catalysts for HER and their superiorities for achieving enhanced catalytic activity.

because heterostructured catalysts may have a number of benefits over single catalysts as shown in Figure 1.10. The majority of heterostructured catalysts, including active/active and active/nonactive kinds, demonstrate higher HER activities than their individual counterparts. First, a productive method for boosting the quantity of active sites is to build heterostructured HER catalysts. With their precise nanostructures and significantly exposed edges, the majority of these heterostructured HER catalysts offer enough adsorption sites for HER [151–153]. Secondly, the durability of the catalyst in electrolyte can be enhanced by creating certain precisely defined nanostructures [152]. Using a core@shell structure as an example, long-lived HER activity can be supported by a thin layer of stable species protecting the active but unstable species. Third, electron transfer between components in heterostructured catalysts may be induced by differences in their electronegativity. This is often indicated by a binding energy change in x-ray photoelectron spectra (XPS). The

electrical or band structures of the components will be regulated by the electron redistribution, which is essential to some heterostructures' higher HER activity [138,154–156]. Lastly, a major factor in the heterostructures' improved HER kinetics is the synergistic effect [148,157].

1.4.1 Electrochemical HER Mechanism

Fundamentally, HER is an mechanism involving electrochemical redox reactions at the electrode-electrolyte interface. H_2 is produced by the reduction of either proton ($H^{+)}$ or water, depending on the electrolyte's pH level, *i.e.*, whether the electrolyte is acidic or basic. Both processes need a number of basic steps.

1.4.1.1 HER in Acidic Electrolyte

It is widely acknowledged that, in acidic conditions, there are two sequential stages involved in the HER at the surface of different catalysts (Figure 1.11a) [158–160]. An adsorbed hydrogen atom (H*), where * denotes an active site on the catalyst surface, is formed at the start of HER when an H^+ is adsorbed on the catalyst surface. Equation (14) represents this this process known as the Volmer step or the discharge step. Next, as shown in Equation (15), a H* joins with an H^+ and an electron (e^-) to generate an H_2 molecule. This process is known as the Heyrovsky step or the electrochemical desorption step.

An alternative method for producing H_2 would be the Tafel step, sometimes referred to as the chemical desorption step, which involves combination two H* on the catalyst surface as described by Equation (16). Equation (17) represents the overall reaction of HER in which the standard electrode potential (E°) that serves as a reference for calculating the standard electrode potential of electrochemical processes [161].

$$H^+ + e^- \rightarrow H^* \quad (14)$$

$$H^+ + H^* + e^- \rightarrow H_2 \quad (15)$$

$$2H^* \rightarrow H_2 \quad (16)$$

$$2H^* + 2e^- \rightarrow H_2 \quad (17)$$

The interaction between the catalyst and H* is a major determinant of the HER kinetics, according to the Sabatier principle [162,163]. S. Trasatti created the first volcano curve for the HER by plotting the reaction rate of the HER along y-axis and the hydride formation energy along x-axis for different electrocatalyst [164]. Since there were no theoretical or experimental data available at the time for the hydrogen adsorption energy (ΔG_H°), the adsorption behavior was described by the hydride formation energy. Nørskov's group gathered experimental data on exchange current densities for HER on different metals and computed ΔG_H° using the density functional theory (DFT). Finally, they were successful in deriving first modern volcano plot [165].

1.4.1.2 HER in Alkaline Electrolyte

Regarding the HER in alkaline media, ΔG_H° is still effective in characterizing the hydrogen adsorption behavior on catalyst surfaces. Further, it is interesting to observe that, in contrast to the volcano plot in an acidic solution, the alkaline electrolyte volcano plot shifts just up and down, not left or right [166]. In particular, most metal catalysts have exchange current densities of HER in alkaline solutions that are two to three orders of magnitude lower than those in acidic electrolytes [167,168]. The fact that the alkaline HER follows a different pathway from that in acidic solutions is one among the main causes of this lower catalytic activity. The HER in alkaline media begins with the dissociation of H_2O molecules to provide protons because of the absence of H^+ (Figure 1.11b). This process is involved in both the Volmer Equation (18) and the Heyrovsky Equation (19) of alkaline HER, while the Tafel step is unchanged from that in acid solutions. Equation (20) describes

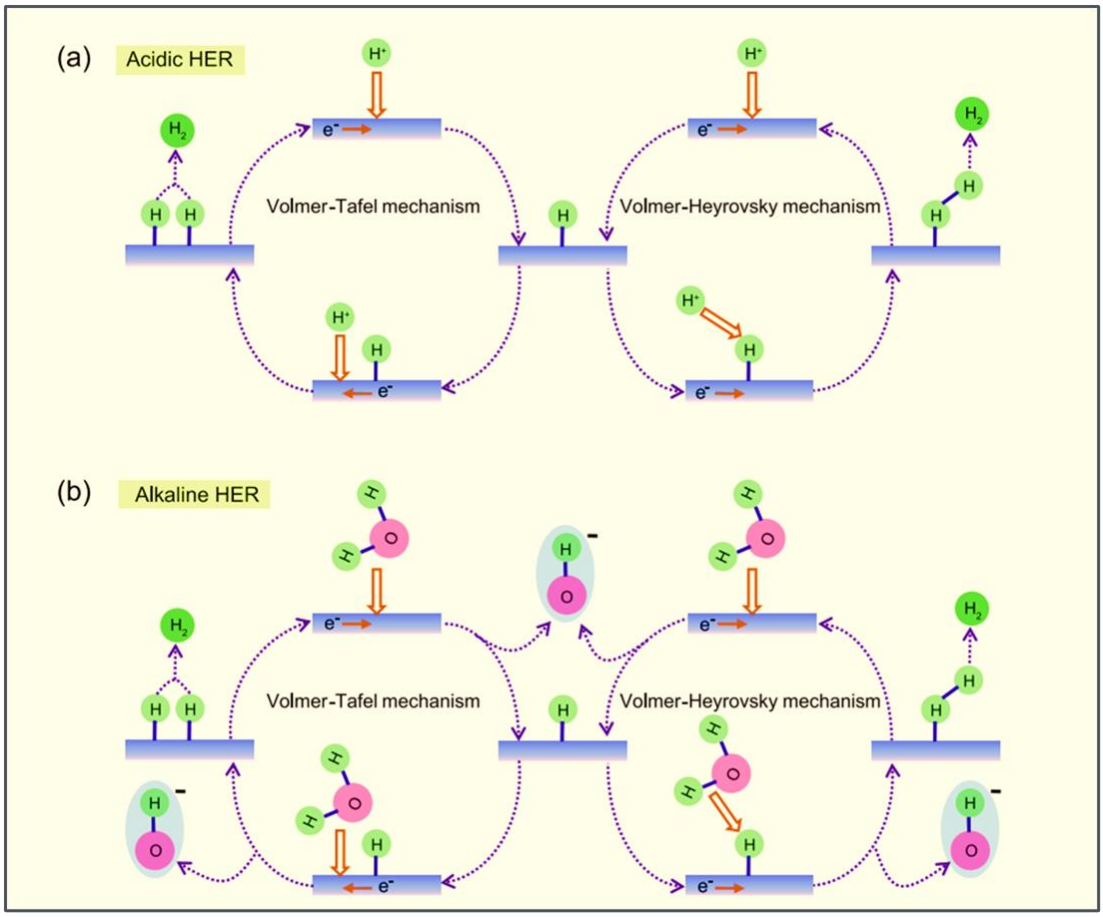

Figure 1.11: HER Pathways in the (a) Acidic and (b) Alkaline Electrolyte [169].

the complete reaction processes. Further, E° of this reaction with respect to the standard hydrogen electrode (SHE), is −0.826 V.

$$H_2O + e^- \rightarrow H^* + OH^- \quad (18)$$

$$H^* + H_2O + e^- \rightarrow H_2 + OH^- \quad (19)$$

$$2H_2O + 2e^- \rightarrow H_2 + 2OH^- \quad (20)$$

The HER kinetics on most catalysts are slower in alkaline electrolytes because it takes more energy to produce protons in alkaline medium. According to reports, the activity of alkaline HER is regulated by a fine equilibrium between ΔG_H° and the energy needed to separate

H_2O [160]. Thus, an effective way to build catalysts toward alkaline HER is to encourage the water dissociation process while maintaining a reasonable hydrogen adsorption energy.

1.5 Transition Metal-based Semiconductor for HER

For the HER process, transition metal dichalcogenides (TMDs) have been chosen over the other materials based on transition metal because of their better catalytic performance, which is partly attributable to their inherent electrocatalytic activity. When comparing TMDs to other transition metal-based materials, there are additional benefits beyond these inherent characteristics:

(i) The semiconducting or metallic crystal phases that TMDs offer enable the management of their functioning.

(ii) TMDs can accommodate dopants easily because of the fact that TMDs morphologically more flexible [170]

Recently, TMD nanosheets have been widely employed and investigated for HER application. As two-dimensional materials, they have a vast electrochemical surface area that can effectively be used as possible sites for reactions that transfer electrons to protons, resulting in the production of hydrogen (Figure 1.12). Because these nanosheets are metallic-based arrays and benefit from the catalytic activity of metals included into their architecture, they may function effectively in relation to HER. Transition metal dichalcogenides have received a lot of attention lately for HER.

It is unveiled that, in comparison to their bulky equivalent, TMD nanostructures, such as nanosheets or nanoflakes have distinct catalytic attributes, a characteristic that can provide varying HER performances [171].TMDs nanosheets with varying conductivity values can

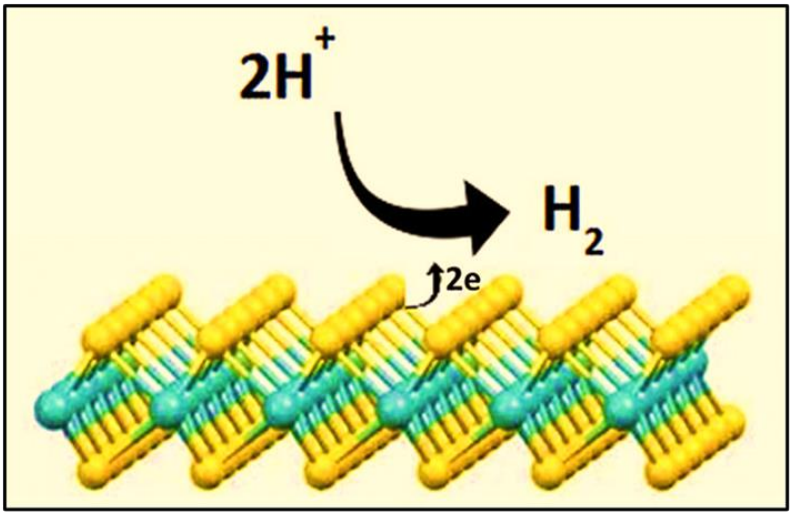

Figure 1.12: TMDs for Hydrogen Evolution by Reduction of Proton in Aqueous System [170].

be produced using electrochemical and exfoliation approaches. This is because multiple structural phases are provided by the actual exfoliation process [172]. It has been observed that, Polymorph plays a key role in regulating the overall conductivity and HER performance [173] due to its different tuned bandgaps [174–176]. Further, the performance of TMD-based electrocatalysts for HER might be significantly enhanced by incorporation of a range of functional variables and parameters. Therefore, it is critical to identify and develop the fundamental elements that will enhance the functionality of these TMD-based systems for the sake of future hydrogen energy systems.

1.6 Objectives and Scope of the Thesis

The increasing popularity of transition metal-based electrochemistry makes them a strong candidate for use as high-performing electrode materials for energy storage systems and next generation portable devices. Furthermore, the hydrogen economy has emerged as a visionary future and a long-term replacement for the current fossil-fuel-based economy, with hydrogen as a commercial fuel expected to contribute considerably to global energy

needs. This necessitates the use of transition metal-based nanostructures as electrocatalysts for hydrogen evolution processes. Transition metal-based systems can provide all of these benefits due to their high energy state, multi-oxidation states of metal ions, abundance, and low environmental toxicity, among other factors. It can easily lend and receive electrons from other molecules due to its multi-oxidation states. Besides, these materials have better electrochemical stability than polymers and a greater energy density than carbonaceous materials due to a balance between the pore size at the electrode surface and the ionic size of the electrolyte [177]. As a result, the focus of this research will be on the synthesis, detailed characterization, and property analysis of these transition metal-based complexes. In comparison to bulk composite, direct growth of this transition metal-based nanostructure over several other nanoforms is a well-known process. When this type of hierarchical nanoform is realized, it often results in unique interface phenomena, a large surface area, and several functionalities, as well as a synergistic effect from each individual, which suppresses all individual shortcomings. This can be done either between two transition metal-based systems or between carbonaceous and transition metal-based systems. In addition, composites will be fabricated and thoroughly investigated.

The following are my research's primary objectives:

- To design suitable wet chemical, hydrothermal synthesis techniques for transition metal oxides and chalcogenides.
- Advanced techniques including as XRD, HRTEM, FESEM, AFM, and XPS will be used to characterize the produced materials in detail structural and morphological terms.
- Graphene and other transition metal dichalcogenides, as well as composites, will be used to manufacture and test superstructures for unique material features and novel applications.

- By creating suitable electrodes, as synthesized nanomaterials will be explored for energy storage applications.
- The electrocatalytic characteristics of such systems will be investigated for possible catalytic applications.
- To comprehend electrical and electronic processes, proper theoretical models will be developed, as well as detailed data analysis.

1.7 Outcomes of the Thesis

Following the objectives, this thesis focuses on the synthesis and characterization of transition metal-based nanostructures namely, $CuCo_2O_4$, MnO_2 and MoS_2 and their hierarchies as well as their possible usage in energy related applications such as supercapacitor devices, HER analysis. In the first work, using a two-step low temperature hydrothermal synthesis route, the hierarchy of $CuCo_2O_4$@MnO_2 nanostructure was realized on a flexible carbon substrate. In the second work hierarchy of MoS_2 Nanosheets (NSs) and polymer (PNMA) hollow spheres was realized to synthesize PNMA@MoS_2 core@shell heterostructure. Further, high temperature annealing altered crystallinity of MoS_2 NSs and converted PNMA to N-doped carbon (NC). The structural, morphological, and superficial analysis of the as-synthesised nanostructures were studied using a variety of characterization techniques namely, X-Ray diffraction (XRD), RAMAN analysis, Field Emission Scanning Electron Microscopy (FESEM), Transmission Electron Microscopy (TEM), X-ray Photoelectron Spectroscopy (XPS), Fourier-transform infrared spectroscopy (FTIR), Atomic Force Microscopy (AFM), BET (Brunauer–Emmett–Teller) analysis etc. PGSTAT302N Autolab instrument was used to carry out all the measurements techniques viz. Cyclic Voltammetry (CV), Galvanostatic Charge-Discharge (GCD), Hydrogen Evolution Reaction (HER) and Electrochemical impedance spectroscopy (EIS).

The outcomes of this thesis are enumerated below:

(1) $CuCo_2O_4$@MnO_2 hybrid heterostructure was synthesized in a 2D–2D hierarchical construction on a flexible carbon fiber using a two-step hydrothermal technique. This hybrid illustrated its potential application as an electrode for high-performance SCs. Cu atom incorporation in the Co_3O_4 lattice led to the synthesis of spinel cobaltite $CuCo_2O_4$, one of the constituents of the hybrid. By changing the reaction temperature, morphological diversity in $CuCo_2O_4$ was achieved, and the growth process was investigated further. $CuCo_2O_4$ flakes further served as a foundation for forming porous MnO_2 structures. The well-optimized hybrid displayed superior specific capacitance and cycling stability due to the subsequent development of porous MnO_2 nanoform over $CuCo_2O_4$ flakes. A symmetric solid-state supercapacitor device was further designed using the optimized hybrid, which showed a high gravimetric capacitance along with high energy density.

(2) Further, we developed a hierarchical core@shell-like structure consisting of few-layer MoS_2 NSs and nitrogen-doped graphitic carbon hollow spheres, which manifested excellent electrocatalytic performance in HER. Initially, using an interfacial polymerization approach, PNMA hollow polymer spherical nanostructure was synthesized, which further acted as a core scaffold for the hydrothermal growth of the hierarchy of the MoS_2 shell surrounding PNMA. The catalytic performance changed significantly due to subtle alterations in the annealing temperature as this annealing increased the crystallinity of MoS_2 and converted PNMA into NC. The optimized integrated hierarchy demonstrated outstanding HER performance with a low overpotential, benefiting from the interfacial Mo–N–C bonds at the junction of NC and MoS_2 NSs.

(3) We also synthesized TiO_2@MoS_2 hierarchical heterostructure following a two-step facile hydrothermal route. The electrochemical properties of the synthesized hybrid were found to be significantly higher than those of the TiO_2 sphere.

Finally, this thesis aims to report on the fundamental improvements in understanding the electrochemical reactivity of transition metal-based semiconductors and to discuss the latest explorations of employing transition metal-based nanostructures as electrode materials for their potential utilization in electrochemical energy storage devices.

1.8 References

[1] Y. Wang, M. Qiao, X. Mamat, Appl Surf Sci 540 (2021) 148352.

[2] G. Zan, T. Wu, H. Chen, F. Dong, Q. Wu, J Alloys Compd 852 (2021) 157035.

[3] Z. Sun, F. Li, Z. Ma, Q. Wang, F. Qu, J Alloys Compd 854 (2021) 157114.

[4] M. Sethi, U.S. Shenoy, D.K. Bhat, J Alloys Compd 854 (2021) 157190.

[5] D. Prakash, S. Manivannan, J Alloys Compd 854 (2021) 156853.

[6] P.-Y. Liu, J.-J. Zhao, Z.-P. Dong, Z.-L. Liu, Y.-Q. Wang, J Alloys Compd 854 (2021) 157181.

[7] K.S. Kumar, N. Choudhary, D. Pandey, L. Hurtado, H.-S. Chung, L. Tetard, Y. Jung, J. Thomas, Nanotechnology 31 (2020) 435405.

[8] Y.-P. Gao, Z.-B. Zhai, Q.-Q. Wang, Z.-Q. Hou, K.-J. Huang, J Colloid Interface Sci 539 (2019) 38–44.

[9] Y. Liu, I. Murtaza, A. Shuja, H. Meng, Chemical Engineering Journal 379 (2020) 122326.

[10] S. Shin, M.W. Shin, Appl Surf Sci 540 (2021) 148295.

[11] J. Yu, X. Gao, Z. Cui, Y. Jiao, Q. Zhang, H. Dong, L. Yu, L. Dong, Energy Technology 7 (2019) 1900018.

[12] A. Burke, J Power Sources 91 (2000) 37–50.

[13] B.E. Conway, Electrochemical Supercapacitors: Scientific Fundamentals and Technological Applications, Springer Science & Business Media, 2013.

[14] R. Kötz, M. Carlen, Electrochim Acta 45 (2000) 2483–2498.

[15] R. Kötz, M. Carlen, Electrochim Acta 45 (2000) 2483–2498.

[16] M. Salanne, B. Rotenberg, K. Naoi, K. Kaneko, P.-L. Taberna, C.P. Grey, B. Dunn, P. Simon, Nat Energy 1 (2016) 1–10.

[17] D.P. Dubal, O. Ayyad, V. Ruiz, P. Gomez-Romero, Chem Soc Rev 44 (2015) 1777–1790.

[18] Y. Wang, Y. Song, Y. Xia, Chem Soc Rev 45 (2016) 5925–5950.

[19] D.P. Dubal, P. Gomez-Romero, B.R. Sankapal, R. Holze, Nano Energy 11 (2015) 377–399.

[20] H. Bin Wu, G. Zhang, L. Yu, X.W.D. Lou, Nanoscale Horiz 1 (2016) 27–40.

[21] Z. Wu, L. Li, J. Yan, X. Zhang, Advanced Science 4 (2017) 1600382.

[22] Z. Yang, J. Ren, Z. Zhang, X. Chen, G. Guan, L. Qiu, Y. Zhang, H. Peng, Chem Rev 115 (2015) 5159–5223.

[23] K. Naoi, W. Naoi, S. Aoyagi, J. Miyamoto, T. Kamino, Acc Chem Res 46 (2013) 1075–1083.

[24] B.E. Conway, Electrochemical Supercapacitors: Scientific Fundamentals and Technological Applications, Springer Science & Business Media, 2013.

[25] A. Yu, V. Chabot, J. Zhang, Electrochemical Supercapacitors for Energy Storage and Delivery: Fundamentals and Applications, Taylor & Francis, 2013.

[26] S. Yang, R.E. Bachman, X. Feng, K. Müllen, Acc Chem Res 46 (2013) 116–128.

[27] I.N. Jiya, N. Gurusinghe, R. Gouws, Electronics (Basel) 7 (2018) 268.

[28] B.E. Conway, J Electrochem Soc 138 (1991) 1539.

[29] P. Sharma, T.S. Bhatti, Energy Convers Manag 51 (2010) 2901–2912.

[30] A. Schneuwly, R. Gallay, in: Proceeding PCIM, Citeseer, 2000.

[31] M.S. Halper, J.C. Ellenbogen, The MITRE Corporation, McLean, Virginia, USA 1 (2006).

[32] A. Chu, P. Braatz, J Power Sources 112 (2002) 236–246.

[33] A. Burke, J Power Sources 91 (2000) 37–50.

[34] R. Drummond, C. Huang, P.S. Grant, S.R. Duncan, J Power Sources 433 (2019) 126579.

[35] C. Yan, P.S. Lee, Small 10 (2014) 3443–3460.

[36] S.-Y. Lee, K.-H. Choi, W.-S. Choi, Y.H. Kwon, H.-R. Jung, H.-C. Shin, J.Y. Kim, Energy Environ Sci 6 (2013) 2414–2423.

[37] S. Yao, Y. Zhu, Advanced Materials 27 (2015) 1480–1511.

[38] Y. Zhang, Y. Huang, J.A. Rogers, Curr Opin Solid State Mater Sci 19 (2015) 190–199.

[39] W. Liu, M. Song, B. Kong, Y. Cui, Advanced Materials 29 (2017) 1603436.

[40] K. Guo, N. Yu, Z. Hou, L. Hu, Y. Ma, H. Li, T. Zhai, J Mater Chem A Mater 5 (2017) 16–30.

[41] T.Q. Trung, N. Lee, Advanced Materials 29 (2017) 1603167.

[42] H. Wang, A.C. Forse, J.M. Griffin, N.M. Trease, L. Trognko, P.-L. Taberna, P. Simon, C.P. Grey, J Am Chem Soc 135 (2013) 18968–18980.

[43] P. Simon, Y. Gogotsi, Acc Chem Res 46 (2013) 1094–1103.

[44] V. Augustyn, P. Simon, B. Dunn, Energy Environ Sci 7 (2014) 1597–1614.

[45] F. Béguin, V. Presser, A. Balducci, E. Frackowiak, Advanced Materials 26 (2014) 2219–2251.

[46] J.R. Miller, A. Burke, Electrochem Soc Interface 17 (2008) 53.

[47] P. Simon, Y. Gogotsi, Nat Mater 7 (2008) 845–854.

[48] J.R. Miller, P. Simon, Science (1979) 321 (2008) 651–652.

[49] N.A. Choudhury, S. Sampath, A.K. Shukla, Energy Environ Sci 2 (2009) 55–67.

[50] H. Xiao, Z.-S. Wu, L. Chen, F. Zhou, S. Zheng, W. Ren, H.-M. Cheng, X. Bao, ACS Nano 11 (2017) 7284–7292.

[51] S. Zheng, Z.-S. Wu, S. Wang, H. Xiao, F. Zhou, C. Sun, X. Bao, H.-M. Cheng, Energy Storage Mater 6 (2017) 70–97.

[52] C. Largeot, C. Portet, J. Chmiola, P.-L. Taberna, Y. Gogotsi, P. Simon, J Am Chem Soc 130 (2008) 2730–2731.

[53] J. Chmiola, G. Yushin, Y. Gogotsi, C. Portet, P. Simon, P.-L. Taberna, Science (1979) 313 (2006) 1760–1763.

[54] G. Lota, E. Frackowiak, Electrochem Commun 11 (2009) 87–90.

[55] H. Shi, Electrochim Acta 41 (1996) 1633–1639.

[56] M. Deschamps, E. Gilbert, P. Azais, E. Raymundo-Piñero, M.R. Ammar, P. Simon, D. Massiot, F. Béguin, Nat Mater 12 (2013) 351–358.

[57] C. Merlet, B. Rotenberg, P.A. Madden, P.-L. Taberna, P. Simon, Y. Gogotsi, M. Salanne, Nat Mater 11 (2012) 306–310.

[58] A.J. Bard, L.R. Faulkner, H.S. White, Electrochemical Methods: Fundamentals and Applications, John Wiley & Sons, 2022.

[59] L.B.R. Puri, I.R. Sharma, M.S. Pathania, Principles of Physical Chemistry, Vishal, 2013.

[60] P.W. Atkins, J. De Paula, J. Keeler, Atkins' Physical Chemistry, Oxford university press, 2023.

[61] O. Stern, Z. Elektrochem 30 (1924) 1014–1020.

[62] L.L. Zhang, X.S. Zhao, Chem Soc Rev 38 (2009) 2520–2531.

[63] M.Z. Bazant, B.D. Storey, A.A. Kornyshev, Phys Rev Lett 106 (2011) 046102.

[64] A.A. Kornyshev, J Phys Chem B 111 (2007) 5545–5557.

[65] S. Kondrat, A. Kornyshev, J. Phys.: Condens. Matter 25 (2013) 1pp.

[66] S. Kondrat, N. Georgi, M. V Fedorov, A.A. Kornyshev, Physical Chemistry Chemical Physics 13 (2011) 11359–11366.

[67] M.Z. Bazant, B.D. Storey, A.A. Kornyshev, Phys Rev Lett 106 (2011) 046102.

[68] R. Futamura, T. Iiyama, Y. Takasaki, Y. Gogotsi, M.J. Biggs, M. Salanne, J. Ségalini, P. Simon, K. Kaneko, Nat Mater 16 (2017) 1225–1232.

[69] A. Balakrishnan, K.R. V Subramanian, Nanostructured Ceramic Oxides for Supercapacitor Applications, CRC Press, 2014.

[70] X. Wang, G. Yushin, Energy Environ Sci 8 (2015) 1889–1904.

[71] M. Salanne, B. Rotenberg, K. Naoi, K. Kaneko, P.-L. Taberna, C.P. Grey, B. Dunn, P. Simon, Nat Energy 1 (2016) 16070.

[72] M. Khalid, P. Bhardwaj, H. Varela, Science, Technology and Advanced Application of Supercapacitors (2018) 1–18.

[73] E. Frackowiak, V. Khomenko, K. Jurewicz, K. Lota, F. Béguin, J Power Sources 153 (2006) 413–418.

[74] J.P. Zheng, T.R. Jow, J Electrochem Soc 142 (1995) L6–L8.

[75] J.P. Zheng, P.J. Cygan, T.R. Jow, J Electrochem Soc 142 (1995) 2699–2703.

[76] K. Jurewicz, S. Delpeux, V. Bertagna, F. Béguin, E. Frackowiak, Chem Phys Lett 347 (2001) 36–40.

[77] Z. Lei, J. Zhang, X.S. Zhao, J. Mater. Chem. 22 (2012) 153–160.

[78] J. Yang, C. Yu, X. Fan, S. Liang, S. Li, H. Huang, Z. Ling, C. Hao, J. Qiu, Energy Environ Sci 9 (2016) 1299–1307.

[79] X. Tang, R. Jia, T. Zhai, H. Xia, ACS Appl Mater Interfaces 7 (2015) 27518–27525.

[80] B. Ding, X. Wu, J Alloys Compd 842 (2020) 155838.

[81] H. Li, L. Cheng, Y. Xia, Electrochemical and Solid-State Letters 8 (2005) A433.

[82] X. Wang, J.P. Zheng, J Electrochem Soc 151 (2004) A1683.

[83] A. Du Pasquier, I. Plitz, S. Menocal, G. Amatucci, J Power Sources 115 (2003) 171–178.

[84] W.G. Pell, B.E. Conway, J Power Sources 136 (2004) 334–345.

[85] G.G. Amatucci, F. Badway, A. Du Pasquier, T. Zheng, J Electrochem Soc 148 (2001) A930.

[86] M. Zheng, X. Xiao, L. Li, P. Gu, X. Dai, H. Tang, Q. Hu, H. Xue, H. Pang, Sci China Mater 61 (2018) 185–209.

[87] P. Sharma, T.S. Bhatti, Energy Convers Manag 51 (2010) 2901–2912.

[88] Y. He, W. Chen, C. Gao, J. Zhou, X. Li, E. Xie, Nanoscale 5 (2013) 8799.

[89] S.A. Delbari, L.S. Ghadimi, R. Hadi, S. Farhoudian, M. Nedaei, A. Babapoor, A. Sabahi Namini, Q. Van Le, M. Shokouhimehr, M. Shahedi Asl, M. Mohammadi, J Alloys Compd 857 (2021) 158281.

[90] H. Liu, X. Liu, S. Wang, H.-K. Liu, L. Li, Energy Storage Mater 28 (2020) 122–145.

[91] S. Trasatti, G. Buzzanca, J Electroanal Chem Interfacial Electrochem 29 (1971) A1–A5.

[92] C.-C. Hu, K.-H. Chang, M.-C. Lin, Y.-T. Wu, Nano Lett 6 (2006) 2690–2695.

[93] C. Jing, X. Song, K. Li, Y. Zhang, X. Liu, B. Dong, F. Dong, S. Zhao, H. Yao, Y. Zhang, J Mater Chem A Mater 8 (2020) 1697–1708.

[94] C. Choi, D.S. Ashby, D.M. Butts, R.H. DeBlock, Q. Wei, J. Lau, B. Dunn, Nat Rev Mater 5 (2020) 5–19.

[95] D. Kong, J. Luo, Y. Wang, W. Ren, T. Yu, Y. Luo, Y. Yang, C. Cheng, Adv Funct Mater 24 (2014) 3815–3826.

[96] S. Jin, H. Lee, S. Yim, RSC Adv 9 (2019) 31846–31852.

[97] L. Hu, L. Wu, M. Liao, X. Hu, X. Fang, Adv Funct Mater 22 (2012) 998–1004.

[98] T. Wei, C. Chen, H. Chien, S. Lu, C. Hu, Advanced Materials 22 (2010) 347–351.

[99] S. Li, Y.-F. Dong, D.-D. Wang, W. Chen, L. Huang, C.-W. Shi, L.-Q. Mai, Front Phys (Beijing) 9 (2014) 303–322.

[100] B.G. Choi, Y.S. Huh, W.H. Hong, D. Erickson, H.S. Park, Nanoscale 5 (2013) 3976–3981.

[101] J. Duay, S.A. Sherrill, Z. Gui, E. Gillette, S.B. Lee, ACS Nano 7 (2013) 1200–1214.

[102] Y. Li, Z. Fu, B. Su, Adv Funct Mater 22 (2012) 4634–4667.

[103] Y. Yue, H. Liang, J Power Sources 284 (2015) 435–445.

[104] D.O. Ozgur, Fuel (2022) 125538.

[105] Z.W. Seh, J. Kibsgaard, C.F. Dickens, I.B. Chorkendorff, J.K. Nørskov, T.F. Jaramillo, Science (1979) 355 (2017) eaad4998.

[106] Y. Cao, ACS Nano 15 (2021) 11014–11039.

[107] H. Sun, Z. Yan, F. Liu, W. Xu, F. Cheng, J. Chen, Advanced Materials 32 (2020) 1806326.

[108] B. Song, S. Jin, Joule 1 (2017) 220–221.

[109] X. Ren, Q. Ma, H. Fan, L. Pang, Y. Zhang, Y. Yao, X. Ren, S.F. Liu, Chemical Communications 51 (2015) 15997–16000.

[110] C. Sun, J. Zhang, J. Ma, P. Liu, D. Gao, K. Tao, D. Xue, J Mater Chem A Mater 4 (2016) 11234–11238.

[111] S. Yang, M. Xie, L. Chen, W. Wei, X. Lv, Y. Xu, N. Ullah, O.C. Judith, Y.B. Adegbemiga, J. Xie, Int J Hydrogen Energy 44 (2019) 4543–4552.

[112] Q. Tang, D. Jiang, ACS Catal 6 (2016) 4953–4961.

[113] Y. Zheng, Y. Jiao, A. Vasileff, S. Qiao, Angewandte Chemie International Edition 57 (2018) 7568–7579.

[114] Y. Shi, B. Zhang, Chem Soc Rev 45 (2016) 1529–1541.

[115] N. Ullah, W. Zhao, X. Lu, C.J. Oluigbo, S.A. Shah, M. Zhang, J. Xie, Y. Xu, Electrochim Acta 298 (2019) 163–171.

[116] P. Xiao, X. Ge, H. Wang, Z. Liu, A. Fisher, X. Wang, Adv Funct Mater 25 (2015) 1520–1526.

[117] L. Ma, L.R.L. Ting, V. Molinari, C. Giordano, B.S. Yeo, J Mater Chem A Mater 3 (2015) 8361–8368.

[118] W. Liu, E. Hu, H. Jiang, Y. Xiang, Z. Weng, M. Li, Q. Fan, X. Yu, E.I. Altman, H. Wang, Nat Commun 7 (2016) 10771.

[119] H. Jin, J. Wang, D. Su, Z. Wei, Z. Pang, Y. Wang, J Am Chem Soc 137 (2015) 2688–2694.

[120] J. Kibsgaard, C. Tsai, K. Chan, J.D. Benck, J.K. Nørskov, F. Abild-Pedersen, T.F. Jaramillo, Energy Environ Sci 8 (2015) 3022–3029.

[121] J. Wang, W. Cui, Q. Liu, Z. Xing, A.M. Asiri, X. Sun, Advanced Materials 28 (2016) 215–230.

[122] C.G. Morales-Guio, L.-A. Stern, X. Hu, Chem Soc Rev 43 (2014) 6555–6569.

[123] L. Shao, H. Sun, L. Miao, X. Chen, M. Han, J. Sun, S. Liu, L. Li, F. Cheng, J. Chen, J Mater Chem A Mater 6 (2018) 2494–2499.

[124] Y. Shi, B. Zhang, Chem Soc Rev 45 (2016) 1529–1541.

[125] Y. Zheng, Y. Jiao, A. Vasileff, S. Qiao, Angewandte Chemie International Edition 57 (2018) 7568–7579.

[126] X. Zou, Y. Zhang, Chem Soc Rev 44 (2015) 5148–5180.

[127] N.-T. Suen, S.-F. Hung, Q. Quan, N. Zhang, Y.-J. Xu, H.M. Chen, Chem Soc Rev 46 (2017) 337–365.

[128] D. Voiry, H. Yamaguchi, J. Li, R. Silva, D.C.B. Alves, T. Fujita, M. Chen, T. Asefa, V.B. Shenoy, G. Eda, Nat Mater 12 (2013) 850–855.

[129] Y. Kim, D.H.K. Jackson, D. Lee, M. Choi, T. Kim, S. Jeong, H. Chae, H.W. Kim, N. Park, H. Chang, Adv Funct Mater 27 (2017) 1701825.

[130] C. Xu, S. Peng, C. Tan, H. Ang, H. Tan, H. Zhang, Q. Yan, J Mater Chem A Mater 2 (2014) 5597–5601.

[131] C. Ouyang, X. Wang, S. Wang, Chemical Communications 51 (2015) 14160–14163.

[132] L. Tao, X. Duan, C. Wang, X. Duan, S. Wang, Chemical Communications 51 (2015) 7470–7473.

[133] J.-X. Feng, J.-Q. Wu, Y.-X. Tong, G.-R. Li, J Am Chem Soc 140 (2018) 610–617.

[134] C. Wan, Y.N. Regmi, B.M. Leonard, Angewandte Chemie 126 (2014) 6525–6528.

[135] H. Ang, H.T. Tan, Z.M. Luo, Y. Zhang, Y.Y. Guo, G. Guo, H. Zhang, Q. Yan, Small 11 (2015) 6278–6284.

[136] H. Ang, H. Wang, B. Li, Y. Zong, X. Wang, Q. Yan, Small 12 (2016) 2859–2865.

[137] W. Chen, K. Sasaki, C. Ma, A.I. Frenkel, N. Marinkovic, J.T. Muckerman, Y. Zhu, R.R. Adzic, Angewandte Chemie International Edition 51 (2012) 6131–6135.

[138] H. Yan, C. Tian, L. Wang, A. Wu, M. Meng, L. Zhao, H. Fu, Angewandte Chemie 127 (2015) 6423–6427.

[139] D.Y. Chung, S.W. Jun, G. Yoon, H. Kim, J.M. Yoo, K.-S. Lee, T. Kim, H. Shin, A.K. Sinha, S.G. Kwon, J Am Chem Soc 139 (2017) 6669–6674.

[140] J. Zhang, T. Wang, P. Liu, S. Liu, R. Dong, X. Zhuang, M. Chen, X. Feng, Energy Environ Sci 9 (2016) 2789–2793.

[141] Z. Zhang, B. Lu, J. Hao, W. Yang, J. Tang, Chemical Communications 50 (2014) 11554–11557.

[142] A.-L. Wang, J. Lin, H. Xu, Y.-X. Tong, G.-R. Li, J Mater Chem A Mater 4 (2016) 16992–16999.

[143] H. Lin, Z. Shi, S. He, X. Yu, S. Wang, Q. Gao, Y. Tang, Chem Sci 7 (2016) 3399–3405.

[144] D. Wang, Q. Li, C. Han, Z. Xing, X. Yang, ACS Cent Sci 4 (2018) 112–119.

[145] K. Rui, G. Zhao, Y. Chen, Y. Lin, Q. Zhou, J. Chen, J. Zhu, W. Sun, W. Huang, S.X. Dou, Adv Funct Mater 28 (2018) 1801554.

[146] S. Dou, J. Wu, L. Tao, A. Shen, J. Huo, S. Wang, Nanotechnology 27 (2015) 045402.

[147] Y. Chen, Q. Zhou, G. Zhao, Z. Yu, X. Wang, S.X. Dou, W. Sun, Adv Funct Mater 28 (2018) 1705583.

[148] M.-R. Gao, J.-X. Liang, Y.-R. Zheng, Y.-F. Xu, J. Jiang, Q. Gao, J. Li, S.-H. Yu, Nat Commun 6 (2015) 5982.

[149] X. Yan, L. Tian, M. He, X. Chen, Nano Lett 15 (2015) 6015–6021.

[150] N.G. Einspruch, W.R. Frensley, Heterostructures and Quantum Devices, Elsevier, 2014.

[151] R.D. Nikam, A.-Y. Lu, P.A. Sonawane, U.R. Kumar, K. Yadav, L.-J. Li, Y.-T. Chen, ACS Appl Mater Interfaces 7 (2015) 23328–23335.

[152] L. Yang, W. Zhou, D. Hou, K. Zhou, G. Li, Z. Tang, L. Li, S. Chen, Nanoscale 7 (2015) 5203–5208.

[153] Q. Qu, J.-H. Zhang, J. Wang, Q.-Y. Li, C.-W. Xu, X. Lu, Sci Rep 7 (2017) 41542.

[154] X. Zhou, Y. Liu, H. Ju, B. Pan, J. Zhu, T. Ding, C. Wang, Q. Yang, Chemistry of Materials 28 (2016) 1838–1846.

[155] F. Wang, P. He, Y. Li, T.A. Shifa, Y. Deng, K. Liu, Q. Wang, F. Wang, Y. Wen, Z. Wang, Adv Funct Mater 27 (2017) 1605802.

[156] H. Yan, C. Tian, L. Wang, A. Wu, M. Meng, L. Zhao, H. Fu, Angewandte Chemie 127 (2015) 6423–6427.

[157] L. Chen, J. Zhang, X. Ren, R. Ge, W. Teng, X. Sun, X. Li, Nanoscale 9 (2017) 16632–16637.

[158] B.E. Conway, B. V Tilak, Electrochim Acta 47 (2002) 3571–3594.

[159] A.J. Bard, L.R. Faulkner, J. Leddy, C.G. Zoski, New York, NY.[Google Scholar] (1980).

[160] N. Danilovic, R. Subbaraman, D. Strmcnik, V. Stamenkovic, N. Markovic, Journal of the Serbian Chemical Society 78 (2013).

[161] H.P. Lehmann, X. Fuentes-Arderiu, L.F. Bertello, Pure and Applied Chemistry 68 (1996) 957–1000.

[162] R. Parsons, Transactions of the Faraday Society 54 (1958) 1053–1063.

[163] P. Quaino, F. Juarez, E. Santos, W. Schmickler, Beilstein Journal of Nanotechnology 5 (2014) 846–854.

[164] S. Trasatti, J Electroanal Chem Interfacial Electrochem 39 (1972) 163–184.

[165] J.K. Nørskov, T. Bligaard, A. Logadottir, J.R. Kitchin, J.G. Chen, S. Pandelov, U. Stimming, J Electrochem Soc 152 (2005) J23.

[166] Z.W. Seh, J. Kibsgaard, C.F. Dickens, I.B. Chorkendorff, J.K. Nørskov, T.F. Jaramillo, Science (1979) 355 (2017) eaad4998.

[167] T.J. Schmidt, P.N. Ross Jr, N.M. Markovic, Journal of Electroanalytical Chemistry 524 (2002) 252–260.

[168] N. Danilovic, R. Subbaraman, D. Strmcnik, K. Chang, A.P. Paulikas, V.R. Stamenkovic, N.M. Markovic, Angewandte Chemie 124 (2012) 12663–12666.

[169] S. Zhang, X. Zhang, Y. Rui, R. Wang, X. Li, Green Energy & Environment 6 (2021) 458–478.

[170] Q. Yu, Y. Luo, A. Mahmood, B. Liu, H.-M. Cheng, Electrochemical Energy Reviews 2 (2019) 373–394.

[171] W. Yin, Z. Ye, X. Bai, D. He, X. Zhang, H. Song, W.Y. William, Nanotechnology 30 (2018) 045603.

[172] H. Chen, J. Si, S. Lyu, T. Zhang, Z. Li, C. Lei, L. Lei, C. Yuan, B. Yang, L. Gao, ACS Appl Mater Interfaces 12 (2020) 24675–24682.

[173] M.A. Lukowski, A.S. Daniel, C.R. English, F. Meng, A. Forticaux, R.J. Hamers, S. Jin, Energy Environ Sci 7 (2014) 2608–2613.

[174] Z. Liu, N. Li, C. Su, H. Zhao, L. Xu, Z. Yin, J. Li, Y. Du, Nano Energy 50 (2018) 176–181.

[175] J. Li, M. Hong, L. Sun, W. Zhang, H. Shu, H. Chang, ACS Appl Mater Interfaces 10 (2018) 458–467.

[176] S. Bagheri, N. Mansouri, E. Aghaie, Int J Hydrogen Energy 41 (2016) 4085–4095.

[177] B. Pal, A. Yasin, R. Kaur, M. Tebyetekerwa, F. Zabihi, S. Yang, C.-C. Yang, Z. Sofer, R. Jose, Renewable and Sustainable Energy Reviews 149 (2021) 111418.

Chapter 2: Literature Review

2.1 Transition Metal-based Nanostructures and their Hierarchies for Energy Application: A Brief Review

An extensive literature survey was performed to find the current status of the existing knowledge on the selected problems, as mentioned in the objectives and scope section in the previous chapter. In this chapter main findings described in some of the already published work as available in the literature are mentioned. This brief review discusses the supercapacitive performances of transition metal oxides, such as ruthenium oxides, manganese oxides, cobalt oxides, copper oxides, titanium oxides, and other ternary metal cobaltite-based binary oxides like nickel cobaltite, copper cobaltite, etc. and their hierarchies synthesized using this hydrothermal approach. Besides, the HER performances of hierarchical transition metal sulfides are also discussed. The literature survey is presented under different subheadings as follows:

2.1.1 Ruthenium Oxides (RuO_2)

Ruthenium oxides (RuO_2). and composites are well-known electrode materials for SCs. Their inherent properties consist of high redox activity, wide potential window, good electrochemical reversibility, and great electrical conductivity. The most researched pseudocapacitive transition metal oxide for energy storage is RuO_2. Numerous investigations have demonstrated the exceptional efficacy of RuO_2 produced by the hydrothermal process as supercapacitor electrode material [1,2]. Ruthenium in RuO_2 has +4 oxidation state. Its manifests theoretical specific capacitance of around 1400–2000 F g^{-1} [3]. A number of studies have concentrated on hybridizing CNT and RuO_2 in the form of composite materials as the exceptional chemical stability, huge specific surface area, rapid charge transport, and large mechanical strength of carbon nanotubes (CNTs) make them

appealing electrode materials for SCs [4]. This would combine the benefits of both components (*i.e.*, CNT and RuO_2) and their synergistic effects and minimize production costs [5–8]. Chang et al. [9] investigated the effect of temperature on the capacitive performance of $RuO_2.xH_2O$ nanoparticles produced by a hydrothermal method. Initially, at a temperature of 200–250 °C, there is a noticeable increase in capacitance as a result of the creation of crystallites, with no decrease in the water content. But as the temperature rises higher, a lot more inactive oxo-bridged bonds form, which lowers the capacitance value. The traditional hydrothermal process can be modified to raise the system capacitance. The template-assisted hydrothermal protocol raises the aspect ratio of the nanostructure, which includes that of nanotubes, nanosheets, nanorods, and nanoparticles [10–13]. Hydrous RuO_2 nanotubes, for instance, have an improved specific capacitance of up to 1300 F g^{-1} at a high aspect ratio [14]. The function of a surfactant like polyethylene glycol (PEG) in the hydrothermal process of RuO_2 nanosheet formation was investigated by Vijayabala et al. [15]. In a 3 M KCl aqueous solution, the electrode material demonstrated a specific capacitance of 600 F g^{-1} at a scan rate of 5 mV s^{-1}. Nevertheless, pristine RuO_2 has a number of drawbacks, including agglomeration during ongoing charge-discharge cycles, a high manufacturing cost, and trouble in maintaining hydrous RuO_2 form. To attain the superior electrochemical performance, all of the above-mentioned limitations encouraged research community to hybridize RuO_2 with other materials, such as carbonaceous materials or other metal oxides/composites. Chaitra et al. [16] reported on an asymmetric supercapacitor system based on hydrous RuO_2-MWCNT composite produced by hydrothermal method. At a scan rate of 2 mV s^{-1} in 1 M H_2SO_4 electrolyte solution, the composite displayed a large specific capacitance of 1585 F g^{-1} compared to pristine h-RuO_2 (604 F g^{-1}). At a scan rate of 2 mV s^{-1}, the device as a whole demonstrated a specific capacitance of 61.8 F g^{-1}, and after 20,000 charge-discharge cycles, it

demonstrated 88% capacitive retention. A comparison investigation using pure RuO_2 and RuO_2/G nanocomposite [17] was conducted by Thangappan and colleagues. The RuO_2/G nanocomposite exhibited a specific capacitance of 441 F g^{-1} at 0.1 A g^{-1} current density. The electrode demonstrated a specific energy of 61.2 W h kg^{-1} at a specific power of 1838.2 W kg^{-1} along with 94% capacitive retention after 1000 galvanostatic charge-discharge (GCD) cycles, in a three-electrode configuration using a 1 M Na_2SO_4 solution. A one-pot hydrothermal process was carried out to hybridize graphene oxide sheets with RuO_2 nanoclusters in order to prevent the aggregation of RuO_2 nanostructures [18]. In the presence of 1 M H_2SO_4 aqueous electrolyte, electrode material displayed a specific capacitance of 512 F g^{-1} at a current density of 2.5 A g^{-1}. Additional low-cost transition metal oxides are mixed with RuO_2 to produce the combined redox activity of both. This leads to an improvement in electrochemical performance while lowering the manufacturing cost of RuO_2. A scalable microwave-assisted hydrothermal technique was used to produce a TiO_2/ RuO_2 composite electrode [19]. The electrode prepared after drop casting the active material onto titanium substrate showed a high specific capacitance of 992 F g^{-1} at a scan rate of 100 mV s^{-1}. In an effort to improve electrochemical performance further, recent research has also focused on reducing the dimension of metal oxide nanoparticles. For example, a composite based on RuO_2/graphene sheets was created via a hydrothermal technique, with RuO_2 particles ranging in size from 5 to 20 nm grown on graphene sheets [20]. After 1000 cycles, the composite with a high specific capacitance exhibited 97.9% c retention of capacitance with a very low RuO_2 deposition percentage.

2.1.2 Manganese Oxides

Among the transition metals that are most prevalent in the earth's crust is manganese. It has multiple valent states and can be found in oxide form as MnO_2 (+4), Mn_2O_3 (+3), Mn_3O_4 (+2, +3), and MnO (+2), among other oxide forms [21]. Mn is a highly

ideal electrode material for SCs because of its various morphology, porosity, defect chemistry, and crystal structures. The most stable oxide form of Mn is Mn_3O_4, which is utilized extensively as a catalyst and in SCs, batteries, fuel cells, and other applications [22]. There are multiple structural configurations seen in the crystalline form of MnO_2, including α-, β-, γ-, and δ-MnO_2 [23]. Manganese oxides are regarded as next-generation SC electrode materials because of their remarkable pseudocapacitive nature, great natural availability, environmental friendliness, and high specific capacitance. They are even being investigated as an alternative to electrode materials based on RuO_2. Conductivity, homogeneity, porosity, particle size, and surface morphology are the key reasons behind. MnO_2's exceptional electrochemical performance. Different approaches have been used to synthesize manganese oxide in different forms for their use as SC electrode materials. These include of the hydrothermal process, microwave treatment, sol-gel method, electrodeposition technique, and thermal deposition [24]. The hydrothermal process is determined to be the most appropriate of all the methods for the synthesis of inorganic materials. For the uniform deposition of active materials on the conductive substrates, the hydrothermal protocol offers a homogeneous environment [100]. Numerous studies have demonstrated this technique's outstanding performance in the production of materials based on MnO_2 for SC electrodes. Li et al. [25] were able to synthesis MnO_2 nanobelts by a hydrothermal procedure. High porosity, increased specific surface area, and high conductivity are displayed by the materials made using this method. The asymmetric supercapacitor device based on MnO_2 nanoparticles demonstrated 91% capacitance retention after 10,000 cycles and a high energy density of 33.8 W h kg^{-1} and power density of 5000 W kg^{-1} throughout a high voltage range of 0 - 2 V. Bai et al. [26] revealed how temperature affects the shape of MnO_2 nanoparticles throughout the hydrothermal production process. They found that at a temperature below 140 °C, δ-MnO2 nanoparticles,

resembling cauliflower like structure, were created, whereas at a temperature over 140 °C, α-MnO_2 nanorods, which resemble needles, were prepared. It was found that needle-like nanoparticles had a greater specific surface area (114 m^2 g^{-1}) than cauliflower-like nanostructure. Using a straightforward hydrothermal protocol, Dai et al. [27] reported MnO_2 nanowires that were evenly distributed over graphene oxide nanosheets. MnO_2 nanowires were measured to have dimensions of 20–40 nm and lengths between 0.5 and 2 mm. The as-synthesized sample deposited on nickel foam showed specific capacitance of 360 F g^{-1} at 0.5 A g^{-1} in a 1 M Na_2SO_4 solution. A composite electrode based on MnO_2/graphene/polyester was described by Guo et al. [28] which was created using a scalable hydrothermal process. It's interesting to note that controlling the reaction time allowed an easy control over the MnO_2 shape. At a sweep rate of 2 mV s^{-1}, MnO_2/graphene/polyester nanocomposite resulted in a specific capacitance of 332 F g^{-1}. An asymmetric solid-state supercapacitor based on Na-MnO_2 was created by Aziz et al. [29]which showed an energy density of 82 W h kg^{-1} in 1 M of Na_2SO_4 and a specific capacitance of 73 F g^{-1} at 5 mV s^{-1}. At a high current density of 0.5 A g^{-1}, the device maintained remarkable cycling stability, maintaining 93.05% of its initial capacitance after 5000 cycles. Misnon et al. [30] has thoroughly examined the important role of morphology and the relationship between the ionic size of the electrolyte and the pore size distribution in the electrode. Due to the distinctive flower-like shape of δ-MnO_2 nanostructures electrolyte ions can travel through a short, highly conducting channel inside the electrode. δ-MnO_2 as SC electrode showed a specific capacitance 363 F g^{-1} at 2 mV s^{-1} in 1 M LiOH. Radhiyah et al. [31] have thoroughly examined the impact of pre-intercalated Na^+ ions on the capacitance enhancement in the nanoflake-like shape of δ-MnO_2. The Na-MnO2 based electrode produced a high specific capacitance of 200 F g^{-1} in 1 M Na_2SO_4. The

aforementioned studies indicate the potential use of the Mn-based oxides synthesized through hydrothermal protocol in the production of SC electrodes.

2.1.3 Copper Oxides

Copper oxides, *i.e.*, CuO and Cu_2O-based Supercapacitors have gained a lot of attention due to their abundance, low cost, nontoxicity, and ease of synthesis for a wide range of micro and nanostructures [32–35]. Unfortunately, their poor cycling ability and low electrical conductivity limit the efficiency of their storage. For example, Zhang and colleagues [36] produced flower-like CuO nanostructures, which resulted in a specific capacitance of 133.6 F g^{-1} in KOH electrolyte, whereas Li and his team [37] focused on growing CuO nanostructures directly onto Cu foam surface and reported a specific capacitance of 212 F g^{-1} in the same electrolyte. CuO nanosheet arrays were created onto Ni foam surface by Wang and his group [38] in order to achieve a high specific capacitance of 569 F g^{-1}. Nevertheless, the synthesis pathway is a quite intricate process with a very less yield. Recently, a straightforward method using carbon cloths (Cu_2O/CuO@Cu-CCs) has been used to manufacture Cu_2O/CuO-based mesoporous nanosheets for use as a binder-free electrode. a current density of 10 mA cm^{-2} (3.57 A g^{-1}) and a specific capacitance of 835.2 F g^{-1} [39]. Further, in another investigation a 3D porous gear-like CuO nanostructure on a Cu substrate produced a specific capacitance of 348 F g^{-1} [40] Pseudocapacitive materials can be added to copper oxides to improve their low specific capacitance value. The primary Faradaic reaction mechanism, as reported in earlier papers [41–44], can be summed up as the quasi-reversible redox conversion of Cu^{1+} and Cu^{2+} by the following equations:

$$2CuO + H_2O + 2e^- \leftrightarrow Cu_2O + 2OH^- \quad (1)$$

$$Cu_2O + 2OH^- \leftrightarrow 2CuO + H_2O + 2e^- \quad (2)$$

$$Cu_2O + 2OH^- + H_2O \leftrightarrow 2Cu(OH)_2 + 2e^- \quad (3)$$

$$CuOH + OH^- \leftrightarrow CuO + H_2O + e^- \quad (4)$$

$$CuOH + OH^- \leftrightarrow Cu(OH)_2 + e^- \quad (5)$$

Increasing the active sites of CuO electrodes that are accessible to electrolytes will help to overcome the challenges of low capacitances, energy densities, and limited rate abilities. This will give precise diffusion paths for fast reaction kinetics. Wang et al. [45] used an affordable, simple-to-use hydrothermal treatment and calcination procedure to create hierarchical, heteroatom-doped carbon/copper oxide/cuprous oxide (CuOx@C) nanocomposites. Here, the discarded bamboo leaves are converted into porous carbon in order to maintain their unique hierarchical structures and inherent heteroatoms. The hierarchical porous carbon architectures facilitate accurate diffusion and facilitate electrolyte-ion transport to the active components during the electrochemical reaction. As a result, the final composite showed outstanding specific capacitance of 147 F g^{-1} and long cyclic life of 93% over 10,000 cycles. The development of metal oxide/carbon nanocomposites as stable SC electrodes with superior energy storage performance is demonstrated in this work.

2.1.4 Cobalt Oxide (Co_3O_4)

Among all the metal oxides available, spinal cobalt oxide (Co_3O_4) has drawn the most interest for a variety of electrochemical applications, including catalysis [46,47], energy storage [48,49], and electrochemical sensing [50,51] because of its superior electrical conductivity [52], multiple oxidation states, and high theoretical specific capacitance (~3560 F g^{-1}) [36]. The spinel structure of Co_3O_4 (Figure 2.1) has Co^{3+} and Co^{2+} states in the octahedral and tetrahedral locations which makes it very intriguing during faradaic redox reaction. Co_3O_4 with variety of structural morphologies, such as

nanoparticles [53,54], nanowires [55,56], nanoflowers [57,58], nanoflakes [59,60], hierarchical structures [61,62] etc. has been produced for energy storage applications. Besides due to low cost

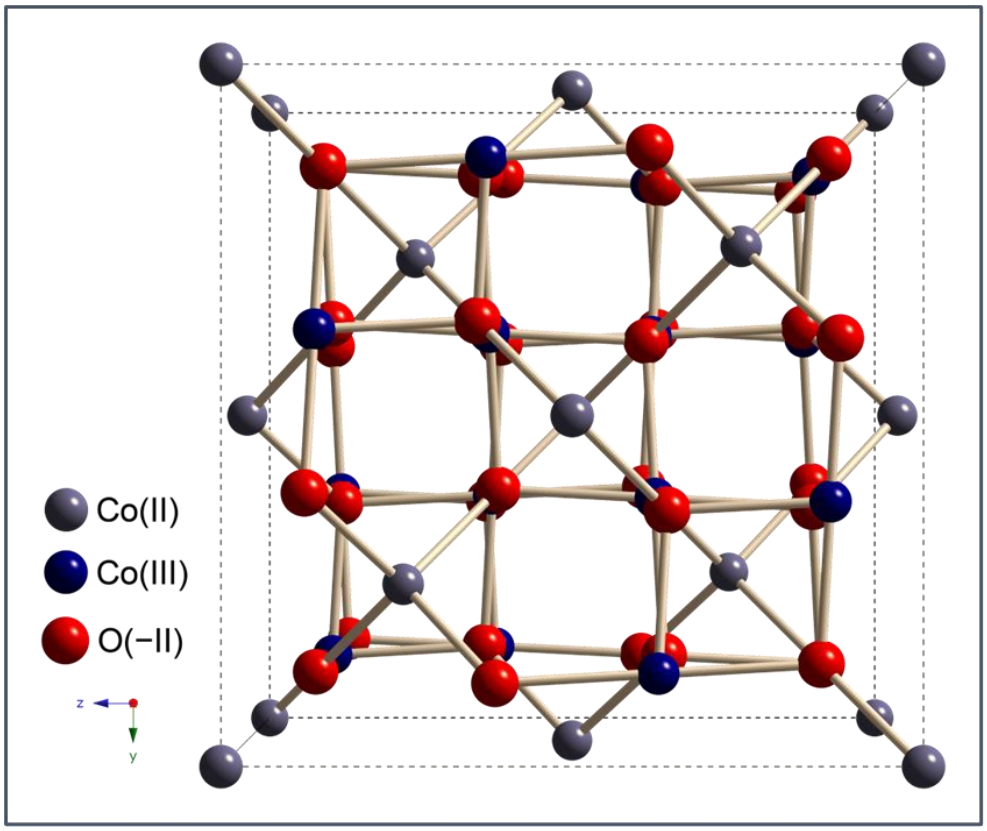

Figure 2.1: Lattice Structure of Spinel Co_3O_4 (*Wikimedia Commons*).

it can be a potential substitute of costly and environmentally hazardous RuO_2 as an electrode material. Gao et al. [63] and Xu et al. [64] reported Co_3O_4 with specific capacitance values of 746 F g^{-1} and 574 F g^{-1} at current densities of 5.0 mA cm^{-2} and 0.1 A g^{-1} respectively. Further, Hu and Hsu [65] and Kandalkar et al. [66] reported Co_3O_4 electrodes with the specific capacitance values of 230 F g^{-1} and 235 F g^{-1}, respectively. Recently, the development of Co_3O_4 electrodes has attracted the attention of more number of researchers. Using the mesoporous silica material MCM-41 as a template, Wang et al. [67] produced Co_3O_4 which yielded a high specific capacitance of 102 F g^{-1} at the scan rate

of 3 mV s^{-1} in 4.0 M KOH. Zheng et al. [68] have proposed a method of manufacturing Co_3O_4 by employing KIT-6 as template. The specific capacitance of 370 F g^{-1} at a current density of 0.5 A g^{-1} was observed with Co_3O_4-KIT-6, which was synthesized at 40 °C hydrothermal temperature and calcined at 200 °C. Moreover, Cui et al. [69] use cetyltrimethylammonium bromide (CTAB) as a template to create Co_3O_4 nanorods by a hydrothermal process aided by a microwave. The as-prepared sample delivered specific capacitance of 456 F g^{-1}. A special technique for creating loosely packed, mesoporous nanocrystalline Co_3O_4 is suggested by Cao et al. [70]. The Co_3O_4 was created (160 °C) by supplying heat at 70 °C with the slope of annealing rate of 1 °C min^{-1} and it resulted in a large surface area of about 212 m^2 g^{-1} and specific capacitance of 401 F g^{-1} in 2.0 M KOH. Till now numerous synthesis protocols have been used to synthesize cobalt oxide, including microwave irradiation [71], potentiostatic deposition [72], solvothermal [73–75], solprecipitation [76,77], sol-gel [78], hydrothermal [77,79], chemical bath depositon [80], spray pyrolysis [81], microemulsion [82], polyol process [83], thermal decomposition [84] etc. The following equations are possible conversion reaction between the several cobalt oxidation states in the electrolyte [85].

$$Co_3O_4 + OH^- + H_2O \leftrightarrow 3CoOOH + e^- \quad (6)$$

$$CoOOH + OH^- \leftrightarrow CoO_2 + H_2O + e^- \quad (7)$$

Though Co_3O_4-based supercapacitors have attracted a great deal of attention from researchers' community because of its remarkable supercapacitive performances, Co_3O_4 does, however, have certain disadvantages, including low electrical conductivity, toxicity, and scarcity [86,87]. Research on lowering the Co content in Co_3O_4 advanced in response to its sluggish electrical conductivity, manufacturing ternary metal cobalt oxides, also known as Cobaltites (TMCs) or Ternary Transition Metal Oxides (TTMOs), using Cu^{2+},

Mn^{2+}, Ni^{2+}, Mg^{2+}, Zn^{2+}, and Fe^{2+} [88]. The reported ternary metal cobaltites are $CuCo_2O_4$ [89], $NiCo_2O_4$ [90], $CaCo_2O_4$ [91], $ZnCo_2O_4$ [92], $MnCo_2O_4$ [93], and $MgCo_2O_4$ [94]. Moreover, these TMCs may increase the parent compound's bandgap or bandwidth, which might raise the material's electrochemical activity [95,96]. Table 2.1 compares the bandgap, electrical conductivity, and oxidation states of different TMCs.

Materials	Oxidation States	Electrical Conductivity	Bandgap (eV)	Ref.
Co_3O_4	+2, +3	$\sim 10^{-5}$	1.6–2.10	[97]
$NiCo_2O_4$	+2, +3	$\sim 10^{-4}$ to $\sim 10^{-3}$	2.1–3.6	[98]
$CuCo_2O_4$	+2, +3	$\sim 10^{-4}$	2.12–2.15	[99]
$MnCo_2O_4$	+2, +3	$\sim 10^{-4}$	2.1	[100]
$CaCo_2O_4$	+2, +3	$\sim 10^{-4}$	2.11	[91]
$ZnCo_2O_4$	+2, +3	$\sim 10^{-4}$	1.71–2.77	[101]
$MgCo_2O_4$	+2, +3	$\sim 10^{-4}$	~ 4	[102]

Table 2.1: Comparative study of Oxidation states, Electrical Conductivity, and Bandgap of different Ternary Metal Cobaltites for Electrochemical Applications.

2.1.5 Copper Cobaltite ($CuCo_2O_4$)

Copper Cobaltite ($CuCo_2O_4$) is one of the above mentioned TMCs-based electrode materials with battery-like behaviours which has many inherent properties, such as natural abundance, environmental friendliness, low cost, and excellent electrochemical properties. All these properties make it appealing for use in Li-ion batteries [103,104], supercapacitors [105], sensors [106–108], and catalysts [109,110]. $CuCo_2O_4$ has two distinct crystal

structures which are normal ($Cu[Co]_2O_4$) and inverse ($Co[CuCo]O_4$) spinel structure. According to S. Angelov et al. [111], a normal spinel can get transformed into an inverse

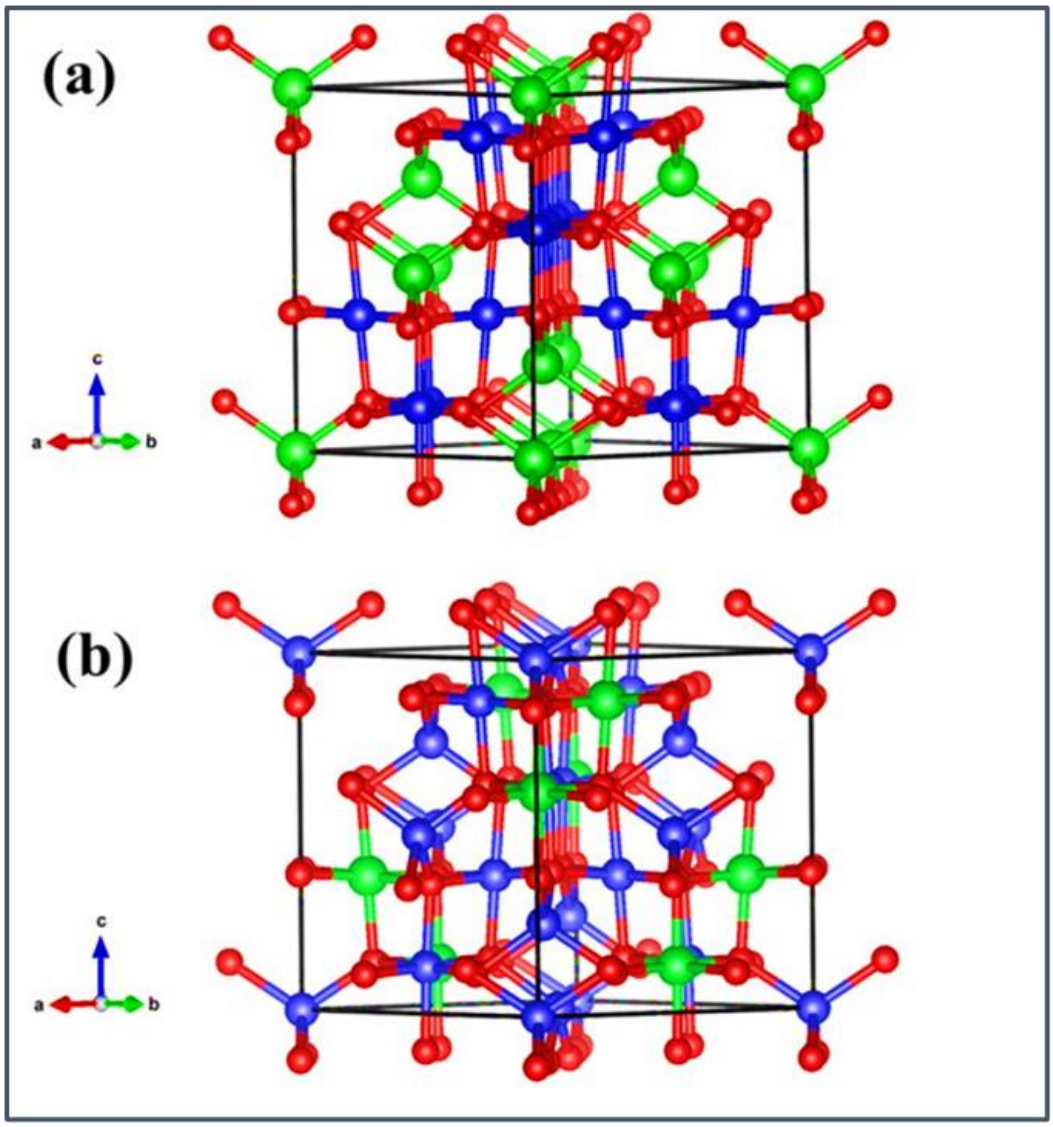

Figure 2.2: The ball-and-stick model of (a) normal and (b) inverse spinel structure of $CuCo_2O_4$. The green, blue and red spheres are Cu, Co, and O atoms, respectively [96].

spinel structure, when the value of x is greater than 0.2 in the $Cu_xCo_{3-x}O_4$. The cations inside square brackets in $Co[CuCo]O_4$ are thought to be located in the octahedral position whereas the cation outside are thought to occupy tetrahedral sites [112–116]. In this unusual inverse spinel crystal structure, the four tetrahedron apexes are shared by the octahedron

inside three-dimensional networks of interconnected interstitial space, which offers effective pathways for ion diffusion when charge carriers (electrons or holes) hop onto the tetrahedral and octahedral positions for strong electrical conduction [117]. As reported by Zheng et al., the catalytic activity for Co oxidation was significantly improved on Cu-substituted Co_3O_4 nanowires. This finding may suggest that Cu ions replace inactive Co ions close to the active sites, boosting the comprhensive activity of the exposed surfaces [118]. Figure 2.2 depicts both the normal and inverse spinel structure of $CuCo_2O_4$. Moreover, when compared to single metal oxides like CuO and Co_3O_4, $CuCo_2O_4$ typically exhibits superior electrochemical performance. This is because Cu cations enhance the oxide's electric conductivity, Co cations improve electrochemical activities. Besides, electron transport between different metal species in $CuCo_2O_4$ has a comparatively low activation energy [119,120]. Hence, $CuCo_2O_4$ can be used as a superior electrode material in supercapacitors. In spite of all these advantages, it still has certain shortcomings in real-world applications, such as low specific capacity, poor cycling stability, and low conductivity. Enhancing the electrochemical performance of pure $CuCo_2O_4$ or its composites has been the focus of much research. The advancements in the synthesis of $CuCo_2O_4$-based electrode materials, the creation of pure $CuCo_2O_4$ electrode materials, and the creation of $CuCo_2O_4$-based composites are all thoroughly researched and covered in detail in this concise literature review. Further, the advancements made by $CuCo_2O_4$-based electrode materials on supercapacitors and research aimed at bridging the gap between the theoretical and achieved capacities of this electrode material are highlighted.

One of the most popular techniques for producing metal oxides at the micro- and nanoscale is the hydrothermal approach. There are numerous benefits to this synthetic approach, such as easy operation, cost savings, and controllable material morphology and size. $CuCo_2O_4$ has been synthesized via hydrothermal protocol along with post-synthesis annealing. For

instance, oxalic acid and NaOH were used as precipitate agents in the synthesis of $CuCo_2O_4$ nanoparticles by Raja et al. [121]. The oxalic acid-assisted $CuCo_2O_4$ NPs demonstrated a large specific surface area of 133 $m^2 g^{-1}$ and a specific capacitance of 765 F g^{-1} at 2 A g^{-1}. But under the same conditions, the $CuCo_2O_4$ NPs aided by NaOH had a specific surface area of 110 m^2 g^{-1} and a specific capacitance of 407 F g^{-1} with 90% capacitive retention. This is due to the small fine suspended particles of the oxalate precipitation which promote ion diffusion and increase the accessible surface area for redox reactions. Zhao et al. [122] used a one-step hydrothermal approach to synthesize $CuCo_2O_4$ crystals using nitrate and chloride salt as precursors. The as-synthesized $CuCo_2O_4$ samples resembled roses ($CuCo_2O_4$-N) and chrysanthemums ($CuCo_2O_4$-C) respectively,. In a 6 M KOH, the resulting $CuCo_2O_4$-C had a specific capacitance 335.8 F g^{-1} at 0.5 A g^{-1}. In contrast, the $CuCo_2O_4$-N showed 235.3 F g^{-1} at the same current density. Moreover, after 2000 cycles at 3 A g^{-1}, the $CuCo_2O_4$-C showed 85% capacitive retention, which was higher than that of $CuCo_2O_4$-N (67%). $CuCo_2O_4$-C performs better than other because of its open-framework structure, which shortens the path for ion diffusion and promotes electron transfer. Vijayakumar et al. [123] reported one-dimensional (1 D) $CuCo_2O_4$ nanobelts, using sodium dodecylsulfate as a surfactant. The $CuCo_2O_4$ nanobelt demonstrated exceptional cycling stability, retaining 127% of its initial capacitance after 1800 cycles at 10.67 A g^{-1}, and specific capacitance of 487 F g^{-1} at 1.46 A g^{-1}. Further, using a hydrothermal technique, Liao et al. [124] directly synthesized maguey-like $CuCo_2O_4$ nanowires on the Ni foam. Due to the activated process, the nickel foam supported maguey-like $CuCo_2O_4$ nanowires showed an excellent 100.9% capacity retention at 50 mV s^{-1} after 3000 cycles. They also displayed a high areal capacity of 3.27 F cm^{-2} at 5 mA cm^{-2}. $CuCo_2O_4$ nanowire assembly showed an energy density of 16.87 W h kg^{-1} at a power density of 513 W kg^{-1}.

The above discussion indicates that pristine $CuCo_2O_4$ powders exhibit a range of electrochemical capacities because of the differences in pore size distribution, morphology, and specific surface area. It is observed that the creation of a functional electrode the use of powdered electrode material necessitates the use of conductive chemicals and binder, which could raise internal resistance and decrease the use of active materials, resulting in limited capacity and poor rate capability. Hence, the synthetic parameters and procedure for $CuCo_2O_4$ must be developed more to get improved electrochemical performances. Nickel foam is the most frequently used substrate for the preparation of binder-free electrode materials because of its inherent qualities, such as huge specific surface area, macroporous structure, and superior conductivity which further results in lowering resistivity and increasing the use of active materials. Wang et al. reported flower-like $CuCo_2O_4$ nanostructures fabricated Ni foam through a hydrothermal approach. Annealed $CuCo_2O_4$ fabricated nickel foam was used as electrode material and it showed a specific capacitance of 243 F g^{-1} at a current density of 1 A g^{-1} along with 85.3% capacitive retention at a current density of 10 A g^{-1} after 3000 cycles [125]. Other studies that have been published in the literature using pristine $CuCo_2O_4$-based materials for binder free electrode applications are $CuCo_2O_4$ nanowires on nickel foam by Lin et al. (608 F g^{-1} at 2 A g^{-1}) [126], grass-like $CuCo_2O_4$ nanowire arrays on Ni foam by Chen et al. (611 F g^{-1} at 1.7 A g^{-1}) [127], cedar-leaf like $CuCo_2O_4$ nanostructure on Ni foam by Wang et al. (1223.2 F g^{-1} at 1.08 A g^{-1}) [128].

Though numerous studies have been carried out for pristine $CuCo_2O_4$ with different nanostructure, its semiconducting nature with low conductivity affects significantly in its electrochemical performances. Hence, hybridization of pristine $CuCo_2O_4$, *i.e.*, preparing hierarchical heterostructure or composites of $CuCo_2O_4$ nanostructure with carbonaceous, polymer materials or other transition metal-based compounds are some additional

approaches for enhancing the electrochemical behavior. Such kind of studies reported by the researchers are Cu-Co LDH/rGO composite by Liang et al. (291 F g^{-1} at 1 A g^{-1}) [129], graphene-wrapped $CuCo_2O_4$ hollow spheres Self-templated by Kaverlavani et al. (1813 F g^{-1} at 2 A g^{-1}) [130], $CuCo_2O_4$/carbon quantum dot composite by Wei et al. (1528.8 F g^{-1} at 1 A g^{-1}) [131], $CuCo_2O_4$@MnO_2 core shell arrays on Ni foam by Kuang et al. (416 F g^{-1} at 1 A g^{-1}) [132], $CuCo_2O_4$/$MnCo_2O_4$/graphite paper by , Liu et al. (1434 F g^{-1} at 0.5 A g^{-1}) [133], 3D $CuCo_2O_4$@$MnMoO_4$ core-shell nanosheet arrays by Chen et al. (1327.5 F g^{-1} at 1 A g^{-1}) [134], $CuCo_2O_4$@$Ni(OH)_2$ on carbon fiber by Zhu et al. (2160 F g^{-1} at 5 A g^{-1}) [135], $CuCo_2O_4$@C on Ni foam by Yan et al. (1432.4 F g^{-1} at 1 A g^{-1}) [136], $CuCo_2O_4$/rGO composite (1813 F g^{-1} at 2 A g^{-1}) [137], $CuCo_2O_4$/CuO@RuO_2 arrays by Zhang et al. (862.5 mAh cm^{-2} at 5 mA cm^{-2}) [138], CNT-$CuCo_2O_4$@Ag nanoflowers by Vadiyar et al. (543 mAh g^{-1} at 1 A g^{-1}) [139], $NiCo_2O_4$ NSs/$CuCo_2O_4$ nanocones/NF by Wen et al. (4.97 F cm^{-2} at 1 mA cm^{-2}) [140], Hollow $CuCo_2O_4$/CuO@$NiCo_2S_4$/NF by Zhang et al. (10.33 F cm^{-2} at 10 mA cm^{-2}) [141].

2.1.6 Titanium Oxide (TiO_2)

Titanium oxide (TiO_2) is one of the transition metal oxides that has drawn the most interest as a potential pseudocapacitive electrode material for supercapacitor application. Its unique qualities are highly alluring, including its abundance, low cost, rich electrochemical behavior, low toxicity, and chemical stability [142]. The redox couple Ti (+4)/Ti (+3) is responsible for the charge storing mechanism, and the material is found in either rutile or anatase phases [143]. Despite its pseudocapacitive behavior, semiconducting and hence poor electrical conductivity resulted in its poor specific capacitance value (< 50 F g^{-1}) [144]. Creating nanoarchitectures with high conductivity and short paths for the electrolyte ions to reach the electrode is a good solution to address these problems. Lu et al. successfully synthesized hydrogenated TiO_2 (H-TiO_2) nanotube arrays, calcining the

material at a temperature range of 300–600 °C in a hydrogen environment. In 0.5 M Na_2SO_4 H-TiO_2 showed a specific capacitance of 3.24 mF cm^{-2} at a scan rate of 100 mV s^{-1} [145]. Moreover, doping metallic or non-metallic components or their oxides might enhance the electrical behavior of TiO2 [146]. Pal et al. [147] investigated tungsten doped TiO_2 (W-TiO2) and tungsten trioxide doped (WO_3/TiO_2) for SC electrodes in order to achieve superior electrochemical properties, and they were successful in synthesizing the materials using a unique hydrothermal method. The electrode materials exhibited behavior similar to that of a battery. In 6 M aqueous KOH, the WO_3/TiO_2 demonstrated the highest storage capacity of 40 mA h g^{-1} at a current density of 2 A g^{-1}. The electrode-electrolyte contact and the synergistic effect from both materials are the prime reason for the enhanced performance. To further enhance the pristine TiO_2's electrochemical behavior, it can be hybridized with carbonaceous components. TiO2@C nanotube bundles were reported by Wang et al. [148] using a scalable hydrothermal process. After 5000 cycles, the hybridized material maintained 81% of its specific capacitance, delivering 274.2 F g^{-1} specific capacitance at 0.5 A g^{-1} current density in 0.5 M Na_2SO_4 solution. Other studies based on TiO_2-based materials for SCs have been documented in the literature which are rGO-TiO_2 nanobelts [149] TiO_2/CNT [150], TiO_2-graphene hydrogel [151], and so on. However, more development is still required to achieve the device-oriented power and energy densities.

2.1.7 Heterostructured Catalysts for HER

One of the best methods for reducing the agglomeration of the active components is to realize hierarchical heterostructured catalyst on supporting substrates. Carbon nanotubes (CNTs), graphene-based materials, graphitic carbon nitride (g-CN), nitrogen doped carbon (NC) and other substrates are among the most often utilized ones. In addition to effectively maximizing the exposure of active sites, the hierarchical feature as well as

the underlying substrate make them suitable current collectors during electrochemical HER.

2.1.7.1 Carbonaceous Material Supported Heterostructures for HER

It was found in 2005 that the MoS_2 (100) edge-sites have a similarity to the active sites of hydrogenase enzymes, acquiring a ΔG_H° of 0.08 eV [152]. Thus, exposing more edge sites of MoS_2 is a viable tactic for raising its HER catalytic activity [153]. A MoS_2/rGO hybrid catalyst was realized by Li et al. using MoS_2 hierarchy grown on rGO nanosheets [154]. As Li et al. claimed strong chemical and electrical coupling between MoS_2 particles and rGO sheets played the major role for the growth of highly dispersed MoS_2 on rGO. rGO meanwhile, provides a faster charge transfer channel in addition to serving as the supporting substrate. Despite RGO's electrochemical inertness, significantly higher active edges and high electrical conductivity of the MoS_2/rGO heterostructure provides the better catalytic activity. Further, the MoS_2/rGO heterostructure displayed Tafel slope of 41 mV dec^{-1} which was the lowest of any MoS_2-based catalyst reported previously.

Building heterostructures can also increase the catalyst's stability, which is essential for the practical use of water electrolysis devices. Transition metal-based catalysts have the potential to replace noble metals but the majority of these transition metals are corrosive in acidic environments. Figure 2.3a,b illustrates how Deng et al. encapsulated Fe, Co, and FeCo alloy inside N-doped CNTs (NCNTs). Figure 2.3c,d shows the HER activity in the FeCo@NCNTs heterostructure [155]. Again, enhancing the nitrogen content in NCNTs, the resultant hybrid FeCo@NCNTs-NH heterostructure demonstrated enhanced HER activity, showing an overpotential of around 280 mV at 10 mA cm−2. DFT calculations were

employer further to study the source of the increased HER activity. The DFT results demonstrated that metal and nitrogen introduction might modify the CNTs' electronic

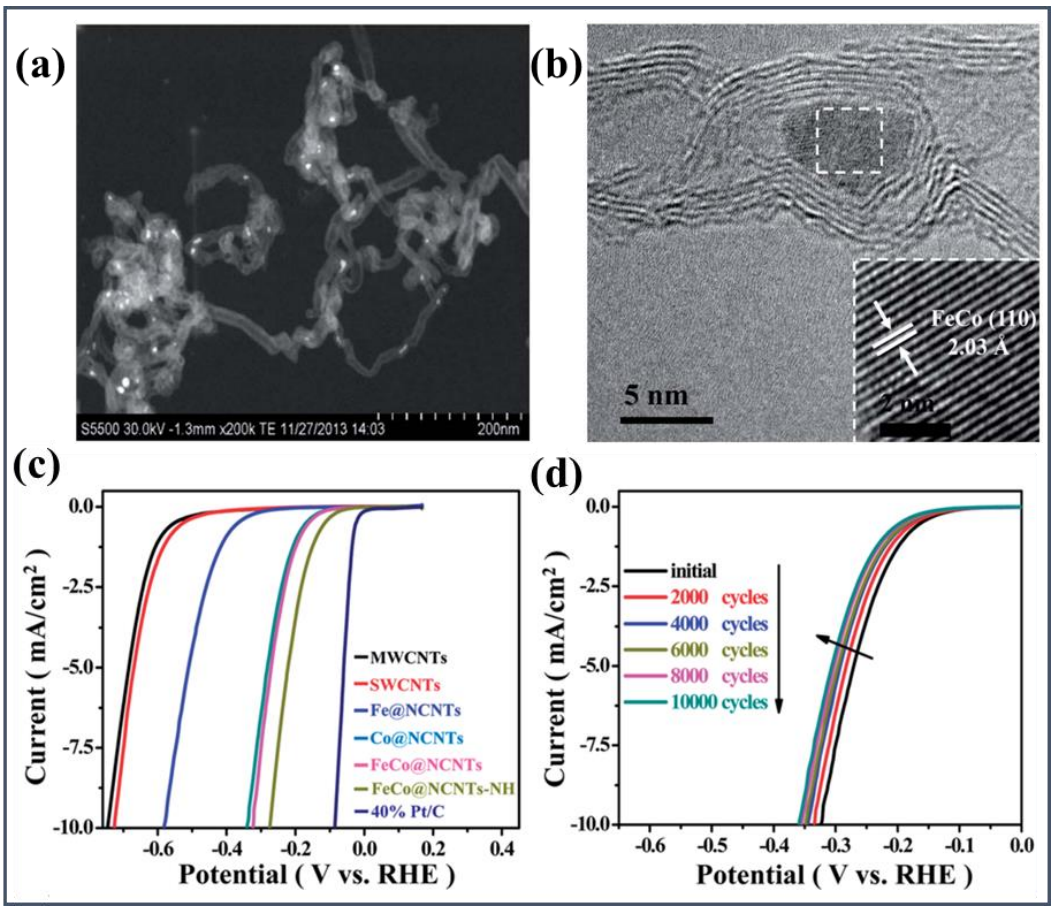

Figure 2.3: (a) STEM image of FeCo@NCNTs. (b) HRTEM image of FeCo@NCNTs, the inset shows the (110) crystal plane of the FeCo nanoparticle. (c) LSV curves of various catalysts as indicated, electrolyte: 0.1 M H_2SO_4, catalyst loading: 0.28 mg cm^{-2}, sweep rate: 2 mV s^{-1}. (d) Durability measurement of FeCo@NCNTs: LSV curves recorded initially and after every 2000 CV sweeps between +0.77 and −0.18 V (vs RHE) at 100 mV s^{-1} [155].

structure and control its ΔG_H°. FeCo@NCNTs heterostructure demonstrated remarkable stability in 0.1 M H_2SO_4 throughout 10000 CV cycles. The elevated intrinsic activity is owing to the molecular interaction between MoS_2 and $CoSe_2$ as well as the significantly higher number of active sites. $CoSe_2$/DETA nanobelts are also a great support for the growth

of TMD nanomaterials due to their high conductivity and outstanding electrocatalytic activity. A similar kind of $CoS_2/CoSe_2$ heterostructure was reported further [156] showing significantly increased HER activity with well-dispersed CoS_2 nanoparticles distributed on the surface of $CoSe_2$/DETA. Spectra from X-ray photoelectron spectroscopy (XPS) was studied to look into the potential enhancement mechanism. The S 2p and Se 3d spectra of $CoS_2/CoSe_2$ heterostructures moved toward lower and greater binding energy, in comparison to their counterparts. These differences in binding energies are typically understood to be a sign of chemical binding or electron transport between various heterostructure components [156–158]. Deeper explanations of how HER activity is impacted by electron transport, however, are typically failed to notice. The carbonaceous substrates in the carbonaceous material-supported heterostructures may play a pivotal role in exposing active sites for the HER. Furthermore, these carbonaceous substrates with high conductivity readily allow rapid charge transfer, which is essential for attaining high catalytic activity. Furthermore, the presence of heteroatom dopants or other components in the heterostructures may modify the electronic structure of the carbonaceous substances and hence triggering the hybrid's HER activity. Therefore, one efficient method for creating improved HER catalysts is to grow active materials on carbonaceous substrates.

2.1.8 Transition Metal Dichalcogenide-based Heterostructures for HER

Earth-abundant TMDs, such as 2D layered TMDs (e.g., MoS2, MoSe2, WS2, etc.) and cubic pyrite-type or orthorhombic marcasite-type TMDs (e.g., CoS2, CoSe2, NiS2, FeS2, etc.), have recently attracted a lot of interest in electrochemical water splitting [159–163]. A vertical $MoSe_2$/NiSe heterostructure was reported by Zhou et al. [164], who also investigated the XPS binding energy change inside the heterostructure. The Mo 3d binding

energy of the $MoSe_2$/NiSe heterostructure shifts towards lower binding side in the XPS spectra when compared to that of $MoSe_2$. An electron transfer from NiSe to $MoSe_2$ was suggested, and electron energy loss spectroscopy (EELS) investigation was used to confirm it. Additionally, the valence band (E_v) and work function (ϕ) of $MoSe_2$ and NiSe were determined using ultraviolet photoelectron spectroscopy (UPS) spectra. The charge transfer from metallic NiSe into $MoSe_2$ is made easier by the increased Fermi level of NiSe, increasing the conductivity of the $MoSe_2$/NiSe heterostructure. Because of the well-established nanostructures, these TMD/TMD heterostructures typically retain a large number of active sites, much as carbonaceous material/TMD heterostructures [165]. In addition, the superior HER activity is also a result of electron transfers and the synergistic impact among the various TMD components [158,166]. Furthermore, hybridizing with CNT, rGO, NC, etc. can further enhance the HER activity of these TMD/TMD heterostructures [157,167,168]. This will not only boost the electrical conductivity and quantity of active sites but also allow for quick mass transportation [169].

2.2 References

[1] C.-C. Hu, K.-H. Chang, M.-C. Lin, Y.-T. Wu, Nano Lett 6 (2006) 2690–2695.

[2] K.-H. Chang, C.-C. Hu, Electrochemical and Solid-State Letters 7 (2004) A466.

[3] S. Trasatti, G. Buzzanca, J Electroanal Chem Interfacial Electrochem 29 (1971) A1–A5.

[4] W. Gu, G. Yushin, WIREs Energy and Environment 3 (2014) 424–473.

[5] S. Kong, K. Cheng, T. Ouyang, Y. Gao, K. Ye, G. Wang, D. Cao, Electrochim Acta 246 (2017) 433–442.

[6] M. Rose, Y. Korenblit, E. Kockrick, L. Borchardt, M. Oschatz, S. Kaskel, G. Yushin, Small 7 (2011) 1108–1117.

[7] Y. Yin, X. Wang, Z. You, Int J Electrochem Sci 12 (2017) 3883–3906.

[8] T.-F. Hsieh, C.-C. Chuang, W.-J. Chen, J.-H. Huang, W.-T. Chen, C.-M. Shu, Carbon N Y 50 (2012) 1740–1747.

[9] K.-H. Chang, C.-C. Hu, C.-Y. Chou, Chemistry of Materials 19 (2007) 2112–2119.

[10] K.-H. Chang, C.-C. Hu, C.-Y. Chou, Chemistry of Materials 19 (2007) 2112–2119.

[11] B.-O. Park, C.D. Lokhande, H.-S. Park, K.-D. Jung, O.-S. Joo, J Power Sources 134 (2004) 148–152.

[12] D. Susanti, D.-S. Tsai, Y.-S. Huang, A. Korotcov, W.-H. Chung, The Journal of Physical Chemistry C 111 (2007) 9530–9537.

[13] A. Ananth, S. Dharaneedharan, M.S. Gandhi, M.-S. Heo, Y.S. Mok, Chemical Engineering Journal 223 (2013) 729–736.

[14] X. Leng, J. Zou, X. Xiong, H. He, RSC Adv. 4 (2014) 61596–61603.

[15] V. Vijayabala, N. Senthilkumar, K. Nehru, R. Karvembu, Journal of Materials Science: Materials in Electronics 29 (2018) 323–330.

[16] K. Chaitra, P. Sivaraman, R.T. Vinny, U.M. Bhatta, N. Nagaraju, N. Kathyayini, Journal of Energy Chemistry 25 (2016) 627–635.

[17] R. Thangappan, M. Arivanandhan, R. Dhinesh Kumar, R. Jayavel, Journal of Physics and Chemistry of Solids 121 (2018) 339–349.

[18] K.Y. Kumar, S. Archana, R. Namitha, B.P. Prasanna, S.C. Sharma, M.S. Raghu, Mater Res Bull 107 (2018) 347–354.

[19] C.-C. Hu, Y.-L. Yang, T.-C. Lee, Electrochemical and Solid-State Letters 13 (2010) A173.

[20] N. Lin, J. Tian, Z. Shan, K. Chen, W. Liao, Electrochim Acta 99 (2013) 219–224.

[21] B.D. Desai, J.B. Fernandes, V.N.K. Dalal, J Power Sources 16 (1985) 1–43.

[22] P. Wang, S. Sun, S. Wang, Y. Zhang, G. Zhang, Y. Li, S. Li, C. Zhou, S. Fang, J Appl Electrochem 47 (2017) 1293–1303.

[23] X. Tang, H. Li, Z.-H. Liu, Z. Yang, Z. Wang, J Power Sources 196 (2011) 855–859.

[24] M. Huang, F. Li, F. Dong, Y.X. Zhang, L.L. Zhang, J Mater Chem A Mater 3 (2015) 21380–21423.

[25] J. Li, M. Yin, C. Guo, H. Zhang, T. Li, H. Wang, Y. Wei, L. Hou, C. Jia, Surf Coat Technol 359 (2019) 175–182.

[26] X. Bai, X. Tong, Y. Gao, W. Zhu, C. Fu, J. Ma, T. Tan, C. Wang, Y. Luo, H. Sun, Electrochim Acta 281 (2018) 525–533.

[27] K. Dai, L. Lu, C. Liang, J. Dai, Q. Liu, Y. Zhang, G. Zhu, Z. Liu, Electrochim Acta 116 (2014) 111–117.

[28] M.-X. Guo, S.-W. Bian, F. Shao, S. Liu, Y.-H. Peng, Electrochim Acta 209 (2016) 486–497.

[29] R. Abd Aziz, R. Jose, Journal of Electroanalytical Chemistry 799 (2017) 538–546.

[30] I.I. Misnon, R. Abd Aziz, N.K.M. Zain, B. Vidhyadharan, S.G. Krishnan, R. Jose, Mater Res Bull 57 (2014) 221–230.

[31] A.A. Radhiyah, M.I. Izwan, V. Baiju, C.K. Feng, I. Jamil, R. Jose, RSC Adv 5 (2015) 9667–9673.

[32] W. Xu, S. Dai, G. Liu, Y. Xi, C. Hu, X. Wang, Electrochim Acta 203 (2016) 1–8.

[33] P. Xu, J. Liu, T. Liu, K. Ye, K. Cheng, J. Yin, D. Cao, G. Wang, Q. Li, RSC Adv 6 (2016) 28270–28278.

[34] Y. Yang, L. Pei, X. Xu, J. Xu, J. Shen, M. Ye, Electrochim Acta 221 (2016) 56–61.

[35] B. Saravanakumar, C. Radhakrishnan, M. Ramasamy, R. Kaliaperumal, A.J. Britten, M. Mkandawire, Journal of Electroanalytical Chemistry 852 (2019) 113504.

[36] H. Zhang, J. Feng, M. Zhang, Mater Res Bull 43 (2008) 3221–3226.

[37] Y. Li, S. Chang, X. Liu, J. Huang, J. Yin, G. Wang, D. Cao, Electrochim Acta 85 (2012) 393–398.

[38] G. Wang, J. Huang, S. Chen, Y. Gao, D. Cao, J Power Sources 196 (2011) 5756–5760.

[39] L. Xu, J. Li, H. Sun, X. Guo, J. Xu, H. Zhang, X. Zhang, Front Chem 7 (2019) 420.

[40] L. Yu, Y. Jin, L. Li, J. Ma, G. Wang, B. Geng, X. Zhang, CrystEngComm 15 (2013) 7657–7662.

[41] J. Ruan, Y. Huo, B. Hu, Electrochim Acta 215 (2016) 108–113.

[42] Z. Li, M. Shao, L. Zhou, R. Zhang, C. Zhang, J. Han, M. Wei, D.G. Evans, X. Duan, Nano Energy 20 (2016) 294–304.

[43] J. Zhao, X. Shu, Y. Wang, C. Yu, J. Zhang, J. Cui, Y. Qin, H. Zheng, J. Liu, Y. Zhang, Surf Coat Technol 299 (2016) 15–21.

[44] G. Wang, J. Huang, S. Chen, Y. Gao, D. Cao, J Power Sources 196 (2011) 5756–5760.

[45] Q. Wang, Y. Zhang, J. Xiao, H. Jiang, T. Hu, C. Meng, J Alloys Compd 782 (2019) 1103–1113.

[46] D. He, X. Song, W. Li, C. Tang, J. Liu, Z. Ke, C. Jiang, X. Xiao, Angewandte Chemie International Edition 59 (2020) 6929–6935.

[47] W. Liu, R. Liu, X. Zhang, Appl Surf Sci 507 (2020) 145174.

[48] J. Chen, Z. Xu, H. Zhu, R. Liu, X. Song, Q. Song, J. Wu, C. Zhang, L. Ding, J. Dong, Vacuum 174 (2020) 109219.

[49] Y. Mao, X. Shen, Z. Wu, L. Zhu, G. Liao, J Alloys Compd 816 (2020) 152604.

[50] R. Zhang, S. Gao, T. Zhou, J. Tu, T. Zhang, Appl Surf Sci 503 (2020) 144167.

[51] H. Sun, H. Lv, J Alloys Compd 823 (2020) 153742.

[52] S.K. Meher, G.R. Rao, The Journal of Physical Chemistry C 115 (2011) 15646–15654.

[53] J. Yang, X. Xu, X. Zhou, S. Jiang, W. Chen, S. Shi, D. Wang, Z. Liu, The Journal of Physical Chemistry C 124 (2020) 9225–9232.

[54] A. UmaSudharshini, M. Bououdina, M. Venkateshwarlu, C. Manoharan, P. Dhamodharan, Surfaces and Interfaces 19 (2020) 100535.

[55] W. Liu, X. Li, M. Zhu, X. He, J Power Sources 282 (2015) 179–186.

[56] B. Vidyadharan, R.A. Aziz, I.I. Misnon, G.M. Anil Kumar, J. Ismail, M.M. Yusoff, R. Jose, J Power Sources 270 (2014) 526–535.

[57] Q. Yan, X. Li, Q. Zhao, G. Chen, J Hazard Mater 209–210 (2012) 385–391.

[58] X. Qing, S. Liu, K. Huang, K. Lv, Y. Yang, Z. Lu, D. Fang, X. Liang, Electrochim Acta 56 (2011) 4985–4991.

[59] R.A. Soomro, Z.H. Ibupoto, . Sirajuddin, S.T.H. Sherazi, M.I. Abro, M. Willander, S.A. Mahesar, N.H. Kalwar, Materials Express 5 (2015) 437–444.

[60] S. Raj, S.K. Srivastava, P. Kar, P. Roy, Electrochim Acta 302 (2019) 327–337.

[61] Y. Xiao, S. Liu, F. Li, A. Zhang, J. Zhao, S. Fang, D. Jia, Adv Funct Mater 22 (2012) 4052–4059.

[62] X. Luo, M. Zhong, P. He, J. Shao, Q. Wang, K. Li, W. Zhao, J Alloys Compd 826 (2020) 154241.

[63] Y. Gao, S. Chen, D. Cao, G. Wang, J. Yin, J Power Sources 195 (2010) 1757–1760.

[64] J. Xu, L. Gao, J. Cao, W. Wang, Z. Chen, Electrochim Acta 56 (2010) 732–736.

[65] C.-C. Hu, T.-Y. Hsu, Electrochim Acta 53 (2008) 2386–2395.

[66] S.G. Kandalkar, H.-M. Lee, H. Chae, C.-K. Kim, Mater Res Bull 46 (2011) 48–51.

[67] L. Wang, X. Liu, X. Wang, X. Yang, L. Lu, Current Applied Physics 10 (2010) 1422–1426.

[68] M. Zheng, J. Cao, S. Liao, J. Liu, H. Chen, Y. Zhao, W. Dai, G. Ji, J. Cao, J. Tao, The Journal of Physical Chemistry C 113 (2009) 3887–3894.

[69] L. Cui, J. Li, X.-G. Zhang, J Appl Electrochem 39 (2009) 1871–1876.

[70] L. Cao, M. Lu, H.-L. Li, J Electrochem Soc 152 (2005) A871.

[71] Y. Lu, Y. Wang, Y. Zou, Z. Jiao, B. Zhao, Y. He, M. Wu, Electrochem Commun 12 (2010) 101–105.

[72] H. Heli, H. Yadegari, Electrochim Acta 55 (2010) 2139–2148.

[73] Y. Xu, C. Wang, Y. Sun, G. Zhang, D. Gao, Mater Lett 64 (2010) 1275–1278.

[74] X. Wang, X. Chen, L. Gao, H. Zheng, Z. Zhang, Y. Qian, J Phys Chem B 108 (2004) 16401–16404.

[75] T. He, D. Chen, X. Jiao, Y. Xu, Y. Gu, Langmuir 20 (2004) 8404–8408.

[76] J.P. Cheng, X. Chen, R. Ma, F. Liu, X.B. Zhang, Mater Charact 62 (2011) 775–780.

[77] B. Guo, C. Li, Z.-Y. Yuan, The Journal of Physical Chemistry C 114 (2010) 12805–12817.

[78] S. Thota, A. Kumar, J. Kumar, Materials Science and Engineering: B 164 (2009) 30–37.

[79] G. Wang, X. Shen, J. Horvat, B. Wang, H. Liu, D. Wexler, J. Yao, The Journal of Physical Chemistry C 113 (2009) 4357–4361.

[80] S.G. Kandalkar, J.L. Gunjakar, C.D. Lokhande, O.-S. Joo, J Alloys Compd 478 (2009) 594–598.

[81] V.R. Shinde, S.B. Mahadik, T.P. Gujar, C.D. Lokhande, Appl Surf Sci 252 (2006) 7487–7492.

[82] J. Ahmed, T. Ahmad, K. V Ramanujachary, S.E. Lofland, A.K. Ganguli, J Colloid Interface Sci 321 (2008) 434–441.

[83] A.-M. Cao, J.-S. Hu, H.-P. Liang, W.-G. Song, L.-J. Wan, X.-L. He, X.-G. Gao, S.-H. Xia, J Phys Chem B 110 (2006) 15858–15863.

[84] T. He, D. Chen, X. Jiao, Chemistry of Materials 16 (2004) 737–743.

[85] H. Li, Y. Li, R. Wang, R. Cao, J Alloys Compd 481 (2009) 100–105.

[86] D. Guragain, C. Zequine, R.K. Gupta, S.R. Mishra, Processes 8 (2020) 343.

[87] H. Chen, X. Du, R. Wu, Y. Wang, J. Sun, Y. Zhang, C. Xu, Nanoscale Adv 2 (2020) 3263–3275.

[88] X. Zhao, L. Mao, Q. Cheng, J. Li, F. Liao, G. Yang, L. Xie, C. Zhao, L. Chen, Chemical Engineering Journal 387 (2020) 124081.

[89] M. V. Reddy, M. Rajesh, S. Adams, B.V.R. Chowdari, ACS Sustain Chem Eng 4 (2016) 3076–3086.

[90] C. Yuan, J. Li, L. Hou, X. Zhang, L. Shen, X.W. (David) Lou, Adv Funct Mater 22 (2012) 4592–4597.

[91] M. Cabello, F. Nacimiento, J.R. González, G. Ortiz, R. Alcántara, P. Lavela, C. Pérez-Vicente, J.L. Tirado, Electrochem Commun 67 (2016) 59–64.

[92] M. V. Reddy, K.Y.H. Kenrick, T.Y. Wei, G.Y. Chong, G.H. Leong, B.V.R. Chowdari, J Electrochem Soc 158 (2011) A1423.

[93] S. Ma, L. Sun, L. Cong, X. Gao, C. Yao, X. Guo, L. Tai, P. Mei, Y. Zeng, H. Xie, R. Wang, The Journal of Physical Chemistry C 117 (2013) 25890–25897.

[94] Y. SHARMA, N. SHARMA, G. SUBBARAO, B. CHOWDARI, Solid State Ion 179 (2008) 587–597.

[95] K.J. Kim, Y.R. Park, Solid State Commun 127 (2003) 25–28.

[96] S. Liu, D. Ni, H.-F. Li, K.N. Hui, C.-Y. Ouyang, S.C. Jun, J Mater Chem A Mater 6 (2018) 10674–10685.

[97] J.M. Xu, J.P. Cheng, J Alloys Compd 686 (2016) 753–768.

[98] B. Cui, H. Lin, Y. Liu, J. Li, P. Sun, X. Zhao, C. Liu, The Journal of Physical Chemistry C 113 (2009) 14083–14087.

[99] H.-Y. Chen, J.-H. Chen, Mater Lett 188 (2017) 63–65.

[100] X. Cheng, X. Zhou, Z. Liu, Y. Zhang, Q. Liu, Q. Liu, B. Li, Advances in Applied Ceramics 118 (2019) 466–472.

[101] H. Guo, J. Chen, W. Weng, Q. Wang, S. Li, Chemical Engineering Journal 239 (2014) 192–199.

[102] M. Silambarasan, P.S. Ramesh, D. Geetha, V. Venkatachalam, Journal of Materials Science: Materials in Electronics 28 (2017) 6880–6888.

[103] J. Ma, H. Wang, X. Yang, Y. Chai, R. Yuan, J Mater Chem A Mater 3 (2015) 12038–12043.

[104] W. Sun, Y. Wang, H. Wu, Z. Wang, D. Rooney, K. Sun, Chemical Communications 53 (2017) 8711–8714.

[105] A. Pendashteh, M.S. Rahmanifar, R.B. Kaner, M.F. Mousavi, Chemical Communications 50 (2014) 1972–1975.

[106] X. Luo, M. Huang, L. Bie, D. He, Y. Zhang, P. Jiang, RSC Adv 7 (2017) 23093–23101.

[107] S. Jain, A. Patrike, S.S. Badadhe, M. Bhardwaj, S. Ogale, ACS Omega 3 (2018) 1977–1982.

[108] S. Cui, S. Gu, Y. Ding, J. Zhang, Z. Zhang, Z. Hu, Talanta 178 (2018) 788–795.

[109] Y. Liu, L.-J. Cao, C.-W. Cao, M. Wang, K.-L. Leung, S.-S. Zeng, T.F. Hung, C.Y. Chung, Z.-G. Lu, Chemical Communications 50 (2014) 14635–14638.

[110] M. Nekoeinia, F. Salehriahi, O. Moradlou, H. Kazemi, S. Yousefinejad, New Journal of Chemistry 42 (2018) 9209–9220.

[111] S. Angelov, E. Zhecheva, K. Petrov, D. Menandjiev, Mater Res Bull 17 (1982) 235–240.

[112] S. Singh, P. Pramanik, S. Sangaraju, A. Mallick, L. Giebeler, S. Thota, J Appl Phys 121 (2017).

[113] B. Chi, H. Lin, J. Li, Int J Hydrogen Energy 33 (2008) 4763–4768.

[114] T.W. Kim, M.A. Woo, M. Regis, K.-S. Choi, J Phys Chem Lett 5 (2014) 2370–2374.

[115] B. Chi, H. Lin, J. Li, Int J Hydrogen Energy 33 (2008) 4763–4768.

[116] E. Alizadeh-Gheshlaghi, B. Shaabani, A. Khodayari, Y. Azizian-Kalandaragh, R. Rahimi, Powder Technol 217 (2012) 330–339.

[117] Z.-Y. Yu, L.-F. Chen, S.-H. Yu, J Mater Chem A Mater 2 (2014) 10889–10894.

[118] M. Zhou, L. Cai, M. Bajdich, M. García-Melchor, H. Li, J. He, J. Wilcox, W. Wu, A. Vojvodic, X. Zheng, ACS Catal 5 (2015) 4485–4491.

[119] S. Vijayakumar, S.-H. Lee, K.-S. Ryu, Electrochim Acta 182 (2015) 979–986.

[120] S.K. Kaverlavani, S.E. Moosavifard, A. Bakouei, J Mater Chem A Mater 5 (2017) 14301–14309.

[121] R. BoopathiRaja, M. Parthibavarman, A.N. Begum, Vacuum 165 (2019) 96–104.

[122] Y. Zhao, Y. Zhang, K. Xu, Int J Electrochem Sci 14 (2019) 3885–3896.

[123] S. Vijayakumar, S.-H. Lee, K.-S. Ryu, Electrochim Acta 182 (2015) 979–986.

[124] L. Liao, H. Zhang, W. Li, X. Huang, Z. Xiao, K. Xu, J. Yang, R. Zou, J. Hu, J Alloys Compd 695 (2017) 3503–3510.

[125] T. Wang, M. Liu, H. Ma, Nanomaterials 7 (2017) 140.

[126] J. Lin, H. Liang, H. Jia, S. Chen, J. Guo, J. Qi, C. Qu, J. Cao, W. Fei, J. Feng, J Mater Chem A Mater 5 (2017) 24594–24601.

[127] H. Chen, X. Chen, Y. Zeng, S. Chen, J. Wang, RSC Adv 5 (2015) 70494–70497.

[128] Y. Wang, D. Yang, J. Lian, J. Pan, T. Wei, Y. Sun, J Alloys Compd 735 (2018) 2046–2052.

[129] P. Liang, F. Wang, Z.-A. Hu, Chemical Engineering Journal 350 (2018) 627–636.

[130] S.K. Kaverlavani, S.E. Moosavifard, A. Bakouei, J Mater Chem A Mater 5 (2017) 14301–14309.

[131] G. Wei, J. He, W. Zhang, X. Zhao, S. Qiu, C. An, Inorg Chem 57 (2018) 7380–7389.

[132] M. Kuang, X.Y. Liu, F. Dong, Y.X. Zhang, J Mater Chem A Mater 3 (2015) 21528–21536.

[133] S. Liu, K. San Hui, K.N. Hui, J.M. Yun, K.H. Kim, J Mater Chem A Mater 4 (2016) 8061–8071.

[134] S. Chen, S. Cui, S. Chandrasekaran, C. Ke, Z. Li, P. Chen, C. Zhang, Y. Jiang, Electrochim Acta 341 (2020) 135893.

[135] D. Zhu, X. Sun, J. Yu, Q. Liu, J. Liu, R. Chen, H. Zhang, R. Li, J. Yu, J. Wang, J Colloid Interface Sci 557 (2019) 76–83.

[136] H. Yan, Y. Lu, K. Zhu, T. Peng, X. Liu, Y. Liu, Y. Luo, Appl Surf Sci 439 (2018) 883–890.

[137] S.K. Kaverlavani, S.E. Moosavifard, A. Bakouei, J Mater Chem A Mater 5 (2017) 14301–14309.

[138] P. Zhang, X. Liu, H. He, Y. Peng, Y. Wu, J Alloys Compd 832 (2020) 154962.

[139] M.M. Vadiyar, X. Liu, Z. Ye, J Power Sources 415 (2019) 154–164.

[140] S. Wen, Y. Liu, H. Bai, R. Shao, W. Xu, W. Shi, J Solid State Chem 262 (2018) 327–334.

[141] P. Zhang, H. He, Appl Surf Sci 497 (2019) 143725.

[142] B. Vidyadharan, P.S. Archana, J. Ismail, M.M. Yusoff, R. Jose, RSC Adv 5 (2015) 50087–50097.

[143] V. Augustyn, P. Simon, B. Dunn, Energy Environ Sci 7 (2014) 1597–1614.

[144] S.G. Krishnan, P.S. Archana, B. Vidyadharan, I.I. Misnon, B.L. Vijayan, V.M. Nair, A. Gupta, R. Jose, J Alloys Compd 684 (2016) 328–334.

[145] X. Lu, G. Wang, T. Zhai, M. Yu, J. Gan, Y. Tong, Y. Li, Nano Lett 12 (2012) 1690–1696.

[146] H. Zhou, X. Zou, K. Zhang, P. Sun, M.S. Islam, J. Gong, Y. Zhang, J. Yang, ACS Appl Mater Interfaces 9 (2017) 18699–18709.

[147] B. Pal, B.L. Vijayan, S.G. Krishnan, M. Harilal, W.J. Basirun, A. Lowe, M.M. Yusoff, R. Jose, J Alloys Compd 740 (2018) 703–710.

[148] J. Wang, W. Li, Y. Ge, J. Shen, Y. Zhao, Y. Zhang, J. Yuan, Ceram Int 43 (2017) 2876–2880.

[149] C. Xiang, M. Li, M. Zhi, A. Manivannan, N. Wu, J Mater Chem 22 (2012) 19161–19167.

[150] J. Li, J. Ao, C. Zhong, T. Yin, Appl Surf Sci 563 (2021) 150301.

[151] J. Kim, W.-H. Khoh, B.-H. Wee, J.-D. Hong, RSC Adv 5 (2015) 9904–9911.

[152] B. Hinnemann, P.G. Moses, J. Bonde, K.P. Jørgensen, J.H. Nielsen, S. Horch, I. Chorkendorff, J.K. Nørskov, J Am Chem Soc 127 (2005) 5308–5309.

[153] M. Ledendecker, G. Clavel, M. Antonietti, M. Shalom, Adv Funct Mater 25 (2015) 393–399.

[154] Y. Li, H. Wang, L. Xie, Y. Liang, G. Hong, H. Dai, J Am Chem Soc 133 (2011) 7296–7299.

[155] J. Deng, P. Ren, D. Deng, L. Yu, F. Yang, X. Bao, Energy Environ Sci 7 (2014) 1919–1923.

[156] Y. Guo, C. Shang, E. Wang, J Mater Chem A Mater 5 (2017) 2504–2507.

[157] X. Zhou, X. Yang, M.N. Hedhili, H. Li, S. Min, J. Ming, K.-W. Huang, W. Zhang, L.-J. Li, Nano Energy 32 (2017) 470–478.

[158] M. Wang, P. Ju, W. Li, Y. Zhao, X. Han, Dalton Transactions 46 (2017) 483–490.

[159] I.H. Kwak, H.S. Im, D.M. Jang, Y.W. Kim, K. Park, Y.R. Lim, E.H. Cha, J. Park, ACS Appl Mater Interfaces 8 (2016) 5327–5334.

[160] D. Kong, J.J. Cha, H. Wang, H.R. Lee, Y. Cui, Energy Environ Sci 6 (2013) 3553–3558.

[161] S. Xu, D. Li, P. Wu, Adv Funct Mater 25 (2015) 1127–1136.

[162] Q. Lu, Y. Yu, Q. Ma, B. Chen, H. Zhang, Advanced Materials 28 (2016) 1917–1933.

[163] H. Ren, Z.-H. Huang, Z. Yang, S. Tang, F. Kang, R. Lv, Journal of Energy Chemistry 26 (2017) 1217–1222.

[164] X. Zhou, Y. Liu, H. Ju, B. Pan, J. Zhu, T. Ding, C. Wang, Q. Yang, Chemistry of Materials 28 (2016) 1838–1846.

[165] C.H. Mu, H.X. Qi, Y.Q. Song, Z.P. Liu, L.X. Ji, J.G. Deng, Y.B. Liao, F. Scarpa, RSC Adv 6 (2016) 23–30.

[166] M. Wu, Y. Huang, X. Cheng, X. Geng, Q. Tang, Y. You, Y. Yu, R. Zhou, J. Xu, Adv Mater Interfaces 4 (2017) 1700948.

[167] Y.-R. Liu, X. Shang, W.-K. Gao, B. Dong, J.-Q. Chi, X. Li, K.-L. Yan, Y.-M. Chai, Y.-Q. Liu, C.-G. Liu, Appl Surf Sci 412 (2017) 138–145.

[168] Y.-R. Liu, W.-H. Hu, X. Li, B. Dong, X. Shang, G.-Q. Han, Y.-M. Chai, Y.-Q. Liu, C.-G. Liu, Appl Surf Sci 384 (2016) 51–57.

[169] J. Huang, D. Hou, Y. Zhou, W. Zhou, G. Li, Z. Tang, L. Li, S. Chen, J Mater Chem A Mater 3 (2015) 22886–22891.

Chapter 3: Experimental Techniques & Characterization

3.1 Synthesis Methods

Different synthesis protocols used to synthesize nanomaterials must be thoroughly studied. It appears that there are two fundamental approaches for synthesizing nanomaterials and fabricating nanoscale devices which are top-down and bottom-up approaches respectively. An example of a top-down method for preparing nanostructures is ball milling method. On the other hand, colloidal synthesis follows a bottom-up methodology. Lithography is one type of synthesis protocol which comprises both the approaches. Nonetheless, each approach has some benefits and drawbacks. The inconsistency of the surface structure is the primary drawback in top-down method. Thus, bottom-up protocol has gained more attention. It demonstrates the process of assembling structural components atom by atom or molecule by molecule. In this bottom-up protocol, a nanostructure is formed with longer-range ordering, better chemical composition as well as homogeneity, and very less defect. This section has covered a simple but popular chemical synthesis (bottom-up) protocol, namely, hydrothermal approach for the synthesis of nanostructures. Further, a brief overview of many characterization tools used for in-depth investigation of as-synthesized samples has also been covered.

3.2 Hydrothermal Synthesis

The hydrothermal synthesis is one of the most widely used chemical synthesis protocols. The word "hydro" means water, and "thermal" means heat or temperature. Thus, it should be comprehensible as hydrothermal is a synthesis process that incorporates water as the reaction media. The main benefits of employing water as the reaction medium are that it is inexpensive, abundant, non-toxic, non-flammable, and thermodynamically stable. In a broader sense, the process is called solvothermal when any other liquid is used as reaction medium. Hence, hydrothermal process can be demonstrated a heterogeneous

chemical reaction inside a closed chamber in the presence of an aqueous or non-aqueous solvent at a temperature higher than room temperature and a pressure higher than atmospheric pressure.

The main parameters in a hydrothermal protocol are pressure, temperature, precursor concentration, and reaction time. Though this protocol incorporates many benefits, including a high-purity product yield, good chemical homogeneity, narrow particle size distribution, a one-step procedure using basic tools, a quicker reaction time and less energy use etc., it has some drawbacks also. Primary flaw is the requirement for laborious and time-consuming experimental trial and error procedures. Besides, Agglomeration is another issue which can drastically alter the properties. Further this method includes the need of expensive Teflon lined autoclaves and inability to observe the crystal during its growth. However, sample synthesis using this protocol necessitates a sturdy, non-reactive vessel, (also called autoclave), which is a container that can hold a highly corrosive solvent at high temperatures and pressure. The features that should be present in a Teflon lined autoclave are- inertness towards oxidizing agents, acids, and bases, capability to resist temperature and pressure for extended durations etc.

3.3 Synthesis Equipment

3.3.1 Teflon Lined Autoclave

An autoclave is a closed pressure chamber that is typically used in research laboratories for the synthesis of different materials. The procedure entails creation of a reaction environment at high temperatures and self-generated pressure in a closed vessel. Hydrothermal and solvothermal synthesis processes are frequently carried out in autoclaves. They are also used to sterilize surgical tools in medical applications. Dennis Papin developed the steam digester in 1679, which is the precursor of the autoclave. Charles

Figure 3.1: (a) A schematic, (b) a picture of Teflon-lined stainless-steel autoclave for hydrothermal technique, and (c) a digital photograph (bottom) of a stainless-steel Autoclave with inner Teflon liner used for sample synthesis.

Chamberland developed the modern autoclave in 1879. The term "autoclave" refers to a self-locking device. In this instance, an autoclave resembles a cylindrical iron chamber with iron screw cap on it. In order for the cap to resist extremely high pressure during the reaction, it is fitted very firmly with the iron chamber. A cylindrical Teflon tube with a Teflon cap is there within the iron chamber and it functions as the inert reaction chamber.

Teflon is used as the inner liner because of its ability to tolerate high temperatures and pressures as well as extremely corrosive substances. The temperature at which the reaction is conducted is higher than the boiling point of the solvent. The hydrolysis process takes place in the aqueous media, which also acts as a source of gasification and H_2. As soon as the temperature within the chamber starts rising, pressure begins to build up and thermochemical conversion reactions begin. Several studies have shown that the efficient synthesis of extremely porous and ordered nanostructured materials depends critically on exact control over pressure and temperature conditions [1,2]. The method provides highly ordered nonporous materials [3], easy experiment setup, inexpensive, safe experimental settings, and no development of hazardous gasses. The technology is also termed as "green technology" because of its closed system, which hardly causes any harmful gas emissions during the synthesis time and minimal chemical consumption.

In this thesis, most of the samples have been synthesized in a Teflon-lined autoclave using this facile hydrothermal approach. The digital image of a Teflon-lined stainless-steel autoclave is shown in Figure 3.1c.

3.3.2 Hot Air Oven

Hot air oven is an electrical appliance generally used in a synthesis lab operating in the temperature range between 40 and 300 °C. To provide thermal insulation and conserve heat energy, the ovens are manufactured with double walls with the inclusion of suitable insulators in between. Blowers are frequently included in these ovens in order to maintain a constant interior temperature. These ovens are equipped with thermostat and PID (Proportional – Integral – Derivative) controller to regulate the temperature. These kinds of ovens are used for low temperature hydrothermal synthesis (less than 300 °C) and general air drying of samples and equipment.

3.3.3 Vacuum Oven

Vacuum ovens are modified ovens that have an enclosed chamber equipped with a vacuum pump to remove air from the chamber. Within these ovens, reactions and sample drying are carried out in a vacuum, or extremely low air pressure environment. The lack of air inside vacuum chamber prevents sample from getting oxidized by air, convectional heat loss, and any potential contamination. Since many samples are susceptible to aerial oxidation at high temperatures, a vacuum oven is required for the materials' drying.

3.3.4 Furnace

For annealing and high temperature hydrothermal applications, a furnace is utilized. They are capable of reaching temperatures up to 1700 °C. Different types of furnaces are available such as tube furnace, muffle box furnace, vacuum furnace etc. Typically, a PID controller regulates the heating rate and keeps the temperature constant within an accuracy of ±0.2 °C. The materials are annealed in vessels made of quartz and alumina. Samples must be annealed in order to increase their crystallinity.

3.3.5 Sonicator

Sonicator is another sample synthesizing tool which works on the basis of sonication, which is the process of agitating sample particles using the energy supplied by ultrasonic sound waves. Sonication has several applications, including the dispersion of solids in liquids, emulsion formation, nanocrystal formation, degassing, ink and paint manufacturing, and ultrasonic cleaning in scientific labs. When it comes to cleaning substrates before chemical deposition, sonicators are highly efficient. They often fall into two categories:

(a) Bath Sonicator: In this device, a liquid is placed within the cavity, causing the walls to vibrate and impart their ultrasonic vibrations to the liquid.

(b) Probe Sonicator: This device transfers ultrasonic vibrations from a vibrating probe to a liquid by dipping it inside the liquid.

3.3.6 Centrifuge

Centrifuge is another scientific instrument used for separating insoluble materials from liquid dispersions, colloids, or two immiscible liquids. This instrument functions on the basis of the sedimentation principle, in which the lighter materials rise to the top of the centrifuge tubes and the denser materials separate out in a radial direction as a result of the high centripetal acceleration created by the high-speed spinning.

3.4 Characterization Tools

In any scientific investigation, after the completion of sample synthesis, detailed structural, morphological and chemical analysis of the samples must be carried out. To indentify the proper phase, stoichiometry, structural and other properties of the as-synthesized samples different characterization tools necessary.

3.4.1 X-ray Diffractometer (XRD)

X-ray diffraction (XRD) is a non-destructive method for studying the structure of a sample, essentially at the atomic or molecular level. Although it is used dominantly to analyze crystalline materials, it works good on non-crystalline or partially crystalline materials also.

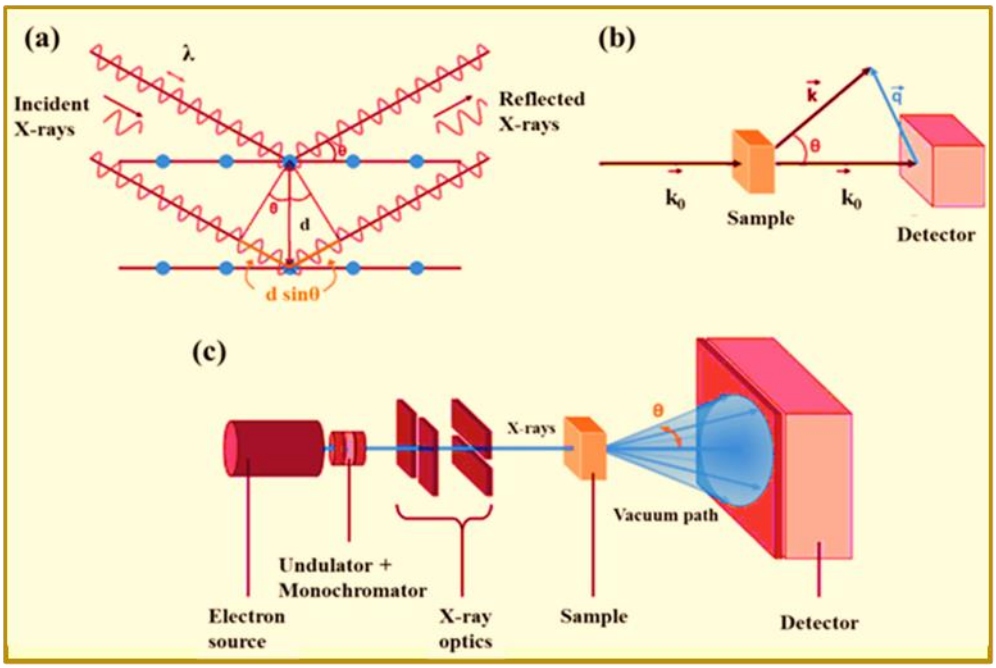

Figure 3.2: (a) The diagram of Bragg's condition for X-rays scattering, (b) the outline of geometrically constructed scattering and (c) diagram of the setup for a small-angle X-ray scattering experiment.

X-rays are a type of electromagnetic ray having wavelengths of the order of nanometers, When X-rays scatter from a nanomaterial having structure at that length scale of x-rays, an interference pattern with varying intensities can arise. This is qualitatively comparable to the multi-coloured patterns made by soap bubbles, where various colors are seen from various angles. XRD yields a diffraction pattern that reveals details about the interior structure on length scales ranging from 0.1 to 100 nm [4,5]. Whan sample is exposed to an X-ray beam, the angle that separates the direction of the outgoing and incoming beams is commonly referred to as 2θ. In XRD, a collimator beam of X-rays is incident on the sample and is diffracted by the crystalline phases in the sample. When Bragg's condition (Figure 3.2) is satisfied, constructive interference occurs due to diffraction of x-rays from the parallel crystalline planes spaced apart by a distance (d) given by the equation,

$$2dsin\theta = n\lambda$$

Here, λ is the wavelength of the x-ray beam, θ is half of the previously indicated scattering angle 2θ, and n is an integer (1, 2, 3,...). Although actual materials are naturally more complex, the overall conclusion is that there is a relation between the angles at which the scattered intensity is maximum and the interplanar distances (d) within the sample, *i.e.*, greater d values are associated with smaller scattering angles 2θ. The diffracted X-ray intensity is evaluated as a function of orientation of the sample and the scattering angle 2θ. Sample's structural analysis is carried out using this diffraction pattern. It is possible to evaluate the homogeneous and inhomogeneous strains from the diffraction peak position obtained using XRD data. The change in d-spacing, which indicates the change in the lattice

Figure 3.3: Digital image of X-rays diffractometers - (a) D8 Advance Bruker set-up and (b) Rigaku MiniFlex 600 set-up (top), inner chamber of Rigaku MiniFlex (bottom).

constant under homogeneous strain, can be computed from the shift in peak position. Inhomogeneous strain alters from crystallite to crystallite or within a single crystallite which further results in peak broadening and increases with $sin\theta$. The crystalline size also affects in broadening, but in this case $sin\theta$ has no bearing on the broadening. Scherrer's formula can be used to determine the crystallite size (D), in the absence of any inhomogeneous strain.

$$D = \frac{k\lambda}{Bcos\theta_B}$$

Where, B is the full width at half maximum (FWHM) of the diffraction peak,

θ_B is the angle of diffraction, and

k is the Scherrer's constant.

The XRD characterization of the synthesized samples were carried out using Bruker X-ray diffractometer (D8, AXS, Advance) (Figure 3.3a) and Rigaku XRD (MiniFlex 600) set-up (Figure 3.3b).

3.4.2 Raman Spectrometer

Raman spectroscopy is a non-destructive analytical technique which yields precise data on molecular interactions, phase, crystallinity, chemical structure and vibrational energy modes of a sample [6,7]. This characterization tool is based upon the interaction of light with the chemical bonds within a sample.. Raman spectroscopy is named after the Indian physicist C. V. Raman as he discovered this scattering in 1928 with his research partner K. S. Krishnan. Raman spectroscopy extracts the structural information through the detection of Raman scattering from the sample.

Typically, a monochromatic laser light at visible or near-infrared wavelengths, is used by Raman Spectrometer to probe the samples. When a sample is illuminated by the laser, most of the light is scattered by the sample without a change in energy and this elastic scattering is termed as Rayleigh scattering. Further, a small part of the incident photon is scattered with a loss or gain of energy, which is known as Raman Effect. Raman scattering is inelastic scattering because here photon interacts with molecules of the sample resulting in excitations. Hence, the resultant effect is a shift in the energy of the photons, either higher or lower than the energy of the incident photon. This shift in energy corresponds to shift in frequency/wavelength of the inelastically scattered photons, known as Raman Shift. The inelastically scattered photons having frequency lower than that of the incident photons is called Stokes lines whereas the scattered photons having frequency higher than the incident

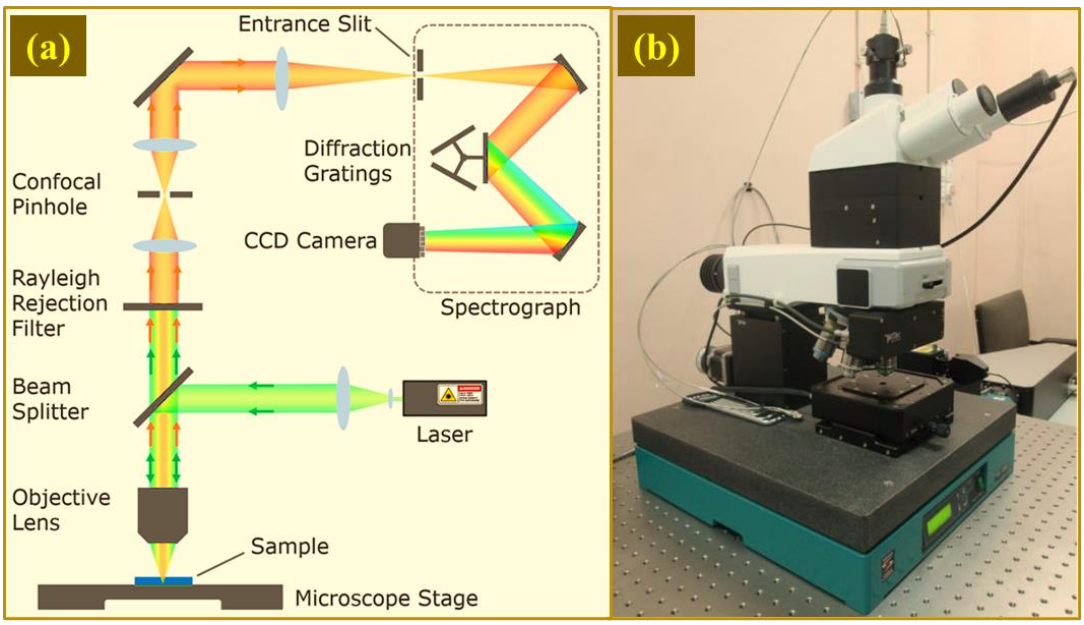

Figure 3.4: (a) Schematic representation (taken from webpage) and (b) digital image of Raman Spectrometer.

photons are called anti-Stokes lines. Compared to anti-Stokes lines, Stokes-shifted Raman spectra are more intense because they involve transitions from lower to higher vibrational

energy levels. In general, Stokes lines are measured in traditional Raman spectroscopy [8,9]. However, anti-Stokes lines are typically used for measurement for samples having intense fluorescence. For the Raman characterization of our synthesized samples, a confocal Raman spectrometer (alpha 300R, WITec, Germany) has been incorporated to get the Raman spectra of all the samples under the excitation of a 532 nm laser source. Figure 3.4a-b display the schematic diagram of a Raman Spectrometer and the digital image of Raman spectrometer (alpha 300R, WITec, Germany) used for characterization.

3.4.3 Field Emission Scanning Electron Microscope (FESEM)

Scanning Electron Microscopy (SEM) is an extremely handy technique for obtaining precise surface information and high-resolution pictures of as-synthesized nanostructure [10,11]. This kind of electron microscopy creates images at a far higher resolution than optical microscopy by scanning the surface of a specimen with the help of a concentrated electron beam. SEM equipment have resolutions ranging from less than one nanometer to several hundred nanometers. A focussed stream of electrons is projected and scanned over the sample's surface using a SEM, which uses specialized detectors to collect various signals obtained from the surface of the sample. The interaction between the electrons in the beam and the atoms in the sample results in a variety of signals that can be utilized to determine the composition and topography of the surface. Real-time images can be shown on an external monitor with software that links the position of the beam with the intensity of electrons detected by the detector(s). The two most popular types of detectors utilized for high-resolution imaging in a SEM are the secondary electron detector (SED) and the backscattered electron detector (BSD). Energy dispersive X-ray spectroscopy (EDS) detectors provide access to microanalysis of the surface composition. The electron generating technology is the primary distinction between Scanning Electron Microscope and Field Emission Scanning Electron Microscope (FESEM). Though, FESEM generally

operates on the same principles as SEM, a Field Emission Gun (FEG) serves as the electron source in FESEMs. Whereas, thermionic emission is employed in SEM. a potential gradient is applied in FEGs to emit the electron beam.

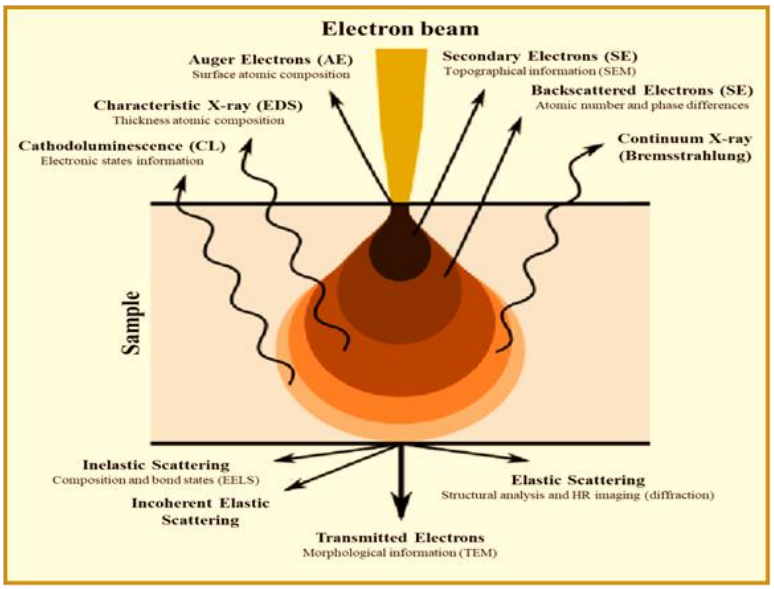

Figure 3.5: Interaction of electron beam on a sample surface.

As mentioned previously, the interaction of electrons with a surface atom of the sample is the fundamental idea of FESEM. Electron energy and speed may either change or remain unchanged in this interaction process. Elastic scattering occurs when electron energy remains conserved, whereas inelastic scattering occurs when there is a change in momentum or velocity of the electron. Electrons from atomic orbits are knocked out due to inelastic scattering and another electron from a higher orbit fills the resulting electron vacancy. This results in release of an X-ray photon. The EDS X-ray detector counts the number of released X-ray photons along with their energy. The energy of the X-ray is characteristic of the element from which the X-ray is emitted. When sample is bombarded with high-energy electron, emission of photons of characteristic wavelengths occurs from a sample, know as Cathodoluminescence (CL). The Auger electrons are emitted at discrete

energies that are characteristic of the elements present on the sample surface. The characteristic energies of the Auger electrons are such that only the electrons from the outer 0.5 to 5 nm can escape and be detected. The three methods through which atoms release energy to relax are by X-rays, Auger electrons, and Cathodoluminescence. This relaxation energy is the fingerprint of each element. Figure 3.5 depicts the impact of bombarding the sample with electrons schematically. To obtain the surface image, low energy secondary electrons (~ 50 eV) are used. FESEM can be used for direct analysis of a broad range of solid materials. To reduce the surface charge effect and probability of beam damage, separate imaging techniques like low-vacuum or low-kV imaging are frequently needed for biological samples and insulating samples. To reduce charging effect, insulating samples should have a small layer of gold or platinum sputter coated on them.

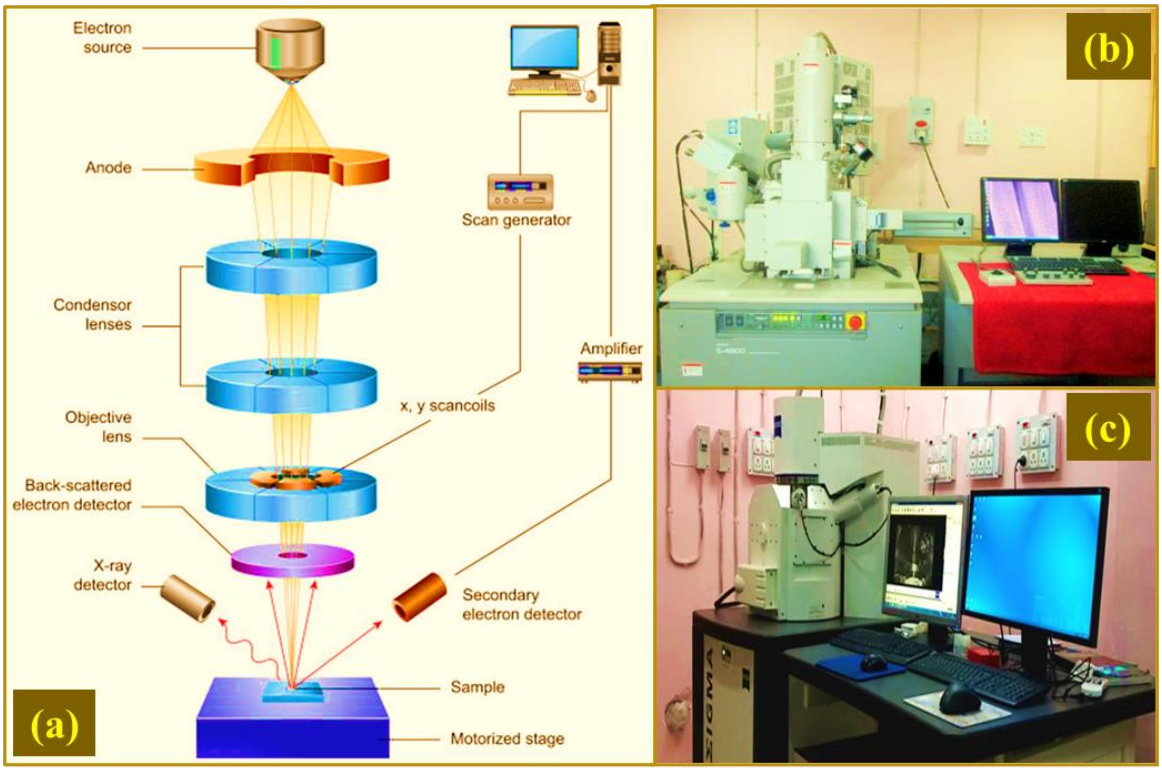

Figure 3.6: (a) Schematic (taken from webpage) and (b-c) Digital photograph of FESEM instruments.

FESEM S-4800, Hitachi and ZEISS SIGMA FESEM were used for the morphological characterization of the as-prepared samples. Figure 3.6 displays the schematic diagram of FESEM (Figure 3.6a) and the digital images of FESEM instruments used for characterization (Figure 3.6b-c) respectively.

3.4.4 Energy dispersive X-ray spectroscopy (EDS)

An essential characterisation tool for assessing elemental compositions and figuring out stoichiometry of an as-prepared sample is Energy dispersive X-ray spectroscopy (EDS). EDS is an essential component of FESEM. Inner shell electrons of the atoms from sample's surface are knocked out when they are subjected to an electron beam bombardment. Hence, electrons from the outer shell come to fill the vacancy created, causing an X-ray to be released. The energy of the X-rays released is measured by the EDS detector as the released energy is the distinctive fingerprint of a specific element which constitutes the sample.

3.4.5 Transmission Electron Microscope (TEM)

Transmission Electron Microscopy (TEM) is another analytical method used for observing the tiniest details in matter. By magnifying nanoscale structures up to 50 million times, TEM may reveal astonishing detail at the atomic scale [10,11]. When electrons are accelerated through an extremely strong electromagnetic field, they can have a wavelength that is substantially shorter than visible light (about 100,000 times smaller), enhancing the microscope resolution by many orders of magnitude [12]. A high energy electron beam is propelled through an incredibly thin sample, usually thinner than 100 nm, to create a TEM image. The microscope's column is equipped with a number of electromagnetic lenses and apertures that are used to concentrate the beam on the sample, reduce distortion, and enlarge the picture that is produced on a phosphor screen or a specialized camera. Though TEMs have many different shapes, they all have the same basic elements and working principle.

The traditional TEM and the STEM (Scanning Transmission Electron Microscope) are the two main categories of TEM instruments. Additional TEM versions are the E-S/TEM (where E is for "environmental") and the AC-S/TEM (where AC stands for "aberration corrected"). Nearly a century of research and development has culminated in the first demonstration of electron optics in the early 1930s, making TEM an essential method for applications in nanomaterials and life sciences. The most potent TEMs available today have extra detectors and modifications that not only improve the stability and functionality of the electron microscope but also give it the ability to gather chemical and electrical data at sub-nanometer length scales from a variety of nanomaterials. Scientists can get a fundamental understanding of materials and biological systems by being able to observe atoms through TEM. Scientists can observe the basic components of functional materials such as catalyst nanoparticles, batteries, and semiconductor devices by magnifying into the atomic size. In situ material manipulation with focused electron beams enables the study and discovery of "nanofabrication" and other unique phenomena. This scale of detail is really astounding, and it helps scientists in understanding the relationships between structure, property, and performance so they can build nanomaterials from the bottom up.

The electron cannon, which incorporates to a high voltage source to adjust the kinetic energy of electron beam, is located at the top of the column of a TEM structure. Accelerating voltages typically vary from 80 kV to 300 kV. To concentrate the electron beam on the sample and enlarge the TEM picture on the viewing screen, the microscope column is made up of a number of electromagnetic lenses and apertures (or detectors). Maintaining the necessary vacuum levels throughout the column is done with a vacuum system. Owing to the intricacy of the instrumentation, the microscopist only has control over a small number of crucial parameters; the majority of the components are automatically computer controlled. The sample stage position, magnification, objective

lens current, beam current (spot size), and the choice of which apertures and detectors to use are the primary user-controlled parameters. In order to assess composition of the sample, the majority of TEMs additionally come with an X-ray detector that may be placed in between the objective lens pole-pieces. Electron energy-loss spectroscopy (EELS) is performed using optional electron energy-loss spectrometers at the end of the column.

Three forms of interactions between the electron beam and the sample are observed in a TEM instrument, which are- electrons that are unscattered (transmitted beam), electrons that are elastically scattered (diffracted beam), and electrons that are inelastically scattered [13]. In case of *Bright Field* imaging, the unscattered electron beam is used for TEM image generation. Typically, the objective aperture selects the diffracted beams for *Dark Field* imaging [12,14].

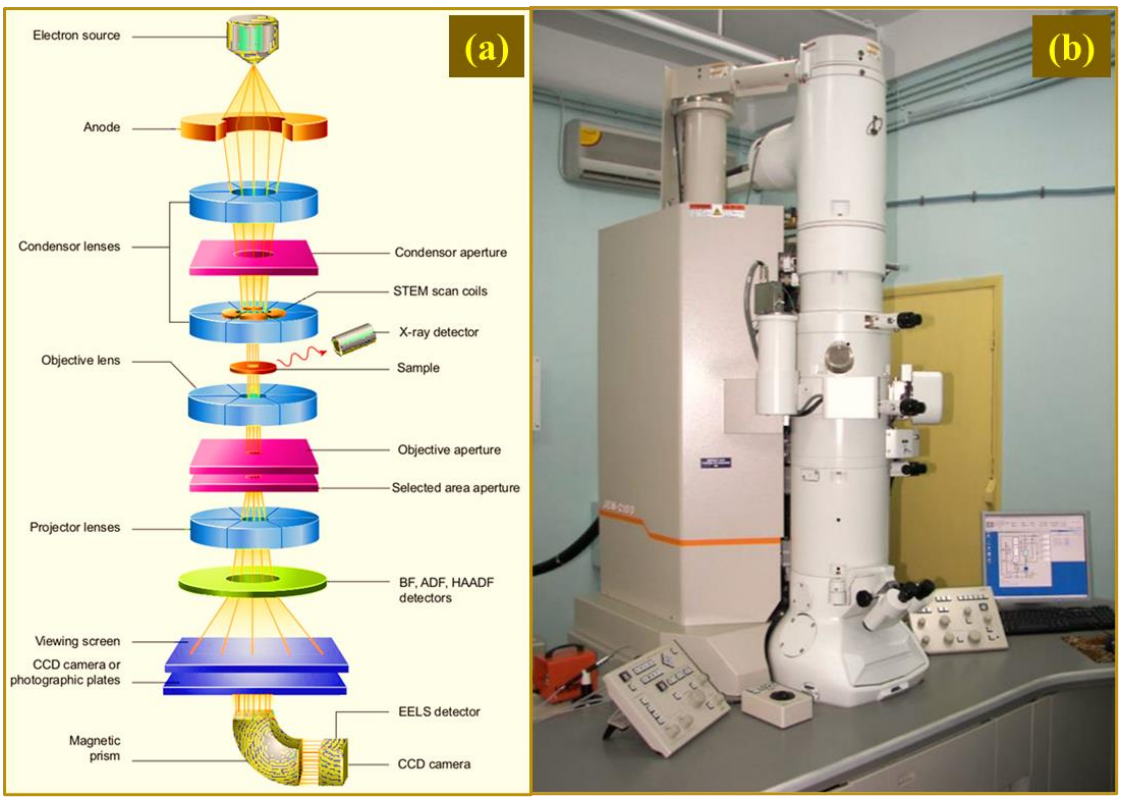

Figure 3.7: (a) Schematic diagram (taken from webpage) and (b) photograph of HRTEM Instrument.

The crystalline structures and morphologies of all as-synthesized samples were characterized using a high-resolution TEM instrument (JEOL, JEM 2100). A schematic representation of the TEM instrument and an image of the instrument are displayed in Figure 3.7a-b.

3.4.6 X-ray electron photoelectron spectrometer

X-ray electron photoelectron spectroscopy (XPS) is a quantitative spectroscopic approach utilized for measuring the elemental composition of the material's surface as well as its chemical and electronic states. XPS has its foundation in the photoelectric effect which was first successfully demonstrated by Einstein in 1905. He received Nobel Prize later in 1921 for this. Throughout the two decades in 1950s and 60s, Kai Siegbahn and colleagues transformed this effect into one of the most effective instruments for investigating the electronic structure and composition of surfaces of different materials. In 1981, Siegbahn was awarded the Nobel Prize in Physics for the development of XPS [15]. XPS is also a surface spectroscopic technique like EDS.

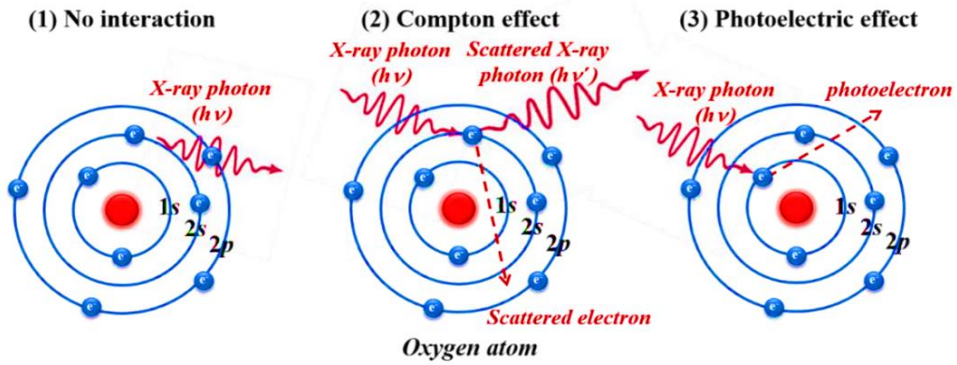

Figure 3.8: Photon interaction with an oxygen atom: (1) No interaction, (2) Compton effect, (3) Photoelectric effect.

When a sample's surface is exposed to a photon source, three phenomena may occur (Figure 3.8) : (a) the photon may pass through without any interaction with the sample, (2) the photon can partially loose its energy by a scattering with an atomic orbital electron (inelastic scattering) which is observed in Compton effect, and (3) the photon can be absorbed and total energy of the photon is transferred to the atomic orbital electron which results in an emission of electron from that atom. The last phenomenon is called photoelectric effect.

The photoemission process would only occur if the energy of the exciting photon is higher than the binding energy of the irradiated electron. Generally, low energy monochromatic X-ray photons are utilized to irradiate the sample surface which causes the photoelectrons to emit from the surface. The kinetic energy (KE) distribution of the ejected photoelectrons is measured by the hemispherical energy analyzer. The core level electrons of the atom are knocked out by the photons. Both the binding energy (E_B) of these core level electrons and the corresponding energy level in the atom are the characteristics of the specific element. If the energy of the incident X-ray photon is known, the measured kinetic energy of a core-level photoelectron can be easily converted to its characteristic binding energy E_B using the relation

$$E_B = h\nu - E_k$$

Where, $h\nu$ is the energy of the incident X-ray photon, and

E_k is the kinetic energy of the ejected photoelectron [16].

For accurate measurement of E_B of the photoelectron ejected from the conducting sample, it should be placed in electrical contact with the XPS spectrometer. This puts the Fermi level (E_F) of the sample and the spectrometer at the same energy level. However, the photoelectrons are severely attenuated as they travel through the sample and hence, the

information is only available from the sample surface. 5–10 nm is a common sample depth from which data can be extracted. Therefore, the bulk of a sample cannot yield any chemical information using this technique. Measurable shifts in binding energies result from the chemical bonding of element atoms. These shifts are used to determine the oxidation states of the constituent elements in a compound.

All the as-prepared samples in this thesis were characterized using the hemispherical XPS analyzer (SPECS, HSA 3500) and a monochromatic Al K_α ($h\nu$ = 1486.6 eV) X-ray source to investigate the chemical states of the constituent elements. The schematic of the XPS process, hemispherical analyzer and digital image of the instrument used for XPS characterization are shown in Figure 3.9a-b.

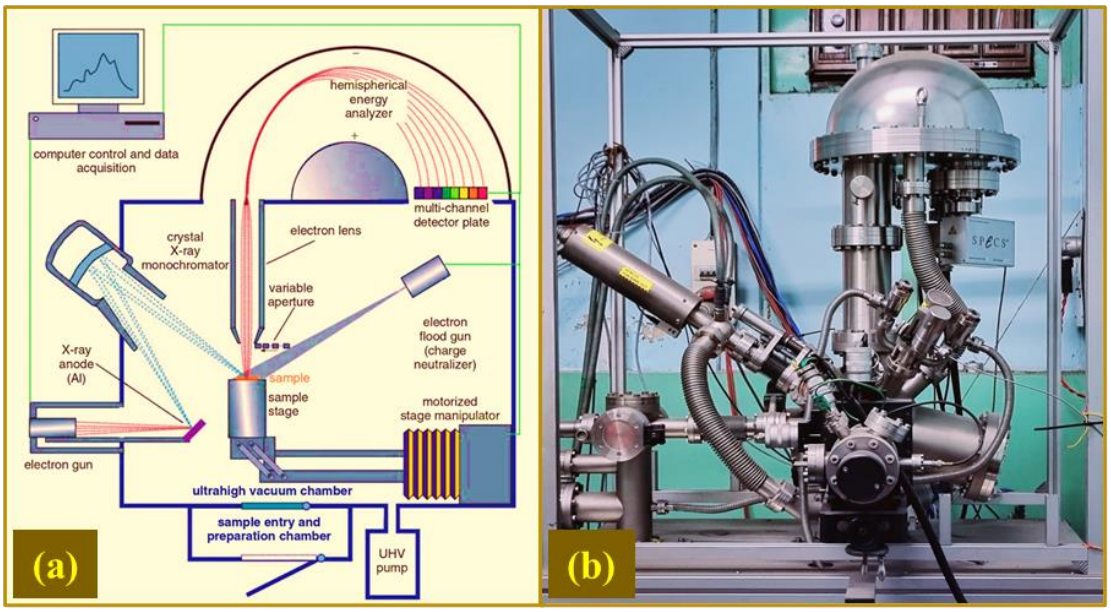

Figure 3.9: (a) Schematic of XPS process, hemispherical analyzer component (taken from webpage) and (b) digital image of X-ray Photoelectron Spectrometer.

3.4.7 UV-Vis-NIR Spectrophotometer

UV-Vis-NIR Spectrophotometer is used to study the optical characteristics of semiconducting materials. Typically, this spectroscopic tool is employed to investigate the absorption, transmission, and reflection spectra of the sample. From these spectra, band-gap can be determined. Photons with specific energies are typically directed towards the sample and their interaction with the sample is recorded. The experiment provides a precise measurement of the band-gap because photons with energies greater than the band-gap are absorbed and photons with energies lower than the band-gap are transmitted.

The relationship between the band-gap (E_g) of the semiconducting sample and absorption coefficient (α) is as follows:

$$\alpha h\nu = \left(h\nu - E_g\right)^{\gamma}$$

Where, γ = 1/2 for allowed direct transition, γ = 2 for allowed indirect transition, γ = 3 for forbidden indirect transition, and γ = 3/2 for forbidden direct transitions. $h\nu$ is the energy of the incident photon. The absorption coefficient α can be determined by $\alpha = 2.303(A/d)$, where d is the thickness. A is defined as $A = log(I/I_0)$ where I_0 and I respectively denote the incident and transmitted beam intensities. E_g is the optical band-gap of the material defined as the energy difference between the conduction and valence bands. A plot between $(\alpha h\nu)^2$ and $h\nu$ should give a straight line and the intercepts on the energy axis at $(\alpha h\nu)^2 = 0$, gives the optical band-gap of a semiconducting sample. The monochromator, sample and reference cells, detector, and an appropriate light source are the fundamental components of a UV spectrometer. Rotating prism disperses the radiations emitted by the primary light source. A succession of steadily increasing wavelengths are produced by the rotation and pass through slits to be used in data acquisition. The monochromatic beam is further separated into two beams with the help of a second prism.

The sample solution is passed through by one beam, while the reference solution is passed through by the other. Photocells in the sample and reference cells receive the emitted beams and further produces an alternative or pulsing current. The spectrum is shown on a computer monitor once the generated signal has been amplified. A Shimadzu UV-Vis-NIR (UV 3600) spectrophotometer was used to measure the band-gap of the samples. A schematic diagram of a UV-Vis-NIR spectrophotometer along with a digital image of the spectrometer used are depicted in Figure 3.10a-b.

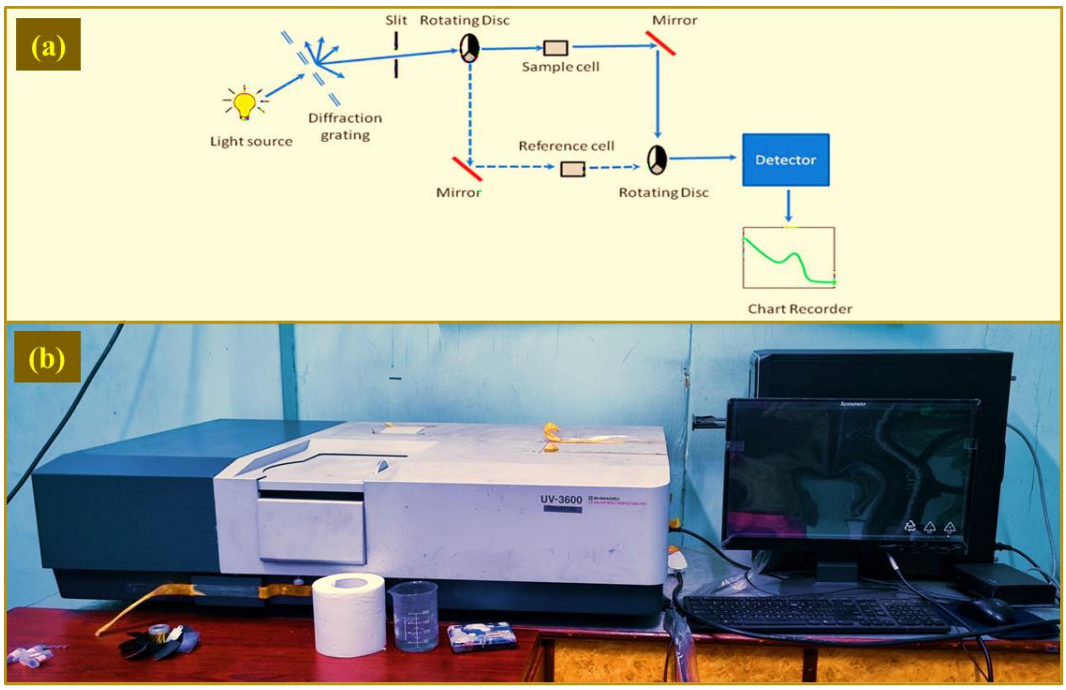

Figure 3.10: (a) Schematic diagram (taken from webpage) and (b) digital photograph of UV-Vis-NIR Spectrophotometer.

3.4.8 Fourier Transform Infrared Spectrometer

The infrared (IR) radiation zone in the electromagnetic spectrum falls in between visible and microwave radiation. The infrared region can further be splitted into three smaller regions : far-IR (400–20 cm^{-1}), mid-IR (4000–400 cm^{-1}), and near-IR (14000–4000 cm^{-1}). Most substances in the mid-IR range alter their basic vibrational levels. Using an interferometer, the infrared spectrometer collects an interferogram of a sample signal. Applying a Fourier Transform on the interferogram yields the spectrum. An infrared (IR) spectrometer measures the frequencies at which the samples absorb radiation by analyzing the interaction of IR radiation with samples. The number of molecules sampled determines the absorption intensity in all types of infrared spectrometers. The Beer-Lambert law expresses a straightforward relationship between the amount of sample in the beam and the intensity of the transmitted (I) and incedent radiation (I_0):

$$log\ (I/I_0) = \varepsilon cl$$

Where c is the concentration, l is the cell thickness and ε is the frequency dependent extinction coefficient. The foundation of all quantitative infrared spectroscopy is the Beer-Lambert law. Finding the frequencies of the absorbed energy enables one to identify the chemical bonding that exists inside the sample's chemical structure. Majority of modern FTIR systems incorporate a Michelson Interferometer, which consists of two mirrors and a beam splitter. This device creates interference between two beams that have travelled via two different optical paths. Interference only occurs when two beams have same frequency and constant phase difference. Figure 3.11a-b displays a schematic representation and an image of the FTIR spectrometer used for sample characterization.

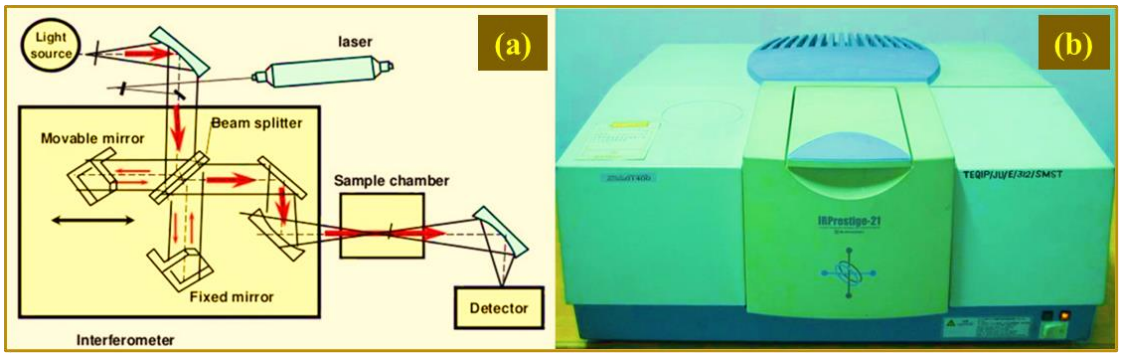

Figure 3.11: (a) Optical path diagram (taken from webpage) and (b) photograph of FTIR Spectrometer.

3.4.9 Brunauer-Emmett-Teller Measurement Technique

Brunauer-Emmett-Teller technique is another major characterizing tool utilizing which we can measure specific surface area (SSA), pore size distribution, and pore volume of as-prepared nanostructure. Three scientists Stephen Brunauer, Paul Hugh Emmett, and Edward Teller developed the fundamental hypothesis and published their work in the Journal of the American Chemical Society in 1938 [17]. The physical adsorption of an inert gas such as nitrogen on the sample's solid surface serves as the basis of this theory. The measured SSA is expressed in $m^2 g^{-1}$. The inert gas is used because it does not affect the adsorptive (the sample to which the gas attaches) chemically. BET theory is beneficial for systems with multilayer and porous structures that assist in efficient adsorption of inert gas. The gaseous medium in most cases is liquid nitrogen at 77 K. However, other inert gases which can be utilized are carbon dioxide, argon, etc. In order to evaluate the SSA, the BET technique integrates both the estimation from external area and pore area of the sample. This information is also useful for evaluating surface porosity and particle sizes and their distributions, which are crucial factors to take into account for a variety of applications.

Figure 3.12: Photograph of BET Specific Surface Area Analyzer.

Applications for BET analysis can be found in a wide range of research domains and sectors, including the pharmaceutical, nanotechnology (catalyst characterization, the adsorption capability of activated carbon), cosmetic, textile, medical implant, medical device, filter, ceramic, cement (analyzing the fineness of cement) , and paint industries. Using the instrument Nova 1000e, Quantachrome (Figure 3.12), the SSA and pore size distribution of the as-synthesized samples and composites were determined in our lab.

3.5 Electrochemical Measurements

In electrochemical analysis measurements can be done in two ways, namely potentiometry and amperometry. In potentiometry, potential between the electrodes is measured whereas amperometry method measures the current between the electrodes. The electrochemical characteristics of an electrode material are studied in an electrolyte medium using different methods like cyclic voltammetry (CV), galvanostatic charge discharge (GCD), linear sweep

voltammetry (LSV), chronoamperometry, electrochemical impedance spectroscopy (EIS) etc. One kind of potentiodynamic electrochemical measurement is cyclic voltammetry [18]. In this CV method, the working potential ramps up linearly with time and when upper potential limit is achieved, working potential ramps down towards opposite direction, i.e. lower potential limit. But this is not the case in LSV, the potential is scanned from a lower limit to a higher limit only. Plotting current against the potential of the working electrode gives us the required CV curve. For different potential sweep rate, each set of repetitive curves can be traced. The CV plot contains the detail about the complicated redox potentials, electrochemical reaction rates in the reactions taking place at the electrode-electrolyte interface and more. The electrochemical reactions are controlled by Nernst equation. Selecting the right potential window is crucial in CV measurement since the electrode material needs to be redox active within the specified potential range. The reversible CV curves exhibit both the anodic and cathodic peaks for redox reaction. All the measurements are carried out in a three-electrode configuration which comprises a reference electrode, a working electrode, and a counter electrode. An appropriate electrolyte (aqueous or non-aqueous) is used to submerge the electrodes. With the application of appropriate voltages and currents, this three-electrode configuration enables the redox processes to happen. In addition to CV, there are other potentiometric studies viz. GCD, EIS, LSV etc. EIS is a technique to analyse the electrode's impedance in response to various frequencies. The Bode plot or Nyquist plot are the two graphical representations of EIS data [19,20]. In GCD, a steady current is provided through the electrodes to analyse the charge-discharge phenomena with time. In different fields of electrochemistry, Cyclic Voltammetry has been a popular electroanalytical method for studying electron transfer kinetics, diffusion coefficient measurement and estimating the performance of devices like Li-ion batteries, Supercapacitors etc. [21,22].

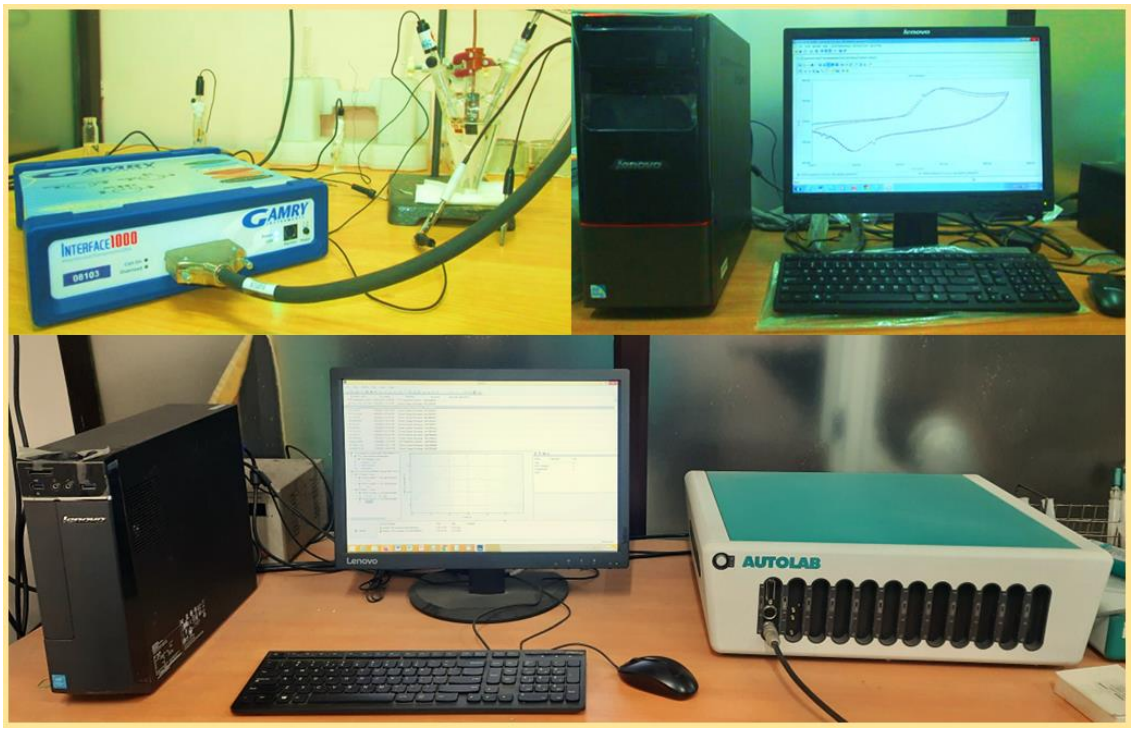

Figure 3.13: Photograph of Gamry Interface (above) and the Autolab interface (below)

To analyse our transition metal-based hierarchical nanostructures, measurements like CV, GCD, LSV, EIS etc. have been performed using Gamry Interface 1000 (Potentiostat/ Galvanostat/ ZRA) and PGSTAT 302N Autolab set-up (Figure 3.13).

3.6 References

[1] S. Sahoo, P. Pazhamalai, V.K. Mariappan, G.K. Veerasubramani, N.-J. Kim, S.-J. Kim, Inorg Chem Front 7 (2020) 1492–1502.

[2] K.T. Kubra, R. Sharif, B. Patil, A. Javaid, S. Shahzadi, A. Salman, S. Siddique, G. Ali, J Alloys Compd 815 (2020) 152104.

[3] B. Santara, P.K. Giri, Mater Chem Phys 137 (2013) 928–936.

[4] B.D. Cullity, S.R. Stock, Upper Saddle River, NJ (2001) 388.

[5] M.J. Buerger, (No Title) (1942).

[6] P. Graves, D. Gardiner, Springer 10 (1989) 973–978.

[7] D. Wolverson, Characterization of Semiconductor Heterostructures and Nanostructures: Chapter 17. Raman Spectroscopy, Elsevier Inc. Chapters, 2013.

[8] E. Smith, G. Dent, Modern Raman Spectroscopy: A Practical Approach, John Wiley & Sons, 2019.

[9] H.H. Willard, L.L. Merritt Jr, J.A. Dean, F.A. Settle Jr, (1988).

[10] P.L. Gai, E.D. Boyes, Electron Microscopy in Heterogeneous Catalysis, CRC Press, 2003.

[11] B.J. Inkson, in: Materials Characterization Using Nondestructive Evaluation (NDE) Methods, Elsevier, 2016, pp. 17–43.

[12] B. Fultz, J.M. Howe, Transmission Electron Microscopy and Diffractometry of Materials, Springer Science & Business Media, 2012.

[13] P.E. Champness, Electron Diffraction in the Transmission Electron Microscope, Garland Science, 2020.

[14] J.M. Thomas, P.L. Gai, Advances in Catalysis 48 (2004) 171–227.

[15] K. Siegbahn, in: ESCA, 1967.

[16] P. Van der Heide, X-Ray Photoelectron Spectroscopy: An Introduction to Principles and Practices, John Wiley & Sons, 2011.

[17] S. Brunauer, P.H. Emmett, E. Teller, J Am Chem Soc 60 (1938) 309–319.

[18] N. Elgrishi, K.J. Rountree, B.D. McCarthy, E.S. Rountree, T.T. Eisenhart, J.L. Dempsey, J Chem Educ 95 (2018) 197–206.

[19] S. Wang, J. Zhang, O. Gharbi, V. Vivier, M. Gao, M.E. Orazem, Nature Reviews Methods Primers 1 (2021) 41.

[20] A.Ch. Lazanas, M.I. Prodromidis, ACS Measurement Science Au 3 (2023) 162–193.

[21] V.S. Bagotsky, A.M. Skundin, Y.M. Volfkovich, Electrochemical Power Sources: Batteries, Fuel Cells, and Supercapacitors, John Wiley & Sons, 2015.

[22] A. Yu, V. Chabot, J. Zhang, Electrochemical Supercapacitors for Energy Storage and Delivery: Fundamentals and Applications, Taylor & Francis, 2013.

Chapter 4: Hierarchical Assembly of MnO_2 Nanosheet on $CuCo_2O_4$ Nanoflake over Fabric Scaffold for Symmetric Supercapacitor

The soaring fidelity of spinel cobaltite system in electrochemistry presents its candidature as an electrode material for high-performance energy storage system and next generation portable devices. In this work, geometrically intricate heterostructure comprising $CuCo_2O_4$ and MnO_2 is realized on flexible carbon fabric to utilise as an electrode material. Facile hydrothermal technique was adopted to synthesize mesoporous spinel copper cobaltite on fabric substrate which further act as scaffold for the growth of MnO_2 hierarchy. Distinctive hierarchical designing of the hybrid capitalizes the combined effects from large specific capacitance of the shape-controlled nanoforms and good electrical conductivity of the carbon fabric platform. Optimized hybrid sample with maximum porosity in it and high surface area offered specific capacitance of 1458 F/g at 0.5 A/g with stable rate capability. Cycle stability analysis of the electrode suggest 93% retention of its initial capacitance value even after 5000 long cycles. Electrochemical performance delivered by the synthesized hybrid are far better compared to pristine samples. Observed differences in electrochemical behaviour among the synthesized nanoforms were elucidated on the basis of geometry-porosity-property relationship. Flexible symmetric solid-state supercapacitor was devised with the optimized hybrid which attains a high gravimetric capacitance of 181.3 F/g. Additionally, the device offers a high energy density of 64.1 Wh/kg at a power density of 1.5 kW/kg corresponding to a current density of 2.8 A/g and displayed high cycle stability. Such electrochemical results reveal the impact of amalgamation low dimensional nanoform in a geometrically intricate hybrid and nanostructure morphology controlling in device performance maximization and thereby providing a pathway for rational development of noble electrode materials.

4.1 Introduction

In today's scientific consortium the rudimental inquisition regarding research pays heed to alternative energy because of the climate variability and its upshots on environment [1,2]. This ensues enormous interest in proliferating the efficiency of the energy sources and developing more sustainable, pecuniary and ingenious sources. Supercapacitor (SC) is such a kind of device which has been fledged adequately over the last few years accomplishing its emanation as a potential energy storage device [3,4]. Basic physics of the supercapacitors, also coined as electrochemical capacitors or ultracapacitors, lies in the fact that it incorporates high surface area of the electrodes and much thinner electrolytic dielectrics resulting in decrement of the inter electrode distance to attain capacitances having magnitude much larger than conventional capacitors. Thus, SCs as an effectual energy-storage device, have been of ample interest for its manifestation of greater energy densities and longer lifetime than conventional electrochemical batteries, higher capacitance in comparison to conventional capacitor yet sustaining the superior power density [5,6]. Based on charge storage principle, SCs is generally branded into two different classes viz. pseudocapacitors and electrochemical double-layer capacitors (EDLCs) [7,8]. Pseudocapacitor depends on faradaic process which involves reversible oxidation-reduction (redox) reactions on the electrode offering superior electrochemical performance as compared to EDLCs. In EDLCs, non-faradaic process occurs relying mostly on ion adsorption. Carbonaceous materials are generally used for the realization of EDLCs [9,10]. On the other hand, pseudocapacitors are mostly fabricated using transition metal-based oxides (TMOs), sulphides and halides etc. as active electrode material [11,12]. TMOs are considered as a promising electrode material for pseudocapacitors due to their high energy state, multi- oxidation states of the metal ions, abundance, environmentally less-toxic etc. EDLCs store charges electrostatically, i.e., non-faradaically often deliver high power but

suffer from low energy density. Again contrariwise, TMOs based pseudocapacitors accumulate charges via redox reaction process also called faradaic process ensuring high energy density. Here come, the hybrid capacitor devices which incorporate both faradaic and non-faradaic contribution of pseudocapacitor and EDLC to get high capacitance, superior energy and power density accomplishing market demand.

Among the broad range of TMOs such as monometallic, bimetallic and spinel oxides exhibit numerous unique features which are advantageous for electrochemical applications. Again, spinel cobaltites with chemical formula MCo_2O_4 (M = Ni, Mn, Cu, Zn etc.) possess superior electrical conductivity and higher electrochemical redox property than the rest [4,13–15]. Charged carriers can easily channel through different transition-metal cations with apparently lower activation energy which leads to enhanced storage property of MCo_2O_4. Spinel copper cobalt oxide ($CuCo_2O_4$) has been chosen as active electrode material owing to its fast-reversible redox behaviour, high theoretical capacitance and conductivity as well as corrosion stability [14,16–18]. However, it suffers from low-rate capability, capacitive retention as active electrode material. Till date, several modifications of $CuCo_2O_4$ were achieved to address the above issues. But geometrically intricate 2D flake-like $CuCo_2O_4$ on flexible current collector like carbon fiber is not realised so far. Again, TMO like manganese oxide (MnO_2) has already established its precedence as electrode material because of its low toxicity, easy abundance, high porosity etc [19–21]. Despite these advantages, it suffers from shabby electrical conductivity (10^{-6} S/cm) which restrict its practical utilization as a single electrode material [22,23]. Thus, to boost the electrochemical activity of these different TMOs i.e., to accomplish their individual shortcomings sometimes incorporation or blending them is necessary. Introduction of carbonaceous materials to integrate with TMOs to get composite electrode [5,24], blending of different TMOs with different metal cations [25], direct integration of TMOs to realize

hybrid structure are few well-known routes [26–28]. Besides these protocols, direct integration of TMO over carbon base conducting substrate (such as graphite paper, carbon cloth) exhibited much superior electrode performance compared to individual components [14,29,30]. On the other hand, protocols of two blended TMOs sometimes still suffer from weak conductivity, low-rate capability, low specific surface area which resulted in further optimization of the electrode architecture and proper electroactive material selection.

Direct growth of a porous TMO nanostructure over different nanoforms of other TMOs is a very recognized protocol as compared to bulk composite of TMOs. Realization of hybrid nanoforms often result novel interface phenomenon, high surface area and multi-functionalities along with synergistic effect from individual TMOs, suppressing all individual shortcomings [31]. Realization of these hybrid nanoforms on conducting flexible substrate like carbon cloth have other aids also. Beside electrochemical performance boosts up, underlying fabric platform offer mechanical stability and robust adhesion to the nanoforms over it. It is also beneficial for the preparation of binder free flexible electrodes as it reduces resistivity imposed by auxiliary binder on electrodes [32]. Electrodes supported on conductive carbon fabrics evade the requirement of polymeric binders or carbon additives. It also eliminates the formation of “dead volume” significantly. Due to cost effectiveness, woven-wire like porous geometry, higher conductivity carbon cloth proved to be superior current collector compared to others like nickel foam, titanium foil etc. Furthermore, these electrodes have ascertained excellent electrochemical activity by i) providing more active sites for effective electron transport, (ii) reducing effective diffusion path for ion transport by utilizing free interspaces among nanoforms.

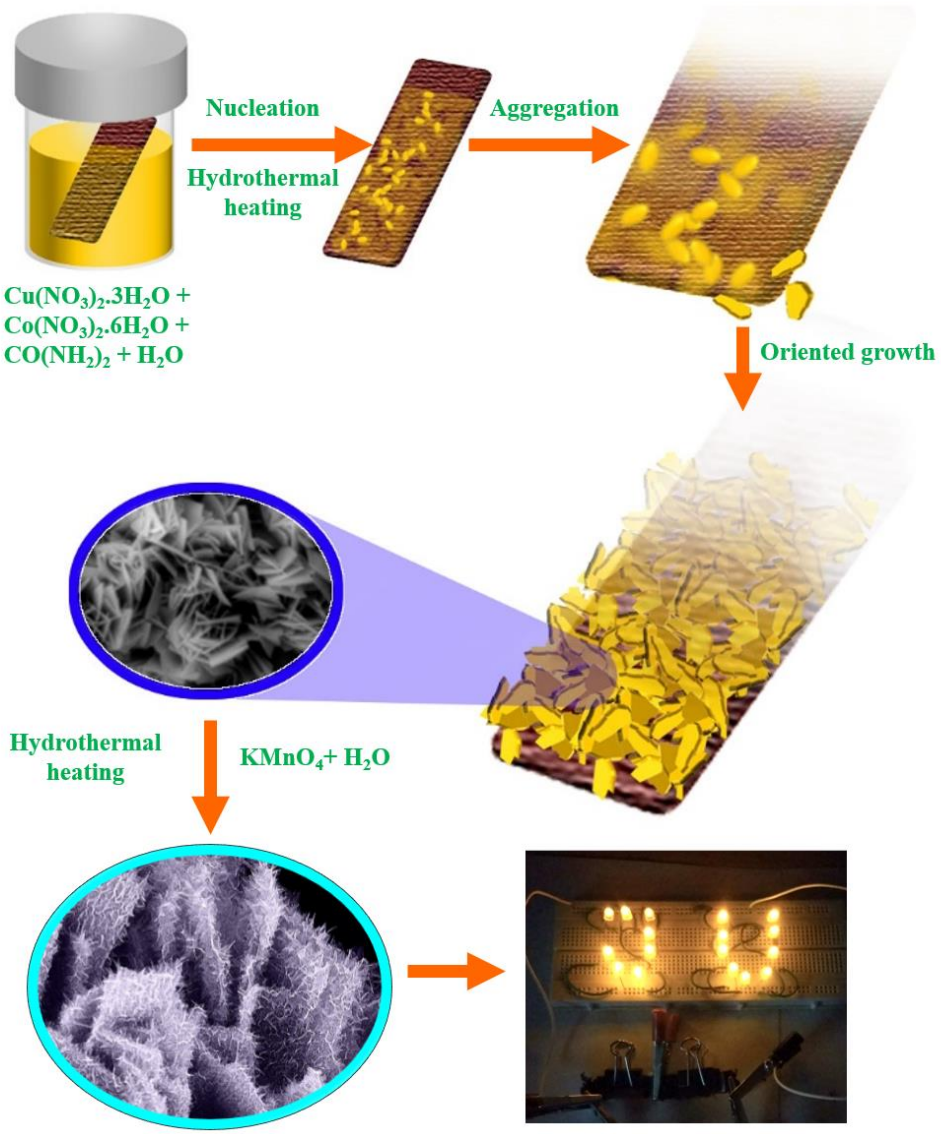

Scheme 4.1: Schematic illustration of $CuCo_2O_4$-MnO_2 hierarchy over carbon fiber and usage in supercapacitor.

Here, we have reported geometrically intricate hybrid comprising 2D nanoforms of $CuCo_2O_4$ and MnO_2 on flexible carbon fiber with improved electrochemical performance and storage features. Two-step facile hydrothermal route was adopted to realize $CuCo_2O_4$ flakes followed by birnessite type δ-MnO_2 hierarchy overcasting the pristine one. With subtle adjustment in reaction parameters, porosity in pristine $CuCo_2O_4$ flakes changed significantly. Optimised sample shows high specific capacitance with good rate capability.

The electrode displayed great cyclic stability even after 5000 long cycles operation. Symmetric SC device was also realized which delivered high energy density with high cycle stability. Furthermore, morphology controlling of the hybrid nanoform and its impact on the overall electrochemical performance have been also explored in details. The entire work in nutshell is presented schematically in Scheme 4.1.

4.2 Experimental

4.2.1 Activation of carbon cloth substrate

Reagents used for the preparation of $CuCo_2O_4$-MnO_2 heterostructure on carbon fiber substrates were of analytical grade. Primarily, carbon cloths were cleaned ultrasonically in acetone, ethanol and deionized water (D.I.) one by one and dried. For the preparation of $CuCo_2O_4$ nanoform, all the cleaned fiber substrates were dip-coated in a stock solution. The solution was prepared by adding appropriate amount copper nitrate trihydrate ($Cu(NO_3)_2$, $3H_2O$), cobalt nitrate hexahydrate ($Co(NO_3)_2.6H_2O$), ethanol and ethyl cellulose. These dip-coated substrates were dried overnight followed by annealing at 300°C.

4.2.2 Synthesis of $CuCo_2O_4$ nanoform

Prior to the preparation of $CuCo_2O_4$ on carbon fabric, all of the substrates with size of 2.4 cm × 5.0 were cleaned and activated properly. Initially, 0.25 g $Cu(NO_3)_2$, $3H_2O$, 0.60 g $Co(NO_3)_2$, $6H_2O$ and 0.3 g urea were mixed with 80 mL D.I. water via stirring. Once the solution became transparent, it was transferred to a Teflon-lined stainless-steel autoclave of 100 mL capacity. An activated carbon cloth substrate was also placed inside the autoclave with help a glass slide. Thereafter the autoclave was placed inside a regular laboratory oven at 120°C for 6 h. The autoclave was allowed to cool down naturally after the reaction span.

The substrates were washed with D.I. water for multiple times and dried for overnight to yield Cu-Co precursor. Finally, the substrate was annealed at 350 °C for 1 h in air.

For structural variation of the nanoforms, same experimental procedure was repeated except the temperature during the hydrothermal process was changed to 180 °C. Henceforth, we will designate the sample prepared at 120 °C and 180 °C as CL and CH, respectively.

4.2.3 Synthesis of MnO_2 hierarchy over $CuCo_2O_4$

Deposition of MnO_2 was performed over the aforementioned as-grown $CuCo_2O_4$ on carbon fiber. Prior to MnO_2 growth, $CuCo_2O_4$ samples were merged into the glucose solution which ensured carbonization and formed a thin carbon layer over $CuCo_2O_4$. This thin carbon layer acted as the interfacial template for MnO_2 growth. These substrates were further hydrothermally treated in 0.05 M $KMnO_4$ solution for 1.5 h at 165°C. Finally, the samples were washed with copious amount of D.I. water and dried in oven for overnight. Hereafter, we will label the hybrid sample prepared on CL and CH as CML and CMH, respectively.

4.2.4 Size of the electrode and calculation of mass of the active material

For hydrothermal growth of the active material at first the carbon fiber substates ware cut in to the size 4 cm x 2.5 cm and then the substrate was washed and dried properly. The dried substrates were weighed carefully and noted. Then the active materials were grown on the substrates (mentioned in the experimental process). The as prepared electrodes were again dried and weighed. The difference of the corresponding weights of the same substrate gives the weight of the active material in an electrode.

4.2.5 Electrochemical measurements

Electrochemical behaviour of all the samples was examined at ambient in a PGSTAT 302N Autolab set up. Ag/AgCl and platinum wire were used as reference and counter electrodes respectively. As synthesised samples on carbon cloth were acted as working electrode. 1 M aqueous solution of KOH was used as electrolyte. Cyclic voltammetry (CV) measurements were recorded within the potential window of -0.2 to 0.6 V vs. Ag/AgCl at different scan rates. Both the, Galvanostatic charge discharge (GCD) and electrochemical impedance spectroscopy (EIS) were also performed in the same instrument.

4.2.6 Fabrication of symmetric supercapacitor

In two-electrode measurements, a gel made with polyvinyl alcohol (PVA) and KOH was used as the electrolyte. 3 g PVA and 1.5 g KOH was mixed with 60 ml D.I. water via vigorous stirring. Temperature of the stirrer was increased to 90 °C and the stirring was continued till the solution became translucent. Two CMH electrodes were soaked into the gel and attached together with a filter paper as separator.

4.3 Results and Discussion

XRD profiles of CH and CMH are shown in Figure 4.1a whereas the same for CL and CML is presented in Figure 4.2a. Diffraction peaks with 2θ values positioned at 18.9°, 31.2°, 36.8°, 38.6°, 44.8°, 59.3° and 65.2° corresponds to crystallographic planes of (111), (220), (311), (222), (400), (511), (440) of cubic spinel $CuCo_2O_4$ for CH and CL samples which agrees well with the literature (JCPDS Card No. 1-1155) [33]. These peaks also indicate that as obtained $CuCo_2O_4$ possess high crystallinity and has a face-centred cubic structure (space group: Fd3m) [33]. It is noteworthy to mention here that there is no visible

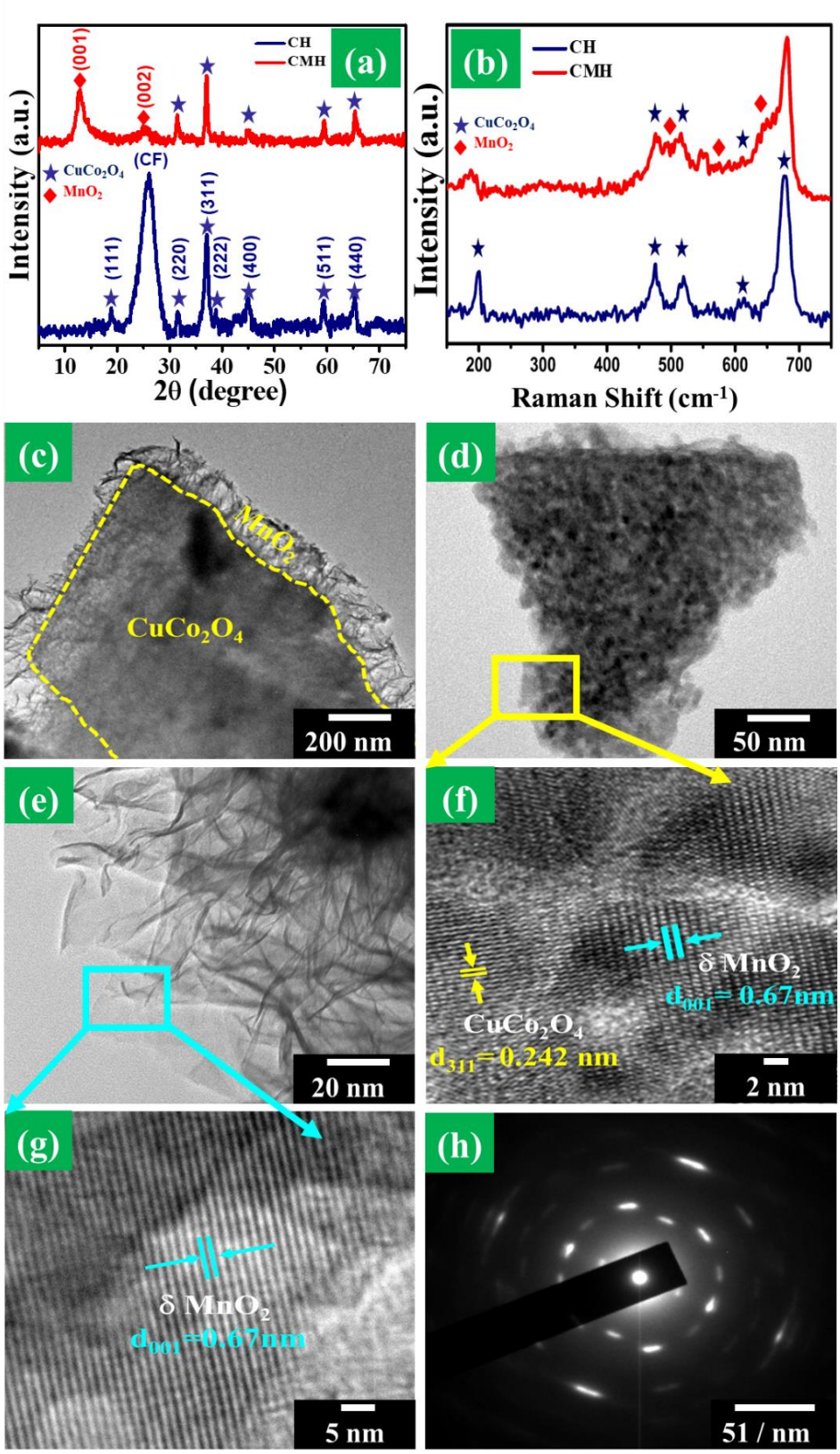

Figure 4.1: (a) XRD, (b) Raman Spectra comparison of the CH and CMH, (c–e) TEM, (f-g) HRTEM images and (h) SAED pattern of CMH sample.

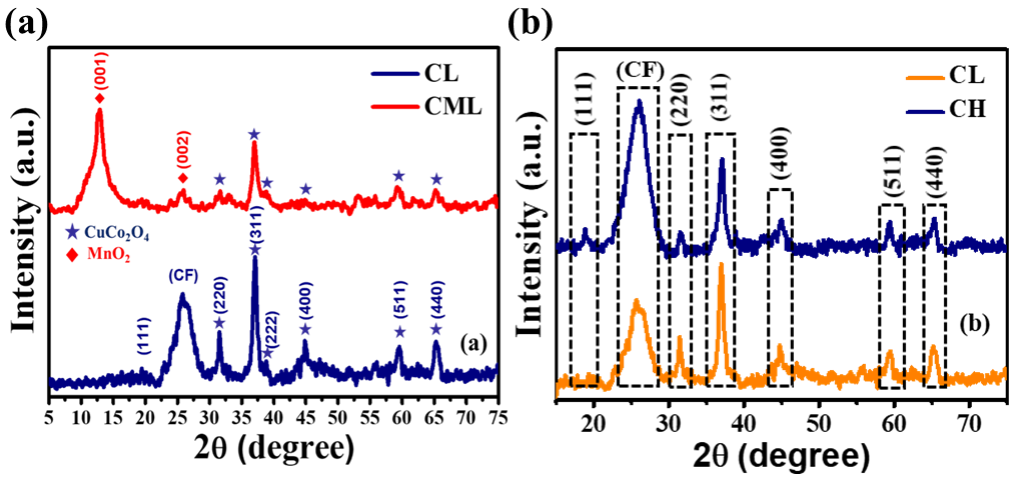

Figure 4.2: (a) XRD patterns for CL and CML sample, (b) XRD peaks under temperature variation for CL and CH sample.

difference in the XRD profile for both CL and CH samples (Figure 4.2b). Non-existence of any peaks related to impurity phases like CuO, CoO, Cu_2O, CoO_2 etc. in pristine samples indicate the formation of pure spinel structure. Broad peak at ~ 26° in spectrum for all the samples appear due to the presence of carbon cloth underneath. Dimension of unit cell of spinel $CuCo_2O_4$ was evaluated considering *d*-spacing of the most intense (311) plane. Assessed value 'a_0' is 8.111 Å which agree well with the literature (a_0= 8.105 Å, JCPDS card No. 37-0878). However, this value is greater than the same of spinel Co_3O_4 (a_0= 8.083 Å, ICDD card No. 42-1462) which suggest that introduction of Cu resulted an increment in the a_0-value. Increment in the a_0-value can be accredited to the increase in unit cell volume by attuning Cu^{2+} ion (having higher radius in comparison to Co^{2+}) in spinel $CuCo_2O_4$. Plausible substitution of Co^{2+} by the Cu^{2+} ion at the octahedral sites in spinel structure leads an increment in a_0-value and thereby total volume of the unit cell [17,34,35]. After the secondary growth over pristine $CuCo_2O_4$ flakes the XRD pattern of CML & CMH shows few additional peaks as compared to CL and CH. Not only additional peaks at ~ 12.4° and ~ 25° appeared in the hybrid samples but also the intensity of peak at ~ 26° is

suppressed to a great extent in hybrids. Both the additional peaks are related with birnessite type δ-MnO_2 (JCPDS No: 80-1098) [36,37].

For further identification of structural features of pristine and hybrid sample Raman analysis was performed. Raman spectra of CH and CMH is presented in Figure 4.1b. Raman spectra of CH reveal peaks at ~ 198, ~ 475, ~ 519, ~ 612, and ~ 677 cm^{-1} which are associated with F_{2g}, E_g, F_{2g}, F_{2g} and A_{1g} mode of vibration of cobalt oxides respectively [38,39]. However, careful observation of these peaks suggested shift by several cm^{-1} as compared to pristine cobalt oxide. Phonon confinement in copper cobaltite resulted in uncertainty in phonon wave vectors and downshift in Raman peak positioning occurred [40]. Few additional peaks appeared in the CMH spectra due to the growth of MnO_2 over CH. Peaks at ~ 498, 575 and 649 cm^{-1} are in well accordance with the vibrational modes of MnO_2 [36,41]. The intense A_{1g} symmetric peak at ~ 677cm^{-1} of the pristine samples gets deformed due to MnO_2 growth and peak becomes asymmetric. Peak intensities also reduced in CMH due to secondary growth over $CuCo_2O_4$.

For transmission electron microscopy (TEM) study, samples were delaminated from carbon fiber by ultrasonication in ethanol and drop-casted on TEM grid. Figure 4.3a and 4.3c shows TEM images of CL and CH flakes which indicate difference in flake size. Magnified view of one flake from Figure 4.3c (yellow marked) is in shown in Figure 4.3d. Transparency of the flakes indicates that these flakes are very thin. This image also reveals particulate nature of flakes as well as porosity within. High resolution TEM image of the selected region of Figure 4.3d (cyan coloured) reveals parallel lattice fringes. Accessed value of lattice spacing is ~ 0.242 nm which corresponds to (311) planes of spinel $CuCo_2O_4$ [38]. Lattice fringes with spacing ~ 0.20 nm related to (400) planes are also visible from

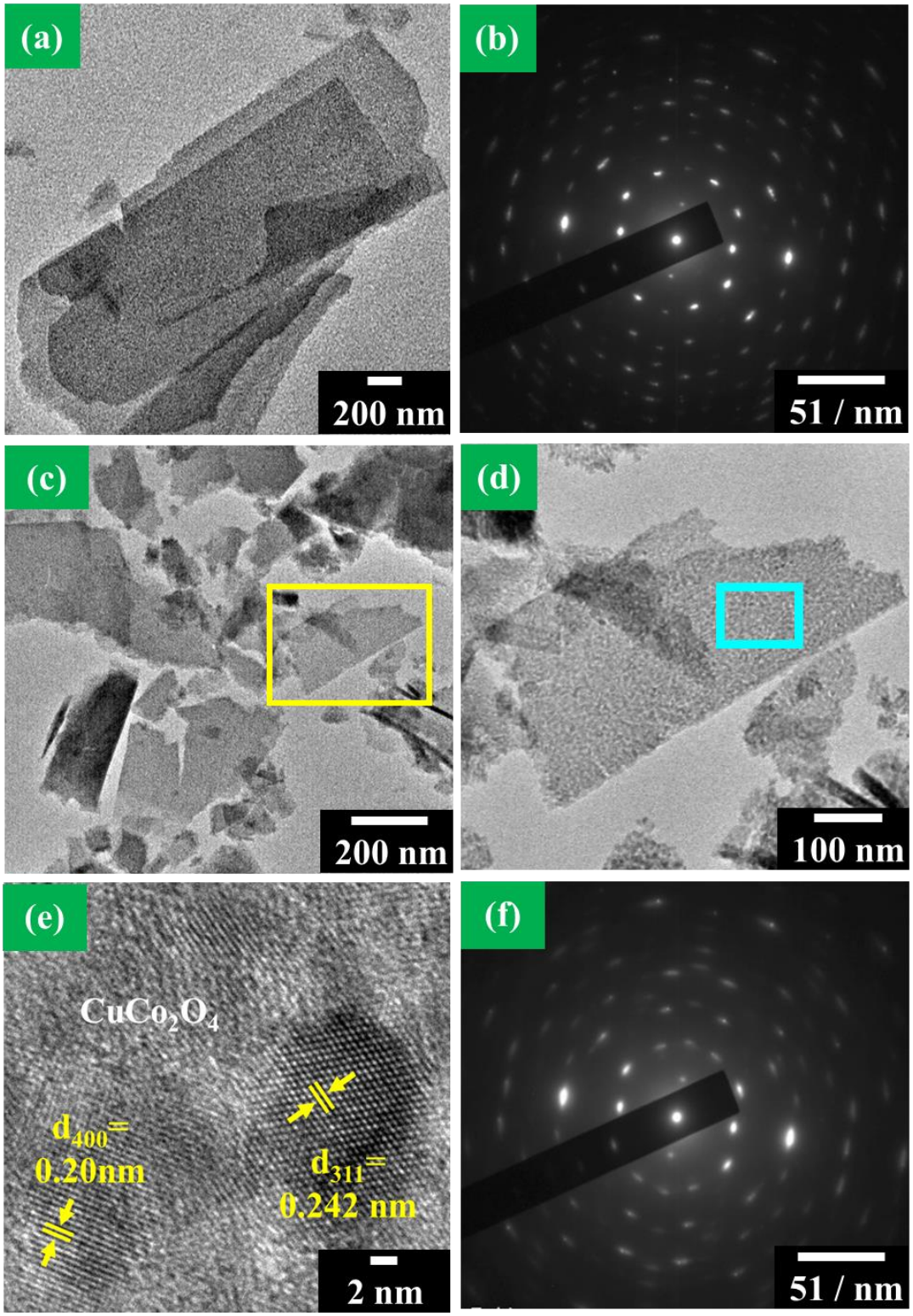

Figure 4.3: (a) TEM images and (b) SAED pattern of CL; (c-d) TEM images of CH at different magnification, (e) HRTEM image and (f) SAED patterns of CH sample.

Figure 4.3e [17]. Selected area diffraction (SAED) pattern measured from CL and CH reveal circular ring pattern with few bright and distinct circular spots which confirms polycrystalline nature of the flakes [Figure 4.3 (b,f)]. Figure 4.1c-d exhibits that $CuCo_2O_4$ flakes are homogenously covered by MnO_2 sheets. Further magnification of the MnO_2 sheet is presented in Figure 4.1e. These sheets are randomly oriented over the $CuCo_2O_4$ flakes and form the outer shell of the heterostructure. HRTEM of marked region in Figure 1(e) discloses inter planner spacing of 0.67 nm, related with (001) plane of MnO_2 (Figure 4.1g) [4,36,42]. HRTEM image the selected area in Figure 4.1d revels the coexistence of the crystal planes (Figure 4.1f) of $CuCo_2O_4$ (311) plane as well as MnO_2 (001) plane [4]. Such results confirm the co-existence of these two oxides. Further SAED pattern on the hybrid exhibits circular spots indicating crystalline $CuCo_2O_4$ overlapped by weak reflection halos coming from the MnO_2 contribution (Figure 4.1h).

Elemental composition of the hybrid was examined using energy dispersive X-ray (EDX) attached with SEM and TEM. EDX spectrum (SEM) of the CMH sample is shown in Figure 4.4a. Peaks associated with C, Cu, Co, O and Mn are obvious from this spectrum. Appearance of the C related peak in the EDX profile is resulted from the underlying carbon cloth substrate. EDX spectra of CMH in Figure 4.5 collected from TEM imitate the EDX resulted from SEM exactly. Mapping of the constituent elements over carbon strand of fiber in Figure 4.4b-g reveal even distribution of Cu, Co, O and Mn.

XPS analysis was executed further to get confirmation of the elemental composition and their corresponding oxidation states. Survey scan profile of the CH and CMH is shown in Figure 4.6. Spectrum corresponding to CH confirms the presence of C, Cu, Co and O whereas the same for CMH indicates additional peak of Mn in it. These results corroborate well with the XRD, Raman and EDX analysis. Cu 2p spectrum in Figure 4.7a, reveals two

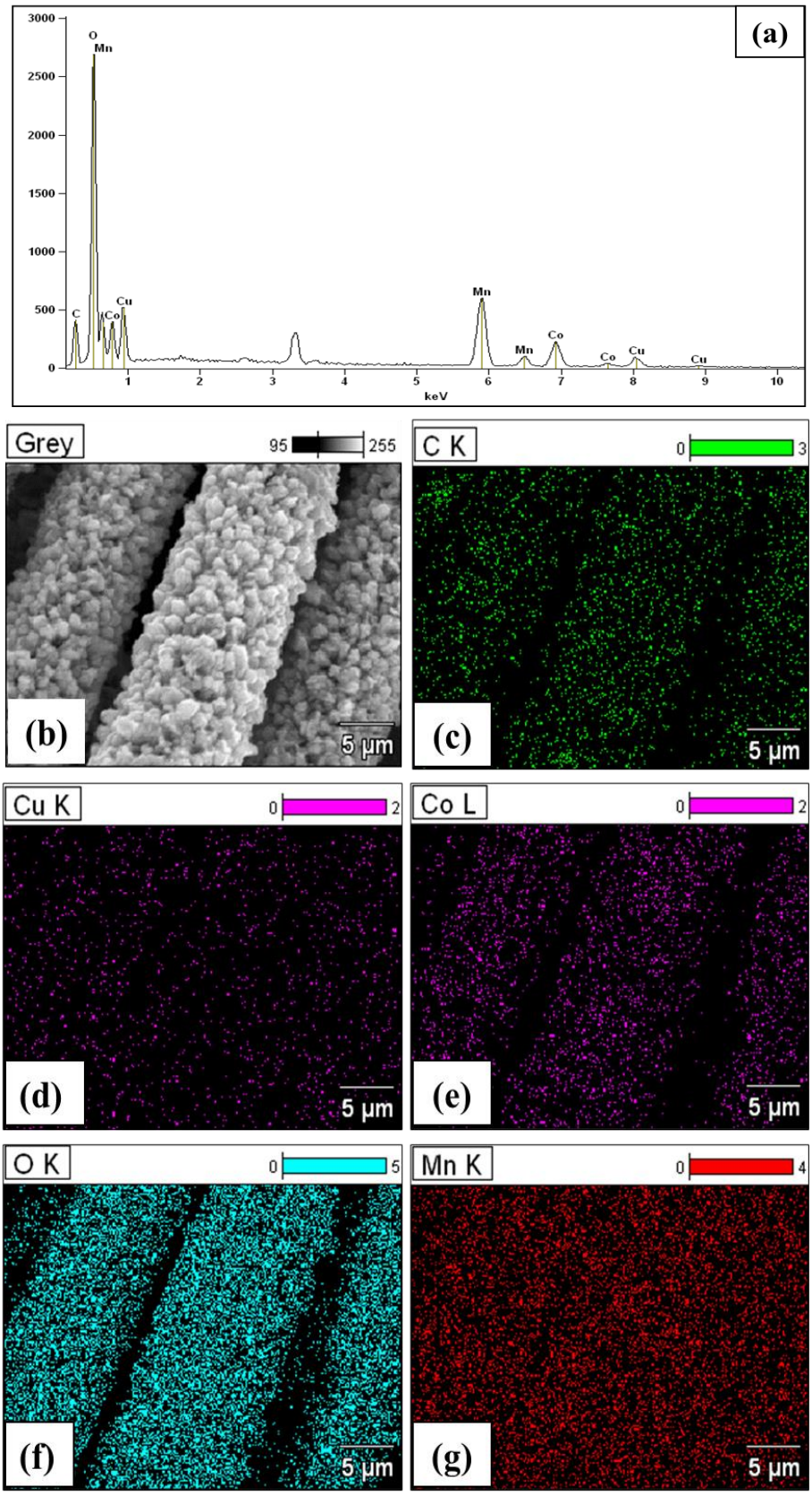

Figure 4.4: (a) EDX Spectrum, (b-g) corresponding FESEM and elemental mapping of CMH.

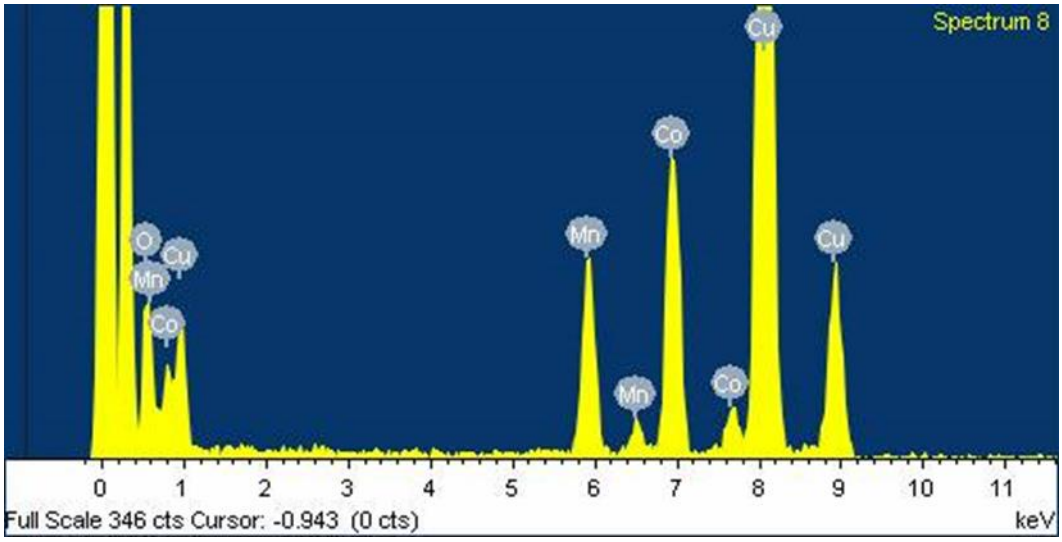

Figure 4.5: EDX Spectra for CMH (TEM Characterization).

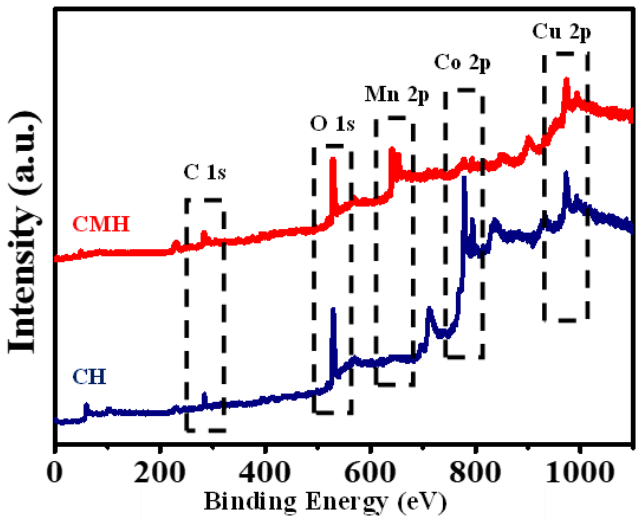

Figure 4.6: XPS survey scans of CH and CMH.

components namely Cu $2p_{3/2}$ and Cu $2p_{1/2}$ at binding energies 934.3 and 954.5 eV respectively. Two additional satellite peaks also observed at 942.2 and 962.5 eV. Such positioning of the peaks ensures 2+ electronic state for Cu [35,43]. Fitted Co spectrum in Figure 4.7b discloses Co $2p_{3/2}$ and Co $2p_{1/2}$ peaks at 780.0 and 795.1 eV respectively. Spin-energy separation between these two peaks ~ 15 eV indicates the presence of mix oxidation states of Co^{2+} and Co^{3+} [35,43,44]. As fitted resolved peaks at binding energies 779.8 and

794.9 eV belongs to Co^{3+}, whereas other two peaks ~783.3 and 796.3 eV signifies Co^{2+} [35]. Asymmetric O 1s spectrum can be resolved into three components (Figure 4.7c). O1 component appeared at 529.7 is related to the metal-oxygen bonds (i.e., bonding of oxygen with copper and cobalt) [23,44]. The O2 component at ~531.2 corresponds to the defect constitution with low oxygen coordination. Less intense O3 component at ~532.6 eV is due to the presence of physiosorbed and chemically bonded water on the nanoform surface [23]. Further, the profile related to Mn is also fitted. This profile reveals the presence (Figure 4.7d) of two peaks appeared at ~641.8 and ~653.6 eV correspond to Mn^{2+} and Mn^{3+} ions respectively [45,46]. Separation of 11.8 eV between these two peaks are also agrees well with previous report [45].

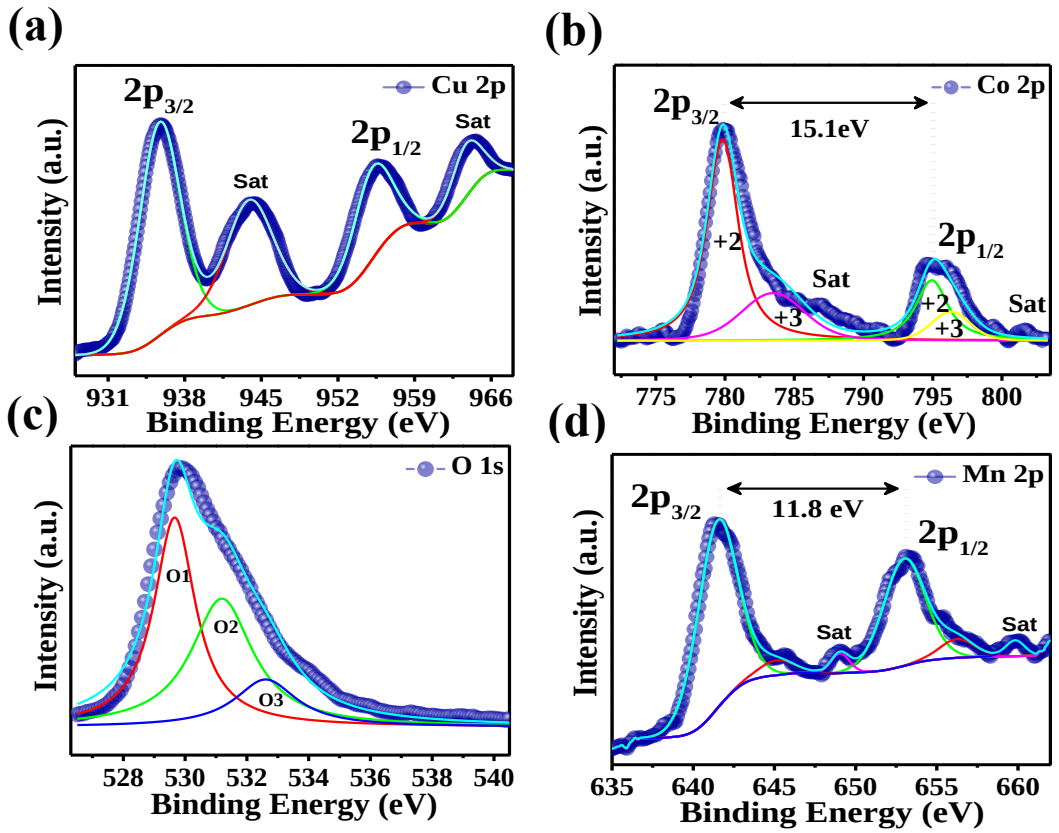

Figure 4.7: XPS spectra of (a) Cu 2p, (b) Co 2p, (c) O 1s and (d) Mn 2p for CMH.

FESEM images of all the synthesized samples are presented in Figure 4.8. Figure 4.8a-c depicts the morphology of CL sample at different magnifications. 2D flakes was found to grow on carbon fiber with a uniformity over the entire cylindrical surface of carbon fiber. These flakes are typically large in length and packed with each other. FESEM image of CH sample is shown in Figure 4.8g-i. Careful comparison of these FSEM images suggest difference in their dimension which is already confirmed in TEM characterisation. Further,

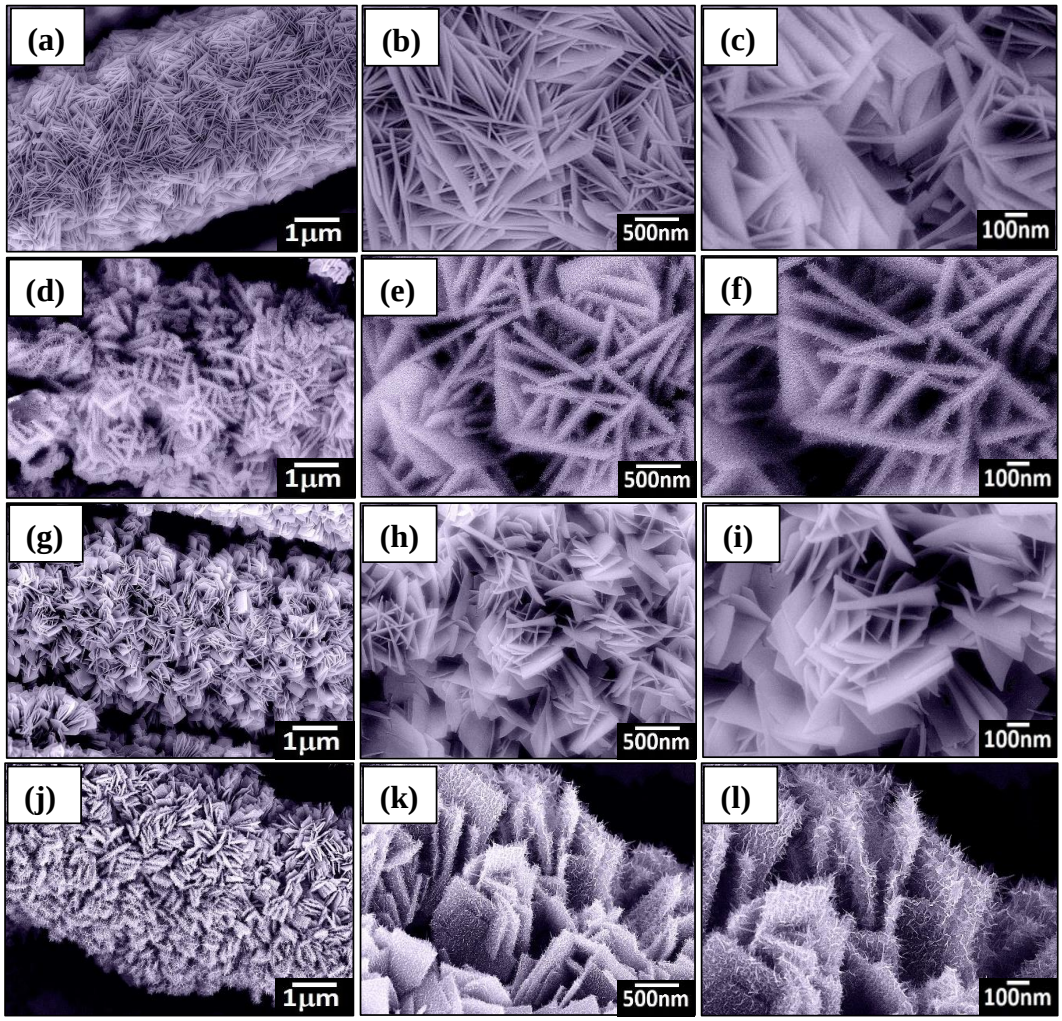

Figure 4.8: FESEM of CL(a–c) CML(d–f) CH(g–i) and CMH (j–l) at different magnifications.

Figure 4.8d-f and 4.8j-l exhibit FESEM morphology of CML and CMH. Underlying $CuCo_2O_4$ nano-flakes becomes almost invisible with the complete concealment of porous MnO_2 nanostructures over them. MnO_2 sheets are so densely interconnected that the edge of the flakes looks like caterpillar in the magnified view. Although the MnO_2 coverage over these nanoflakes is same in the hybrid, however the variances in the dimension of underlying nanoflakes resulted differences in the surface area of hybrids. This surface area differences of the nanoforms have profound impact on electrochemical performances. A plausible explanation behind such kind of nanoform growth is presented in the supporting information.

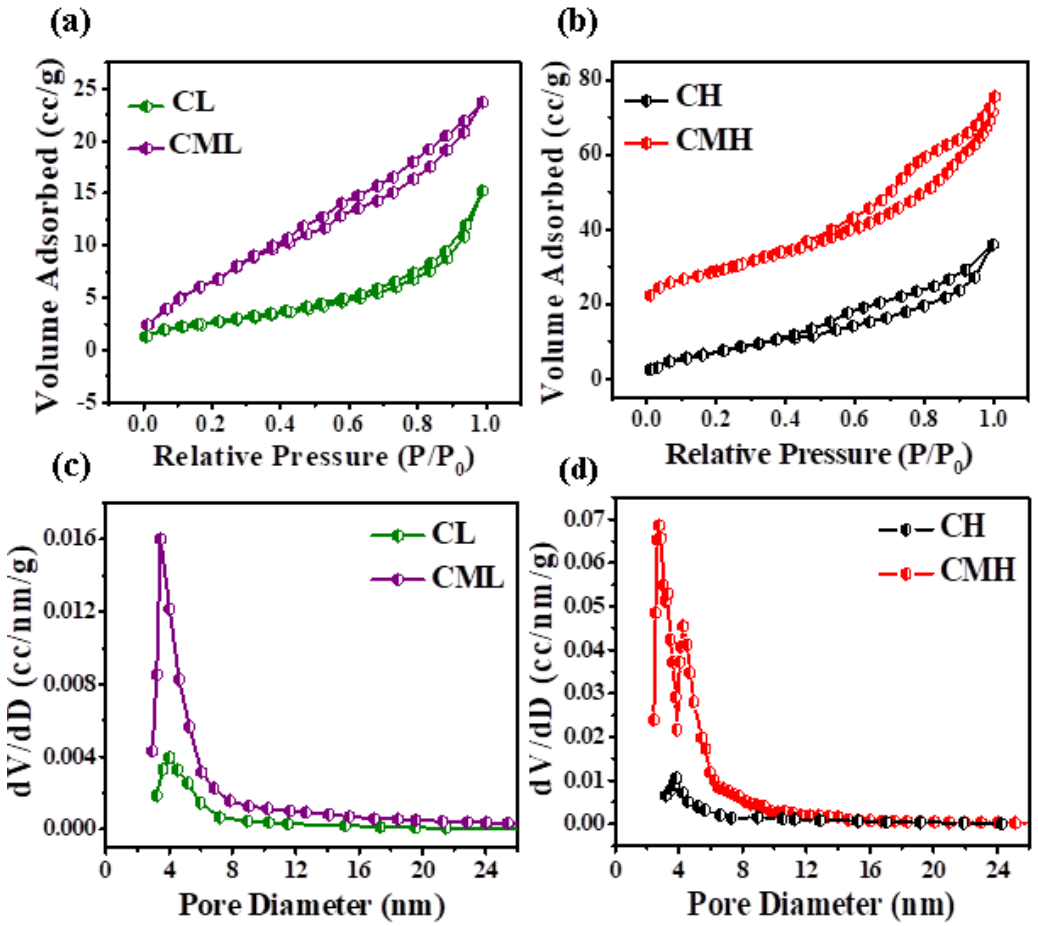

Figure 4.9: N_2 adsorption–desorption isotherms of (a) CL and CML and (b) CH and CMH, BJH Pore size distribution of (c) CL and CML and (d) CH and CMH.

Sample	Specific surface area ($m^2 g^{-1}$)	Pore diameter (nm)	Pore Volume (cc g^{-1})
CL	11.63	4.0	0.016
CH	30.53	3.8	0.031
CML	32.04	3.4	0.049
CMH	111.6	2.7	0.105

Table 4.1: BET parameters of the synthesized samples.

Electrochemical activity of the nanoforms largely depend on the surface area and porosity of nanoform. Brunauer-Emmett-Teller (BET) surface area and porosity of all samples were measured through Nitrogen adsorption-desorption at 77 K (Figure 4.9a-b). BET specific surface area of CL and CH is found to be only 11.63 and 30.53 m^2/g respectively. After MnO_2 growth, surface area increases. For CML and CMH, surface area values increased to 32.04 and 111.6 m^2/g respectively. A comparative table on BET measurement results for all the synthesized nanoforms is described in Table 4.1. According to the IUPAC standard classification all the samples followed type-IV nature at high relative pressure in between 0.4 and 1 resulted in H3 hysteresis loop which indicated the presence of mesopores (2 nm < pore size < 50 nm) [47]. Pore size distributions of the samples exhibited gradual decrease in pore diameters upon hybrid formation. At the same time, overall pore volumes increase. CMH sample showed maximum pore volume and lowest pore diameter among all the synthesised samples (Figure 4.9c-d).

CV and GCD analysis were performed to determine the electrochemical behaviour of the all samples in three-electrode configuration. 1 M aqueous KOH solution was used as electrolyte in all CV and GCD measurements. CV plots of all the samples are presented in Figure 4.10a at 2 mV s^{-1}. Integral area under the CV curves for CMH and CML electrodes are much greater in comparison to pristine electrodes CH and CL indicating superior

capacitive behaviour. Figure 4.10a also reveals highest specific capacitance of CMH among all. In addition to integral area, high currents for hybrid electrodes are also prominent from this Figure. This may be accredited to MnO_2 sheets decoration over $CuCo_2O_4$ flakes. CV curves for CMH electrode registered at different scan rates ranging from 2 s to 20 mV s^{-1} within same potential window in Figure 4.10b. Similar experiments are also performed for other electrodes and the results are shown in Figure 4.11a-c. With increase in scan rate, current increases thoroughly for all samples and CV curves nearly resembles each other at all scan rates indicating good reversibility. Charge storage procedure consists of two mechanisms namely faradaic and non-faradaic process. A faradaic process is governed by oxidation-reduction and involves inter-conversion of oxidation states of metal ions (Cu, Co, Mn) combining K^+ ion intercalation/deintercalation process. Redox reactions at the electrolyte-electrode interfaces involving $Co^{2+}/Co^{3+}/Co^{4+}$, Cu^{+}/Cu^{2+} and Mn^{3+}/Mn^{4+} redox couples is stated below [33]:

$$CuCo_2O_4 + H_2O + e^- \leftrightarrow 2\ CoOOH + CuOH \quad (4.1)$$

$$CoOOH + OH^- \leftrightarrow CoO_2 + H_2O + e^- \quad (4.2)$$

$$CuOH + OH^- \leftrightarrow Cu(OH)_2 + e^- \quad (4.3)$$

$$MnO_2 + K^+ + e^- \leftrightarrow MnOOK \quad (4.4)$$

On the other hand, in a non-faradaic process, charges distributed over the electrode surfaces hardly involve in making and breaking of chemical bonds. Integral area under each CV curve is a measure of total charges stored by the faradaic and non-faradaic contribution. Ion intercalation together with redox capacitance give rise to faradaic contribution whereas non-faradaic process has its origin in double layer capacitance. Specific capacitance (C_S) of the electrodes were evaluated from the CV curves using the following equation:

$$C_S = \frac{1}{m \times \upsilon \times \Delta V} \int_{V_1}^{V_2} IdV \tag{4.5}$$

where, $\int_{V_1}^{V_2} IdV$ symbolizes area under CV curve, υ denotes scan rate. m and ΔV denote mass of the working electrode and the working potential window respectively. Variation in the C_S values with respect to scan rate for all the samples is plotted in Figure 4.10c. Among all, CMH displayed the maximum C_S values at all the scan rates and indicated superior

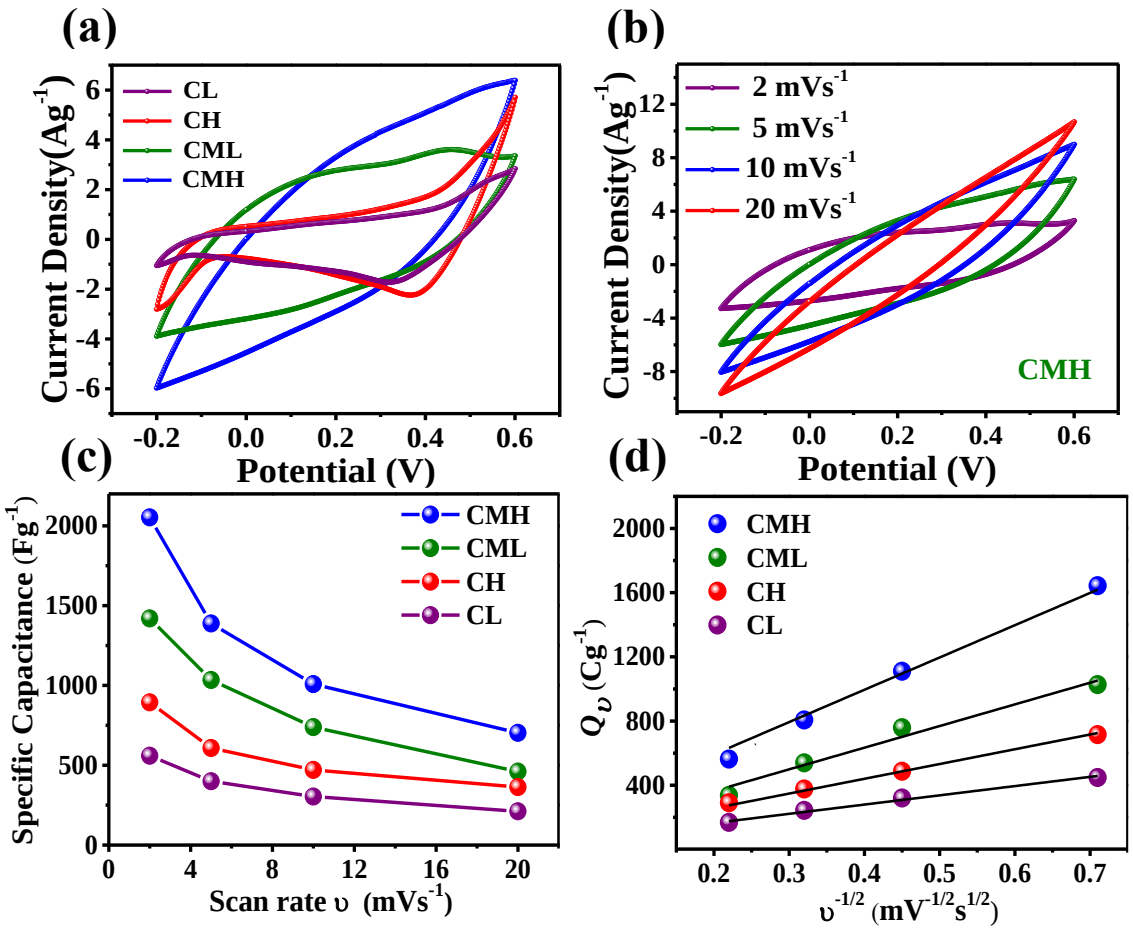

Figure 4.10: CV profile of (a) all samples at scan rate of 2 mV/s (b) CMH electrode at different scan rates. (c) Specific capacitance variation with scan rate, (d) Q_υ vs. $\upsilon^{-1/2}$ plot for all samples.

charge storage capacity than others. With the increase in scan rates values of C_S fall gradually. At low scan rate, electrodes provide greater access to its inner surface to the electrolyte for diffusion induced redox faradaic reaction whereas at higher scan rate inner surface contribution decreases and outer surface bound non-faradaic process dominates. Faradaic and non-faradaic effects can be further explained by plotting log (current density) as function of log (scan rate) using the power law; $i = a\upsilon^b$. Here, υ is scan rate. 'a' and 'b' are two adjusted parameters. Value of 'b' can be evaluated from the slope of the aforesaid plot. When the charge storage mechanism is purely capacitive, value of "b" becomes 1. For semi-infinite diffusion induced redox reaction, the value of same becomes 0.5. At higher scan rate, the capacitive charging mechanism dominates whereas the diffusion induced charge storage process becomes more prominent at lower scan rate. The storage process consists of diffusion induced redox process and surface capacitive charge

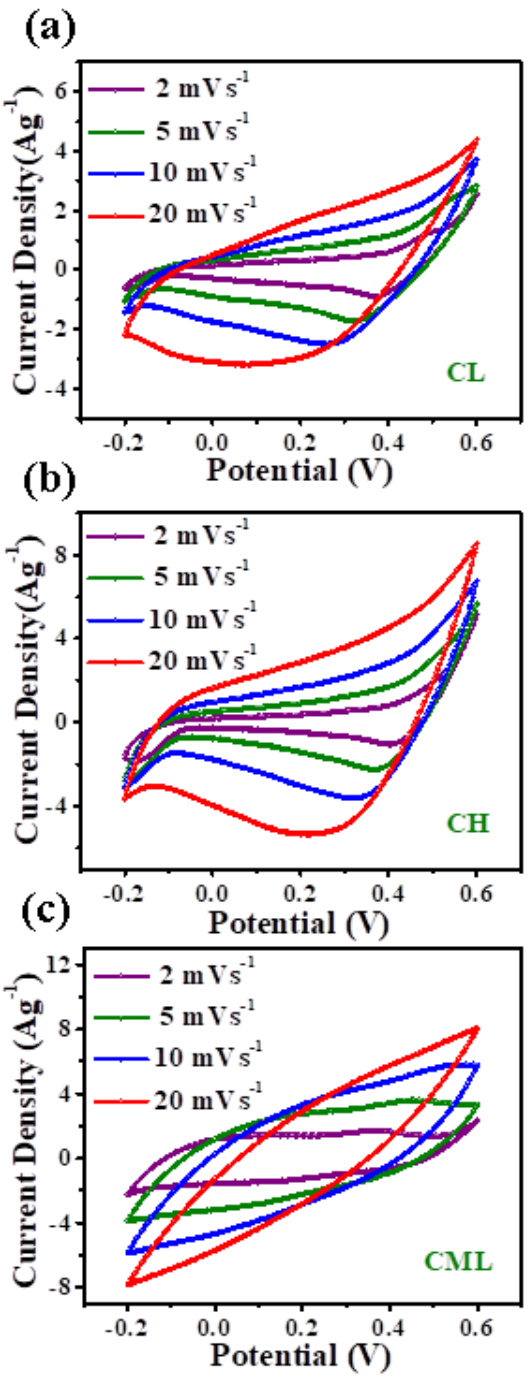

Figure 4.11: CV profiles of (a) CL (b) CH and (c) CML electrodes at different scan rates.

storage for semi-infinite diffusion. Overall charge stored in an electrode can be written as: $Q_\upsilon = Q^S_{Outer} + Q^D_{Inner}$ where, Q^S_{Outer} is the charge due to the outer surface electron transfer and electrochemical double layer charges. Q^D_{Inner} is the charge due to K^+ ion diffusion and intercalation. Thus, for semi-infinite linear diffusion process the above equation can be modified as $Q_\upsilon = Q^S_{Outer} + K.(\upsilon^{-0.5})$ [48], K being arbitrary constant. Value of Q^S_{Outer} can be determined from y intercept of the linearly fitted plot of Q_υ against $\upsilon^{-0.5}$ at different scan rate (Figure 4.10d). Surface capacitive non-faradaic charge storage ability gradually increases from pristine to hybrid samples which may accounted for integration of MnO_2 sheets over $CuCo_2O_4$. Again, the faradaic charge storage is found greater in CH compare to CL electrode. Figure 4.12 demonstrate the Q^D_{Inner} and Q^S_{Outer} charge contribution for CMH and CH. Q^S_{Outer} charge stored in CMH and CH electrode remains constant at all scan rates but in lower scan rates the diffusion induced redox mechanism dominates. Hence, Q^D_{Inner} charge contribution is much larger than Q^S_{Outer} at lower scan rate. In both cases, diffusion induced redox activity gradually decreases at higher scan rates and hence Q^S_{Outer} becomes more dominant.

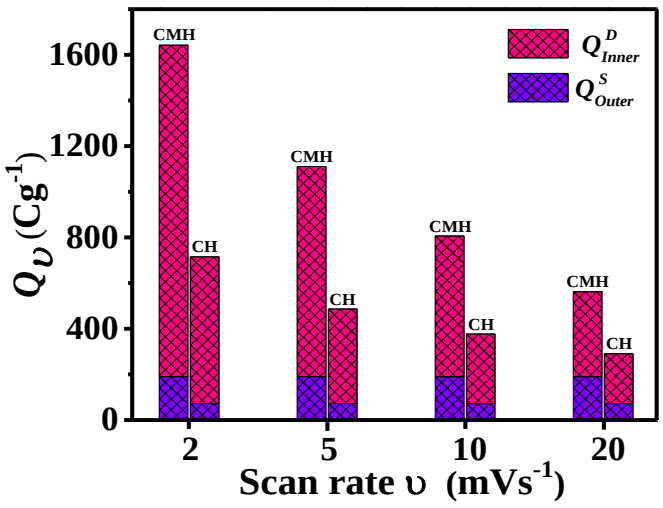

Figure 4.12: Faradaic and non-faradaic charge contribution for CMH and CH electrode.

GCD profiles of all four electrodes at 0.5 A/g presented in Figure 4.13a indicate greater discharging time for hybrids than the pristine samples. C_S values were calculated from these profiles using the relation

$$C_S = \frac{I\Delta t}{m\Delta V} \tag{4.6}$$

where, I and Δt designates discharging current and time respectively. ΔV and m denote potential window of discharge and mass of electrodes respectively. Value of C_S of CMH is

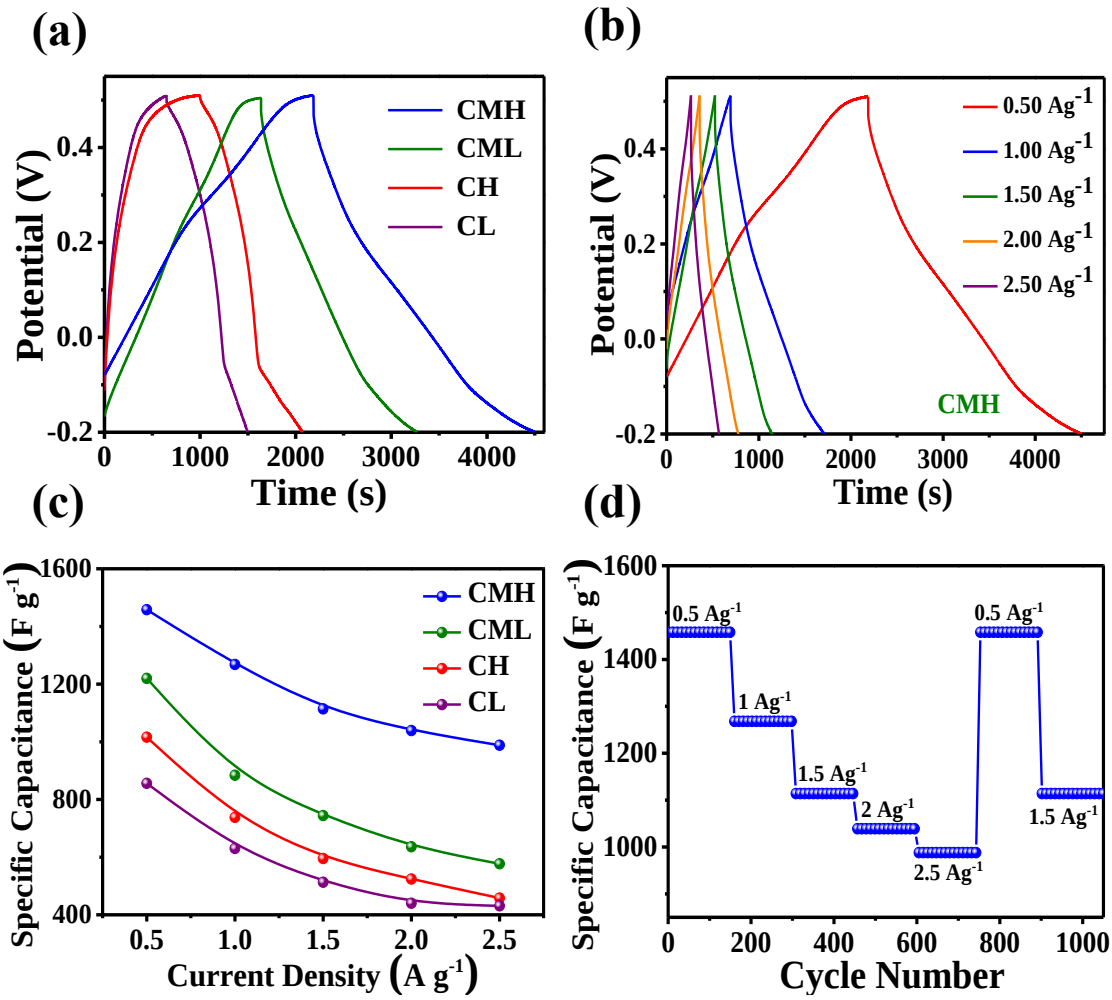

Figure 4.13: GCD curves of (a) all samples at a 0.5 A/g (b) CMH at different current densities (c) specific capacitance variation with current density for all samples, (d) cyclic stability of CMH electrode with gradual variation of current density.

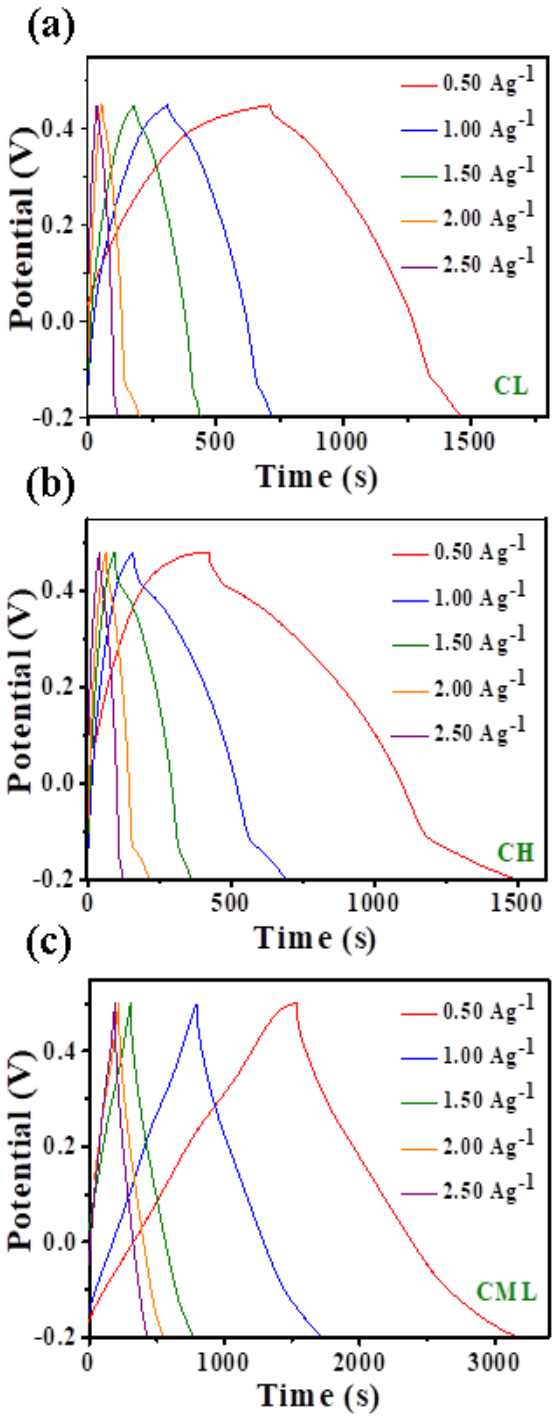

Figure 4.14: GCD profiles of (a) CL (b) CH and (c) CML electrodes at different current densities.

~ 1458 F/g at 0.5 A/g as calculated from GCD curves in Figure 4.13a. This is almost two-fold higher than the CL sample at same current density. Much superior specific capacitance offered by CMH is attributed to its high porosity and large surface area. Discharging time for the hybrid electrodes are also found to greater than that of the pristine electrodes. CMH electrode showed the highest discharging time. GCD curves of CMH electrode monitored at different current densities is shown in Figure 4.13b. Similar kind current densities dependent GCD profiles for other samples are shown in Figure 4.14a-c. Careful observation of these curves suggests two different kinds of discharging profile. Both CL and CH samples unveiled non-linear discharging profiles (battery-type capacitance) and signifies pseudocapacitive nature, i.e., faradaic reactions are more dominating. On the contrary, CML & CMH exhibited discharging profiles with more pronounced linearity, signifying capacitive dominance with underlying diffusion-controlled process within the inner bulk of the active materials.

Furthermore, in all samples, the charging and discharging curve mimics each other. Such symmetry indicates good reversibility of the charging and discharging reaction.

Variation in C_S values with respect to selective current densities for all samples is shown in Figure 4.13c. Increment in the current densities gradually decreased the capacitances values of all the electrodes. Low active material utilization at higher current densities as well as sluggish reaction kinetics of the redox couples resulted such decrement in capacitance values. Aforesaid variation is more visible for the hybrid samples compared to the pristine samples. With sudden change in current density, CMH also sustained its cyclic stability (Figure 4.13d). CMH electrode recovered its initial capacitance completely even after 750 cycles at different current densities. This typical

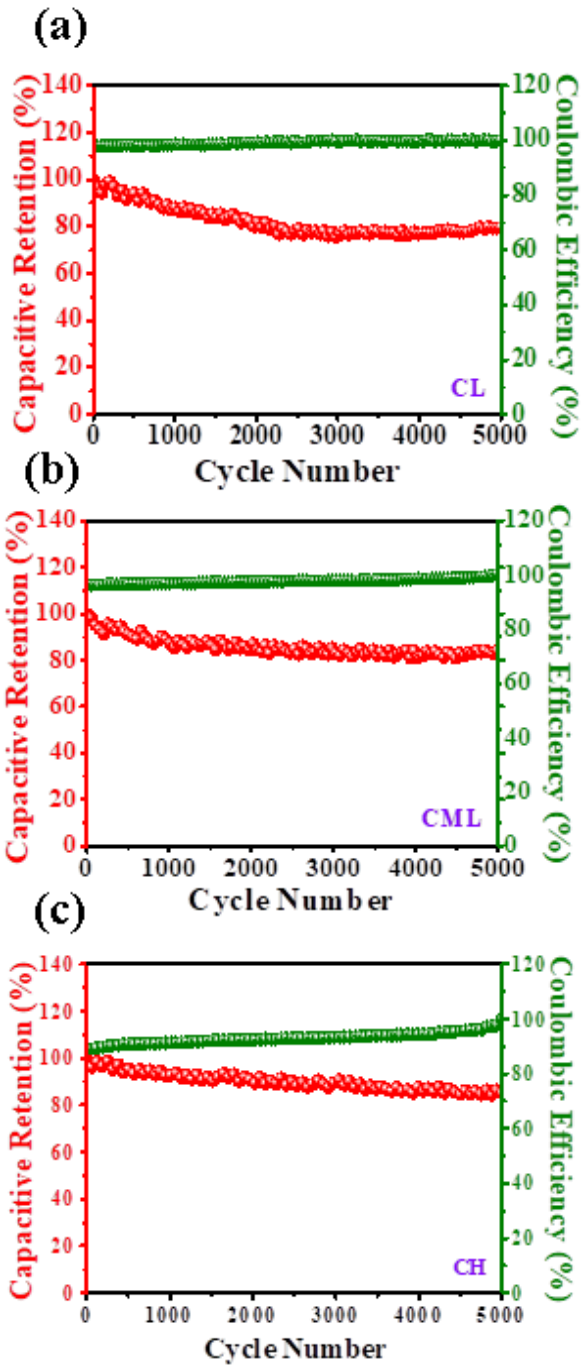

Figure 4.15: Capacitive Retention & Coulombic efficiency of (a) CL, (b) CML and (c) CH.

hierarchical nanostructures with porosity in it shorten the diffusion distance from electrolyte to the interior of surface of electrode. Such long-term stability indicates its

perspective in industrial applications. To check cyclic stability and capacitive retentivity, GCD curves for all the samples were recorded for continuous 5000 cycles at 20 A/g. Pristine samples CL and CH retained 80% and 86% of its initial capacitance (Figure 4.15a, c) whereas the capacitive retention registered from CML and CMH is ~ 84% and 93% (Figure 4.15b and Figure 4.16a). Coulombic efficiency, defined as the ratio of discharging time to charging time for each cycle of GCD was also measured. All the samples showed nearly 100 % coulombic efficiency throughout the 5000 cycles indicating high reversibility of the electrodes. Benefited by the structural stability due to the direct growth of nanoforms

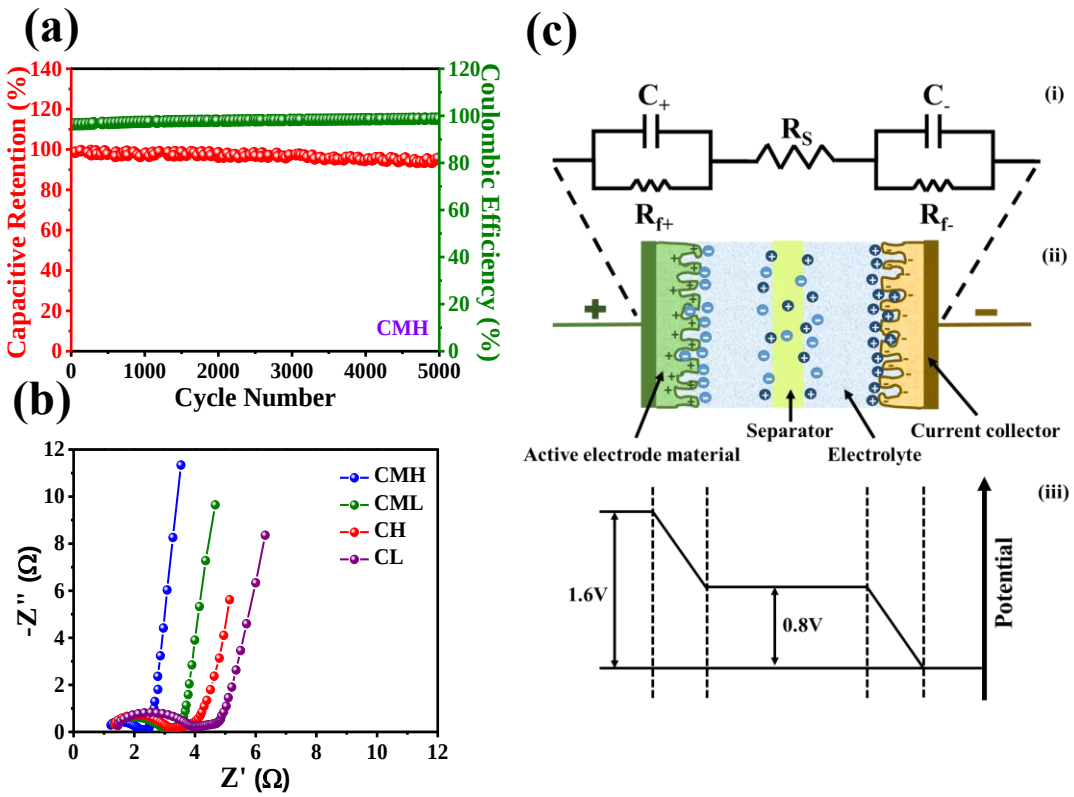

Figure 4.16: (a) Retention capacity & Coulombic efficiency of CMH (b) EIS spectra of all electrodes (c) (i) Equivalent R-C circuit representation (ii) basic operation (iii) Potential window of two-electrode SSFC device.

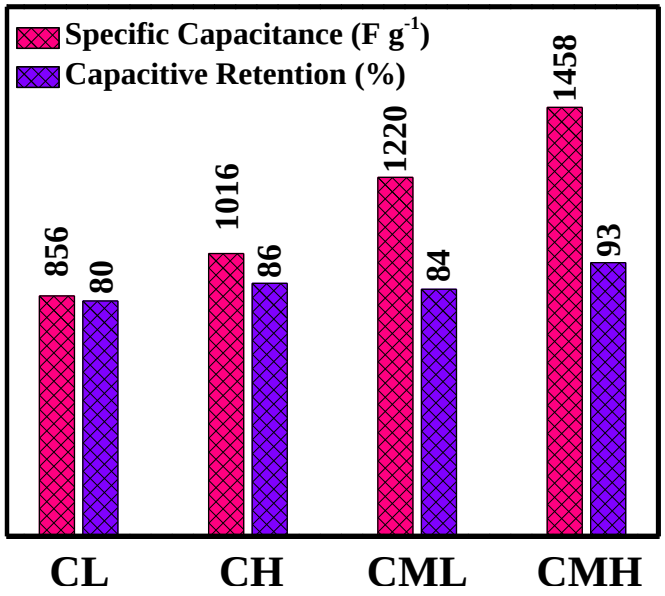

Figure 4.17: Electrochemical performance comparison of all the electrodes.

Morphology/Composition	SC @ Current Density	Cell Configuration	Electrolyte	Cycles, Retention	Reference
$CuCo_2O_4$ nanowire@$NiCo_2O_4$	2.6 F/cm^2 @ 10 mA/cm^2	3E	3M KOH	4500, 80%	[60]
Porous $CuCo_2O_4$ Architectures	466.4 C/g, 2 A/g	3E	2M KOH	5000, 86.3%	[61]
Cedar leaf-like $CuCo_2O_4$	1223 F/g @ 1.08 A/g	3E	2M KOH	5000, 83.5%	[57]
$CuCo_2O_4$ Octahedrons	520 F/g @ 2 A/g	3E	6M KOH	5000, 83%	[62]
Vertically stacked $CuCo_2O_4$	975 F/g @ 0.5 A/g	3E	2M KOH	5000, 76.6%	[63]
$CuCo_2O_4$@$MnCo_2O_4$	1434 F/g @ 0.5 A/g	3E	2M KOH	5000, 81.4%	[63]
CH	961 F/g @ 0.5 A/g	3E	1M KOH	5000, 86%	This work
CMH	1458 F/g @ 0.5 A/g	3E	1M KOH	5000, 93%	This work

Table 4.2: Specific Capacitance and Cycle Retentivity comparison of $CuCo_2O_4$ based system.

over carbon fiber, these electrodes endure long charging discharging cycles. For facile comparison, electrochemical performance of all the electrodes is compared in the Figure 4.17. To judge the figure of merit of this CMH electrode its cyclic retention was compared with the previously reported $CuCo_2O_4$ based system in Table 4.2. This table clearly

signifies excellent electrochemical stability of our sample, which is comparable to/greater than other reported $CuCo_2O_4$ based materials.

EIS analysis was performed to gain more insights about different electrochemical features. Total impedance Z (ω) is the sum of real (Z′) and imaginary (Z″) component. A plot of imaginary component vs. real one is known as Nyquist plot. In this plot, each point corresponds to an impedance at a particular frequency. The impedance of a supercapacitor has the properties dangling between a pure capacitor and a pure resistor. Nyquist plot thus consists of impedance values coming from three regions of frequencies. An electrochemical system acts as pure resistor and pure capacitor at high and low-frequencies respectively because impedance is inversely proportional to frequency results in zero and high impedance for a capacitor. The intermediate-frequency region mainly corresponds to diffusion-controlled zone i.e., diffusion of the K^+ ion from electrolyte to nanostructured interface of the electrode. Nyquist plot for all the electrodes within the frequency window 100 kHz to 0.01 Hz with an a.c. perturbation of 10 mV is shown in Figure 4.16b. These plots provide equivalent series resistance (R_{ESR}) in high frequency region which consists of electrolyte resistance, contact resistance between current collector and active material as well as the intrinsic resistance of the electrode material. The intercept of this plot along Z′-axis represents the value of R_{ESR} which is relatively high for pristine samples and low for hybrids indicating higher conductivity. In high frequency region, a semicircle is observed (Figure 4.16b). Diameter of the aforementioned on Z′ axis denotes the value of charge transfer resistance (R_{ct}) at interface. R_{ct} value for CMH is 1.01 Ω whereas the same for CH is 1.9 Ω. In low-frequency region, all these curves show linear nature. Slope of the curves in this region is related to the diffusive resistance, also coined as Warburg resistance caused

by a semi-infinite diffusion of K^+ ion in the electrode. The slope of CMH is much sharper as compare to others which suggests nominal Warburg resistance than the rest [49].

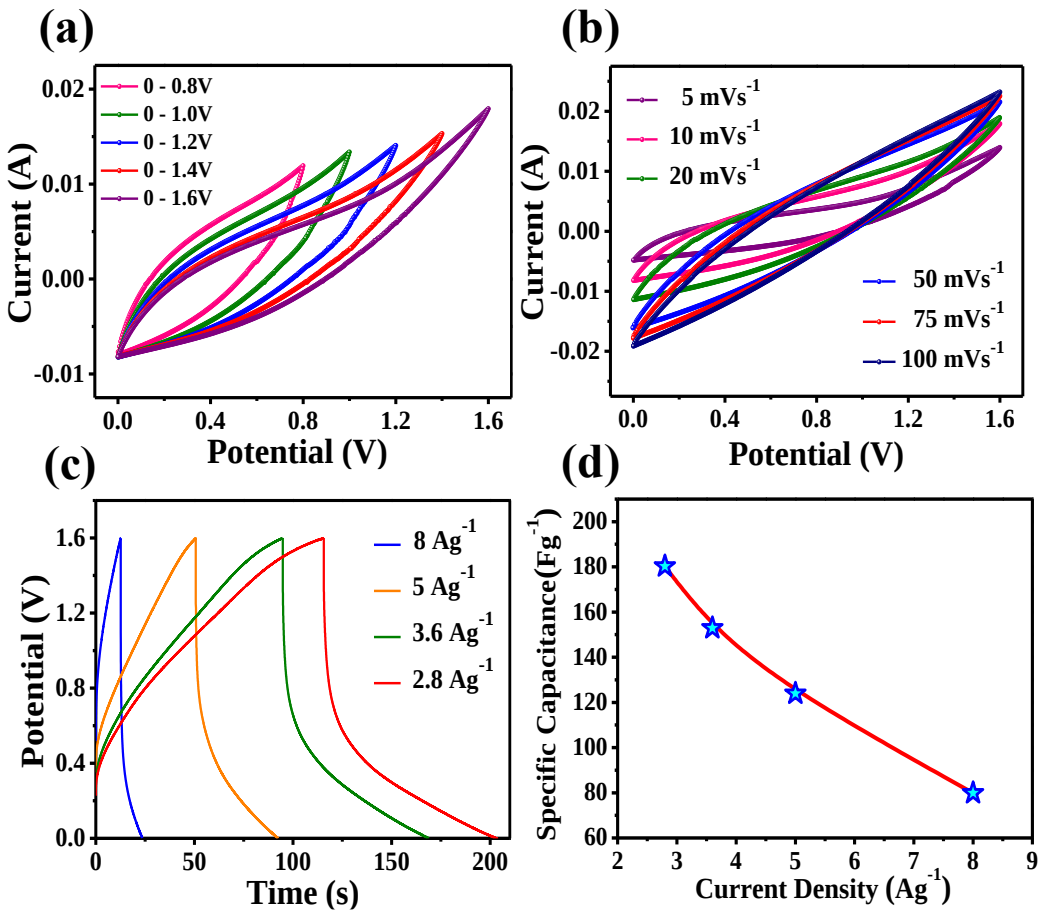

Figure 4.18: CV curves (a) at different potential windows and (b) at different scan rates, (c) GCD profiles at different current densities, (d) specific capacitance vs. current density plot of a single device.

Solid-state devices have several benefits like scalable, compact, safe, easy to handle and etc. over the conventional liquid based SCs. Using two CMH electrodes, polymer gel and a filter paper a symmetric solid-state flexible supercapacitor (SSFC) device was fabricated. Filter paper in this device act as separator. In two-electrode configuration, all device characterises was monitored. Figure 4.16c(i) shows equivalent resistance capacitance (R-C) circuit model of SSFC. All the device characteristics in this work were

investigated in a two-electrode configuration. Device operation mechanism is schematically shown in Figure 4.16c(ii). Specific capacitance of the device (C_{Device}), was evaluated. Specific capacitance of a single electrode (C_S) was usually evaluated from the CV/GCD profiles considering three-electrode measurement which involve reference and counter electrodes. Thus, device specific capacitance C_{Device} value found to be much lower than C_S value. In general, C_{Device} and C_S are connected by the relation $C_{Device} = C_S/4$ [9].

To investigate the SSFC device performance CV measurement was carried out at different potential window at 10 mV/s and the results are presented in Figure 4.18a. Selection of the potential window of 0-1.6 V for the device characterisations is determined by the fact that two CMH electrodes were glued in single device. The potential window of a single electrode (0.8 V) is just doubled (1.6 V) for two electrodes pasted together, depicted in Figure 4.16c(iii). All the CV plots in this Figure 4.18a sustained their characteristic shape within potential range. CV analysis of device was further performed by varying the scan rate (Figure 4.18b). Noticeably, all the CV curves maintained their shapes even in higher scan rate. These CV profiles hardly showed any noticeable redox peak and exhibited almost similar quasi-rectangular nature. Such results confirm the contribution both from faradaic and non-faradaic reactions, however, the latter one dominates. GCD measurement of the SSFC was further carried out by changing the current densities at fixed potential range 0-1.6 V (Figure 4.18c). Gravimetric capacitance values for the as fabricated SSFC device are found to be 181.3, 152.9, 123.9 and 79.85 F/g at 2.8, 3.6, 5 and 8 A/g respectively. With the variation in current densities, capacitance values mimicked the similar behaviour as observed in three-electrode measurement (Figure 4.18d). For practical application, cyclic stability of the device is a very crucial. Device lifetime was further examined for 5000 cycles at 24 A/g inside the same potential window [Figure 4.19a]. As fabricated device was

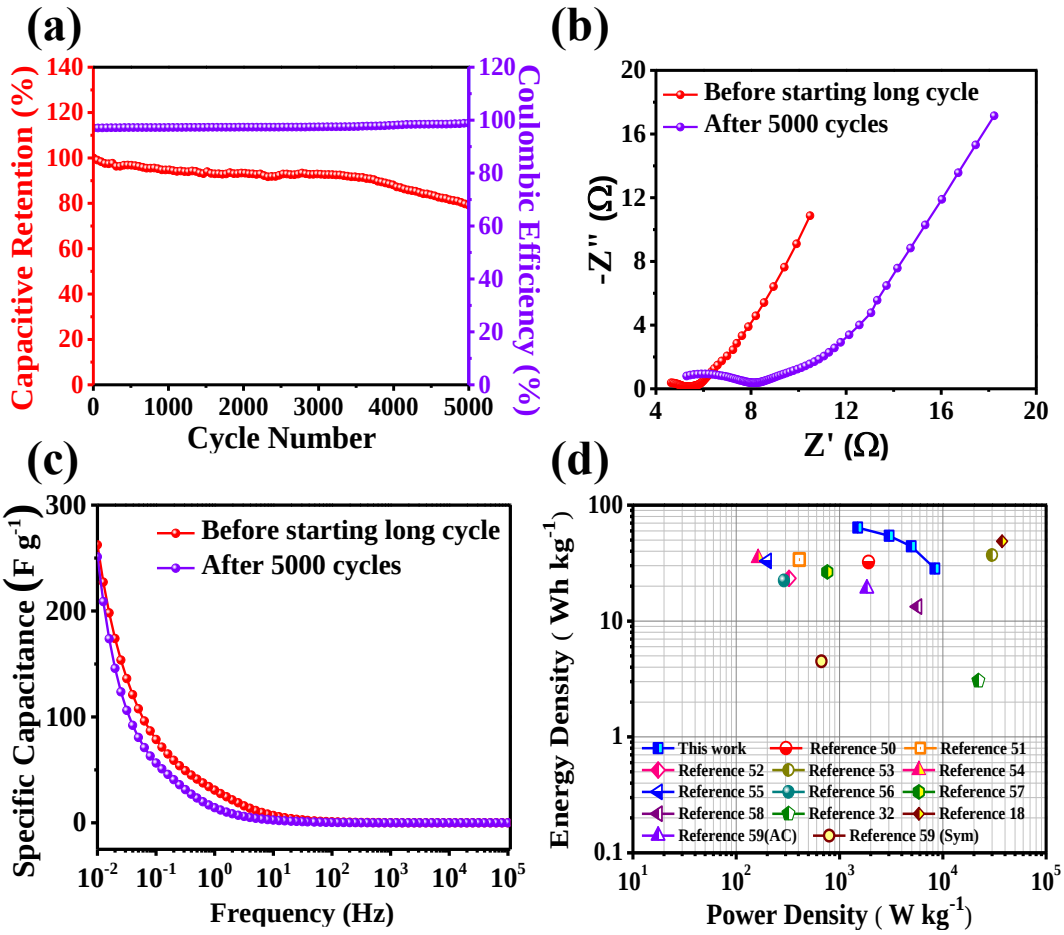

Figure 4.19: (a) Retention capacity & Coulombic efficiency of SSFC device, (b) Electrochemical impedance spectra and (c) Specific capacitance vs. frequency plot of SSFC device before and after long cycle run, (d) Ragone plot SSFC device.

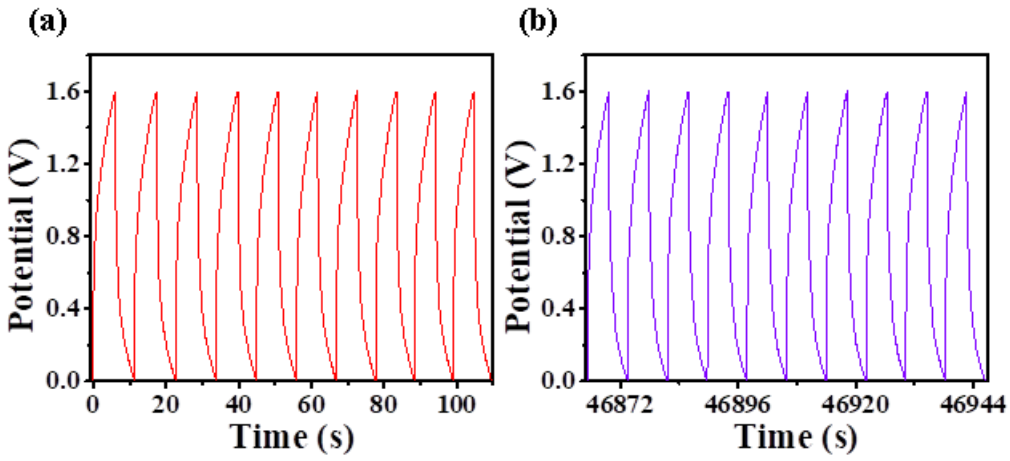

Figure 4.20: (a) First and (b) last 10 cycles of GCD curves of SSFC device.

found to retain almost 80 % of its initial capacitance value at end of 5000 cycles scan. Coulombic efficiency also remained constant at initial value. Initial and final 10 cycles of GCD profiles shown in Figure 4.20a-b exhibit a great stability of the SSFC. EIS measurement for the device before and after the long cycle scan is shown in Figure 4.19b. Similar kind of behaviour of the two Nyquist plot in low frequency region indicates almost same Warburg impedance in both the cases. At high frequency regime, R_{ESR} increases from 4.64 Ω to 5.30 Ω. After long cycle operation R_{ct} value also increases from 0.65 Ω to 2.7Ω. After 5000 long cycle operation, binding strength of the PVA polymer decreases and gel resistance increases. As a consequence, the value of R_{ESR} increases. Overall resemblance of the Nyquist curves also indicates a high stability of the device. Difference in specific capacitance before and after cycle operation is very nominal (Figure 4.19c). With increase in the frequency, specific capacitance value decreases thoroughly in both cases as they satisfy the relation:

$$C = -1/2\pi MfZ'' \tag{4.7}$$

where, f denotes the frequency. For practical use of device, evaluation of two most important parameters of the device namely energy density and power density is quite essential which are given by the following equations:

$$E = \frac{C_{Device}\Delta V^2}{7.2}\ \text{Wh/kg} \tag{4.8}$$

$$P = \frac{3600E}{\Delta t}\ \text{W/kg} \tag{4.9}$$

Improvement in performance for a supercapacitor is described in plot of E vs. P, coined as Ragone plot. Figure 4.19d exhibits one such plot of the fabricated CMH based SSFC device. As fabricated SSFC device delivered maximum energy density of 64.1 Wh/kg at a

power density of about 1.5 kW/kg corresponding to the current density of 2.8 A/g. Such energy storage capacity of the fabricated device highlights its figure of merit over the other reported SCs, mentioned in Ragone plot (Figure 4.19d). Electrochemical features of our fabricated device are further compared with various reported SC devices in Table 4.3. A stable energy density of 28.4 W h/kg at power density of 8.4 kW/kg indicates high power capability of the device. The result indicates the potential of this fabricated device to operate in a large power window with high energy density. Flexibility of the fabricated device was further explored by performing CV operation after bending the device mechanically (Figure 4.21a). CV area after bending was found to be almost same as that of the regular device at the same scan rate (Figure 4.21b).

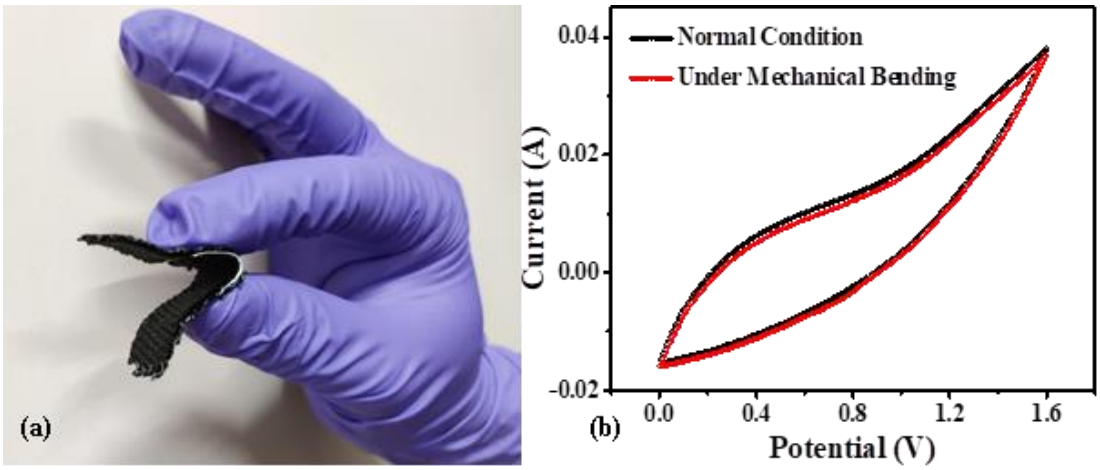

Figure 4.21: (a) Digital image of a device under bending condition, (b) Cyclic voltammetry curve of SSFC device at normal condition and bending condition at scan rate 10 mV s^{-1}.

Serial No.	Morphology/ Composition	Supercapacitor Configuration	Electrolyte	Potential window ΔV (V)	Energy Density (W h kg^{-1})	Power Density (kW kg^{-1})	Ref
1.	Onion like $CuCo_2O_4$	AC	3M KOH	1.5	48.75	37.5	[18]
2.	$CoSe_2$ Nanoarrays	Sym	3M KOH	1.6	32.2	1.915	[50]
3.	$CoNi_2S_4$ Nanosheet Arrays	AC	2M KOH	1.7	33.9	0.409	[51]
4.	$NiCo_2O_4$ / RGO composite	AC	2M KOH	1.3	23.32	0.325	[52]
5.	$ZnMn_2O_4$ / GO	Sym	PVdF-HFP	2.7	37	30.0	[53]
6.	$NiCo_2O_4$@MnO_2	AC	1M NaOH	1.5	35	0.163	[54]
7.	$CuCo_2O_4$/CuO with RGO/Fe_2O_3	AC	2M KOH	1.6	33	0.200	[55]
8.	$Co(OH)_2$/Co_3O_4	AC	2M KOH	1.5	22.4	0.290	[56]
9.	Leaf-like $CuCo_2O_4$	Sym	PVA-KOH	1.2	26.52	0.763	[57]
10.	Ni-P@$NiCo_2O_4$	AC	6M KOH	1.4	13.3	5.7	[58]
11.	$NiCo_2O_4$ microesphere	AC	2 M KOH	1.5	19.1	1.839	[59]
12.	$NiCo_2O_4$ microesphere	Sym	2 M KOH	1.0	4.5	0.669	[59]
13.	Hierarchical $CuCo_2O_4$-MnO_2	Sym	PVA/KOH	1.6	64	1.5	This Work

Table 4.3: Electrochemical performance comparison of $CuCo_2O_4$ based electrodes.

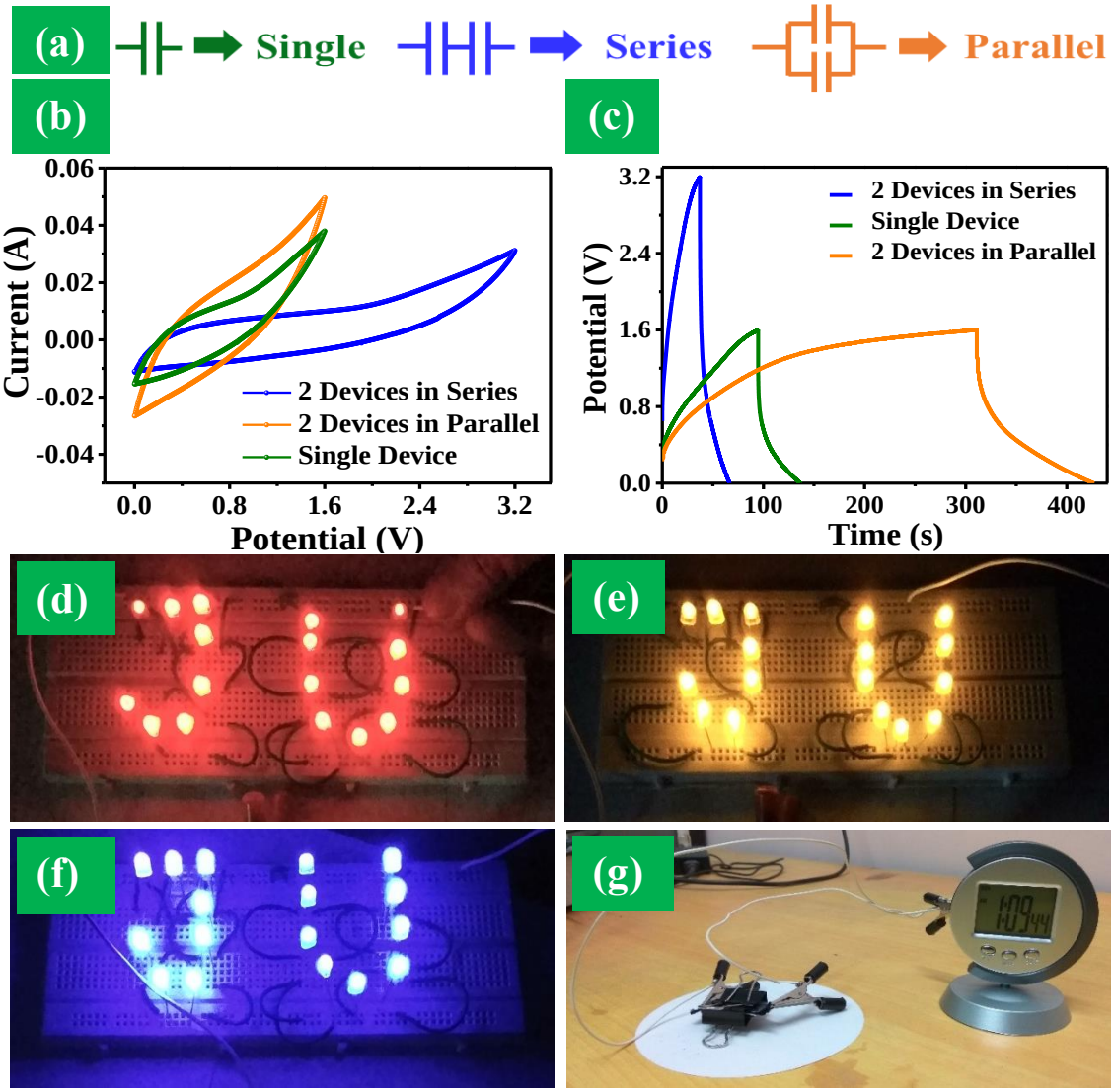

Figure 4.22: (a) Schematic of the device combination (b) CV (c) GCD profiles of the device combination (SM, PM and SD), (d-f) Digital images of different LEDs glowing and (g) digital display clock in operation by the fabricated device.

Capacitive behaviour of the as-fabricated SSFC devices was further examined in series and parallel combination of two devices. Additionally, two fabricated devices are coupled both in the series mode (SM) and parallel mode (PM) separately (Figure 4.22a). CV measurement was carried out at a particular scan rate for SM, PM and the results are compared with single device (SD), shown in Figure 4.22b. Calculated area and hence specific capacitance for PM was found to be much greater than SD. Specific area for SM

was found to be greater than SD but potential window for SM is double of SD. Thus, specific capacitance in SM is much inferior than the same of the SD. It is well established that equivalent capacitance of two capacitors having nearly equal capacitance connected in PM and SM become double and half of the single device (SD). Assessed capacitance value from the graph is not exactly half and double of the single device for SM and PM. Disparity in the capacitance value is resulted from the slight difference in mass of the two devices. Similar kind of result is also observed from the GCD profiles in SM and PM (Figure 4.22c). The measurement resulted in reduced and extended discharging times for SM and PM respectively with respect to the SD which further followed in specific capacitance values also. Operating potential window of our SSFC device is greater than that of the commercial alkaline cells (~1.5 V). However, a single SSFC device cannot fulfil the current and voltage requirements of LEDs, transparent digital display clock and etc. at times. Thus, two or more SSFC devices should be connected together to have enough power to drive those appliances. Figure 4.23 demonstrates the electric connection of the device. Besides, two SSFC devices connected in series mode not only increases the potential window to 3.2 V but also increases the energy density effectively. Two SSFC devices were connected in SM and series combination was charged up to 3 V using 20 mA current and thereafter it was connected across commercial LEDs. Above assembly was able to light up 17 parallelly connected red/yellow and blue/green LEDs for ~60 s and ~ 15 s respectively (Figure 4.22d-f) where in case of two LEDs (blue) in parallel glowing time was ~110 s. Same device assembly managed to drive a digital display clock for near about 45 minutes (Figure 4.22g). Series assembly was again charged to 3.2 V but using a higher current of 80 mA which was able to drive a motor fan for 8 s. Associated movie clips of LED glow, digital clock and fan in operation is presented in the supporting information. In the last but not the least, the sample was subject to repeated charging and discharging for a duration as long as of the

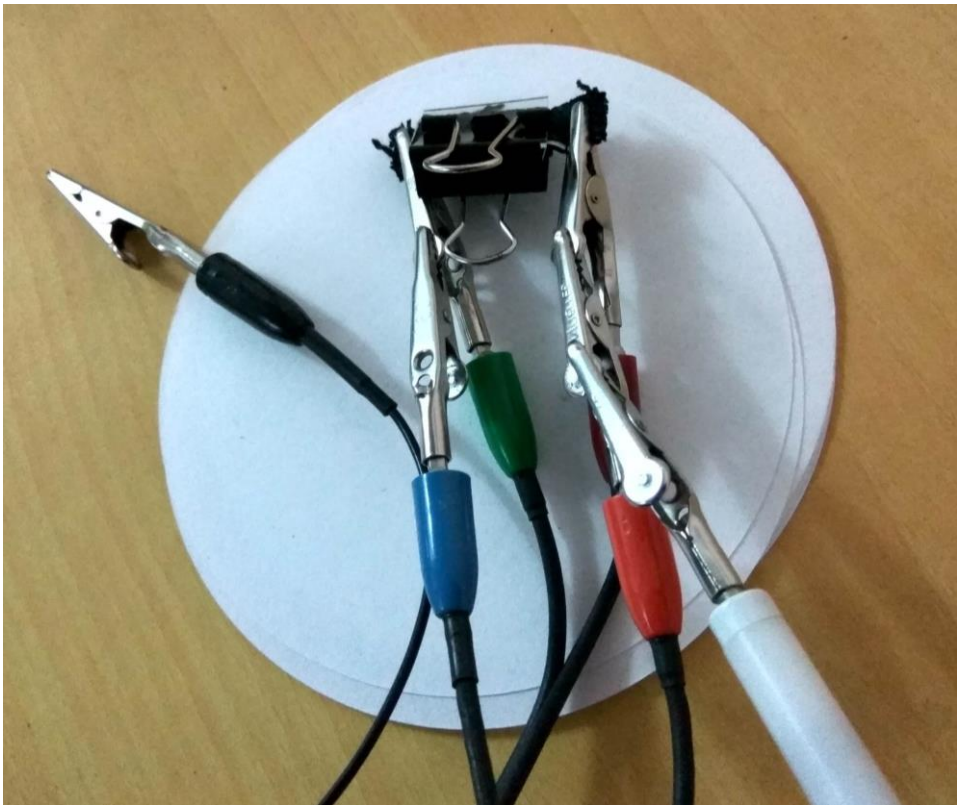

Figure 4.23: Digital image of SSFC device.

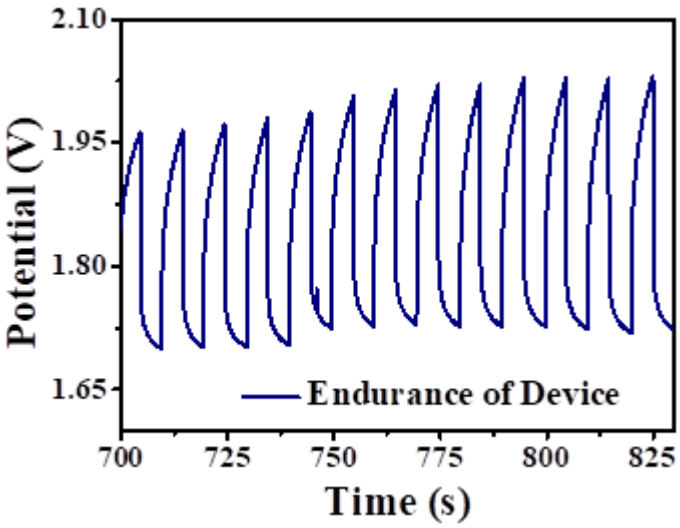

Figure 4.24: Cyclic endurance of the SSFC device.

order of 100 cycles, a portion of which is presented in Figure 4.24. The Figure suggests that the device, in spite of continuous cyclic operations without discharging properly, maintains

its integrity without any detrimental signature in its performance. These electrochemical results establish the potential candidature of this hierarchical assembly on flexible carbon fabric in next-generation SCs devices and in modern day applications.

4.4 Conclusions

In nutshell, two step hydrothermal process was adopted to yield 2D-2D hierarchical assembly comprising $CuCo_2O_4$ and MnO_2 on flexible carbon scaffold and demonstrate its usage perspective as electrode for high-performance SCs. One building components of the hybrid is spinel cobaltite $CuCo_2O_4$ which was synthesized by Cu atom incorporation in Co_3O_4 lattice. As synthesized mesoporous $CuCo_2O_4$ flake nanoform further serve as the hierarchical framework for MnO_2 nanosheet growth. With subsequent growth of porous MnO_2, the hybrid system exhibited enhanced specific capacitance and cycling stability. Symmetric solid-state SC devised using the optimized $CuCo_2O_4$–MnO_2 hybrid achieves a high gravimetric capacitance of 181.3 F/g and an energy density of 64.1 Wh/kg at a power density of about 1.5 kW/kg. It also retained 86 % of the initial specific capacitance even after 2000 cycles at high current density. These SC devices combined both in series and parallel connection can run different coloured commercial LEDs. Assembly of devices also managed to drive digital display clock for near about 45 minutes and able to rotate a motor fan for 8 s. Such realisation of interwoven 3D all oxide-based hybrid nanoform establishes a footstep towards rational designing of novel hybrid material for different applications like fuel cell, ion battery, biosensor and other electronic devices.

4.5 References

[1] J.R. Miller, P. Simon, Science (1979) 321 (2008) 651–652.

[2] J. Yang, C. Yu, X. Fan, J. Qiu, Adv Energy Mater 4 (2014) 1400761.

[3] C. Chen, Y. Huang, Y. Zhu, Z. Zhang, Z. Guang, Z. Meng, P. Liu, ACS Sustain Chem Eng 8 (2020) 1497–1506.

[4] C. Chen, Y. Huang, Z. Meng, Z. Xu, P. Liu, T. Li, Journal of Energy Chemistry 54 (2021) 482–492.

[5] D. Li, Y. Gong, C. Pan, Sci Rep 6 (2016) 29788.

[6] X. Wang, Y. Fang, B. Shi, F. Huang, F. Rong, R. Que, Chemical Engineering Journal 344 (2018) 311–319.

[7] P. Simon, Y. Gogotsi, Nat Mater 7 (2008) 845–854.

[8] M.S. Halper, J.C. Ellenbogen, The MITRE Corporation, McLean, Virginia, USA 1 (2006).

[9] C. Chen, Y. Huang, Z. Meng, M. Lu, Z. Xu, P. Liu, T. Li, Carbon N Y 170 (2020) 225–235.

[10] C. Chen, Y. Huang, Z. Meng, M. Lu, Z. Xu, P. Liu, T. Li, J Mater Sci Technol 76 (2021) 11–19.

[11] V. Augustyn, P. Simon, B. Dunn, Energy Environ Sci 7 (2014) 1597–1614.

[12] C. Yuan, H. Bin Wu, Y. Xie, X.W. Lou, Angewandte Chemie International Edition 53 (2014) 1488–1504.

[13] T. Pettong, P. Iamprasertkun, A. Krittayavathananon, P. Sukha, P. Sirisinudomkit, A. Seubsai, M. Chareonpanich, P. Kongkachuichay, J. Limtrakul, M. Sawangphruk, ACS Appl Mater Interfaces 8 (2016) 34045–34053.

[14] S. Liu, K.S. Hui, K.N. Hui, ACS Appl Mater Interfaces 8 (2016) 3258–3267.

[15] B. Liu, B. Liu, Q. Wang, X. Wang, Q. Xiang, D. Chen, G. Shen, ACS Appl Mater Interfaces 5 (2013) 10011–10017.

[16] H.S. Jadhav, S.M. Pawar, A.H. Jadhav, G.M. Thorat, J.G. Seo, Sci Rep 6 (2016) 31120.

[17] S. Vijayakumar, S.-H. Lee, K.-S. Ryu, Electrochim Acta 182 (2015) 979–986.

[18] A.A. Ensafi, S.E. Moosavifard, B. Rezaei, S.K. Kaverlavani, J Mater Chem A Mater 6 (2018) 10497–10506.

[19] Z. Ma, G. Shao, Y. Fan, G. Wang, J. Song, D. Shen, ACS Appl Mater Interfaces 8 (2016) 9050–9058.

[20] M. Huang, F. Li, F. Dong, Y.X. Zhang, L.L. Zhang, J Mater Chem A Mater 3 (2015) 21380–21423.

[21] P. Zhao, M. Yao, H. Ren, N. Wang, S. Komarneni, Appl Surf Sci 463 (2019) 931–938.

[22] Z. Ma, F. Jing, Y. Fan, L. Hou, L. Su, L. Fan, G. Shao, Small 15 (2019) 1900862.

[23] X.-F. Lu, D.-J. Wu, R.-Z. Li, Q. Li, S.-H. Ye, Y.-X. Tong, G.-R. Li, J Mater Chem A Mater 2 (2014) 4706–4713.

[24] F. Wang, G. Li, Q. Zhou, J. Zheng, C. Yang, Q. Wang, Appl Surf Sci 425 (2017) 180–187.

[25] X.M. Liu, X.G. Zhang, Electrochim Acta 49 (2004) 229–232.

[26] J. Zhi, O. Reiser, F. Huang, ACS Appl Mater Interfaces 8 (2016) 8452–8459.

[27] X. Sun, Q. Li, Y. Lü, Y. Mao, Chemical Communications 49 (2013) 4456–4458.

[28] C. Cui, J. Xu, L. Wang, D. Guo, M. Mao, J. Ma, T. Wang, ACS Appl Mater Interfaces 8 (2016) 8568–8575.

[29] H. Wang, X. Wang, ACS Appl Mater Interfaces 5 (2013) 6255–6260.

[30] Y.-Y. Horng, Y.-C. Lu, Y.-K. Hsu, C.-C. Chen, L.-C. Chen, K.-H. Chen, J Power Sources 195 (2010) 4418–4422.

[31] P. Bairi, K. Minami, W. Nakanishi, J.P. Hill, K. Ariga, L.K. Shrestha, ACS Nano 10 (2016) 6631–6637.

[32] R. Lin, Z. Zhu, X. Yu, Y. Zhong, Z. Wang, S. Tan, C. Zhao, W. Mai, J Mater Chem A Mater 5 (2017) 814–821.

[33] A. Pendashteh, S.E. Moosavifard, M.S. Rahmanifar, Y. Wang, M.F. El-Kady, R.B. Kaner, M.F. Mousavi, Chemistry of Materials 27 (2015) 3919–3926.

[34] E. Alizadeh-Gheshlaghi, B. Shaabani, A. Khodayari, Y. Azizian-Kalandaragh, R. Rahimi, Powder Technol 217 (2012) 330–339.

[35] R. Ning, J. Tian, A.M. Asiri, A.H. Qusti, A.O. Al-Youbi, X. Sun, Langmuir 29 (2013) 13146–13151.

[36] H. Xia, Y. Wang, J. Lin, L. Lu, Nanoscale Res Lett 7 (2012) 1–10.

[37] A. Ogata, S. Komaba, R. Baddour-Hadjean, J.-P. Pereira-Ramos, N. Kumagai, Electrochim Acta 53 (2008) 3084–3093.

[38] J. Cheng, H. Yan, Y. Lu, K. Qiu, X. Hou, J. Xu, L. Han, X. Liu, J.-K. Kim, Y. Luo, J Mater Chem A Mater 3 (2015) 9769–9776.

[39] B.S. Yeo, A.T. Bell, J Am Chem Soc 133 (2011) 5587–5593.

[40] M. Silambarasan, N. Padmanathan, P.S. Ramesh, D. Geetha, Mater Res Express 3 (2016) 095021.

[41] C. Julien, M. Massot, R. Baddour-Hadjean, S. Franger, S. Bach, J.P. Pereira-Ramos, Solid State Ion 159 (2003) 345–356.

[42] H.T. Zhu, J. Luo, H.X. Yang, J.K. Liang, G.H. Rao, J.B. Li, Z.M. Du, The Journal of Physical Chemistry C 112 (2008) 17089–17094.

[43] J. Jia, X. Li, G. Chen, Electrochim Acta 55 (2010) 8197–8206.

[44] J. Cui, X. Zhang, L. Tong, J. Luo, Y. Wang, Y. Zhang, K. Xie, Y. Wu, J Mater Chem A Mater 3 (2015) 10425–10431.

[45] N. Yu, H. Yin, W. Zhang, Y. Liu, Z. Tang, M. Zhu, Adv Energy Mater 6 (2016) 1501458.

[46] D. Kong, J. Luo, Y. Wang, W. Ren, T. Yu, Y. Luo, Y. Yang, C. Cheng, Adv Funct Mater 24 (2014) 3815–3826.

[47] M. Thommes, K. Kaneko, A. V Neimark, J.P. Olivier, F. Rodriguez-Reinoso, J. Rouquerol, K.S.W. Sing, Pure and Applied Chemistry 87 (2015) 1051–1069.

[48] S. Ardizzone, G. Fregonara, S. Trasatti, Electrochim Acta 35 (1990) 263–267.

[49] P. Xiao, Y. Cai, X. Chen, Z. Sheng, C. Chang, RSC Adv 7 (2017) 31558–31566.

[50] T. Chen, S. Li, J. Wen, P. Gui, Y. Guo, C. Guan, J. Liu, G. Fang, Small 14 (2018) 1700979.

[51] W. Hu, R. Chen, W. Xie, L. Zou, N. Qin, D. Bao, ACS Appl Mater Interfaces 6 (2014) 19318–19326.

[52] X. Wang, W.S. Liu, X. Lu, P.S. Lee, J Mater Chem 22 (2012) 23114–23119.

[53] P. Ahuja, R.K. Sharma, G. Singh, J. Mater. Chem. A 3 (2015) 4931–4937.

[54] K. Xu, W. Li, Q. Liu, B. Li, X. Liu, L. An, Z. Chen, R. Zou, J. Hu, J Mater Chem A Mater 2 (2014) 4795–4802.

[55] Y. Wang, C. Shen, L. Niu, R. Li, H. Guo, Y. Shi, C. Li, X. Liu, Y. Gong, J Mater Chem A Mater 4 (2016) 9977–9985.

[56] M. Jing, Y. Yang, Y. Zhu, H. Hou, Z. Wu, X. Ji, Electrochim Acta 141 (2014) 234–240.

[57] Y. Wang, D. Yang, J. Lian, J. Pan, T. Wei, Y. Sun, J Alloys Compd 735 (2018) 2046–2052.

[58] X. Li, R. Ding, L. Yi, W. Shi, Q. Xu, E. Liu, Electrochim Acta 222 (2016) 1169–1175.

[59] S. Khalid, C. Cao, L. Wang, Y. Zhu, Sci Rep 6 (2016) 22699.

[60] K. Zhang, W. Zeng, G. Zhang, S. Hou, F. Wang, T. Wang, H. Duan, RSC Adv 5 (2015) 69636–69641.

[61] B. Sydulu Singu, R. Kuchi, P. Cao Van, D. Kim, K. Ro Yoon, J. Ryul Jeong, ChemNanoMat 5 (2019) 1398–1407.

[62] A.K. Das, N.H. Kim, S.H. Lee, Y. Sohn, J.H. Lee, Compos B Eng 150 (2018) 269–276.

[63] S. Liu, K. San Hui, K.N. Hui, J.M. Yun, K.H. Kim, J Mater Chem A Mater 4 (2016) 8061–8071.

Chapter 5: Crystallinity and Interfacial Mo–N–C Bond Engineered MoS_2 Embedded Graphitic Nitrogen doped Carbon Hollow Sphere for Enhanced HER Activity

To restrain fossil fuel depletion, the need of the hour is the development of efficient, durable, and non-precious electrocatalysts for the hydrogen evolution reaction (HER). The hierarchical nanostructure consisting of transition metal dichalcogenides and graphitic heteroatom-doped carbon with an abundant interfacial M–N–C catalytic site is highly demanding for electrolytic applications. Herein, we report crystallinity-engineered ultrathin MoS_2 nanosheets hierarchy over nitrogen-doped graphitic carbon (NC) hollow spheres as a promising material for HER. The well optimized NC@MoS_2 demonstrates superior HER activity with a low onset overpotential of 9 mV and an overpotential of 145 mV at a current density of –10 $mA.cm^{-2}$. It exhibits low Tafel slope of 39 mV dec^{-1} and excellent chronoamperometric stability. Superior HER activity originates from interfacial Mo–N–C bonds. Density functional theory (DFT) calculations unveils that Mo−N−C bonds between MoS_2 and NC matrix ease electronic transportation and further diminish Gibbs free energy for HER.

5.1 Introduction

One of the major concerns in modern times is climate change, which encompasses global warming guided by human-induced emissions of greenhouse gases and has resulted in large shifts in weather patterns. To circumvent this, the hydrogen economy has emerged as an envisioned future and the sustainable substitute to the ongoing fossil fuel-based economy, where the hydrogen, as commercial fuel [1–4] is going to contribute significantly to the worldwide energy requirement. Economical production of hydrogen can lead to a great retrenchment in fossil fuel consumption, resulting in a diminution of greenhouse gas emissions. Electrochemical water splitting led by an external source of electricity is one of the most significant and eco-friendly pathways to produce hydrogen gases [5–7]. Hydrogen Evolution Reaction (HER) is involved in this process, in which the introduction of an electrocatalyst takes down the activation energy barrier and hence accelerates the hydrogen conversion efficiency [8–11]. A good electrocatalyst must acquire appropriate Gibbs free energy for hydrogen atom (H) adsorption [12,13], deliver abundant active sites, have superior conductivity, and hence enable susceptible electron transfer. It must also possess rich acid stability, the competency to withhold high current densities, earth abundance, and hence low fabrication costs for commercialization. Platinum (Pt)-based electrocatalysts are accepted to be the most vibrant electrocatalysts for HER, manifesting a weeny overpotential and hence greater reaction rates, low adequacy [14,15]. However, the high cost and scarcity of Pt critically hinder its large-scale utilization. Hence, successful accomplishment of clean hydrogen technology demands some economical, ecofriendly, earth-abundant, viable, and fabrication efficient HER electrocatalysts to substitute Pt-based catalysts. Over the last few years, transition metal dichalcogenides (TMDs) [16–21] have emerged as new classes of electrode materials for HER applications that may supersede the conventional Pt-based electrode. Molybdenum disulfide (MoS_2) has manifested itself to be the most promising

electrode material among the above-mentioned TMDs due to its fascinating electrocatalytic activities [18–40]. As an add on, MoS_2 shows stability in harsh acidic environments, an inevitable prerequisite for an efficient electrocatalyst. However, bulk MoS_2 does not show all the above traits. It is widely documented that a lack of exposed active edges and poor interlayer conductivity of bulk MoS_2 result in poor HER activity [23]. Enormous effort has been devoted to attain a favourable morphology for the MoS_2 nanostructure as well as improve the conductivity by presenting these nanoforms over highly conducting substates.

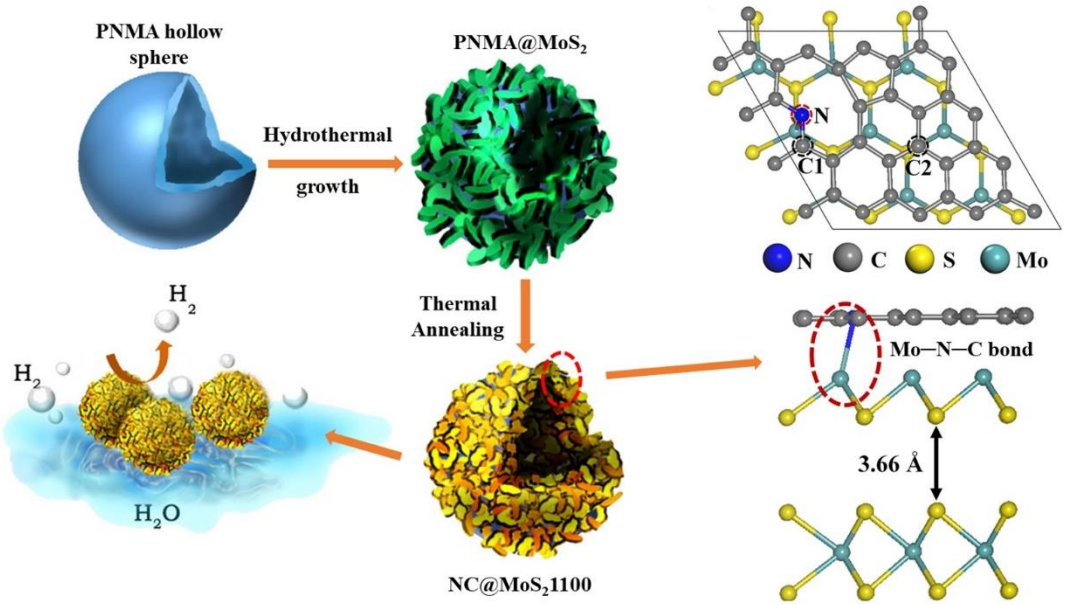

Scheme 5.1: Schematic illustration of the synthesis of high performance HER catalyst NC@$MoS_2$1100 via hydrothermal and thermal annealing at high temperature accompanying the description of Mo–N–C bond structure at the interface between MoS_2 and NC respectively.

Besides these two, the HER activity of the MoS_2 catalyst also profoundly depends on its crystal features, such as crystalline phase, crystallite size, and degree of crystallinity [24]. In crystalline MoS_2, edge sites bear slightly positive energy for hydrogen adsorption (+0.08 eV), which facilitates HER activity [24–40]. Then again, reports suggest that amorphous

MoS_2 can deliver high performance owing to the unsaturated Mo sites [41]. There are several contradictory reports also asserting that pure crystalline MoS_2 possesses little activity, and if any, it is due to impurities like MoO_2 integration [23]. These questionable, counter-intuitive reports beckon systematic study on the impact of crystallinity and chemical composition of MoS_2 on its HER performance.

To broaden up the utility perspective as well as enhance the HER activity of MoS_2, several protocols were adopted, among which the designing of composition-modulated multilevel hierarchical nanoforms with geometrical intricacy is very intriguing [17,42–44]. The amalgamation of MoS_2 with the carbon substances showed improved electrical conductivity and promoted the reaction kinetics, thus enhancing the catalytic behavior [11,17,22,25–39,45]. Carbonaceous materials serve as an essential host in several applications because of their mechanical strength, extraordinary thermal and electrical conductivity, superior chemical and electrochemical stability, and nontoxicity. In unison, carbon (C) doped by nonmetal elements like nitrogen (N), sulfur (S), phosphorus (P), and boron (B) can also act as a new class of electrocatalysts [27,38,46–50]. In the absence of a comprehensive experimental and theoretical report on this kind of amalgamation, it is quite difficult to reveal the exact mechanism of interfacial bonds between MoS_2 and doped C. Thus, a detailed investigation is essential. Encapsulation of a nonmetal N-doped carbon (NC) matrix with the stacked hierarchy of MoS_2 nanosheets (NSs) appears to be an excellent scheme so that the hybrid can capitalize on the individual effects of the NC matrix and MoS_2 NS as well as the synergistic effects to achieve a superior electrical conductivity and enhanced catalytic activity. Such rational designs of MoS_2 based hierarchical electrocatalysts embedded with NC matrix may have the potential to provide ample active sites, good stability, and superior charge transfer for the HER mechanism.

Herein, we have developed a novel electrocatalyst that is a hierarchy of N-doped hollow NC sphere and MoS_2 NSs with the presence of interfacial electrocatalytically active Mo−N−C bonds. Initially, poly (N-methylaniline) (PNMA) hollow conducting polymer sphere was synthesized via the typical interfacial polymerization method. Subsequently, PNMA@MoS_2 heterostructure was realized via facile hydrothermal route at 200 ˚C. Finally, the as synthesized hybrid was annealed at different annealing temperatures of 700, 1000, and 1100˚C in an inert nitrogen atmosphere. With the increase in annealing temperature, the crystallinity of MoS_2 NSs was increased, while the PNMA polymer sphere was gradually converted to graphitic N-doped carbon (NC). It has been observed that MoS_2 supported on N-doped carbon composites of several structures, morphologies, and crystallinity degrees have been previously reported for various electrochemical reactions, including HER. However, as discussed in our previous work [51], to synthesize the PNMA hollow sphere, we used new types of precursors (N-methylaniline, Poly (methyl vinyl ether-alt-maleic acid), and ammonium persulfate) during polymerization. It was observed that the conversion of PNMA hollow spheres into N-doped (pyridinic and pyrrolic) graphitic carbon occurs with a very high doping percentage of nitrogen species (atom % of 8.6) in comparison to previously reported works. Thus, the main novelty lies at the junction of an N-doped hollow carbon sphere and MoS_2 NSs, where an increase in annealing temperature is expected to produce substantially greater Mo—N—C bonds during annealing of PNMA@MoS_2 with different annealing temperatures. Amongst all the samples, hybrid annealed at 1100˚C exhibits the highest catalytic activity with a small overpotential of 145, 220, and 246 mV, corresponding to current densities of -10, -50, and -100 mA cm^{-2}, respectively. It also maintains a low Tafel slope of 39 mV dec^{-1} along with excellent stability in acidic environments. The chemical interaction between the NC matrix and MoS_2 NSs via the interfacial Mo—N—C bond endows ideal H_2 adsorption energy and thus

enhances the HER activity of the overall system as compared to building blocks separately. Density functional theory (DFT) calculation together with X-ray photoelectron spectroscopy (XPS) analysis verified the above-said enhanced HER activity and intimate chemical bonding, respectively. The entire work is presented schematically in Scheme 5.1.

5.2 Results and Discussion

5.2.1 Characterization

To investigate the morphology of the samples, field emission scanning electron microscopy (FESEM) analysis was carried out. FESEM of PNMA nanostructures in Figure 5.1a-b discloses a homogeneous spherical shape with apparently smooth surfaces. From the Voigt fits of the particle size distributions, the average diameter of PNMA was found to be ~ 292 ± 3 nm (Figure 5.1c). A high resolution-transmission electron microscopy (HRTEM) study indicates that the PNMA has a hollow, spherical shell with uniform shell thickness (Figure 5.1d). FESEM images of PNMA@MoS_2 (Figure 5.2a-b) reveal uniform growth of MoS_2 NSs on the PNMA sphere, resulting in a PNMA@MoS_2 hierarchy. The consequences of the annealing at different temperatures are evident from the FESEM images of the NC@$MoS_2$700 and NC@$MoS_2$1000 samples presented in Figures 5.3 and 5.4, respectively. The variation in the MoS_2 NSs thickness is further accessed from the TEM analysis of the aforesaid samples in Figure 5.5. TEM images of PNMA@MoS_2 indicate that MoS_2 sheets (Figure 5.5a-b) are much thicker. This may be due to the rich sulfur content in the sample. With the increase in annealing temperature, the sulfur amount decreases, and thick MoS_2 NSs gradually transform into thin NSs (Figure 5.5c-d). Annealing at a much higher temperature caused MoS_2 NSs to become ultrathin, as evident from the high magnification FESEM image of the NC@$MoS_2$1100 (Figure 5.7a). Uniformity in the morphology of this sample is obvious from Figure 5.6. Ultrathin MoS_2, for the NC@$MoS_2$1100 is obvious from

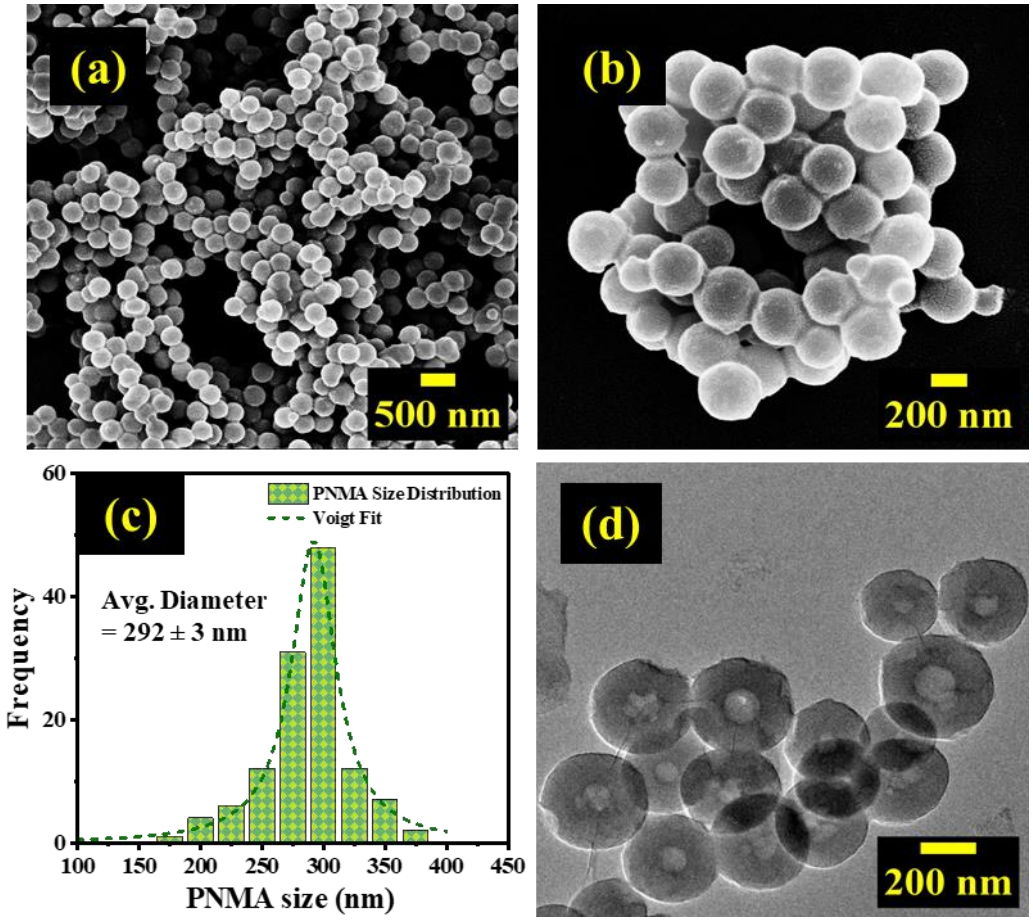

Figure 5.1: (a-b) FESEM images of PNMA hollow spheres at different magnifications, (c) Particle size distributions of PNMA (Voigt fits), (d) TEM images of PNMA hollow spheres.

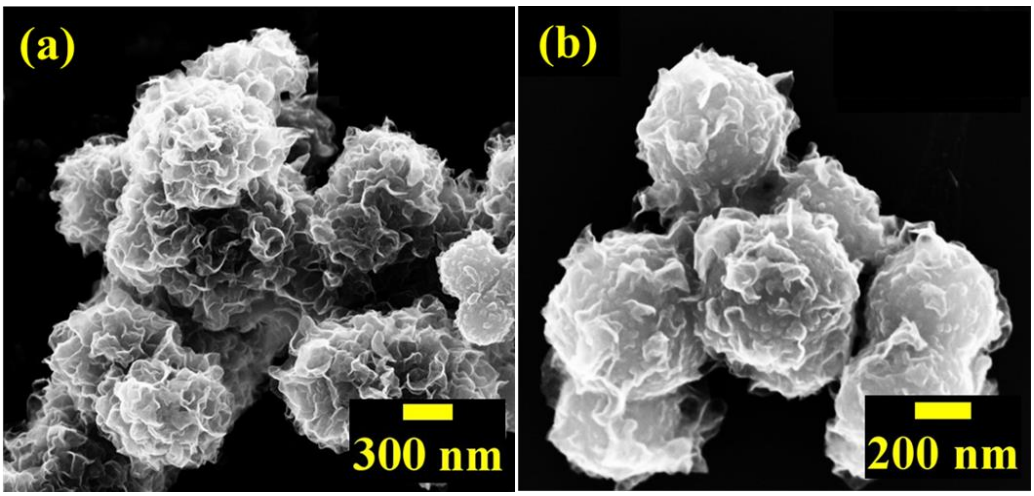

Figure 5.2: (a-b) FESEM images of PNMA@MoS_2 heterostructure at different magnifications.

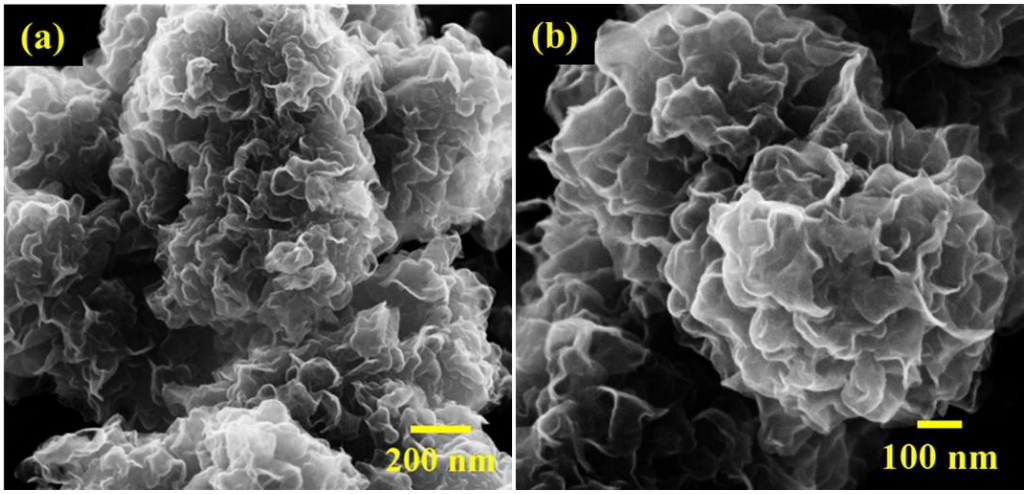

Figure 5.3: (a-b) FESEM images of NC@$MoS_2$700 heterostructure at different magnifications.

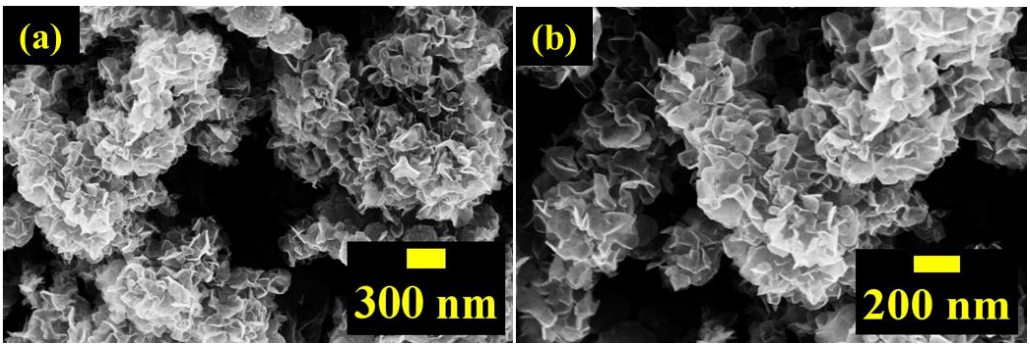

Figure 5.4: (a-b) FESEM images of NC@$MoS_2$1000 heterostructure at different magnifications.

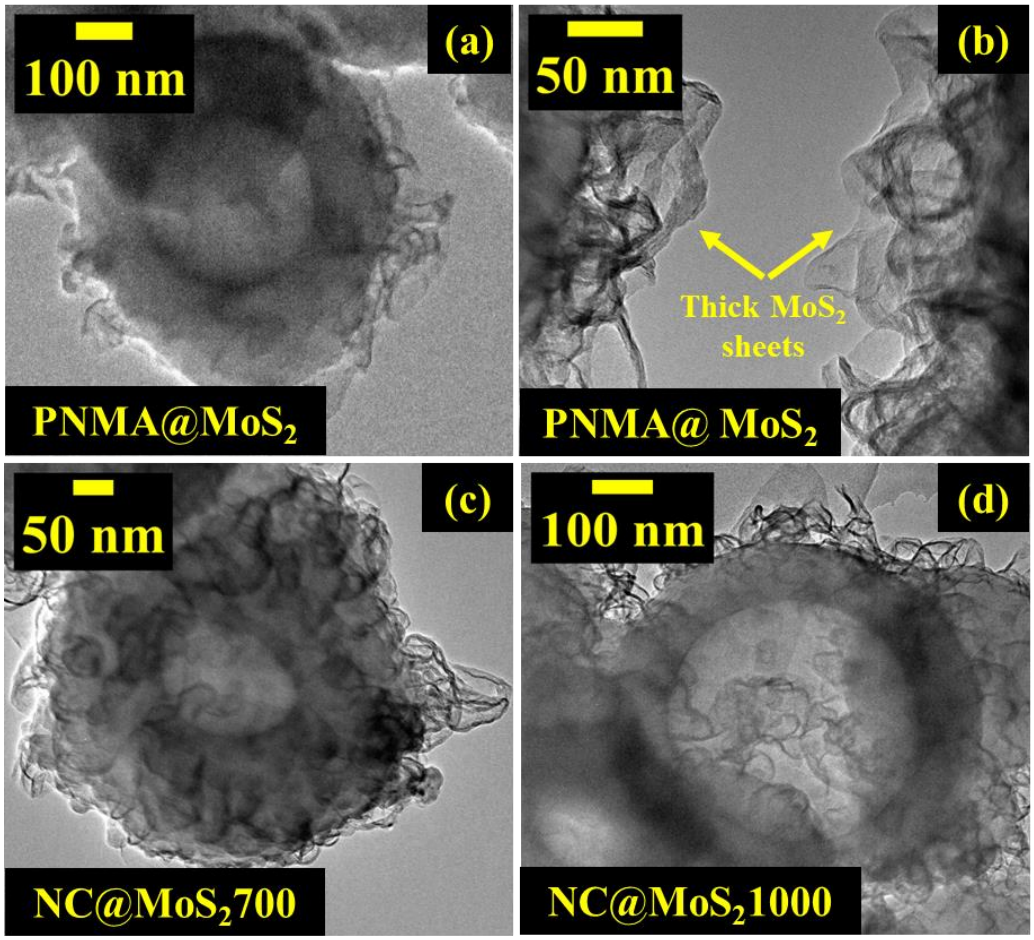

Figure 5.5: TEM images of (a) PNMA@MoS_2, (b) Amorphous thick MoS_2 sheets, (c) NC@$MoS_2$700, (d) NC@$MoS_2$1000.

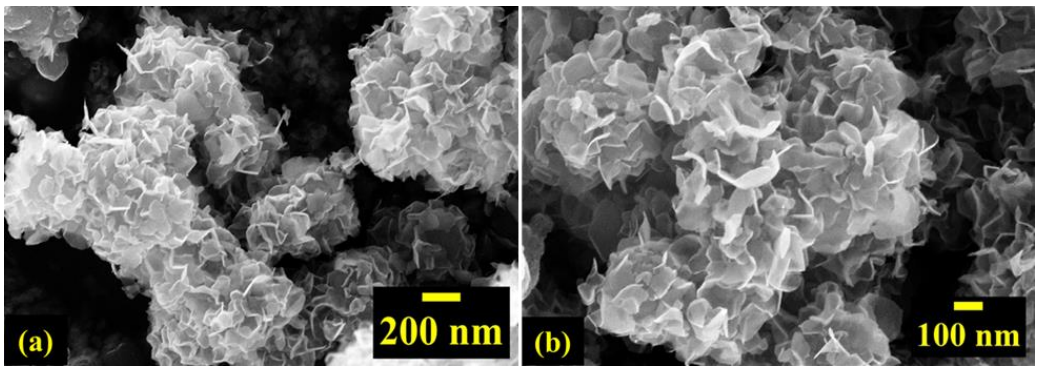

Figure 5.6: (a-b) FESEM images of NC@MoS21100 heterostructure at different magnifications.

the corresponding TEM image, presented in Figure 5.7b. The inset image in Figure 5.7b further indicates the same. To get more insight on crystallinity as well as the layer number of MoS_2, HRTEM studies were further carried out. The HRTEM image of PNMA@MoS_2 (Figure 5.7c) indicates an amorphous hierarchy of thick MoS_2 NSs surrounding the amorphous PNMA sphere. No distinct oriented crystal planes are visible in this image [51]. With the increase in annealing temperature, the crystallinity of MoS_2 started increasing, and oriented crystal planes (Figure 5.7d-f) emerged. HRTEM image of NC@$MoS_2$1100 (Figure 5.7f) reveals the presence of crystal planes with interlayer spacing of 0.27 nm and 0.6 nm, which correspond to (100) and (002) planes of crystalline MoS_2 respectively [22,41,52]. The simultaneous presence of a lattice plane with d-spacing of 0.35 nm is associated with the (002) planes of crystalline graphite [53–55]. At the same time, the high value of d-spacing (0.35 nm) in NC@$MoS_2$1100 signifies the presence of disorder in layers [54-55]. Gradual increment in crystallinity of NSs is also evident from selected area electron diffraction (SAED) patterns (inset images of Figure 5.7c-f). In PNMA@MoS_2 and NC@$MoS_2$700, diffused rings are observed in the SAED pattern for MoS_2 NSs. This confirms the amorphous nature of NSs. A circular ring pattern is appearing for the NSs in NC@$MoS_2$1000. This ring pattern became more prominent in the NC@$MoS_2$1100 sample, which signifies the much-improved crystallinity of MoS_2 NSs. Careful observation of this image also suggests the existence of 11 layers in the MoS_2 NSs (Figure 5.7f). The thickness of MoS_2 NSs was further assessed by atomic force microscopy (AFM) measurement. The thickness of MoS_2 was found to be 5–6 nm (Figure 5.8a-b), which is nearly 10 times that of the monolayer of MoS_2 (~ 0.65 nm) [56]. Thus, the AFM data corroborate with the HRTEM of NC@$MoS_2$1100 (Figure 5.7f).

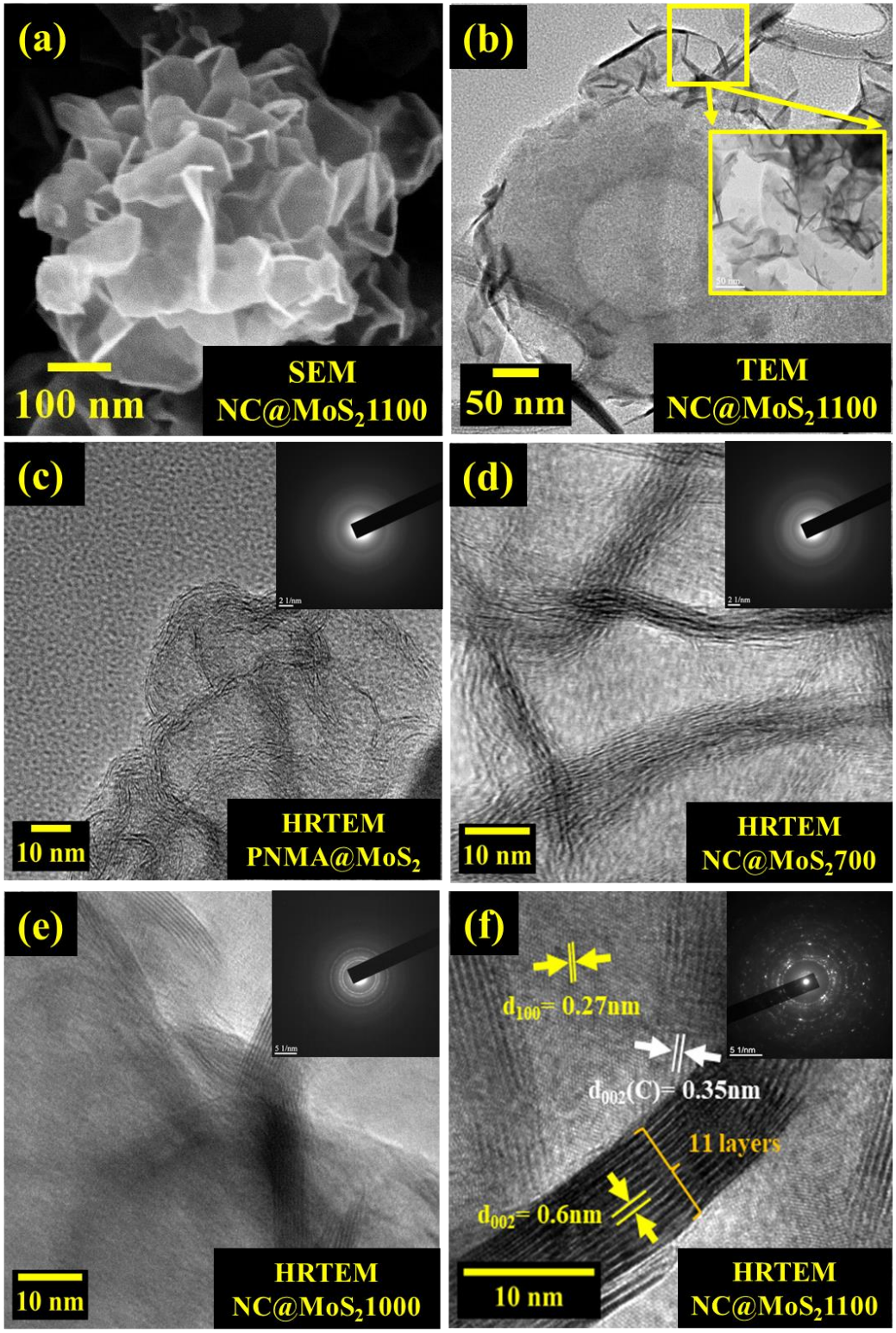

Figure 5.7: (a) SEM and (b) TEM image of NC@$MoS_2$1100. HRTEM of (c) PNMA@MoS_2, (d) NC@$MoS_2$700, (e) NC@$MoS_2$1000, (f) NC@$MoS_2$1100. Inset (c-f) shows corresponding SAED pattern.

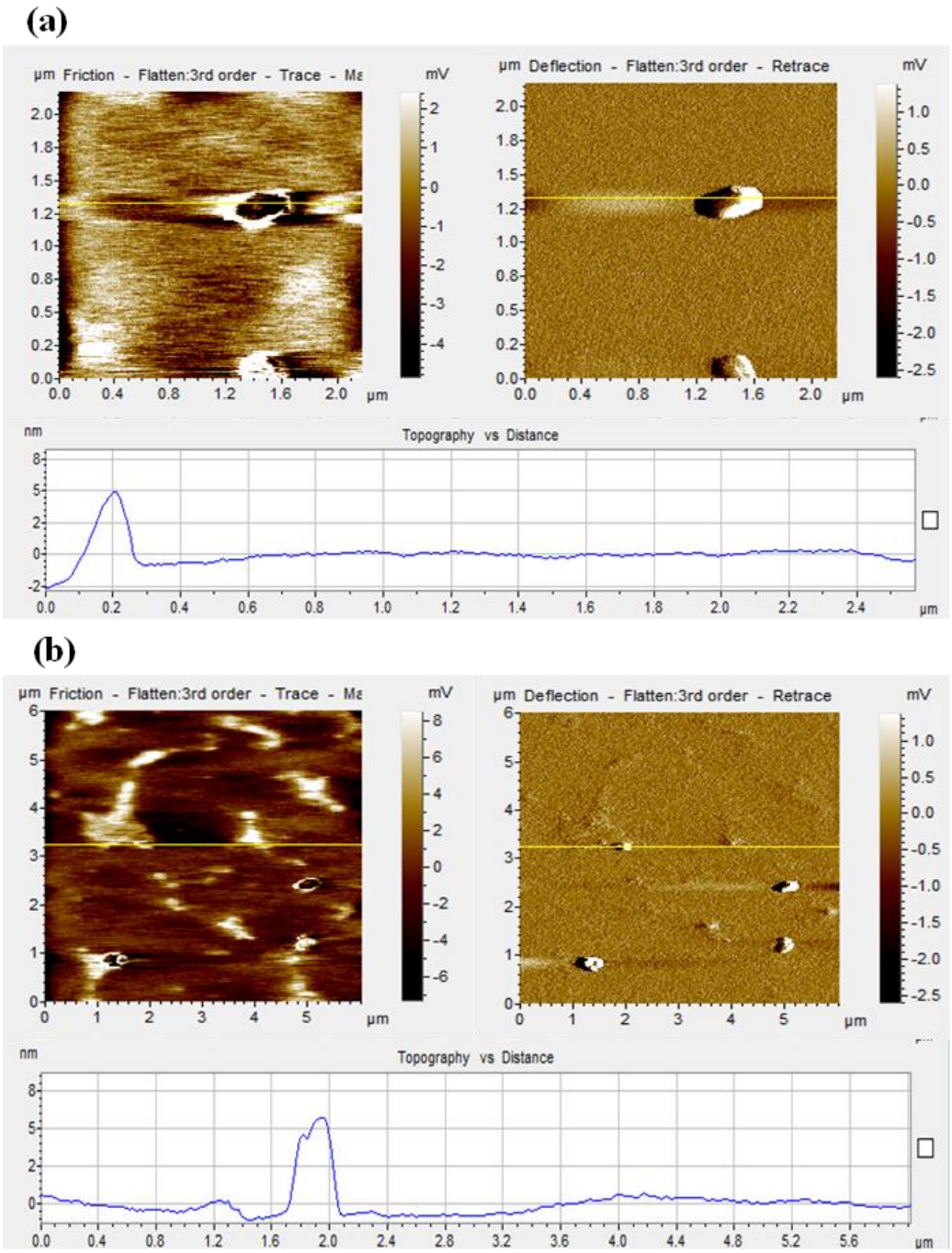

Figure 5.8: (a-b) AFM data of MoS_2 Nanosheets in NC@$MoS_2$1100.

The crystal phases of the synthesized samples were analyzed using the X-ray diffraction (XRD) technique (Figure 5.9a). XRD profile of PNMA hollow sphere without any distinct peaks discloses that it is amorphous. After the secondary growth, the hierarchy, i.e., PNMA@MoS_2 exhibits very faint (100) and (110) diffraction peaks of MoS_2, which

confirms that MoS_2 in this sample is also amorphous in nature. With the increase in annealing temperature, more and more diffraction peaks arise in the profiles. This signifies the appearance of crystallinity in MoS_2 NSs. Peaks related to the (100) and (110) planes of crystalline MoS_2 evolved more strongly in NC@$MoS_2$700. These peaks became more and more intense in NC@$MoS_2$1000 and NC@$MoS_2$1100 and indicate the formation of 2H-phase MoS_2 in hybrid (JCPDS card no. 01-087-2416) [41,50]. Careful observation of XRD profiles also suggests changes in the PNMA sphere. Underlying PNMA spheres chemically transform into N-doped carbon due to thermal carbonization. A sharp peak arises at $2\theta \sim 26.5°$ which corresponds to (002) diffraction planes of graphite [55,57]. Additionally, a less intense peak at $2\theta \sim 43°$ related to (101) planes is also observed, which indicates interlayer ordering in the graphitic carbon layer [53]. These results confirm that annealing at 1100 °C converted the sphere into graphitic carbon due to the shielding effect of MoS_2 surrounding the hollow sphere [53].

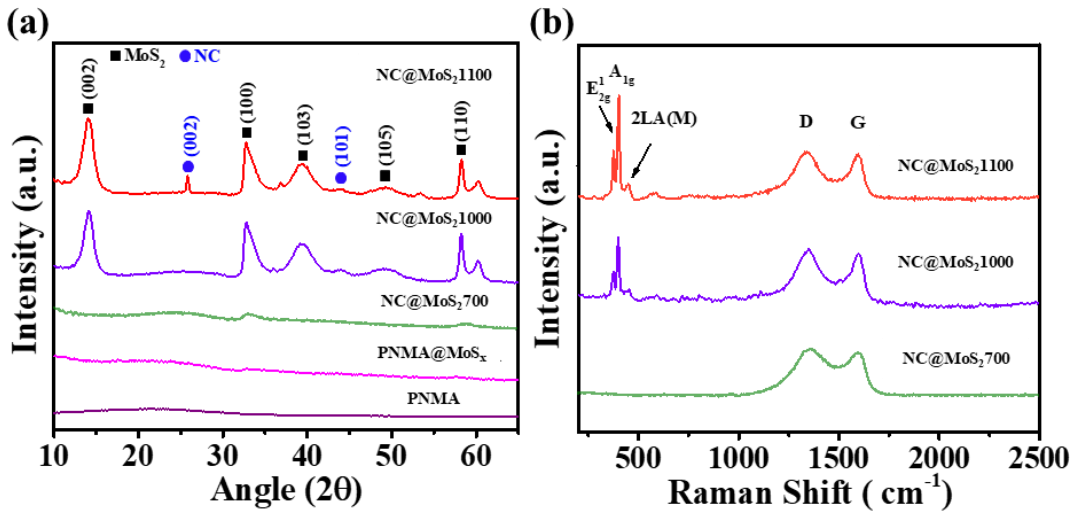

Figure 5.9: (a) Powder XRD pattern of NC@$MoS_2$1100, NC@$MoS_2$1000, NC@$MoS_2$700 together with PNMA@MoS_2 and PNMA at room temperature. (b) Raman spectra of the NC@$MoS_2$1100, NC@$MoS_2$1000, and NC@$MoS_2$700 samples respectively.

Raman spectra of NC@$MoS_2$1000 and NC@$MoS_2$1100 in Figure 5.9b exhibit in-plane Mo-S phonon mode E^1_{2g} (~ 376 cm^{-1}), out-of-plane Mo-S mode A_{1g} (~ 403 cm^{-1}) and second-order Raman scattering 2LA(M) (~ 449 cm^{-1}) of crystalline 2H-MoS_2 [58,59]. Peaks related to E^1_{2g} and A_{1g} vibrational modes are absent in the spectra of PNMA@MoS_2 and NC@$MoS_2$700 which indicates the presence of amorphous phase. Careful observation of the plot of NC@$MoS_2$1000 and NC@$MoS_2$1100 suggests relative intensity differences in these peaks. The intensity of A_{1g} mode is greater than E^1_{2g} in both samples. At the same time, the relative intensity ratio A_{1g}/ E^1_{2g} increases in NC@$MoS_2$1100 which indicates the presence of higher sulfur terminated edge sites and reduced S-Mo-S layers [22,59]. Raman peaks located at ~ 1345 cm^{-1} and ~ 1590 cm^{-1} correspond to the D and G bands of graphitic carbon [55,57]. D-band is a measure of defects i.e., structural disorder inside the carbon matrix whereas the G-band demonstrates the graphitize structure. It is to be noted that during pyrolysis, the intensity ratio I_D/I_G increases with temperature, followed by graphitization, during which the I_D/I_G ratio decreases with temperature [60,61]. Value of the aforesaid ratio increment with the increase in annealing temperature indicates the presence of defects inside the carbon matrix. However, in NC@$MoS_2$1100, this ratio is less than the same in NC@$MoS_2$1000 indicating a higher degree of graphitization in the carbon sphere (Table 5.1).

Sample	I_D/I_G Ratio
NC@$MoS_2$700	1.07
NC@$MoS_2$1000	1.09
NC@$MoS_2$1100	1.05

Table 5.1: Calculated I_D/I_G ratio of the as synthesized samples.

NC@$MoS_2$1100 sample was further characterized using energy dispersive X-ray (EDX) method attached with TEM. Appearance of peaks associated with constituent elements C, N, Mo, S and O are obvious in the EDX spectrum obtained from TEM (Figure 5.10). Elemental mapping of the constituent elements of NC@$MoS_2$1100 (Figure 5.11a-f) discloses even distribution of them inside the sample.

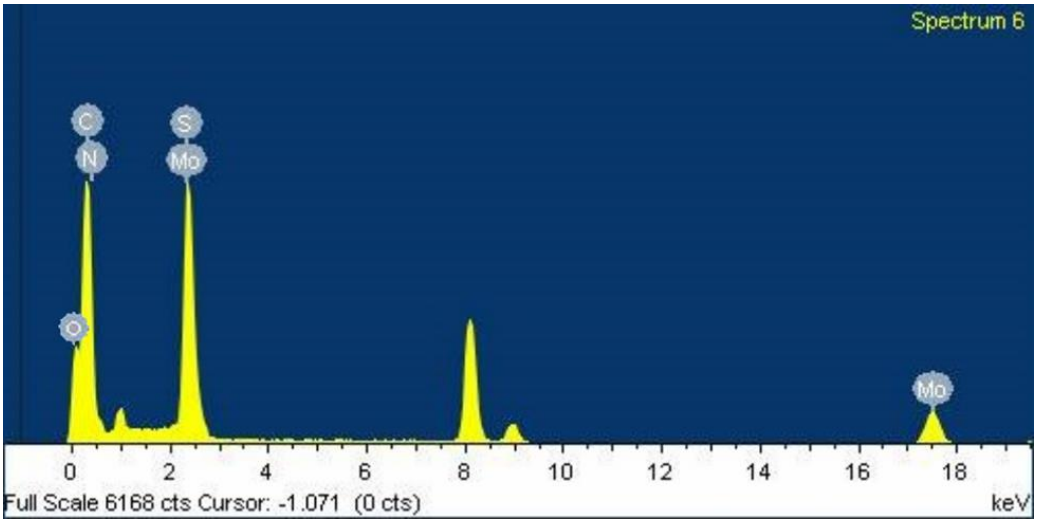

Figure 5.10: EDX Spectra (from TEM) for NC@$MoS_2$1100.

The electrocatalytic activity of a catalyst extensively depends on its surface area and porosity. Hence, these parameters for all the samples were estimated through a nitrogen adsorption-desorption study. All the samples exhibited mesoporous structures as depicted in Figure 5.12a. The hysteresis loops at higher relative pressure (P/P_0) in between 0.4 and 1 indicate the presence of mesopores [62,63]. Theses isotherms also depict fast nitrogen adsorption in the low-pressure region, which indicates the presence of microspores in the samples. Brunauer-Emmett-Teller (BET)-specific surface areas of all the synthesized samples were calculated from these isotherms. The BET-specific surface area of NC@$MoS_2$1100 is found to be maximum (118 $m^2\ g^{-1}$) whereas the value of PNMA is estimated to be 9.8 $m^2\ g^{-1}$. Again, the BJH pore size distribution curves of the as prepared samples (Figure 5.12b) exhibit that pore volume increases gradually with an increase in

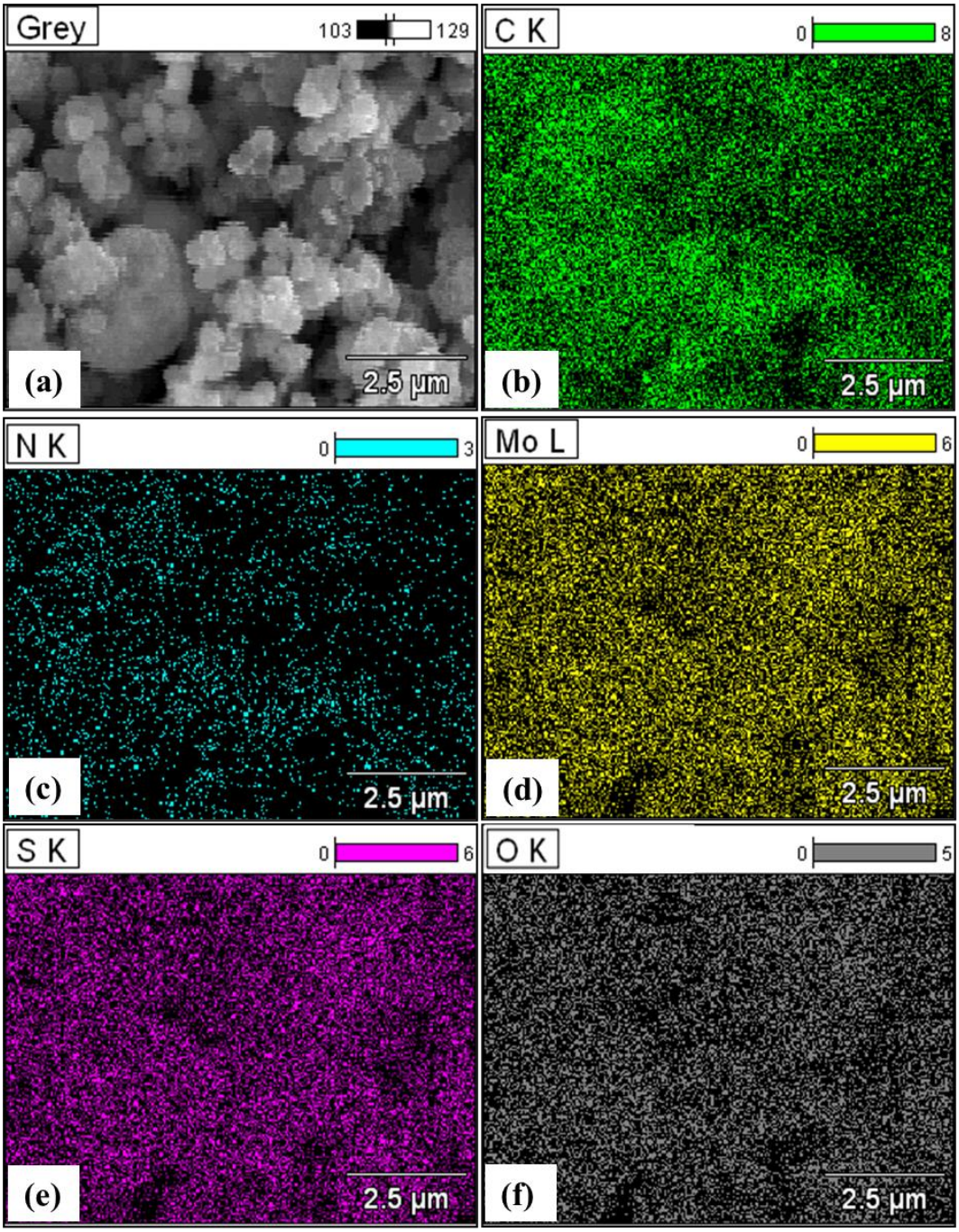

Figure 5.11: (a) FESEM and (b-f) corresponding elemental mapping of NC@$MoS_2$1100.

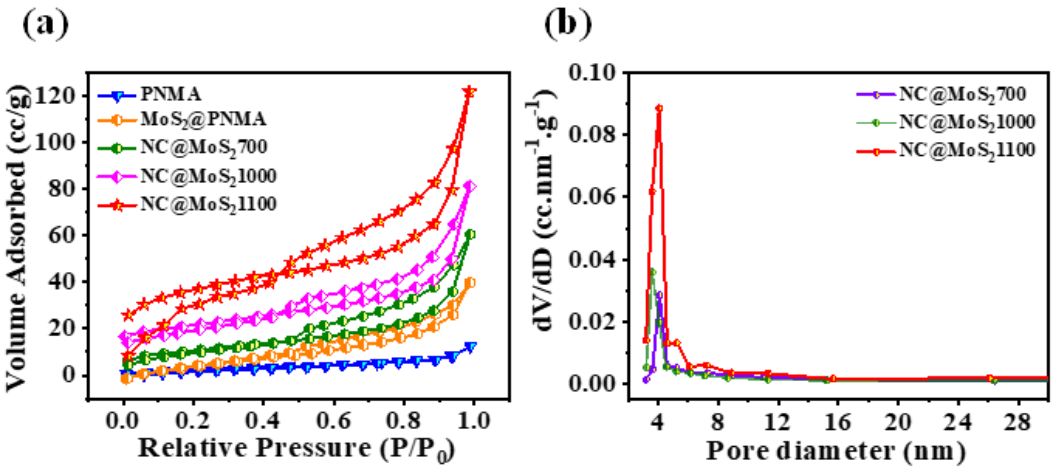

Figure 5.12: (a) N_2 adsorption–desorption isotherms and (b) BJH Pore size distribution of as prepared samples.

Sample	Specific surface area ($m^2 g^{-1}$)	Pore diameter (nm)	Pore Volume (cc g^{-1})
PNMA	9.8	7.7	0.002
PNMA@MoS_2	29.8	4.02	0.065
NC@$MoS_2$700	39.2	4.08	0.093
NC@$MoS_2$1000	47	3.6	0.112
NC@$MoS_2$1100	118	4.06	0.205

Table 5.2: BET parameters of the synthesized samples.

annealing temperature. NC@$MoS_2$1100 shows a maximum pore volume of 0.205 cc/g whereas the same for PNMA is 0.002 cc/g. A comparative table on surface area, pore volume, and diameters of all the samples is shown in Table 5.2. This table clearly suggests that annealing not only results in an increase in surface area but also changes the pore

volume and diameter. With the increase in annealing temperature, elements such as carbon, hydrogen, and nitrogen were decomposed from the PNMA, creating sufficient pore structure in the NC matrix. In a similar way, the increase in annealing temperature forces excess sulfur to go away from the MoS_2 flakes, transforming the thick flakes into ultrathin nanosheets (high surface area). Hence, BET results exhibit maximum pore volume for NC@$MoS_2$1100, whereas the same for PNMA is the least. The porosity of NC@$MoS_2$1100 contributes to the BET surface area and porosity. Volumetric adsorption measurement indirectly provides information about the porosity of a material. Further, the porous structure of a material can be directly observed by FESEM and TEM images. From FESEM and TEM observation, it is evident that with the increase in annealing temperature, the porosity as well as the thickness of the MoS_2 NSs change drastically (Figure 5.5c-d). Annealing at a much higher temperature, MoS_2 NSs became ultrathin (Figure 5.7a). Again, if we compare the TEM images of thick MoS_2 sheets in Figure 5.5b and ultrathin MoS_2 nanosheets in Figure 5.7b (inset), it is evident that the morphology of MoS_2 nanosheets changes drastically with an increase in annealing temperature. For comparison, HRTEM images of NC@$MoS_2$700 and NC@$MoS_2$1100 are shown in Figure 5.13a-b. It is clearly visible from the HRTEM images how annealing creates huge pores in MoS_2 and the NC interface in NC@$MoS_2$1100. Such changes in morphology led to changes in the overall surface area of the samples, which are consistent with the N_2 adsorption data.

An XPS scan was further carried out to analyze the elemental constituents and surface chemistry of NC@$MoS_2$1100. The survey scan of this sample shown in Figure 5.14 confirms the presence of C, N, Mo, S and O. High resolution spectra of C 1s exhibit four deconvoluted peaks at ~ 284.5, 285.5, 288.8, and 281.8 eV (Figure 5.15a). A strong peak at ~ 284.5 eV can be assigned to C─C/ C═C species. On the other hand, peaks with lesser intensity are due to the presence of C─N (~ 285.5 eV) and C─O (~ 288.8 eV) bonds [22,64].

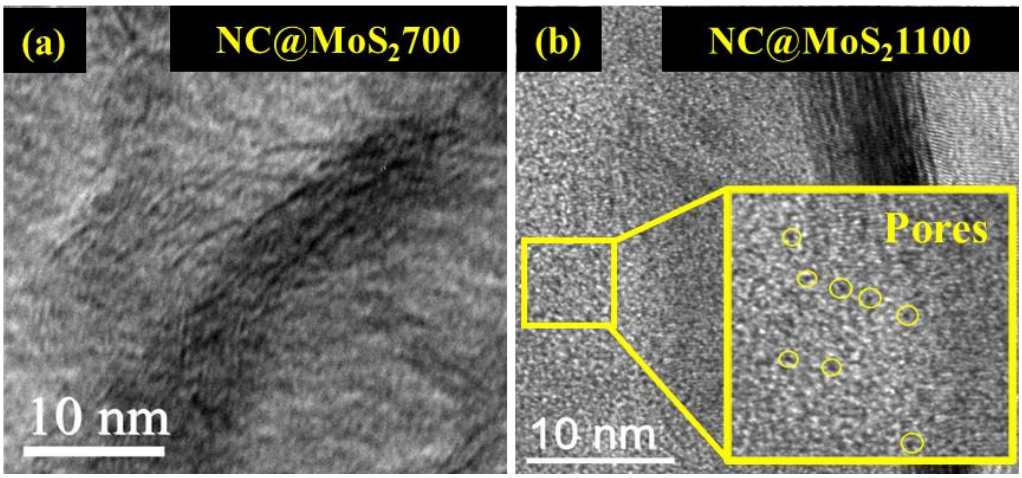

Figure 5.13: HRTEM images for (a) NC@$MoS_2$700 and (b) NC@$MoS_2$1100 to compare porosity.

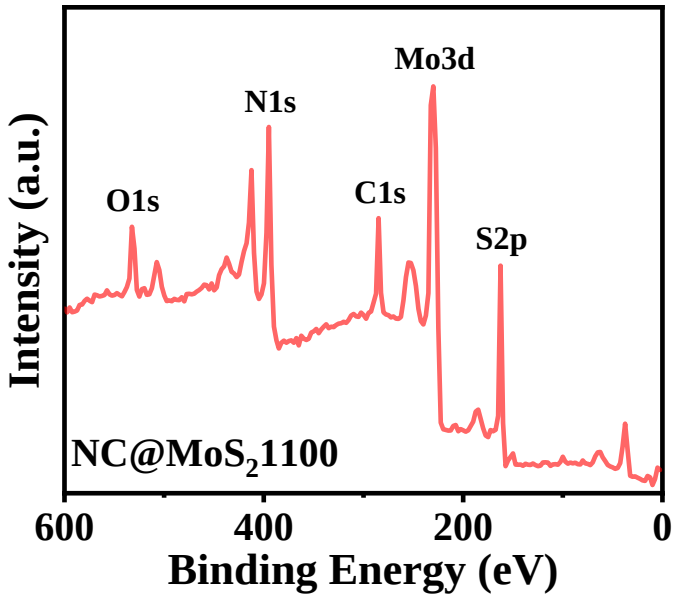

Figure 5.14: XPS survey scan spectrum of NC@$MoS_2$1100.

The weeny peak at ~ 281.8 eV is related to Mo−C bond presence in the hybrid [65]. The Mo 3d spectrum in Figure 5.15b was deconvoluted into five peaks, which are Mo (VI), Mo (IV), Mo (III), Mo (0) and S2s. Two characteristic peaks located at ~ 228.99 and ~ 231.93 eV correspond to the oxidation states of Mo (IV) [17,66,67] respectively. Further peaks at ~ 229.26 eV and 232.25 eV correspond to Mo (III) oxidation state [66,67]. Mo (IV) is

attributed to Mo in MoS_2 whereas lower oxidation state Mo (III) can be assigned to Mo−N bonding state. The later one confirms the presence of the Mo−N bonding state across the interface of the NC matrix and MoS_2 NSs [65–67]. Relatively weaker peaks at binding energies ~ 232.65 and ~ 235.71 eV are attributed to valence state Mo (VI) [22,66]. The reason behind the existence of these two peaks is surface oxidation. A small amount of Mo (IV) on the surface was oxidized in air [68]. Peak at ~ 228.7 eV corresponds to the Mo (0) state. Mo (0) is attributed to Mo−C bond, which is an active site for HER [69]. A very weak peak in the same spectrum at ~ 226.14 eV represents S2s state [22]. Fitting of the peak also reveals that 30 % of the Mo 3d spectrum corresponds to the oxidation state Mo (III), whereas a similar kind of analysis of Mo3d spectra for NC@$MoS_2$700 presented in Figure 5.16a reveals that 18.98 % of the total Mo 3d spectrum corresponds to Mo (III) oxidation state. These results indicate the presence of much higher Mo─N bonds with the increase in annealing temperature. The XPS spectrum for sulfur (Figure 5.15c) consists of two main peaks $S2p_{3/2}$ and $S2p_{1/2}$ at ~ 162.9 and 163 eV. A tiny peak at ~ 168.8 eV is attributed to the binding energy of sulfur in a sulphate group and originates from SO_4^{2-} residue [22]. N 1s peak in Figure 5.15d is further deconvoluted into 5 peaks. The intense peak at ~ 395.3 eV corresponds to Mo 3p core level [17, 69]. Peaks at ~ 398.3, 399.9 and 401.6 eV indicate the presence of active nitrogen species, i.e., pyridinic-N (N1), pyrrolic-N (N2) and graphitic-N (N3) which further implies successful incorporation of N in carbon matrix [17,65–67,70,71]. The presence of Mo─N bond can further be evidenced by the deconvoluted peak at ~ 397.4 eV [70,71]. Again, comparing the N1s plot of NC@$MoS_2$1100 with that of NC@$MoS_2$700 (Figure 5.16b), we found that the Mo−N contribution increases with the increase in annealing temperature. All these XPS results uphold the formation of Mo─N─C and Mo─C junctions between NC and MoS_2 NSs which is the consequence of strong bonding interactions at the interfaces [65–67,70,71]. Finally,

the asymmetric oxygen (O 1s) spectrum in Figure 5.17 for NC@MoS$_2$1100 is deconvoluted. Four peaks are situated at 533.2, 532.4, 531.1, and 530.2 eV, which can be assigned to C─OH, Mo─O, C─O/O─C─N, and O═C bonds, respectively [22]. The existence of Mo─O is because of surface oxidation [68]. C─OH, C─O/O─C─N and O═C bonds mainly arise from water absorbed on the carbon surface or the thermally stable groups in carbon except for oxygen [40].

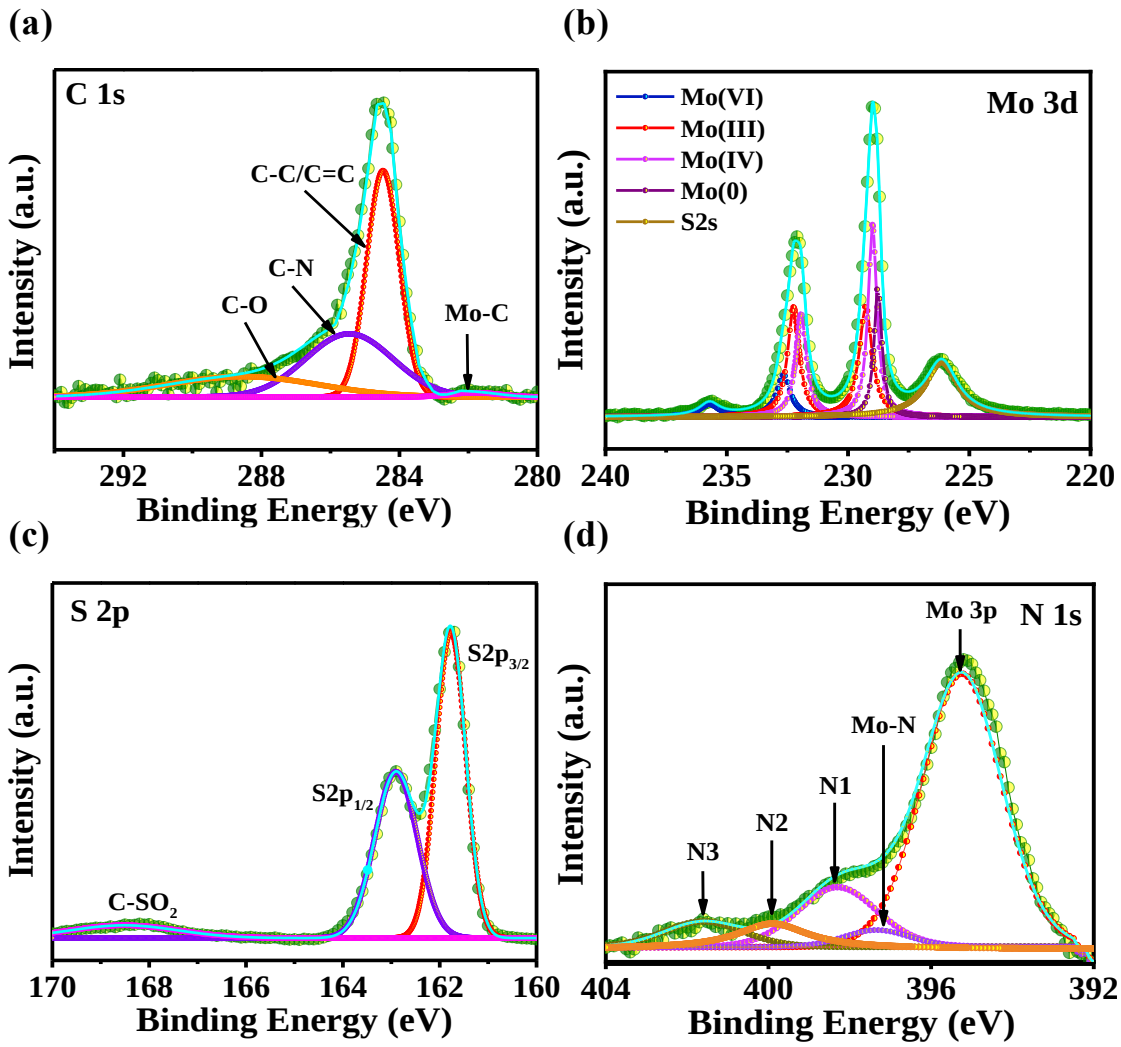

Figure 5.15: High resolution XPS spectra of (a) C 1s, (b) Mo 3d, (c) S 2p and (d) N 1s for NC@MoS$_2$1100.

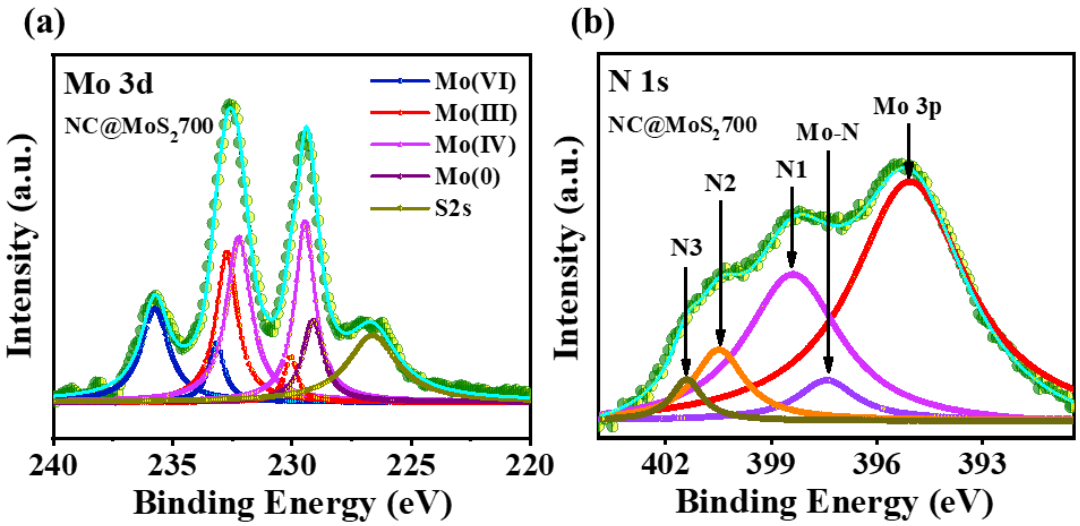

Figure 5.16: High resolution XPS spectrum of (a) Mo 3d and (b) N 1s for NC@$MoS_2$700.

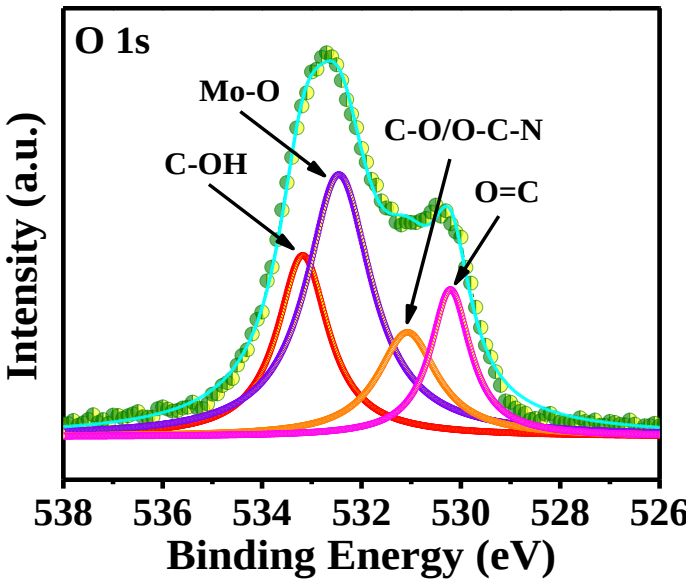

Figure 5.17: High resolution XPS spectrum of O1s for NC@$MoS_2$1100.

The presence of Mo—N—C bond in NC@$MoS_2$1100 can be further ascertained through Fourier transform infrared spectra (FTIR) analysis, as depicted in Figure 5.18. The absorption band at ~ 1407.7 cm^{-1} corresponds to Mo—N—C bond [66]. The band at 1460-1700 cm^{-1} can be attributed to stretching vibrations of C=C and C=N bonds [66]. This Mo—N—C bond can bridge carbon matrix and ultrathin MoS_2 NSs across the interface,

which could accelerate the charge transfer process and result in higher catalytic activity [65,67]. Alongside, successful doping of the heteroatom N inside the carbon matrix can also enhance the reactivity as well as conductivity.

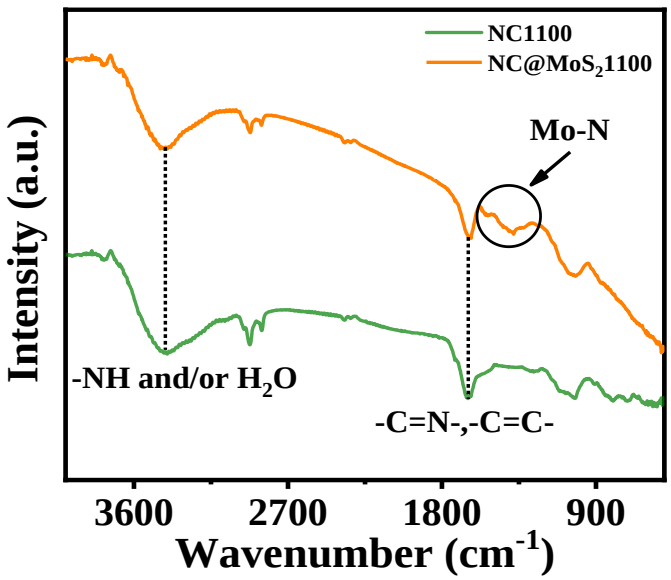

Figure 5.18: FT-IR spectra of NC1100 and NC@$MoS_2$1100.

5.2.2 Electrochemical activity for HER

The electrocatalytic activity of the as prepared samples was explored in a 0.5 M N_2 purged H_2SO_4 solution using a three-electrode system. The catalytic activity study is divided into two parts: (1) total electrode activity determination from linear sweep voltammetry (LSV) polarization curves and electrochemical impedance spectroscopy (EIS) analysis; and (2) inherent activity/turnover frequency (TOF) measurement from cyclic voltammetry (CV) curves.

5.2.2.1 Total Electrode Activity

The glassy carbon electrode (GCE) loaded with catalyst (loading ~ 0.21 mg cm^{-2}) undergoes a LSV experiment at a scan rate of 10 mV s^{-1}. Figure 5.20a. shows LSV polarization curves displaying HER activity for the as prepared samples. We have also

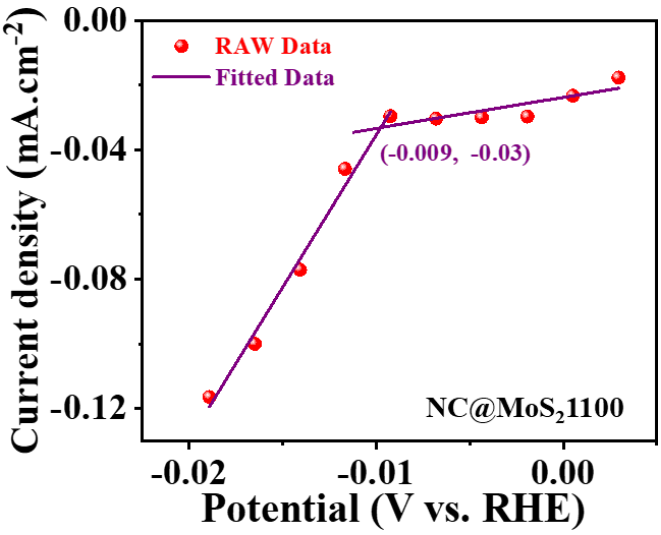

Figure 5.19: Fitted non-Faradic and Faradic zone in LSV curve for NC@$MoS_2$1100 for determination of onset overpotential.

tested the state of the art of Pt/C electrocatalyst for comparison. iR correction due to the ohmic potential drop resulting from solution resistance was carried out for all the measurements. Among all the prepared catalysts, NC@$MoS_2$1100 shows the superior electrocatalytic activity for H_2 evolution with a tiny onset overpotential (η) of nearly 9 mV (at a current density of 0.03 mA cm^{-2}) (Figure 5.19), which is very close to the overpotential (~ 0 mV) of commercial 20 % Pt/C. Besides, overpotential corresponding to current density j =10 mA cm^{-2} (η_{10}) is known to be an essential comparison parameter for HER activities. NC@$MoS_2$1100 only requires η_{10} = 145 mV to reach at j =10 mA cm^{-2}, whereas the η_{10} values for NC@$MoS_2$1000 and NC@$MoS_2$700 are found to be ~ 242 mV and 492 mV, respectively. Quite the reverse, PNMA and PNMA@MoS_2 show sluggish HER activity. Again, Figure 5.21a shows that the η_{10} values for separately prepared MoS_2 are much larger ~ 313 mV.

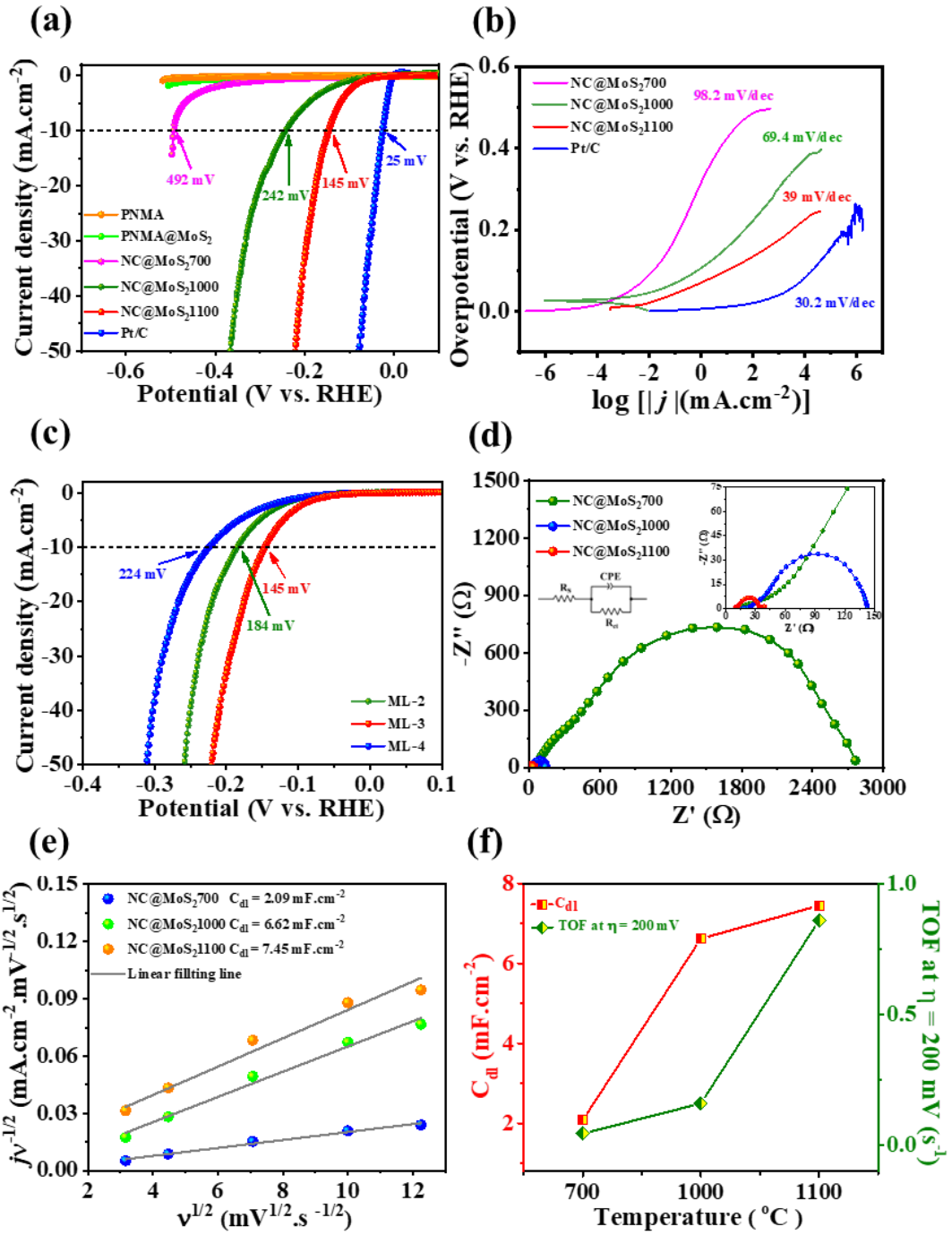

Figure 5.20: (a) LSV curves of as-synthesized samples and Pt/C (20 %); (b) Tafel plots of NC@MoS$_2$700, NC@MoS$_2$1000, NC@MoS$_2$1100 and Pt/C (20 %); (c) LSV curves of NC@MoS$_2$1100 with different mass loading; (d) Nyquist plots. (e) C_{dl} values determined from linear fitting of $j\nu^{-1/2}$ vs $\nu^{1/2}$, (f) C_{dl} and TOF values of NC@MoS$_2$700, NC@MoS$_2$1000 and NC@MoS$_2$1100 respectively.

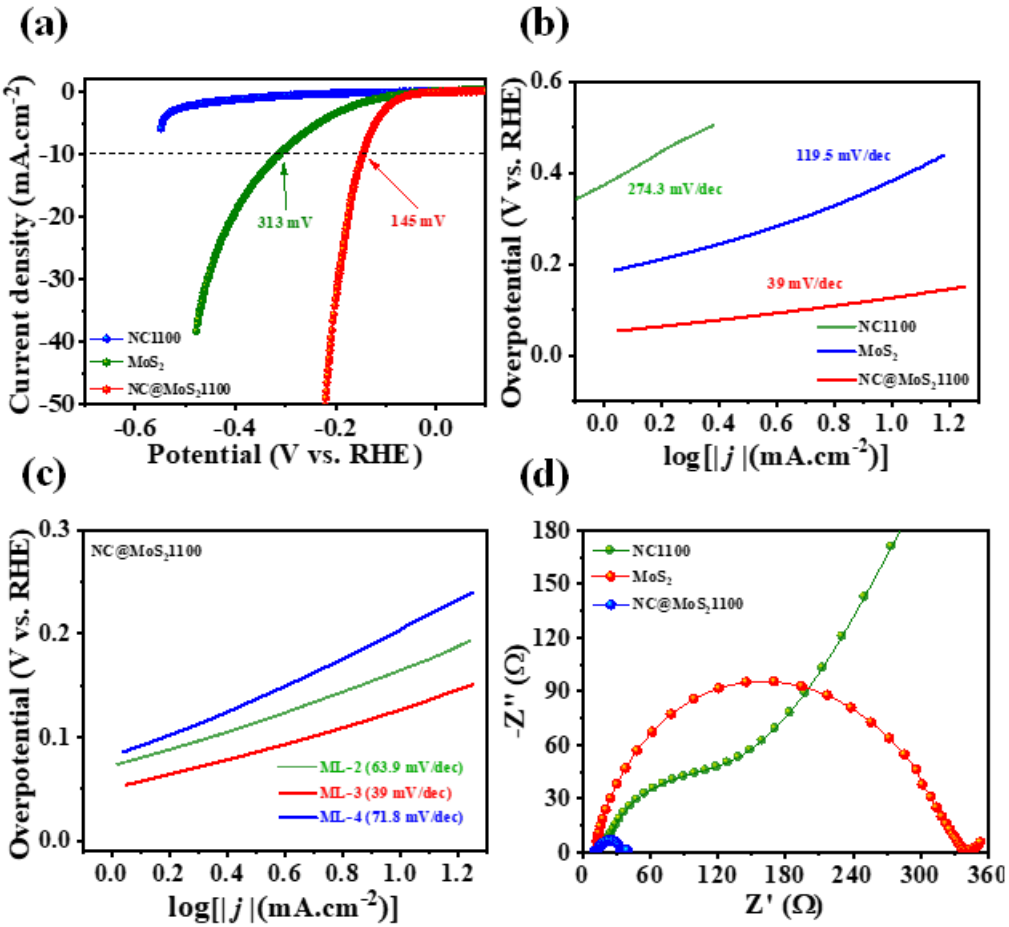

Figure 5.21: (a) LSV polarization curves and (b) Tafel plots of NC1100, MoS_2 and NC@$MoS_2$1100 respectively. (c) Tafel plots of ML-2, ML-3 and ML-4. (d) Nyquist plots of NC1100, MoS_2 and NC@$MoS_2$1100 respectively.

At the same time, NC annealed at 1100 °C (NC1100) did not achieve η_{10} within the scanning window. These results clearly suggest that modifications in MoS_2 NSs as well as in the inner sphere are mainly responsible for the observed differences in HER performance. Porous NSs structures, along with N doping in the system, reduced the energy input for the activation of HER process. This further indicates that the NC@$MoS_2$1100 heterostructure is acquired with much higher HER activity where interfacial Mo─N─C bonding states provide the path for faster electron transfer. Interaction between NC and the

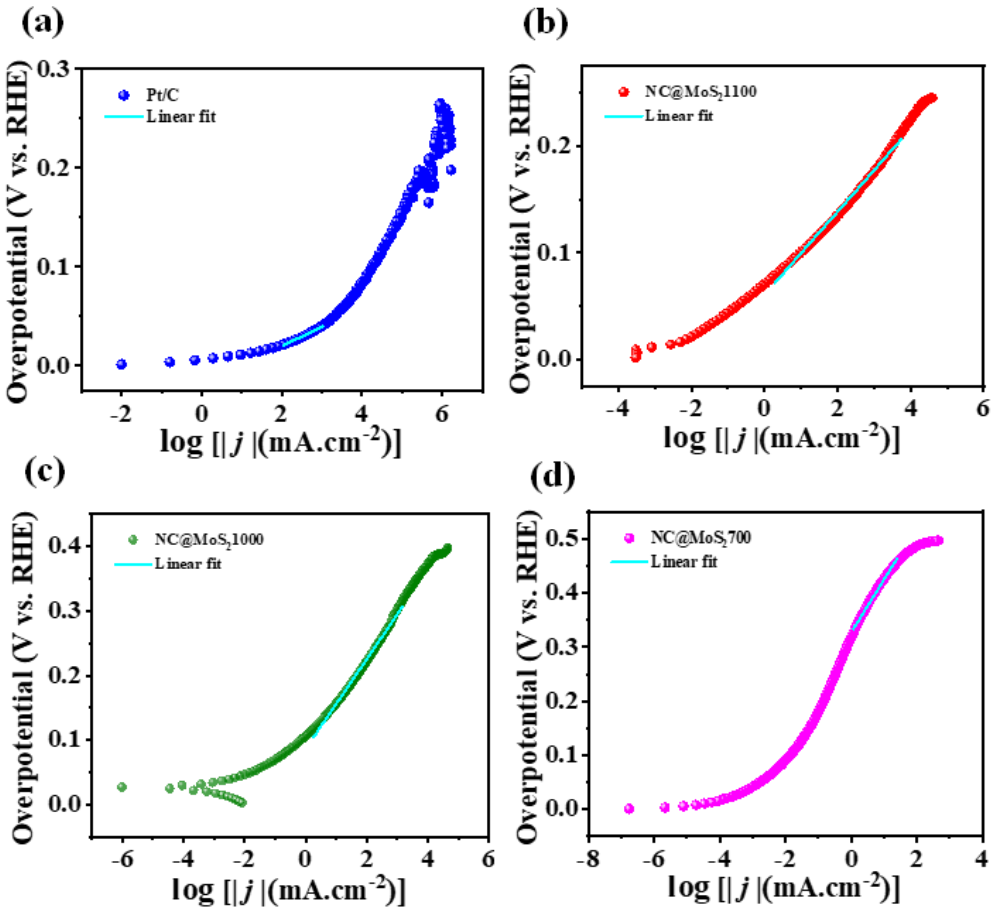

Figure 5.22: Tafel slopes determining regions for Pt/C, NC@$MoS_2$1100, NC@$MoS_2$1000 and NC@$MoS_2$700.

MoS_2 NSs via the Mo─N─C bond also endowed the hybrid system with ideal H_2 adsorption free energy, which guaranteed high electrocatalytic activity [17]. Careful comparison of Figure 5.20a and 5.21a suggests lower HER by NC@$MoS_2$700 than the same by MoS_2. One of the main reasons behind this phenomenon is that the as prepared MoS_2 via hydrothermal route is crystalline in nature. On the other hand, MoS_2 grown over an amorphous PNMA hollow sphere was found to be almost amorphous in nature (consisting of very faint (100) and (110) diffraction peaks of crystalline MoS_2). Though annealing at 700 °C increases crystallinity slightly in MoS_2 flakes in the NC@$MoS_2$700, it remains amorphous with no crystalline MoS_2 peak in RAMAN. Besides, the underlying polymer

does not transform fully into N-doped carbon, resulting in a lower chance of charge transfer interaction between MoS_2 and NC matrix through Mo─N─C bond. Hence, MoS_2 shows better electrocatalytic activity than NC@$MoS_2$700.

To have a better understanding of total electrode activity, the LSV polarization curves were further imprinted in a η vs. log | *j* | plot, known as a Tafel plot, following the Tafel equation $\eta = a + b \log |j|$ where 'b' is the Tafel slope and 'a' is the constant. From Figure 5.20b and Figure 5.21b, the Tafel slopes of NC@$MoS_2$1100, NC@$MoS_2$1000, NC@$MoS_2$700, MoS_2 and NC1100 are found to be 39 mV dec^{-1}, 69.4 mV dec^{-1}, 98.2 mV dec^{-1}, 119.5 mV dec^{-1}, and 274.3 mV dec^{-1} respectively. Besides, in Figure 5.20b, in which region Tafel slope has been determined is shown in Figure 5.22a-d. HER kinetics in an acidic electrolyte are governed by three reactions consisting of the Volmer, Heyrovsky and Tafel reactions, which illustrate the electron transfer kinetics [72,73].

Volmer reaction: $H_3O^+ + e^- \rightarrow H_{ads} + H_2O$ (5.1)

Heyrovsky reaction: $H_{ads} + H_3O^+ + e^- \rightarrow H_2 + H_2O$ (5.2)

Tafel reaction: $H_{ads} + H_{ads} \rightarrow H_2$ (5.3)

The Volmer reaction is the initial discharge step and has a Tafel slope ~ 120 mV dec^{-1}. On the other hand, the Heyrovsky reaction is the desorption step and the Tafel reaction is the recombination step, which provide Tafel slop of ~ 40 mV dec^{-1} and 30 mV dec^{-1} respectively [73]. The Volmer mechanism is followed by either the Heyrovsky or Tafel reactions. From the Tafel plots (Figure 5.20b and Figure 5.21b), it is clear that except for the commercial Pt/C catalyst, the lowest value of Tafel slope is associated with NC@$MoS_2$1100 catalyst. This demonstrates the dominance of the Volmer- Heyrovsky mechanism during electron transfer, which ensures superior HER kinetics. The necessary condition for a good HER electrocatalyst is a low Tafel slope at a high current density along with a tiny overpotential, which is satisfied by NC@$MoS_2$1100.

Exchange current density (j_0), an important index that indicates the electron transfer rate under zero overpotential, can be evaluated by extrapolating the Tafel plots to 0 V overpotential. The larger the value of j_0 signifies the faster HER kinetics. The j_0 value of NC@$MoS_2$1100 is found to be 1.14 mA cm^{-2} which is higher than that of NC@$MoS_2$1000, NC@$MoS_2$700. However, it is lower than the commercial 20 % Pt/C (j_0 = 1.45 mA cm^{-2}). For facile comparison, all the extracted parameters such as η_{10}, b, and j_0 for all the synthesized samples along with 20 % Pt/C are summarized in Table 5.3.

Sample	η_{10} (mV)	Tafel slope (mV dec^{-1})	j_0 (mA cm^{-2})	R_{ct} (Ω)
20 % Pt/C	25	30.2	1.45	-
NC@$MoS_2$1100	145	39	1.14	22
NC@$MoS_2$1000	242.6	69.4	1.09	120
NC@$MoS_2$700	492	98.2	0.48	2749

Table 5.3: Extracted parameters from LSV polarization curves and Tafel plots of Figure 5.20a-b.

To gain more insights about the effect of catalyst dosage on the overall performance, LSV measurements of the NC@$MoS_2$1100 hierarchical hybrid were further carried out with different mass loadings. Three different mass loadings of 0.14 mg cm^{-2}, 0.21 mg cm^{-2}, and 0.28 mg cm^{-2} on GCE are labeled as ML-2, ML-3, and ML-4, respectively, with which the same electrochemical measurements were repeated. It is evident from the curves in Figure 5.20c that all three curves (ML-2, ML-3, and ML-4) exhibit superior activity to that of NC@$MoS_2$1000. However, ML-3 exhibits the best performance compared to the other two. η_{10} value of ML-3 (145 mV) is found to be much lower than ML-2 (184 mV) and ML-4 (224 mV). The greater Tafel slopes of ML-4 (71.8 mV dec^{-1}) and ML-2 (63.9 mV dec^{-1})

than ML-3 (39 mV dec^{-1}) follows the previous result (Figure 5.21c). It is well documented that HER kinetics strongly depend on active edge sites. Thus, ML-4 should provide highest active sites and must deliver best catalytic activity. This is not the case here, as within the small area of GCE there must be an optimal quantity of mass loading, exceeding which may result in aggregation. This can be confirmed further from the electrochemical capacitance surface area (ECSA), explained in a later section. Agglomeration may decrease the exposed surface area of the NC@$MoS_2$1000 active sites. It can hinder the facile electron and ion diffusion, which results in the observed sluggish catalytic performance [16,74].

EIS is an essential measurement that provides us with information about HER kinetics at the interface of electrode and electrolyte. EIS measurements for all the samples were carried out within the frequency window of 100 kHz to 0.01 Hz with an ac perturbation of 10 mV in potentiostatic mode. The magnified nyquist plot for NC@$MoS_2$1100 and NC@$MoS_2$1000 is shown in the inset of Figure 5.20d. The reason behind the superior HER kinetics in NC@$MoS_2$1100 than the rest is due to an effective curtailment in the charge transfer resistance (R_{ct}) shown in the Nyquist plot (Figure 5.20d). The diameter of the semicircle observed in the medium frequency region in Nyquist plot on the Z′ axis is the measure of R_{ct}. The enumerated R_{ct} values in Table 5.3 for the entire sample reveal that NC@$MoS_2$1100 possesses R_{ct} = 22 Ω. This R_{ct} value is very small as compared to that of NC@$MoS_2$700 and NC@$MoS_2$1000. It indicates fast and efficient electron transfer at the electrode-electrolyte interface of NC@$MoS_2$1100. Figure 5.21d indicates that the R_{ct} values of NC@$MoS_2$1100 and NC1100 are very small compared to those of solid crystalline MoS_2. Hence, it can be concluded that the hierarchy of MoS_2 over NC1100, and hence Mo─N─C bond across the interface, accelerates the charge transfer process. EIS plots in Figure 5.20d reveal that all the samples associated with a dominant capacitive semicircle at medium

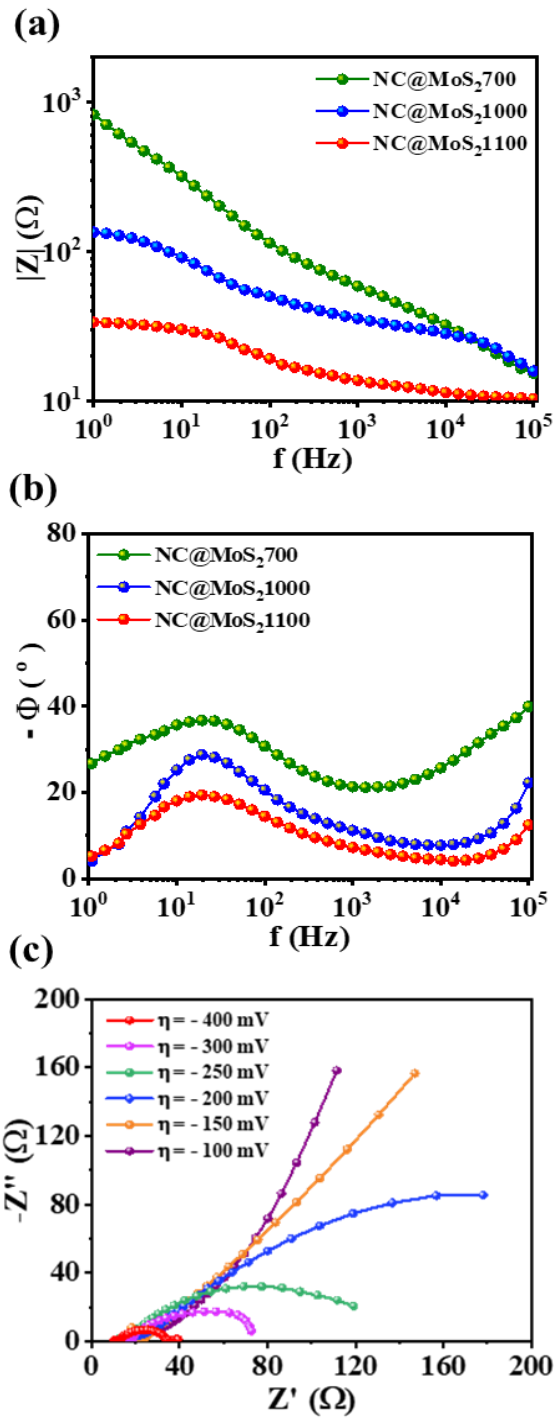

Figure 5.23: (a-b) Bode phase plot of NC@$MoS_2$700, NC@$MoS_2$1000 and NC@$MoS_2$1100 respectively, (c) Nyquist plots of NC@$MoS_2$1100 taken at different overpotential.

frequency range, indicating that the catalytic reaction was characterized by a time constant consisting of a peak at $f \sim 19$ Hz corresponding to the semicircle (as seen from Bode Plots in Figure 5.23a-b. Aside from the dominant semicircle at medium frequency, careful observation reveals that the EIS spectra in Figure 5.20d also contains an additional pattern at high frequency region, which is not exactly straight line and can be considered as an incomplete arc that can be attributed to non-Faradaic origins and were attributed to the distributed resistance inside the electrode or the contact resistance. Qualitatively, the EIS spectra of NC@$MoS_2$1100 showed a much smaller high frequency arc than the rest, indicating less contact resistance and higher catalytic activity for NC@$MoS_2$1100. Further, the CPE is used as a pseudo-capacitive element, corresponding to a combination of capacitive and charge-transfer processes. It is frequently used to model the influence of surface heterogeneity on double-layer behavior. It is shown that charge transfer

resistance (R_{CT}) increases at positive potential (near onset potential), which is well corroborated with the lower active sites. Notably, after -200 mV, the EDLC nature dominates the charge transfer phenomenon shown in Figure 5.23c.

5.2.2.2 Inherent Activity / Turnover Frequency (TOF)

The inherent per-site catalytic activity is another essential parameter to develop a powerful electrocatalysts for clean hydrogen technology. To estimate it, the value of ECSA was determined for all the synthesized samples. The density of these active sites is termed as per-site turnover frequency (TOF) [75]. ECSA is proportional to non-faradic capacitance (C_{dl}) which was calculated from cyclic voltammetry (CV) curves measured at different scan rates (ν) within the potential window 0.15 – 0.25 V vs. RHE (Figure 5.24a-e). In a cyclic voltammogram, if the current density (j) is exactly proportional to ν, the response is purely non-faradic. On the other hand, if j is exactly proportional to $\nu^{1/2}$ the response is purely faradic. Here, the CV curves resembled pseudo-rectangular shapes, but the response from the samples was not purely non-faradic. Thus, current density can be expressed as a sum of both non-faradaic and faradaic response: $j = k_1 \nu + k_2 \nu^{1/2}$ which can further be rearranged as $j \nu^{-1/2} = k_1 \nu^{1/2} + k_2$ [76]. Half of the difference between cathodic and anodic current density ($j_{0.2V}$) at different scan rates from the CV curves at 0.2 V vs RHE was calculated first. Thereafter, from the linear fitting of $j_{0.2V} \nu^{-1/2}$ vs $\nu^{1/2}$ for different scan rates, the capacitance contribution k_1 and k_2 are estimated (Figure 5.20e). The assessed value of the non-faradaic capacitance $C_{dl} = k_1$ for NC@$MoS_2$1100 is 7.45 mF cm^{-2}. The same value for NC@$MoS_2$1000 and NC@$MoS_2$700 is found 6.62 and 2.09 mF cm^{-2} respectively. A comparative study of CV curves at a scan rate of ν = 100 mV s^{-1} for NC@$MoS_2$1100, MoS_2, and NC1100 is shown in Figure 5.24f, which indicates the ECSA for NC@$MoS_2$1100 is much higher than that of NC1100 and MoS_2. The C_{dl} values for NC1100 and MoS_2 are 1.10

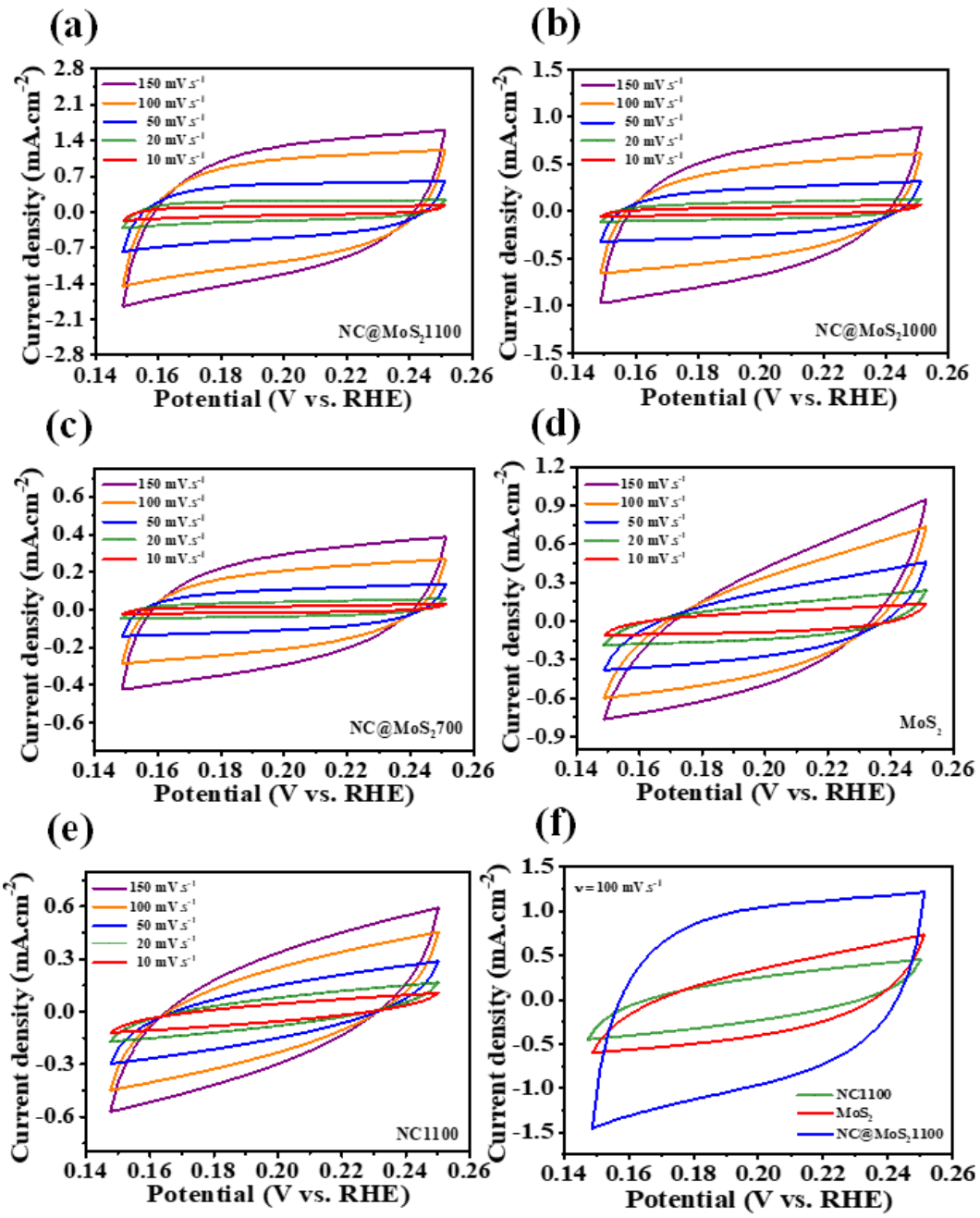

Figure 5.24: CV curves measured at different scan rate ν within the potential window 0.15 – 0.25 V vs RHE of (a) NC@$MoS_2$1100, (b) NC@$MoS_2$1000, (c) NC@$MoS_2$700, (d) MoS_2 and (e) NC1100 respectively. (f) CV curves of NC1100, MoS_2 and NC@$MoS_2$1100 at scan rate of ν = 100 mV s^{-1}.

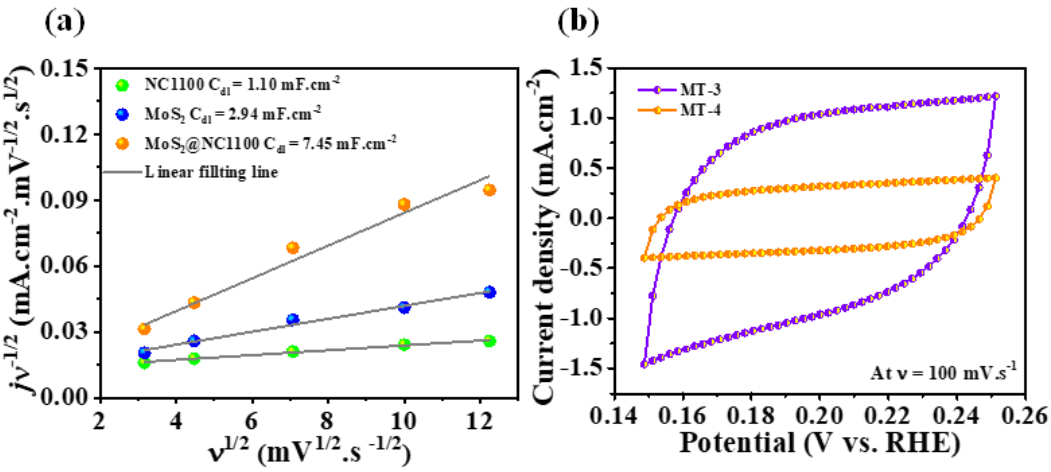

Figure 5.25: (a) C_{dl} values of NC1100, MoS_2 and NC@$MoS_2$1100 determined from linear fitting of $jv^{-1/2}$ vs $v^{1/2}$ plots. (b) CV plots of ML-3 and ML-4 at a scan rate of v = 100 mV s^{-1}.

and 2.94 mF cm^{-2} respectively (figure 5.25a). These results indicate that both hierarchy formation and an increase in annealing temperature resulted in higher ECSA. The previously mentioned inferior catalytic performance registered from greater mass loading of catalyst (ML-4) than ML-3 and ML-2 is further confirmed from the CV plots at a scan rate of v = 100 mV s^{-1} (Figure 5.25b). ECSA values for ML-4 are found to be low as compared to ML-3. This result corroborates with catalyst dosage-dependent HER activity.

The roughness factor (RF) was also estimated from the ratio of the calculated C_{dl} values. RF can be expressed as:

$$RF = \frac{\text{Non-faradaic capacitance of catalyst}}{\text{Non-faradic capacitance of flat standard}}$$

Considering the C_{dl} value of the flat MoS_2 standard electrode (~ 60 µF cm^{-2}) [77], RF value for NC@$MoS_2$1100 was calculated to be 124.167. Using this value, the per-site TOF of NC@$MoS_2$1100 electrode is calculated further. For detailed calculations, please see the supporting information. The per-site TOF of NC@$MoS_2$1100 at η = 200 mV corresponding to the current density of j = 34.38MA cm^{-2} was found to be 0.86 s^{-1}. This value is almost

equal to the previously reported per-site TOF value for crystalline MoS_2 [12]. Figure 5.20f demonstrates the correlation of annealing temperature with non-faradaic capacitance C_{dl} and per-site TOF of evolved H_2 at η = 200 mV (for the electrocatalysts NC@$MoS_2$700, NC@$MoS_2$1000, and NC@$MoS_2$1100). Both C_{dl} and per-site TOF values increase with temperature, and thus maximum values for NC@$MoS_2$1100 are evident from this figure. Banking on these beneficial traits, NC@$MoS_2$1100 delivered superior HER activity.

5.2.3 Electrochemical Stability

Electrochemical stability is another pertinent feature of a catalyst, as commercial device realization demands durability and long-term stability. Hence, a continuous 10000 CV scan was carried out for the NC@$MoS_2$1100 electrode between the potential windows of -0.2 V to 0.2 V vs. RHE at a scan rate of 100 mV s^{-1}. Figure 5.26a depicts the LSV curves before and after 10,000 CV cycles. LSV curves almost overlap with each other. A very nominal shift in the overpotential values and a shift of $\Delta\eta_{10} \sim 12$ mV vs. RHE at j =10 mA cm^{-2} are observed. A chronoamperometric study was further carried out at -0.145 V for the period of 24 hours, which (Figure 5.26b) shows a noticeable stability with current density stable at j =10 ± 0.75 mA cm^{-2}. To support the excellent durability of NC@$MoS_2$1100, ECSA and C_{dl} were also determined after chronoamperometric study by taking CVs in the same potential window. As the electrochemical surface area (ECSA) is directly proportional to C_{dl}, the higher value of C_{dl} indicates a higher ECSA and hence, the formation of the most active sites. The calculated ESCA shows minor degradation from the initial values after long term durability test which results in slight decrease (0.9 mF cm^{-2}) in C_{dl} values. It is clearly visible from the Figure 5.27a-b. This further confirms the durability of NC@$MoS_2$1100 in acidic medium.

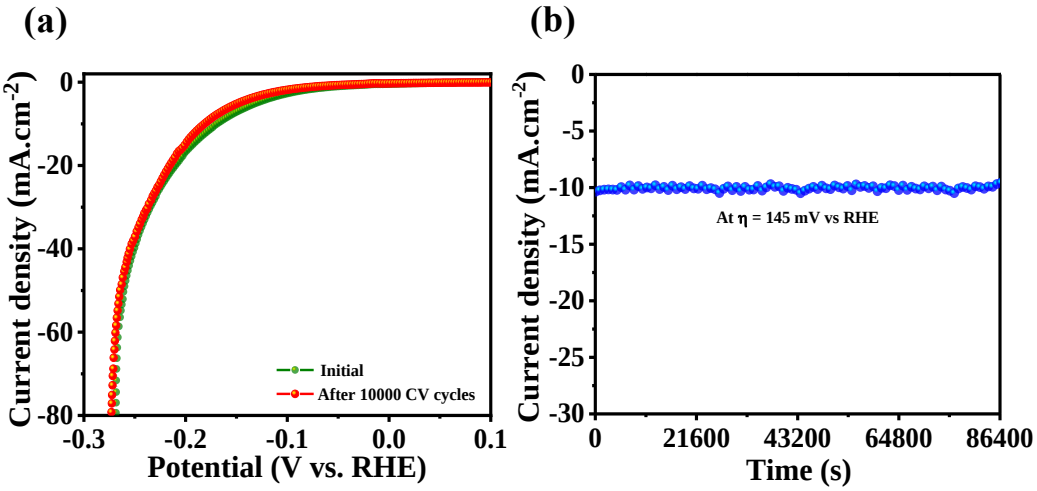

Figure 5.26: (a) LSV curves initially and after 10000 CV cycles respectively, (b) chronoamperometry curve at overpotential of η = 145 mV vs. RHE corresponding to the current density of j = 10 mA cm^{-2} for 24 h of NC@MoS$_2$1100.

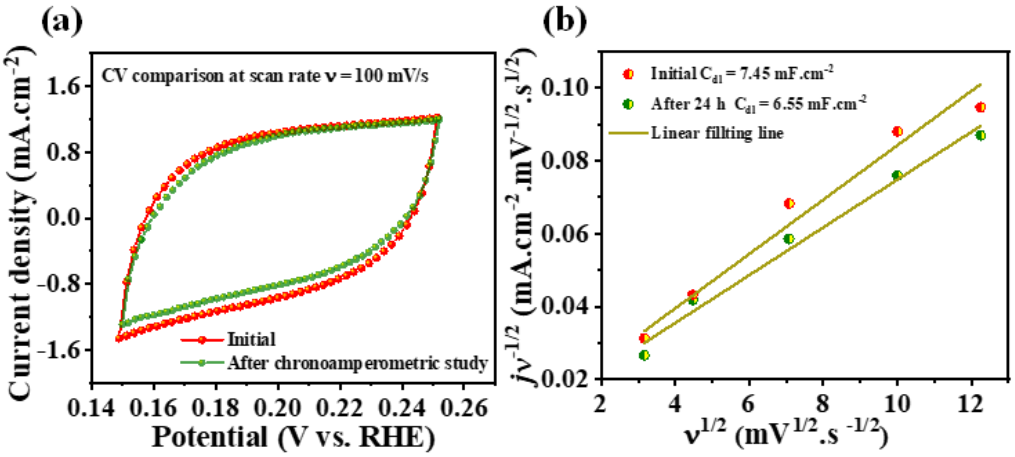

Figure 5.27: ECSA and C_{dl} values of NC@MoS$_2$1100 before and after chronoamperometric stability test.

Further, XPS and XRD method are two suitable characterization tools to determine the surface-active Mo-N-C bond for hydrogen evolution reaction. High resolution XPS spectra of C 1s, Mo 3d, S 2p and N 1s for NC@MoS$_2$1100 after catalysis is shown in

Figure 5.28a-d. From Mo 3d and N 1s spectra, the percentage of Mo-N bond decreases to 1.7 % and 3.17 % respectively (Table 5.4 and 5.5). Additionally, the increment in the percentage of Mo(VI) bond is mainly due to surface oxidation from Mo(IV) to Mo(VI) due to electron donation to intermediate H* ion in the Volmer-Heyrovsky mechanism. However, the intensity of the graphitic (002) plane is highly diminished due to its involvement in the catalytic mechanism (Figure 5.29). In contrast, the intensity of the out-of-plane (002) peak also changes, which eventually leads to the conclusion that the restacking probability of the nanosheet also plays a role in the catalytic mechanism. Hence, we can say that the Mo-N-C bond is relatively stable during the HER process.

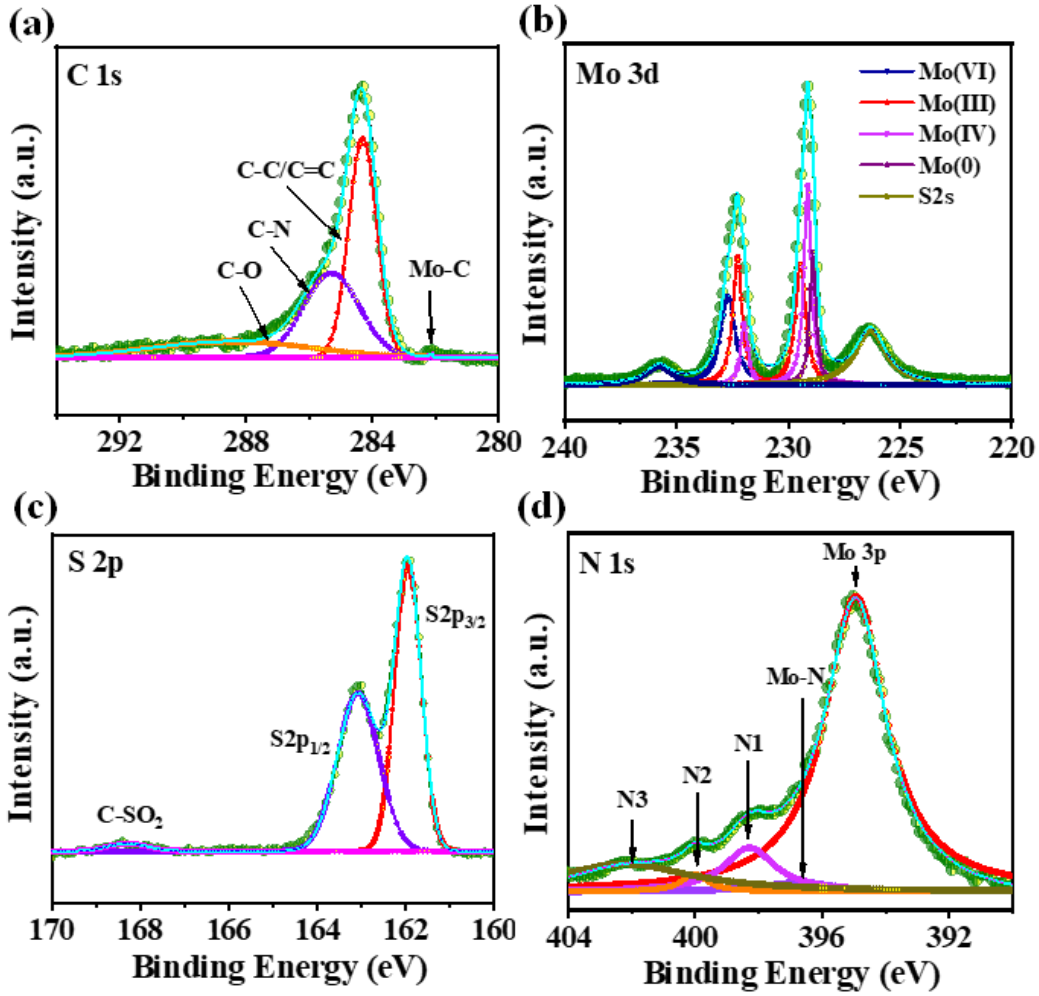

Figure 5.28: High resolution XPS spectra of (a) C 1s, (b) Mo 3d, (c) S 2p and (d) N 1s for NC@$MoS_2$1100 after catalysis.

Mo 3d	Before Catalysis (%)	After Catalysis (%)
Mo(VI)	9.3	20.88
Mo(IV)	30.55	21.98
Mo(III)	30.02	28.31
Mo(0)	10.33	9.33
S2s	19.8	19.50

Table 5.4: Atomic percentage of Mo components of Mo 3d XPS spectra before and after catalysis.

N 1s	Before Catalysis (%)	After Catalysis (%)
Mo 3p	74.35	72.14
Mo-N	5.71	2.54
N1	10.17	8.81
N2	1.59	1.82
N3	8.18	14.69

Table 5.5: Atomic percentage of nitrogen components of N 1s XPS spectra before and after catalysis.

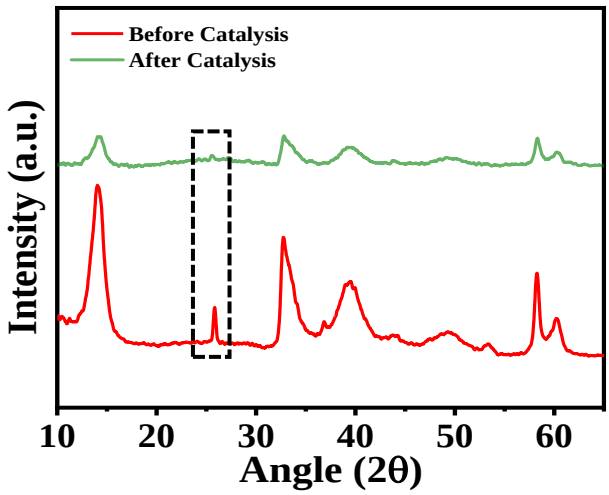

Figure 5.29: XRD profiles of NC@$MoS_2$1100 before and after catalysis.

A comprehensive study on the NC@$MoS_2$1100 indicates that the NC hollow sphere, along with its interfacial interaction with MoS_2 NSs, powers the hybrid to acquire enormous active sites. Hence, an N-doped hollow carbon sphere matrix derived from the pyrolysis of PNMA-based polymer along with the simultaneous formation of a crystalline MoS_2 NSs hierarchy surrounding the NC sphere results in the formation of Mo—N—C channel across the interface, which makes NC@$MoS_2$1100 one of the best reported NC@MoS_2 based electrocatalysts. The catalytic features of this unique electrocatalyst are further compared with those of various previously reported MoS_2-based catalysts shown in Table 5.6.

Catalyst	Mass loading (mg cm^{-2})	Tafel slope (mV dec^{-1})	j (mA cm^{-2})/ η (mV)	C_{dl} (mF cm^{-2})	TOF at η (s^{-1})	Ref
Double-gyroid MoS_2 films	-	50	-	1.1-4.8	-	[78]
MoS_2 / N-doped carbon nanofiber	-	61	8.7 / 200	16.5	-	[79]
MoS_2 / graphene hierarchy on carbon cloth	0.13	53	10 / 78	-	-	[80]
IE-MoS_2 Nanosheets	0.305	41	10 / 167	40.4	-	[81]
Defective-MoS_2 / rGO heterostructures	-	56.17	10 / 154.77	25.98	-	[82]
3D MoS_2-rGO@Mo nanohybrids	-	44	10 / 149	24.6	0.43	[83]
Ru-MoS_2 / CNT	-	62	10 / 50	27.5	-	[84]
MoS_2 nanoflake / CNT	0.286	47	850 / 290	31	-	[85]
Amorphous MoS_2 / graphene CNT	3	41	10 / 141	204	0.14	[86]
MoS_2-Pt NSs / S, N-doped carbon	0.57	55.7	10 / 102	14.9	-	[87]
Pt-decorated MoS_2 / N-doped carbon	0.552	104.2	10 / 20	14.3	-	[14]
MoS_2 nanoparticles / N-doped carbon	0.28	60.3	10 / 152	2.14	-	[88]
CoFe / N-doped carbon / MoS_2	-	45	10 / 64	11.2	-	[9]
Co_9S_8 / N-Doped Carbon/ MoS_2	0.283	68.8	10 / 117	22.98	-	[89]
MoS_2 NSs inlaid in 3D fibrous N-doped carbon	0.535	54	10 / 194	34.3	-	[90]
Hierarchically N-doped carbon nanosheets	0.286	81	10 / 203	47.2	0.066	[91]
S and N doped carbon nanosheets	0.285	67.8	10 / 116	27.4	-	[47]
N and S co-doped nanoporous graphene	-	80.5	10 / 280	-	-	[48]
Conducting Polymer/MoS_2	0.90	76.3	10 / 280	0.708	-	[92]
Defect-rich MoS_2 ultrathin nanosheets	0.285	50	N.A.	-	0.725	[93]
Amorphous MoS_2	-	60	10 / 200	5.4	0.3	[77]
Hollow micro / nano MoS_2 spheres	0.205	74	10 / 214	15.1	0.11	[94]
NC@$MoS_2$1100	**0.21**	**50.6**	**10 / 145**	**7.45**	**0.86**	**This work**

Table 5.6: Comparison of the HER performance of NC@$MoS_2$1100 hierarchical hybrid with other molybdenum sulfide based electrocatalysts.

This Table shows that the fabricated NC@$MoS_2$1100 based electrode outperforms previously reported electrocatalysts such as NC@MoS_2 based hybrid, NC based morphology, and MoS_2 nanoforms. Along with the standard design of the NC@MoS_2 hierarchy, the synergistic effect of the interfacial Mo─N─C bond ensures that the hollow space inside the NC sphere accumulates a large volume of electrolytes and facilitates electrochemical reactions [95] as NC hollow sphere can have a more accessible catalytic site for reactions as compared to a solid sphere. This distinctive morphology of the hybrid ensures low diffusion energy for the migration of ions/electrons through the porous shell, which further promotes the complete utilization of the electroactive materials. Besides, its viability in acidic electrolytes makes it a potential novel electrocatalyst for future hydrogen technology.

5.3 DFT Analysis

The annealing temperature noticeably affected the overall morphology, phase transformation, crystallinity, and composition of the NC@MoS_2 hybrid and delivered different catalytic activities. Density functional theory (DFT) simulations were further employed to gain insights into the NC@MoS_2 hybrid as well as to understand the impact of the Mo−N−C bond in improving the overall HER activity. The interfacial Mo−N−C bond structure model is shown in Figures 6a and 6b with top view and side view, respectively, and the model is used to determine the free energy change of hydrogen atom adsorption (ΔG_H) on various active sites of NC with a single C vacancy. It is well known that an active HER catalyst has an adsorption free energy of H (ΔG_H) near zero [96–99]. This step is known as the Volmer step and can be considered a measure of overpotential (η) for HER. To estimate the efficiency of HER, six active sites were considered, three sites of the NC system and three sites of NC@MoS_2 heterostructure system (shown as red and black circle

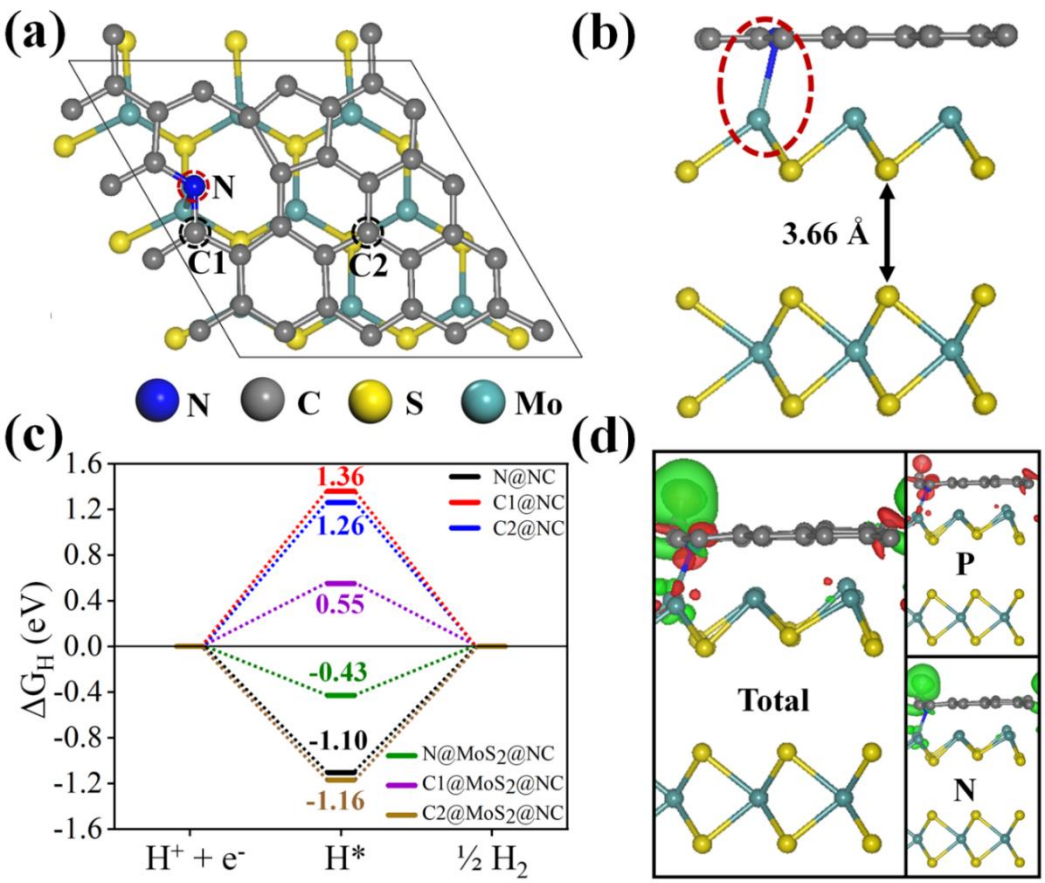

Figure 5.30: Model structures of NC@MoS_2 heterostructure (a) Top View, (b) Side view (c) Calculated HER free energy (ΔG_H) diagram of nitrogen and carbon sites for NC@MoS_2. (d) Calculated charge density difference for the NC@MoS_2 heterostructure with the adsorption of H, where the iso-surface value is set to be 0.002 e/Å^3 and the positive (P) and negative (N) charges are shown in red and green, respectively.

in Figure 5.30a). On the NC system, the hydrogen binding free energy on top of the C1 and C2 sites is 1.26 eV and 1.36 eV, respectively (Figure 5.30c), which is significantly lower. The step is highly endothermic with a high +ve overpotential. Then again, on N site ΔG_H is -1.10 eV which indicates a high -ve overpotential step. Thus, the overall NC system alone is not a suitable catalyst for HER, and further modification is required to make the surface efficient. The scenario is completely different in the NC@MoS_2 system. In the

heterostructure, the N atom forms a Mo−N−C bond by combining with the Mo of MoS_2 (Figure 5.30b). The C atoms in the NC@MoS_2 structure have moderate binding energies with the H atom, indicating that they are the active catalytic sites for the HER process. The N site of NC@MoS_2 structure clearly has the best HER catalytic activity (ΔG_H = -0.43 eV). Overall, a low overpotential | η | = 0.43 V for HER is also found on this heterostructure.

Surface	Bader charge Before adsorption (e)		
	On Mo-atom	On N-atom	On C-atom
NC and MoS_2	-0.533	1.242	-0.524
	Bader charge After adsorption (e)		
	On Mo-atom	On N-atom	On C-atom
NC- MoS_2	-0.951	1.246	-0.464
	Bader charge After H adsorption (e)		
H- NC/MoS_2	On Mo-atom	On N-atom	On C-atom
	-1.000	1.141	-0.356

Table 5.7: Bader charge of before and after adsorption for NC@MoS_2 on different atoms.

In order to check the role of the Mo−N−C bond in enhancing HER activity, Bader charge analysis was also performed, which showed that charge transfer occurs mostly from the Mo atom to the N atom at the Mo−N−C bond, which makes the Mo−N bond stronger (Table 5.7). There is also a charge transfer from the N atom to the neighbouring carbon atom, which facilitates the hydrogen adsorption. The charge density difference of NC@MoS_2 with Hydrogen adsorption was also calculated (Figure 5.30d). Results show that such charge transfer decreases the Gibbs free energy change for hydrogen adsorption on the N

site and increases it on the C site, resulting in higher activity towards HER on sites near the Mo–N–C bond. The density of states (DOS) also showed that the Mo–N bond increases the electron states near the Fermi level (Figure 5.31), indicating high electrical conductivity and carrier density. Hence, the interfacial contact between NC and MoS_2 results in ideal H atom binding strengths on the active sites and decreases the overpotential for HER.

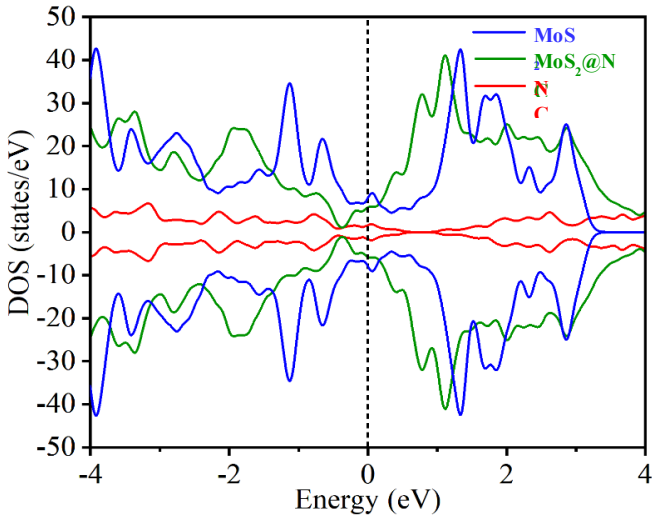

Figure 5.31: Total electronic density of states for NC, MoS_2 layer, and NC@MoS_2 heterostructure.

5.4 Conclusions

In a word, we realized a hierarchical structure composed of few-layer MoS_2 NSs supported by PNMA hollow spheres for high-performance electrochemical HER. In the fabrication, a PNMA hollow polymer spherical nanostructure is first prepared by the interfacial polymerization method, followed by a few layers of MoS_2 NSs being in-situ realized on top of it via a hydrothermal process. Subtle variations in annealing temperature changed the overall crystallinity as well as converted the underlying PNMA sphere to N-doped carbon through carbonization, both of which strongly impacted the catalytic performance. Benefiting from the prospective combination of a typical hollow flower-like

structure, a protective layer of NC, and intimate Mo–N–C bonds at the NC@$MoS_2$1100 interface, the optimized integrated hierarchy displayed high HER performance with a low overpotential of 145 mV at 10 mA cm^{-2} and a small Tafel slope of 39 mV dec^{-1} in acidic media. In our synthetic procedure, flower-like MoS_2 sheets are assembled on the surface of the PNMA sphere and exhibit a large internal void due to the different diffusion rates of the various atoms (Kirkendall effect). At high annealing temperatures, the high diffusion rate and PNMA layer inhibit the aggregation of MoS_2 layers to produce ultrathin MoS_2, which is well correlated with our HRTEM analysis. On the other hand, high etching of sulfur at the edge of the surface creates a dangling bond near Mo and promotes functionalization with the N-C bond. Thus, at higher temperatures, the graphitic Mo-N-C bond predominates for NC@$MoS_2$1100 over other materials, which further accelerates the charge transfer process during HER. Besides, the NC@$MoS_2$1100 sample has exceptional electrochemical durability. LSV curves of the same electrode before and after 10000 CV cycles of operation almost overlap with each other, and a very nominal shift in overpotential and $\Delta\eta_{10}$ values is observed. A protective NC layer could reinforce the structural robustness of the hierarchy and circumvent the corrosion of MoS_2 NSs, thus providing good electrochemical stability. DFT simulations strongly corroborate the observed superior catalytic activity of the NC@MoS_2 and reveal that it is due to the optimal charge transfer from the Mo atom to the N atom at the Mo−N−C bond as well as the N atom to the neighbouring C atom, which promote the H^+ interaction and H_2 adsorption. These charge transfers reduce the Gibbs free energy and thus improve the overall HER performance. DOS analysis further suggests Mo−N bond increases in electron states near the Fermi level, indicating high electrical conductivity and carrier density. Interfacial contact between NC and MoS_2 also decreases the overpotential for HER. Thus, this work highlights the impact of interfacial chemical

bonds and engineering over sample architecture, phase, and crystallinity by controlling annealing temperature for electrocatalytic HER performance enhancement.

5.5 Material Synthesis and Characterization

5.5.1 Materials

N-methylaniline (NMA), poly (methyl vinyl ether-alt-maleic acid) and Thioacetamide (C_2H_5NS) were purchased from Sigma-Aldrich. Ammonium persulphate, Sodium Molybdate (Na_2MoO_4) and Sulfuric acid (H_2SO_4) were procured from Merck. All solutions were prepared using deionized water (D. I.) (18 MΩ, Millipore).

5.5.2 Synthesis of PNMA@MoS_2 hybrid heterostructures

PNMA hollow polymer spherical nanostructure was synthesized by the interfacial polymerization method using poly (methyl vinyl ether-alt-maleic acid) as a polymeric surfactant, explained in our previous work [53]. To prepare PNMA@MoS_2, 10 mg Na_2MoO_4 and 20 mg C_2H_5NS were mixed with 80 mL of D. I. water. 100 mg of PNMA was added to the aforesaid solution and stirred vigorously. Then the blackish solution was transferred to a 100 mL Teflon-lined stainless-steel autoclave, and the autoclave was placed inside a laboratory oven at 200 °C for 24 h. After the reaction period, the autoclave was allowed to cool down naturally. The precipitated sample was washed with copious amounts of D. I. water multiple times and collected via centrifugation. Thereafter, it was dried overnight at 60 °C to yield solid PNMA@MoS_2. Finally, as synthesized, PNMA@MoS_2 was annealed using a tube furnace in an inert nitrogen atmosphere at different annealing temperatures (700, 1000, and 1100 °C). PNMA@MoS_2 samples annealed at 700, 1000, and 1100 °C are henceforth designated as NC@$MoS_2$700, NC@$MoS_2$1000 and NC@$MoS_2$1100 respectively. For comparative study, a PNMA hollow sphere without

secondary MoS_2 growth was also annealed at 1100 °C. This sample is coined as NC1100 henceforth.

5.5.3 Physical and Chemical Characterization

Crystallinity and phase purity of the as prepared nanoforms were checked by XRD (D8 Advanced Bruker) and TEM (JEOL JEM-2100). WITec alpha 300RA Raman Confocal Microscope was used to record Raman spectra. Morphological analysis of the sample was carried out using FESEM (Carl Zeiss Microscopy, ΣIGMA). XPS and EDX measurements were carried out to investigate elemental composition. The Brunauer–Emmett–Teller (BET) surface area and porosity of all the synthesized samples were measured using the Quantachrome NovaWin2 Instrument. AFM characterization was carried out using the Agilent Technologies 5500 (CA, USA) operated in contact mode.

5.5.4 Electrochemical Characterization

All the measurements were carried out using a standard three electrode system at ambient temperature (a PGSTAT 302N Autolab set-up). For HER measurements, catalyst ink was prepared by adding 1.5 mg of catalyst to a 285 mL ethanol (99.99 %) - deionized water in a 1:3 ratio. The solution was then ultrasonically heated for a few minutes to get a uniform black solution. Finally, 15 µL of 5 wt% Nafion was added to the black solution and sonicated further for a few minutes to obtain the catalyst ink. 3 mL of the uniform ink suspension was then drop-casted on a glassy carbon electrode (GCE) and air-dried for 30 minutes to obtain the working electrode. Ag/AgCl and graphite wire were used as reference and counter electrodes, respectively. All the potentials obtained in our measurements were further converted to reversible hydrogen electrodes (RHE) using the relation:

$$E_{RHE} = E_{Ag/AgCl} + 0.059\,\text{pH} + 0.196\,\text{V} \quad (5.4)$$

iR correction was further carried out manually depending on the EIS results as there exists Ohmic potential drop resulting from solution resistance. The corrected potential was estimated following the relation:

$$E_{corrected} = E_{measured} - iR_s \quad (5.5)$$

where, R_s is the series resistance determined from the intercept of the nyquist plot on the Z′ axis. Before performing the experiment, it is necessary to activate the catalytic property towards HER. Hence, the working GCE electrode initially suffered 15 LSV cycles from -0.5 V to 0.1 V vs RHE. 0.5 M aqueous solution of H_2SO_4 was used as electrolyte. Linear sweep voltammetry (LSV) measurements were recorded at scan rate ν = 10 mV s^{-1}. Cyclic voltammetry (CV) in the non-faradaic region and electrochemical impedance spectroscopy (EIS) were also performed on the same instrument.

5.5.5 Computational Details

All DFT calculations are carried out with the Vienna Ab-initio Simulation Package (VASP) [100]. The Perdew-Burke-Ernzerhof (PBE) within the Generalized Gradient Approximation (GGA) [101] functional is adopted to treat exchange-correlation interactions. Model structures are allowed to relax until an energy difference of 10^{-5} eV and the force converges to less than 0.01 eV/Å with the kinetic energy cut off of 450 eV. The van der Waals interaction has been considered using the DFT-D2 scheme [102]. The thickness of vacuum layer was set at 20 Å to sufficiently avoid interactions between mirror images. The k-mesh of 3 × 3 × 1 was sampled by the Monkhorst-Pack method for geometry optimization of the system. To model the NC@MoS_2 heterostructure, we consider a 3 × 3-unit cell of MoS_2 and an N-doped graphene layer with a single C vacancy (NC).

5.6 References

[1] Y. Cao, ACS Nano 15 (2021) 11014–11039.

[2] H. Sun, Z. Yan, F. Liu, W. Xu, F. Cheng, J. Chen, Advanced Materials 32 (2020) 1806326.

[3] Z.W. Seh, J. Kibsgaard, C.F. Dickens, I.B. Chorkendorff, J.K. Nørskov, T.F. Jaramillo, Science (1979) 355 (2017) eaad4998.

[4] D.O. Ozgur, Fuel (2022) 125538.

[5] H. Nolan, C. Schröder, M. Brunet-Cabré, F. Pota, N. McEvoy, K. McKelvey, T.S. Perova, P.E. Colavita, Carbon N Y 202 (2023) 70–80.

[6] J.H. Montoya, L.C. Seitz, P. Chakthranont, A. Vojvodic, T.F. Jaramillo, J.K. Nørskov, Nat Mater 16 (2017) 70–81.

[7] N. Abidi, A. Bonduelle-Skrzypczak, S.N. Steinmann, ACS Appl Mater Interfaces 12 (2020) 31401–31410.

[8] J. Zhang, Y. Zhao, X. Guo, C. Chen, C.-L. Dong, R.-S. Liu, C.-P. Han, Y. Li, Y. Gogotsi, G. Wang, Nat Catal 1 (2018) 985–992.

[9] S.A. Shah, L. Xu, R. Sayyar, T. Bian, Z. Liu, A. Yuan, X. Shen, I. Khan, A.A. Tahir, H. Ullah, Chemical Engineering Journal 428 (2022) 132126.

[10] B. Gao, Y. Zhao, X. Du, D. Qian, S. Ding, C. Xiao, J. Wang, Z. Song, H.W. Jang, Adv Funct Mater (2023) 2214085.

[11] P. Gnanasekar, K.S. Ranjith, P. Manivel, Y.-K. Han, J. Kulandaivel, ACS Appl Energy Mater 3 (2020) 6717–6725.

[12] T.F. Jaramillo, K.P. Jørgensen, J. Bonde, J.H. Nielsen, S. Horch, I. Chorkendorff, Science (1979) 317 (2007) 100–102.

[13] J. Jia, T. Xiong, L. Zhao, F. Wang, H. Liu, R. Hu, J. Zhou, W. Zhou, S. Chen, ACS Nano 11 (2017) 12509–12518.

[14] L. Li, X. Wang, J. Li, Y. Guo, X. Li, Y. Lu, J Alloys Compd 872 (2021) 159562.

[15] N. Cheng, S. Stambula, D. Wang, M.N. Banis, J. Liu, A. Riese, B. Xiao, R. Li, T.-K. Sham, L.-M. Liu, Nat Commun 7 (2016) 13638.

[16] S. Maity, B. Das, M. Samanta, B.K. Das, S. Ghosh, K.K. Chattopadhyay, ACS Appl Energy Mater 3 (2020) 5067–5076.

[17] L. Zhang, X. Cao, C. Feng, W. Zhang, Z. Wang, S. Feng, Z. Huang, X. Lu, F. Dai, Inorg Chem 60 (2021) 12377–12385.

[18] M. Chhowalla, H.S. Shin, G. Eda, L.-J. Li, K.P. Loh, H. Zhang, Nat Chem 5 (2013) 263–275.

[19] J. Kibsgaard, Z. Chen, B.N. Reinecke, T.F. Jaramillo, Nat Mater 11 (2012) 963–969.

[20] Y. Liu, J. Wu, K.P. Hackenberg, J. Zhang, Y.M. Wang, Y. Yang, K. Keyshar, J. Gu, T. Ogitsu, R. Vajtai, Nat Energy 2 (2017) 1–7.

[21] F. Fioravanti, S. Martínez, S. Delgado, G. García, J.L. Rodriguez, E.P. Tejera, G.I. Lacconi, Electrochim Acta 441 (2023) 141781.

[22] Y. Tang, Y. Wang, X. Wang, S. Li, W. Huang, L. Dong, C. Liu, Y. Li, Y. Lan, Adv Energy Mater 6 (2016) 1600116.

[23] J. Yan, A. Rath, H. Wang, S.H. Yu, S.J. Pennycook, D.H.C. Chua, Mater Res Lett 7 (2019) 275–281.

[24] Y. Li, L.A. Zhang, Y. Qin, F. Chu, Y. Kong, Y. Tao, Y. Li, Y. Bu, D. Ding, M. Liu, ACS Catal 8 (2018) 5714–5720.

[25] D. Roy, B. Kumar Das, S.N. Riaz, D. Das, S. Sarkar, K.K. Chattopadhyay, ACS Appl Energy Mater 6 (2023) 4892–4908.

[26] J. Qin, C. Xi, R. Zhang, T. Liu, P. Zou, D. Wu, Q. Guo, J. Mao, H. Xin, J. Yang, ACS Catal 11 (2021) 4486–4497.

[27] I.S. Amiinu, Z. Pu, X. Liu, K.A. Owusu, H.G.R. Monestel, F.O. Boakye, H. Zhang, S. Mu, Adv Funct Mater 27 (2017) 1702300.

[28] J.D. Benck, T.R. Hellstern, J. Kibsgaard, P. Chakthranont, T.F. Jaramillo, ACS Catal 4 (2014) 3957–3971.

[29] H. Yu, Y. Xue, L. Hui, C. Zhang, Y. Zhao, Z. Li, Y. Li, Adv Funct Mater 28 (2018) 1707564.

[30] H. Wang, X. Xiao, S. Liu, C.-L. Chiang, X. Kuai, C.-K. Peng, Y.-C. Lin, X. Meng, J. Zhao, J. Choi, J Am Chem Soc 141 (2019) 18578–18584.

[31] S. Ramakrishnan, M. Karuppannan, M. Vinothkannan, K. Ramachandran, O.J. Kwon, D.J. Yoo, ACS Appl Mater Interfaces 11 (2019) 12504–12515.

[32] D. Li, Q. Luo, H. Xin, C. Wang, Y. Zhao, H. Bai, F. Ma, ACS Sustain Chem Eng 11 (2023) 5462–5472.

[33] S. Chandrasekaran, J. Feaster, J. Ynzunza, F. Li, X. Wang, A.J. Nelson, M.A. Worsley, ACS Materials Au 2 (2022) 596–601.

[34] J. Cui, L. Sun, L. Guo, Q. Sun, X. Feng, H. Yu, Y. Xiong, J Colloid Interface Sci 641 (2023) 166–175.

[35] Y. Zhou, C. Li, Y. Zhang, L. Wang, X. Fan, L. Zou, Z. Cai, J. Jiang, S. Zhou, B. Zhang, Adv Funct Mater 33 (2023) 2304302.

[36] M. Pan, L. Gao, P. Wang, X. Wang, H. Yu, J Alloys Compd 939 (2023) 168721.

[37] S.A. Shah, L. Xu, R. Sayyar, I. Khan, A. Yuan, X. Shen, X. Li, H. Ullah, Adv Mater Interfaces 9 (2022) 2201040.

[38] V.D. Dang, C.-Y. Hsiao, P.A. Le, V.Q. Le, D. Ho Phuong Thao, T.-H. Do, K.-H. Wei, ACS Appl Energy Mater 5 (2022) 12817–12827.

[39] Y.-G. Fu, H.-Q. Liu, C. Liu, Q.-F. Lü, J Alloys Compd 967 (2023) 171748.

[40] J. Ou, Y. Zhang, L. Chen, Q. Zhao, Y. Meng, Y. Guo, D. Xiao, J Mater Chem A Mater 3 (2015) 6534–6541.

[41] X. Hai, W. Zhou, K. Chang, H. Pang, H. Liu, L. Shi, F. Ichihara, J. Ye, J Mater Chem A Mater 5 (2017) 8591–8598.

[42] K. Chanda, S. Maiti, S. Sarkar, P. Bairi, S. Thakur, K. Sardar, N. Besra, N.S. Das, K.K. Chattopadhyay, ACS Appl Nano Mater 4 (2021) 1420–1433.

[43] P. Bairi, K. Minami, W. Nakanishi, J.P. Hill, K. Ariga, L.K. Shrestha, ACS Nano 10 (2016) 6631–6637.

[44] K. Chanda, S. Thakur, S. Maiti, A. Acharya, T. Paul, N. Besra, S. Sarkar, A. Das, K. Sardar, K.K. Chattopadhyay, in: 2018, p. 030138.

[45] P. Gnanasekar, D. Periyanagounder, J. Kulandaivel, Nanoscale 11 (2019) 2439–2446.

[46] W. Zheng, Y. Zhang, K. Niu, T. Liu, K. Bustillo, P. Ercius, D. Nordlund, J. Wu, H. Zheng, X. Du, Chemical Communications 54 (2018) 13726–13729.

[47] Y. Zhou, Y. Leng, W. Zhou, J. Huang, M. Zhao, J. Zhan, C. Feng, Z. Tang, S. Chen, H. Liu, Nano Energy 16 (2015) 357–366.

[48] Y. Ito, W. Cong, T. Fujita, Z. Tang, M. Chen, Angewandte Chemie International Edition 54 (2015) 2131–2136.

[49] Y. Yu, S. Yang, M. Dou, Z. Zhang, F. Wang, J Mater Chem A Mater 8 (2020) 16669–16675.

[50] K. Qu, Y. Zheng, X. Zhang, K. Davey, S. Dai, S.Z. Qiao, ACS Nano 11 (2017) 7293–7300.

[51] D. Merki, S. Fierro, H. Vrubel, X. Hu, Chem. Sci. 2 (2011) 1262–1267.

[52] J. Xie, H. Zhang, S. Li, R. Wang, X. Sun, M. Zhou, J. Zhou, X.W. (David) Lou, Y. Xie, Advanced Materials 25 (2013) 5807–5813.

[53] P. Bairi, K. Sardar, K. Chanda, M. Samanta, S. Thakur, K. Panigrahi, S. Sarkar, T. Paul, K.K. Chattopadhyay, ACS Appl Energy Mater 3 (2020) 5984–5992.

[54] P. Bairi, R.G. Shrestha, J.P. Hill, T. Nishimura, K. Ariga, L.K. Shrestha, J Mater Chem A Mater 4 (2016) 13899–13906.

[55] P. Bairi, S. Maji, J.P. Hill, J.H. Kim, K. Ariga, L.K. Shrestha, J Mater Chem A Mater 7 (2019) 12654–12660.

[56] X. Li, H. Zhu, Journal of Materiomics 1 (2015) 33–44.

[57] P. Bairi, R.G. Shrestha, J.P. Hill, T. Nishimura, K. Ariga, L.K. Shrestha, J Mater Chem A Mater 4 (2016) 13899–13906.

[58] M. Wu, J. Zhan, K. Wu, Z. Li, L. Wang, B. Geng, L. Wang, D. Pan, J Mater Chem A Mater 5 (2017) 14061–14069.

[59] X. Gan, L.Y.S. Lee, K. Wong, T.W. Lo, K.H. Ho, D.Y. Lei, H. Zhao, ACS Appl Energy Mater 1 (2018) 4754–4765.

[60] S. Bernard, O. Beyssac, K. Benzerara, N. Findling, G. Tzvetkov, G.E. Brown Jr, Carbon N Y 48 (2010) 2506–2516.

[61] A.C. Ferrari, J. Robertson, Phys Rev B 61 (2000) 14095.

[62] J. Pampel, T. Fellinger, Adv Energy Mater 6 (2016) 1502389.

[63] S. Makino, Y. Yamauchi, W. Sugimoto, J Power Sources 227 (2013) 153–160.

[64] X. Liu, W. Zhou, L. Yang, L. Li, Z. Zhang, Y. Ke, S. Chen, J Mater Chem A Mater 3 (2015) 8840–8846.

[65] H. Yan, Y. Xie, Y. Jiao, A. Wu, C. Tian, X. Zhang, L. Wang, H. Fu, Advanced Materials 30 (2018) 1704156.

[66] Y. Yun, Z. Shi, J. Shao, Q. Qu, Y. Gao, Z. Chen, Y. Chen, H. Zheng, ChemNanoMat 4 (2018) 1247–1253.

[67] J. Yan, L. Kong, Y. Ji, Y. Li, J. White, S. Liu, X. Han, S.-T. Lee, T. Ma, Commun Chem 1 (2018) 95.

[68] Z. Xu, H. Wang, Z. Li, A. Kohandehghan, J. Ding, J. Chen, K. Cui, D. Mitlin, The Journal of Physical Chemistry C 118 (2014) 18387–18396.

[69] Y. Huang, J. Ge, J. Hu, J. Zhang, J. Hao, Y. Wei, Adv Energy Mater 8 (2018) 1701601.

[70] D. Zhao, K. Sun, W. Cheong, L. Zheng, C. Zhang, S. Liu, X. Cao, K. Wu, Y. Pan, Z. Zhuang, Angewandte Chemie 132 (2020) 9067–9075.

[71] Y. Yun, J. Shao, Y. Chen, Z. Cao, Q. Qu, H. Zheng, ACS Appl Nano Mater 2 (2019) 1883–1889.

[72] N. Pentland, J. Bockris, E. Sheldon, J Electrochem Soc 104 (1957) 182.

[73] W. Sheng, H.A. Gasteiger, Y. Shao-Horn, J Electrochem Soc 157 (2010) B1529.

[74] X. Han, X. Tong, X. Liu, A. Chen, X. Wen, N. Yang, X.-Y. Guo, ACS Catal 8 (2018) 1828–1836.

[75] Z. Huang, W. Luo, L. Ma, M. Yu, X. Ren, M. He, S. Polen, K. Click, B. Garrett, J. Lu, Angewandte Chemie International Edition 54 (2015) 15181–15185.

[76] Á. León-Reyes, M. Epifani, T. Chávez-Capilla, J. Palma, R. Díaz, Int J Electrochem Sci 9 (2014) 3837–3845.

[77] J.D. Benck, Z. Chen, L.Y. Kuritzky, A.J. Forman, T.F. Jaramillo, ACS Catal 2 (2012) 1916–1923.

[78] J. Kibsgaard, Z. Chen, B.N. Reinecke, T.F. Jaramillo, Nat Mater 11 (2012) 963–969.

[79] F. Lai, Y.-E. Miao, Y. Huang, Y. Zhang, T. Liu, ACS Appl Mater Interfaces 8 (2016) 3558–3566.

[80] Z. Zhang, W. Li, M.F. Yuen, T.-W. Ng, Y. Tang, C.-S. Lee, X. Chen, W. Zhang, Nano Energy 18 (2015) 196–204.

[81] H. Huang, L. Chen, C. Liu, X. Liu, S. Fang, W. Liu, Y. Liu, J Mater Chem A Mater 4 (2016) 14577–14585.

[82] W. Dong, H. Liu, X. Liu, H. Wang, X. Li, L. Tian, Int J Hydrogen Energy 46 (2021) 9360–9370.

[83] B. He, L. Chen, M. Jing, M. Zhou, Z. Hou, X. Chen, Electrochim Acta 283 (2018) 357–365.

[84] X. Zhang, F. Zhou, S. Zhang, Y. Liang, R. Wang, Advanced Science 6 (2019) 1900090.

[85] H. Huang, W. Huang, Z. Yang, J. Huang, J. Lin, W. Liu, Y. Liu, J Mater Chem A Mater 5 (2017) 1558–1566.

[86] K.-C. Pham, Y.-H. Chang, D.S. McPhail, C. Mattevi, A.T.S. Wee, D.H.C. Chua, ACS Appl Mater Interfaces 8 (2016) 5961–5971.

[87] J. Rong, G. Zhu, W.R. Osterloh, Y. Fang, Z. Ou, F. Qiu, K.M. Kadish, Chemical Engineering Journal 412 (2021) 127556.

[88] X. Peng, C. Huang, B. Zhang, Y. Liu, Int J Hydrogen Energy 45 (2020) 27193–27201.

[89] H. Li, X. Qian, C. Xu, S. Huang, C. Zhu, X. Jiang, L. Shao, L. Hou, ACS Appl Mater Interfaces 9 (2017) 28394–28405.

[90] X. Wang, S. Fei, S. Huang, C. Wu, J. Zhao, Z. Chen, K. Uvdal, Z. Hu, Carbon N Y 150 (2019) 363–370.

[91] H. Wang, Q. Yi, L. Gao, Y. Gao, T. Liu, Y.-B. Jiang, Y. Sun, G. Zou, Nanoscale 9 (2017) 16342–16348.

[92] L. Xu, Y. Zhang, L. Feng, X. Li, Y. Cui, Q. An, ACS Appl Mater Interfaces 13 (2021) 734–744.

[93] J. Xie, H. Zhang, S. Li, R. Wang, X. Sun, M. Zhou, J. Zhou, X.W. Lou, Y. Xie, Advanced Materials 25 (2013) 5807–5813.

[94] B. Guo, K. Yu, H. Li, H. Song, Y. Zhang, X. Lei, H. Fu, Y. Tan, Z. Zhu, ACS Appl Mater Interfaces 8 (2016) 5517–5525.

[95] P. Bairi, K. Sardar, M. Samanta, K. Chanda, K.K. Chattopadhyay, Mater Chem Front 5 (2021) 7645–7653.

[96] S. Ruidas, B. Mohanty, P. Bhanja, E.S. Erakulan, R. Thapa, P. Das, A. Chowdhury, S.K. Mandal, B.K. Jena, A. Bhaumik, ChemSusChem 14 (2021) 5057–5064.

[97] B.T. Jebaslinhepzybai, T. Partheeban, D.S. Gavali, R. Thapa, M. Sasidharan, Int J Hydrogen Energy 46 (2021) 21924–21938.

[98] R. Shwetharani, S. Kapse, R. Thapa, D.H. Nagaraju, R.G. Balakrishna, ACS Appl Energy Mater 3 (2020) 12682–12691.

[99] S. Sarkar, L. Dheer, C.P. Vinod, R. Thapa, U. V Waghmare, S.C. Peter, ACS Appl Energy Mater 3 (2020) 1271–1278.

[100] G. Kresse, J. Furthmüller, Comput Mater Sci 6 (1996) 15–50.

[101] J.P. Perdew, K. Burke, M. Ernzerhof, Phys Rev Lett 77 (1996) 3865.

[102] S. Grimme, J Comput Chem 27 (2006) 1787–1799.

Chapter 6: Hierarchical Heterostructure of MoS_2 Flake Anchored on TiO_2 Sphere for Supercapacitor Application

Hierarchical architectures realized via rational coupling of several components not only boast synergy driven raised functionality compared to their structural constituents also exhibit noble interface phenomena, thus made them significantly pertinent from research and technological point of view. Here in, geometrically intricate hierarchical nanoform constituting MoS_2 nanoflakes anchored on TiO_2 sphere was realized via two steps hydrothermal protocol. Initially TiO_2 sphere was synthesized using titanium isopropoxide assisted hydrothermal route followed by which the sphere was used as scaffold for secondary growth of MoS_2. As synthesized hybrid sample displayed much improved electrochemical behavior than pristine TiO_2 sphere. Assessed value of specific capacitance for the hybrid is found to 152.2 F/g at current density of 0.1 A/g which is 30-fold than TiO_2 sphere. This electrochemical performance enhancement can be accredited to high surface area of the hybrid sample.

6.1 Introduction

Sustainable research in past decades on electrochemical electronic devices had engaged to the fast evolution of supercapacitors (SCs), also labelled as electrochemical capacitors with high power density, long cycle duration, fast charging discharging rates and etc. [1–3] Using a broader view, on the basis of different charge storage principle SCs can be categorize in two different class namely electrical double-layer capacitors (EDLCs) and pseudocapacitors. Fast reversible redox reaction on the surface of electrode offers more higher performance for pseudocapacitor as compare to EDLCs where the later one rely mainly on ion adsorption. EDLCs are mostly fabricated using carbonaceous materials like activated carbon, graphene, carbon nanotube whereas pseudocapacitors are generally design with transition metal oxides (TMOs), transition metal halides, conducting polymer and etc. Owing to their high energy state and multiple oxidation states TMOs are considered as one of the most promising electrode materials for pseudocapacitors [2]. From the broad genre of TMOs titanium oxide (TiO_2) nanoform have already established their dominance as SCs due to their low toxicity, chemical stability, earth abundance, wide potential window and environmentally benign nature [2] Despite these merits, TiO_2 nanoforms offer relatively small specific capacitance (100–900 $\mu F/cm^2$) due to their poor electrical conductivity which limits their commercial utilization [3]. On the same frame, 2D molybdenum disulfide (MoS_2) nanoforms have garnered increasing attention as electrode material of SCs where its typical layered structure provides support for charge storage via inter and intra sheet layers [4]. In order to increase the electrochemical behavior of binary TMO several protocols were adopted by researchers amongst which facile realization of hybrid via amalgamation of physical and chemical features of multiple materials is one of the well accepted paths [5,6].

In this work, adopting environment friendly, low temperature hydrothermal synthesis protocols we have realized geometrically intricate 3D hierarchical nanoform based on TiO_2 sphere and MoS_2 flake. Successful preparation of nanoform was investigated via different characterization techniques. As an immediate usage of these nanoforms we have examined their electrochemical performance which showed much improved behavior than pristine TiO_2. Such enhancement performance registered from hybrid is explained on the basis of increased surface area due to wrapping of MoS_2 flakes over TiO_2 sphere.

6.2 Experimental

TiO_2 spheres were synthesized via hydrothermal process. In a typical procedure, 0.02 mL diethylenetriamine were mixed with 42 mL of isopropyl alcohol and stirred for 10 minutes. 1.5 mL of titanium isopropoxide was added with the aforesaid solution. Finally the entire solution was transferred into a 60 mL Teflon lined autoclave and maintained at temperature 200°C for 24 h in laboratory oven. After the reaction span it was cool down naturally and product was collected by centrifuging. Prior to secondary growth, the product was annealed at 400°C for 2 h to achieve better crystallinity.

For the preparation of TiO_2-MoS_2 hybrid, appropriate amount as synthesized TiO_2 powder and 0.15 g cetyltrimethylammonium bromide were dissolved in 30 mL de-ionized water and stirred for 20 minutes. Two separate solutions of sodium molybdate and thioacetamide were further added to the above solution and stirred for more 10 min. Thereafter, total suspension solution was transferred to 60 mL autoclave and kept at 180°C for 36 hrs. After cooling to room temperature naturally, the precipitate was collected by centrifugation and dried at 60 °C.

6.3 Preparation of Electrodes

Working electrodes were prepared with synthesized samples, carbon Black, PVDF in a weight ratio of 8:1:1. Small amount of NMP was added with the above mixture to obtain a uniform paste. Finally, the pastes were pressed onto nickel foam and the substrate was then dried overnight at 60°C in vacuum oven.

6.4 Characterization

Morphology of the samples was inspected with field emission scanning electron microscope (FESEM, HITACHI-S4800) whereas their crystalline phase was investigated with X-ray diffraction studies (XRD, D8 Advanced Bruker). EDS analysis was carried out by EDS analyzer attached with FESEM. Electrochemical experiment was performed in a three-electrode cell of Gamry Interface 1000.

6.5 Results and Discussion

FESEM image of TiO_2 sphere is displayed in Figure 1a. Besides large-scale morphological uniformity of the synthesized product this figure also depicts variation in their individual diameter. Average dimensional of the sphere is ~ 1.5 μm. Careful observation of an individual sphere in high magnification view (Fig 1a inset) suggests particulate nature of the surface. Further hydrothermal treatment of these spheres creates a drastic change in their morphology (Figure 1b). Surface of the pristine sphere becomes rough and uneven which is completely different form its previous state. Zoom in view of the side surface discloses appearance of numerous flakes after hydrothermal treatment (Figure 1c). These interconnected flakes covered the entire side surface of sphere and create a flower like pattern. Average thickness of the flake is ~ 20 nm. Phase purity and crystal structure of hybrid along with TiO_2 sphere were investigated via XRD and results are displayed in Figure 1d. All peaks in the figure can be indexed to TiO_2 and MoS_2. Strong

diffraction peaks can be indexed to tetragonal anatase TiO_2 (JCPDS card no. 21-1272). After the secondary growth an additional peak appears in profile which can be indexed to

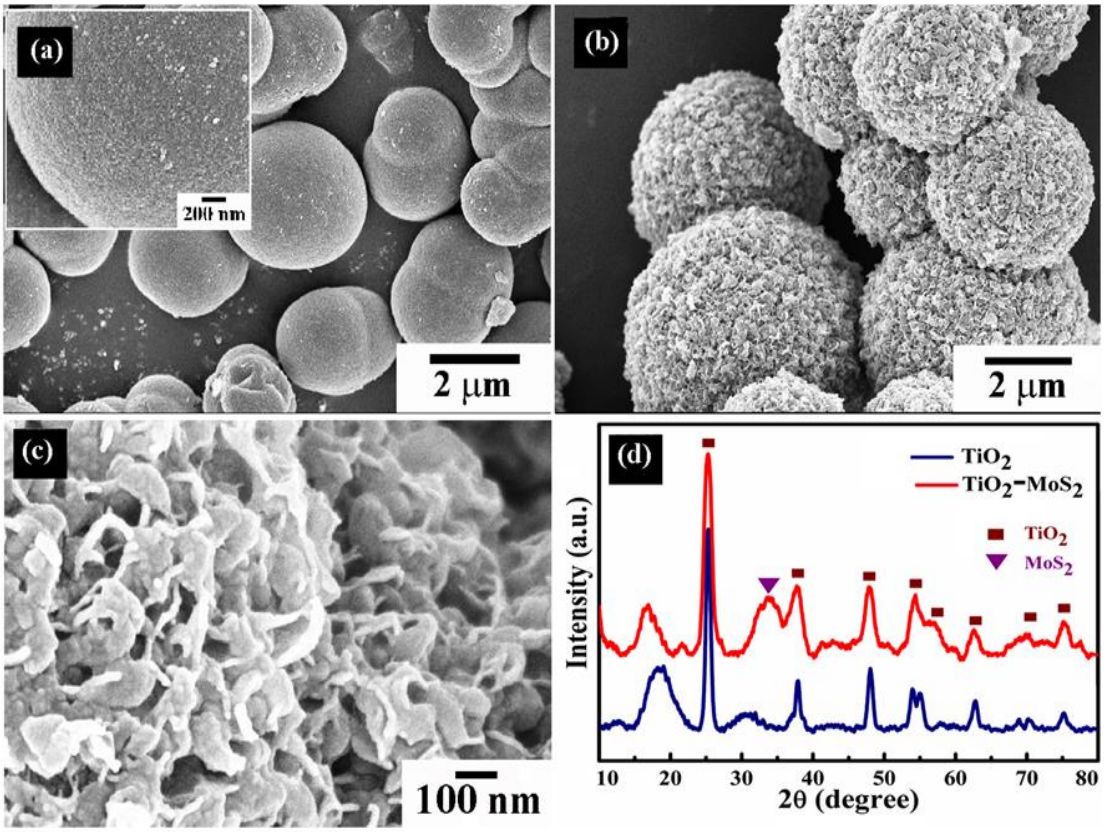

Figure 1: (a-c) FESEM images and (d) XRD profile of the synthesized samples.

MoS_2. Absence of other peaks in XRD patterns validates high purity of the samples. For exact elemental composition of hybrid EDS analysis was carried out and the result is shown in Figure 2. Form the spectrum only presence of Ti, O, Mo, S and C is obvious among which inevitable carbon came from atmosphere. Absence of any impurity related peaks in EDS profile substantiate the XRD result. Elemental mapping of constituent elements of MoS_2 coated TiO_2 sphere were further executed which suggests homogenous distribution of Ti, O, Mo and S in the hybrid.

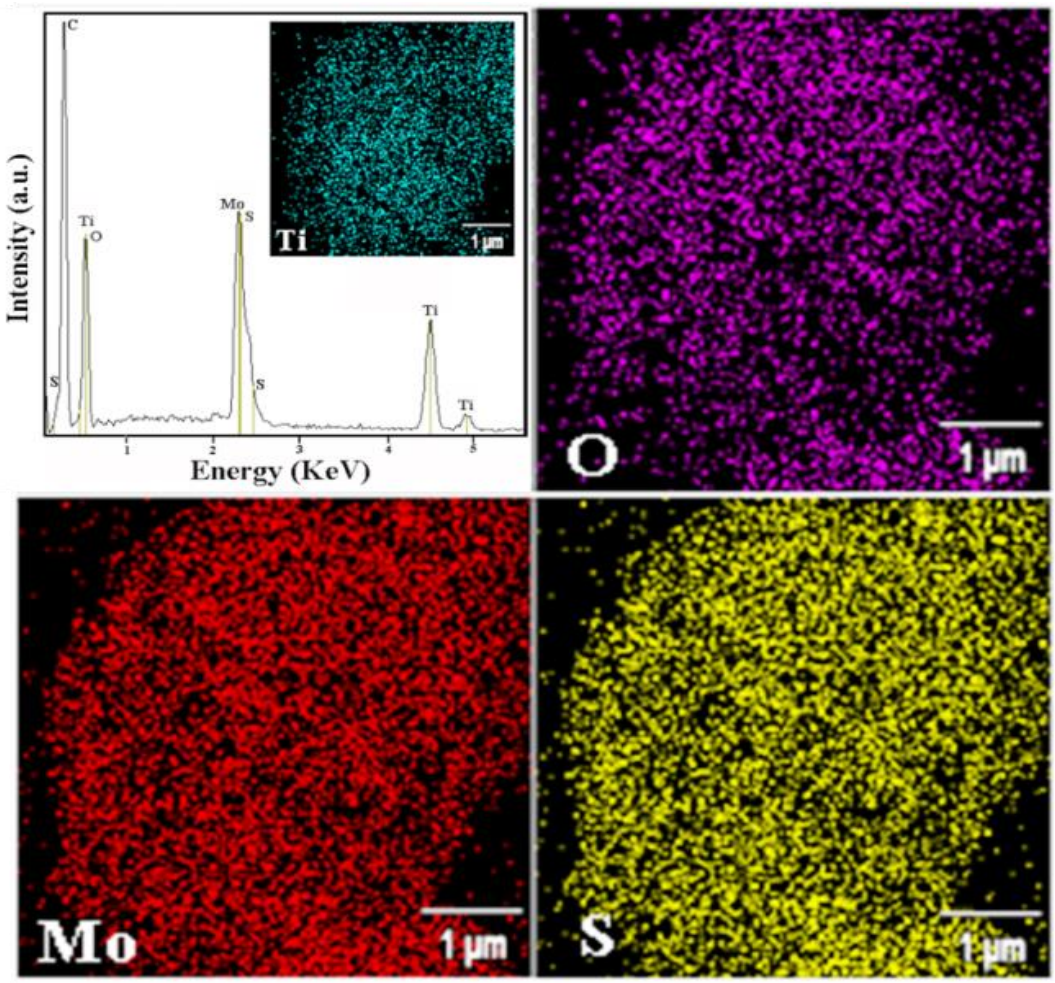

Figure 2: EDS elemental mapping and spectra of the hybrid sample.

Electrochemical performance of the synthesized TiO_2-MoS_2 hybrid and TiO_2 as supercapacitor were examined by taking KOH within the potential range 0-0.6V vs (Ag/AgCl). A pair of redox peaks appears in CV which signifies pseudocapacitive behavior of the hybrid. Enhancement in current as well as in area under curve for hybrid compared to TiO_2 sphere is obvious from Fig. 3a. The CV curves of hybrid at different scan rate are shown in fig 3b. Specific capacitance value is found to increase from 61.3 F/g at a scan rate of 100 mV/s to 280F/g at a scan rate of 5mV/s. Fig 1.c revealed the galvanostatic charge discharge characteristics comparison of TiO_2 and TiO_2-MoS_2. Prolonged charging discharging time for the hybrid may accounted from the longer effective path passage after

MoS_2wrapping on TiO_2. Registered capacitance value for the hybrid is found to 152.2 F/g at a current density of 0.1 A/g where the same for TiO_2 is only ~ 4.83 F/g at same current density. Increment in the specific capacitance value is attributed to the upsurge in overall surface area. Further, to investigate the electrochemical behavior in detail, Electrochemical Impedance Spectroscopy (EIS) analysis was carried out. Calculated equivalent Series resistance (ESR) of the hybrid is found to much lower (1.72Ω) as compared to sole TiO_2 (10.8Ω).

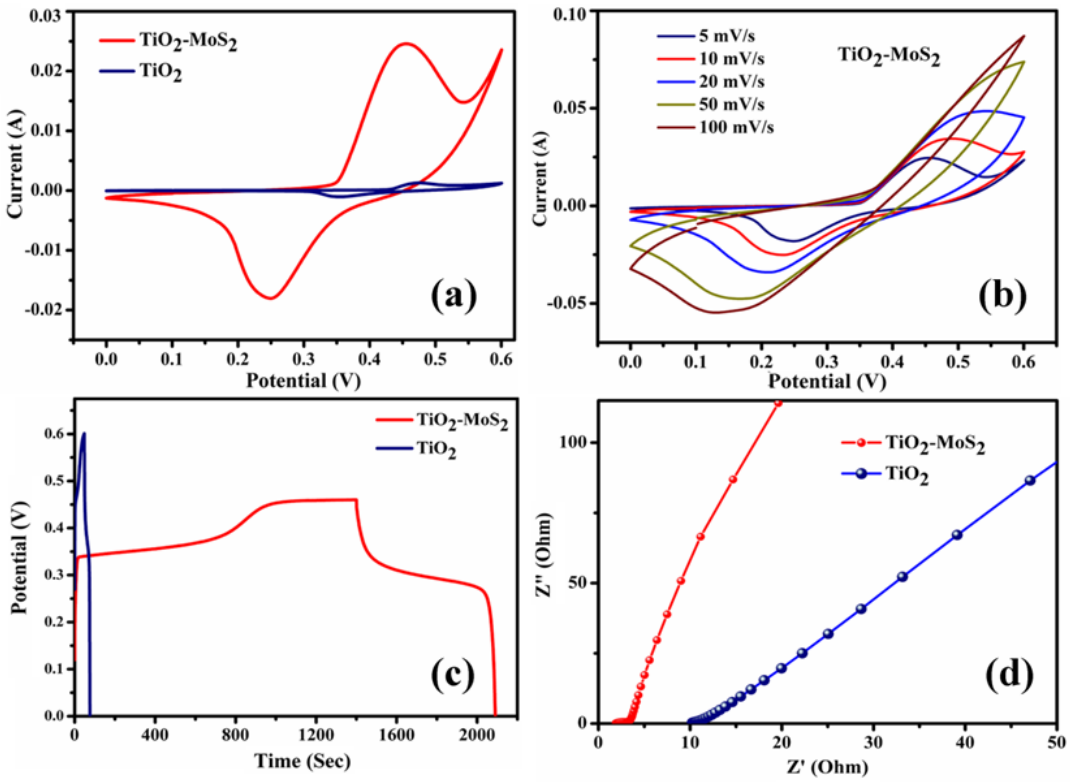

Figure 3: CV curves (a) at a scan rate of 5 mV/s (b) for hybrid at different scan rates, (c) CD curves, (d) EIS spectra.

6.6 Conclusion

In nutshell, we have realized geometrically intricate 3D hierarchical nanoform constituting transition metal oxide namely TiO_2 and transition metal sulfide namely MoS_2 via low temperature hydrothermal method. Successful formation of hybrid nanoform was

confirmed by XRD and EDX analysis. The as prepared hybrid displayed synergy driven much better electrochemical performance than TiO_2. Such enhancement is accredited to overall surface area enrichment due to MoS_2 growth on TiO_2. Besides their usage as supercapacitor this morphology tuned hierarchical nanoform can be utilized for several other applications like photocatalysis, batteries and etc.

6.7 References

[1] R. Lin, Z. Zhu, X. Yu, Y. Zhong, Z. Wang, S. Tan, C. Zhao, W. Mai, J Mater Chem A Mater 5 (2017) 814–821.

[2] A. Ramadoss, S.J. Kim, Int J Hydrogen Energy 39 (2014) 12201–12212.

[3] B. Gao, X. Li, Y. Ma, Y. Cao, Z. Hu, X. Zhang, J. Fu, K. Huo, P.K. Chu, Thin Solid Films 584 (2015) 61–65.

[4] X. Li, X. Li, J. Cheng, D. Yuan, W. Ni, Q. Guan, L. Gao, B. Wang, Nano Energy 21 (2016) 228–237.

[5] Y. Zhao, X. Li, L. Dong, B. Yan, H. Shan, D. Li, X. Sun, Int J Hydrogen Energy 40 (2015) 14338–14344.

[6] H. Zhou, X. Zou, Y. Zhang, Electrochim Acta 192 (2016) 259–267.

Chapter 7: Grand Conclusions & Future Prospect

7.1 Grand Conclusion

Here in this chapter, we will discuss about the significant findings of this dissertation. This thesis mainly focuses on the hierarchy of transition metal-based semiconductor for energy related applications. Electrodes of (i) $CuCo_2O_4$@MnO_2 hierarchy grown on carbon fabric, (ii) hierarchy of nitrogen doped graphitic carbon and MoS_2 and (iii) TiO_2@MoS_2 hierarchical heterostructure have been employed in electrochemical energy applications such as Supercapacitor, HER etc. Hence, noteworthy findings of these works are summarized below:

- A two-step facile hydrothermal synthesis protocol was carried out to yield 2D–2D $CuCo_2O_4$@MnO_2 hierarchy on flexible carbon fabric. The structural morphology and phase purity of the as-synthesised hybrid was rigorously optimised. The carbon fabric supported hierarchical hybrid was directly used as a supercapacitor electrode which further demonstrated its potential usage in high-performance binder free supercapacitor application. In three-electrode configuration the well optimized $CuCo_2O_4$@MnO_2 electrode (CMH) offered a high specific capacitance of 1458 F/g at a current density of 0.5 A/g along with a stable rate capability and ~ 93% retention of capacitance. To fulfil the criterion of flexible electronics, the symmetric solid-state flexible supercapacitor (SSFC) was devised and performance of CMH in this two-electrode configuration was further checked and it displayed a high gravimetric capacitance of 181.3 F/g at a current density of 2.8 A/g along with superior cyclic stability. The obtained results were excellent enough to use this optimized $CuCo_2O_4$@MnO_2 hierarchy in an actual energy storage system. Different assembly (Series and parallel) of SSFC devices were able to run a motor fan for 8 seconds, a digital display clock for roughly 45 minutes and different coloured LEDs for several minutes. Such successful realization of a

hierarchical hybrid system based on transition metal oxides marks a significant advancement towards the methodical creation of innovative hybrid materials for energy storage application.

- In this work, hierarchy of MoS_2 Nanosheets (NSs) and polymer (PNMA) hollow spheres was realized. Initially, PNMA hollow sphere was synthesized following an interfacial polymerization protocol and thereafter a hydrothermal route was carried out to synthesize PNMA@MoS_2 hierarchical nanostructure. Further, high temperature annealing altered crystallinity of MoS_2 drastically and converted PNMA to N-doped carbon (NC) with graphitic ordering, both of which had a significant effect on the electrocatalytic performance. The well optimized hierarchical hybrid (*i.e.* NC@$MoS_2$1100) demonstrated superior HER performance with a low overpotential of 145 mV at a current density of 10 mA cm^{-2}, a small Tafel slope of 39 mV dec^{-1} and a chronoamperometric stability in acidic media. This excellent HER activity results from the combination of the distinctive morphology of NC@$MoS_2$1100 (*i.e.*, a typical hollow flower-like structure), a protective layer of NC, and interfacial Mo–N–C bonds. This Mo−N−C bond at interface of NC Matrix and MoS_2 NSs accelerated the easy charge transfer and reduced the Gibbs free energy for effective HER which was further supported by DFT calculations. Hence, this study emphasises how interfacial chemical bond engineering influences the morphology, phase, crystallinity of the hierarchical nanoform through subtle variation in annealing temperature to achieve superior HER performance.
- In this work, following a two-step hydrothermal process, a hierarchical heterostructure comprising MoS_2 nanoflakes anchored on TiO_2 spheres was synthesized. In the beginning, TiO_2 spherical nanostructure was synthesized

through a hydrothermal protocol taking titanium isopropoxide as precursor. In the second step, again a hydrothermal protocol was carried out in which as synthesized TiO_2 spheres served as the platform for the secondary MoS_2 nanosheet growth. Compared to a pristine TiO_2 sphere, the TiO_2@MoS_2 core-shell type hierarchical hybrid showed significantly better electrochemical performance. At a current density of 0.1A/g, the hybrid demonstrated a specific capacitance value of 152.22 F/g which was found to be 30-fold higher than that of the pristine TiO_2 sphere. The unique hierarchical architecture TiO_2@MoS_2 of incorporates its large specific surface area as well as synergy driven combined effects from both the TiO_2 core and MoS_2 shell to achieve improved electrochemical performance.

Therefore, the application of hierarchical heterostructures comprising transition metal-based semiconductors in the field of energy harvesting and storage is the primary focus of this thesis. The transition metal-based salts or precursors used to synthesize the hierarchy of nanostructures mentioned in Chapter 4-6 are earth abundant, low toxic which further allows the scope for fabricating affordable, environment friendly devices.

7.2 Future Scope

This thesis comprises details analysis of hierarchy transition metal-based materials like $CuCo_2O_4$, MnO_2, MoS_2 and TiO_2 along with carbonaceous materials for their application in energy production and storage. Nonetheless, there is still a huge scope for development in terms of device fabrication, application of appropriate composite materials, synthesis of new hierarchies etc. In addition to having higher functionality due to synergy between their structural constituents, hierarchical architectures that are realised through the rational coupling of multiple components also display noble interface phenomena, making them extremely relevant from a technological and research standpoint. By tuning the

material shape and morphology, optical properties can be enhanced, which can be beneficial for its application in sensors, photodetectors, photocatalysis, etc. These semiconductors can be combined further with carbon nanotubes, other transition metal-based compounds and conducting polymers such as polypyrrole or polyaniline to create novel hierarchies and composite materials that can be employed to create electrodes for supercapacitors, electrochemical HER, ORR, and OER, Na- or Li-ion batteries etc.